

**Femtoscopic $p\Lambda$ and $\gamma\gamma$ Correlations
in Pb-Pb Collisions at $\sqrt{s_{\text{NN}}} = 2.76$ TeV
with ALICE**

Dissertation
zur Erlangung des Doktorgrades
der Naturwissenschaften

vorgelegt beim Fachbereich Physik
der Johann Wolfgang Goethe-Universität
in Frankfurt am Main

Hans Beck
aus Friedberg (Hessen)

Frankfurt 2015
(D 30)

vom Fachbereich Physik der
Johann Wolfgang Goethe-Universität als Dissertation angenommen.

Dekan: Prof. Dr. René Reifarth
Gutachter: Prof. Dr. Christoph Blume
Prof. Dr. Harald Appelshäuser
Datum der Disputation:

Zusammenfassung

Schwerionenkollisionen bei ultrarelativistischen Energien erlauben den Zugang zum Quark-Gluon-Plasma (QGP), der Phase der Quanten-Chromo-Dynamik (QCD) in der die farbgeladenen Partonen frei auftreten und nicht länger in farblosen Hadronen eingeschlossen sind. Die Idee der Existenz eines QGPs existiert schon seit längerem, so zeigten N. Cabibbo und G. Parisi bereits 1975, dass die limitierende Hagedorn-Temperatur in “jedem Modell, wo hadronische Materie einen Phasenübergang zweiter Ordnung hat”, realisiert ist. Ein Problem bei der Untersuchung stark interagierender Systeme ist die Farbladung der Gluonen. Wie von D.J. Gross, F. Wilczek und H.D. Politzer bewiesen, nimmt dadurch die Kopplungskonstante α_s mit kleinerem Impulsübertrag zu. Dies führt dazu, dass perturbative Techniken in der Berechnung der Prozesse nicht länger anwendbar sind. Eine Lösung kann in Gitter-QCD-Rechnungen gefunden werden. Der endliche Abstand der Berechnungspunkte führt zu einer Begrenzung der auftretenden Impulse im ultra-violetten Bereich. Die Einführung dieser Dissertation zeigt, wie Gitter-QCD die Berechnung des Quark-Antiquark-Potentials erlaubt, und erschließt die Vorhersage des Phasenübergangs aus Gitterkalkulationen. Ausserdem wird der Zusammenhang zwischen Skalentransformationen und der Spuranomalie der QCD hergestellt. Dies ist von Interesse, da die Spuranomalie direkt der Zustandsgleichung der stark wechselwirkenden Materie entspricht, die so von Gitterrechnungen bestimmt werden kann.

Wie der Rückblick der Resultate der experimentellen Kollaborationen am Super-Proton-Synchrotron (SPS), dem Relativistischen Heavy-Ion-Collider (RHIC) und dem Large-Hadron-Collider (LHC) zeigt, werden dort bei den untersuchten Schwerionenkollisionen Energiedichten von mehreren GeV/fm^3 erreicht, sodass die theoretisch vorhergesagte Schwelle zur Erzeugung des QGPs überschritten wird.

Die mannigfaltigen, am SPS durchgeführten Analysen ergeben zusammengenommen einen indirekten Beweis der Erzeugung des QGPs. Hierzu zählen unter Anderem die erhöhte Seltensamkeitsproduktion in Schwerionenkollisionen, die der allgemeinen Vorstellung nach durch die verminderte Energieschwelle in der Phase der freien Quarks von ca. 200 MeV im Vergleich zu den ungefähr 670 MeV in der hadronischen Umgebung hervorgerufen wird, oder die Unterdrückung der gemessenen J/ψ -Produktion in zentralen Blei-Blei-Stößen, die aus der Debye-ähnlichen Abschirmung der Farbladung resultieren kann.

Drei essentielle Messungen am RHIC veränderten unsere Sichtweise des QGPs radikal. War, geprägt durch die asymptotische Freiheit, die Vorstellung des QGPs anfangs noch die eines schwach interagierenden Gases, so zeigt die Messung des elliptischen Flusses, der auf Grund der unterschiedlichen Druckgradienten in nicht-zentralen Kollisionen auftritt, dass die Scherviskosität des QGPs verschwindend gering ist, weshalb das QGP auch als perfekte Flüssigkeit bezeichnet wird. Dieses Bild wird außerdem unterstützt durch die Bestimmung des nuklearen Modifikationsfaktors, der Häufigkeit des Auftretens von Teilchen mit hohen Transversalimpulsen in Schwerionenkollisionen im Vergleich zu Proton-Proton-Ereignissen, die mit der Anzahl der anfänglichen harten Stöße skaliert werden. Es ergibt sich eine Unterdrückung von energiereichen Teilchen, was durch die immense Wechselwirkung mit dem farbgeladenen Medium erklärt wird. Genauso wird ein hochenergetisches Triggerteilchen nicht von einem balancierenden Jet begleitet. Vielmehr bewirkt die Triggerbedingung eine Tendenz der Beobachtung von Teilchen aus oberflächennahen harten Stößen wodurch das in die entgegengesetzte Richtung emittierte Parton durch das Medium propagiert und dabei von den heftigen Interaktionen mit der farbgeladenen Materie gestoppt wird.

Der LHC am Europäischen Kernforschungszentrum erlaubt Pb-Pb-Kollisionen mit Schwerpunktsenergien der einzelnen Nukleon-Kollisionen von 2.76 TeV. Diese vorher unerreichte Wucht der Zusammenstöße bringt mit sich, dass die Kernmaterie länger in der QGP-Phase verweilt, sodass die entwickelten Beobachtungsgrößen sensitiver auf die Eigenschaften, wie zum Beispiel die Scherviskosität, des QGPs sind. Während am RHIC die Bestimmung der Charakteristiken des QGPs sich eher auf qualitative Aspekte beschränkte, ist Zielsetzung für die Messungen am LHC die Quantifizierung dieser Merkmale. Den bisherigen Publikationen der ALICE-Kollaboration gelingt dies durch die Veröffentlichung von Daten mit einer nie dagewesenen, hochauflösenden und multidimensionalen Darstellung der Observablen in Abhängigkeit anderer Beobachtungsgrößen. So zeigt sich beispielsweise, dass das am RHIC gefundene Skalieren des elliptischen Flusses mit der Anzahl der Konstituentenquarks am LHC nur approximativ gilt. Die beeindruckende statistische Qualität dieser Analyse zeigt die Schwachstellen der theoretischen Modelle auf und erlaubt so die detaillierte Bestimmung der materiellen Eigenschaften des QGPs. Neue Observablen sind erstmals am LHC zugänglich. Die Untersuchung nicht nur von Teilchen mit hohem Transversalimpuls sondern auch die volle Rekonstruktion des Jets an Spuren in den Detektoren erlaubt es den Energieverlust der Partonen zu verstehen. Es zeigt sich, dass die Unterdrückung im nuklearen Modifikationsfaktor auch für diese kollimierten Jets mit hohem Transversalimpuls sichtbar ist. War die Vorstellung vor dem Start des LHCs, dass Teilchen mit hohem Transversalimpuls ihre Energie in abgestrahlten Partikeln bei kleinen bis mittleren Winkeln relativ zur Achse des Jets verlieren, so zeigt sich durch die Daten von ALICE, dass die winkelabhängige Fragmentation innerhalb der Jets gegenüber Proton-Proton-Kollisionen unverändert ist; die Energie wird demnach zu Teilchen mit kleinem Transversalimpuls bei großen Winkeln transportiert. Ein ähnliches Ergebnis zeigt die Untersuchung des Verhältnisses der Anzahl von Protonen zu Pionen innerhalb des Jets um ein Teilchen mit hohem Transversalimpuls

und außerhalb dessen. Ist generell dieses Verhältnis in Schwerionenkollisionen im Vergleich zu Proton-Proton-Kollisionen erhöht, so ergibt sich in den Pb-Pb-Kollisionen am LHC innerhalb des Jets der gleiche Wert wie in Proton-Proton-Kollisionen. Dies ist besonders interessant, da z.B. ein sonst sehr erfolgreiches Modell durch die Interaktion der Partonen mit hohem Transversalimpuls mit dem Medium einen Imprint des Mediums im Jet erwarten würde. Durch die Daten der ALICE-Kollaboration werden somit die mikroskopischen Interaktionsmechanismen innerhalb des QGP bestimmt.

Das Gros der partonischen Materie wird gut durch hydrodynamische Kalkulationen beschrieben. Diese bieten einen Rahmen in dem Anfangsbedingungen unter Berücksichtigung der Eigenheiten der wechselwirkenden Masse weiterentwickelt werden. Hierbei wird ein lokales thermodynamisches Gleichgewicht angenommen, das es erlaubt die Beschreibung mit statistischen Größen wie Druck und Energiedichte durchzuführen. Eine Relation dieser beiden angesprochenen Observablen ist hierbei eine Bedingung um die numerischen Rechnungen zu ermöglichen, sie kann, wie bereits erwähnt, durch quantenchromodynamische Gitterrechnungen erhalten werden. Die hier vorliegende Arbeit beschreibt anhand einer einfachen hydrodynamischen Modellierung einer Pb-Pb-Kollision den Einfluß der Eigenschaften des QGPs auf die Evolution des Feuerballs. In diesem simplen Beispiel, als auch in modernen Modellen, zeigt sich die Größe des Mediums zum Zeitpunkt des kinetischen Ausfrierens der Teilchen als besonders sensitiv auf die Charakteristiken des QGPs. Diese kann durch die Stärke der Korrelation von quantenstatistisch, stark oder elektromagnetisch wechselwirkenden Teilchenpaaren bestimmt werden.

Von besonderem Interesse ist die dynamische Entwicklung des stark interagierenden Mediums und die korrekte Beschreibung dieser in hydrodynamischen Modellen. Durch das Konkurrieren der thermalen mit der kollektiven Geschwindigkeit ergibt sich eine Abhängigkeit der beobachteten Größe des Feuerballs von der transversalen Masse eines Paares von korrelierten Teilchen. Traditionell werden die Ausmaße des Feuerballs durch die quantenstatistischen Korrelationen von Pionen bestimmt. Experimentell kann der beobachtete Bereich in der transversalen Masse durch das Messen von Paaren aus schwereren Teilchen erweitert werden. Paare aus Protonen und Lambda-Partikeln sind dabei die schwersten Teilchen, die bisher erfolgreich untersucht wurden um einen Quellenradius zu bestimmen. Neben ihrer hohen Masse besitzen Proton-Lambda-Paare weitere Vorteile, zum Beispiel zeigen sie sich im Gegensatz zu Proton-Proton-Paaren sensitiv auf die Ausdehnung der Quelle auch für große Radien. Somit bieten Proton-Lambda-Korrelationen einen Test der Validität des hydrodynamischen Ansatzes bei größten transversalen Massen. Gegenstand einer aktuellen Debatte ist, ob verschiedene Spezies von Teilchen bei gleicher transversalen Masse den selben Quellenradius aufweisen, also der Quellenradius mit der transversalen Masse skaliert. Sowohl in einer theoretischen Rechnung, als auch in experimentellen Daten gewonnen am RHIC und LHC manifestiert sich die Abwesenheit eines solchen Skalierungsverhaltens in unterschiedlichen Quellengrößen für Paare von zwei Pionen

einerseits und für Paare aus zwei Kaonen andererseits. Die Kaon-Daten liefern Hinweise dafür, dass das Skalieren mit der transversalen Masse durch ein Skalieren mit dem transversalen Paarimpuls ersetzt ist. Die hohe Ruhemasse der Proton-Lambda-Paare bietet eine exzellente Unterscheidungsmöglichkeit dieser beiden Szenarien.

In einer explorativen Studie nahm sich diese Arbeit außerdem der Untersuchung von Photon-Photon-Korrelationen bei kleinen Impulsunterschieden an. Rätselhaft ist hier besonders die gleichzeitige Beobachtung eines Überschusses an Photonen in Schwerionenkollisionen im Vergleich zu Proton-Proton-Ereignissen einerseits und eines signifikanten elliptischen Flusses andererseits sowohl am RHIC als auch am LHC. Potentiell lassen die quantenstatistischen Korrelationen der Photonen zu, den Ursprung der Photonen zu ergründen.

ALICE umfasst eine Vielzahl von sich gegenseitig ergänzenden Messanlagen. Verschiedene, schnelle Szintillatoren vermögen einen Interaktionstrigger zur Auslese der weiteren Detektoren auszusenden und eine Abschätzung der Zentralität der Interaktion zu geben. Das innere Spurverfolgungssystem (ITS) aus Silicium ermöglicht die Rekonstruktion geladener Teilchen mit hoher Ortsauflösung und erlaubt es so, auch den primären Interaktionsvertex hochpräzise festzustellen. Die Zeitprojektionskammer (TPC) misst bis zu 159 Spurpunkte für die auch der spezifische Energieverlust der Partikel berechnet wird, was die Zuordnung der Teilchenspezies gestattet. Der Übergangsstrahlungsdetektor verfügt zu seiner Fähigkeit der Spurrekonstruktion außerdem über besondere Elektronidentifikationsfähigkeiten; beides ist sowohl offline als auch online wenige Mikrosekunden nach der Kollision zugänglich. Der Detektor der Flugzeit (TOF) erlaubt in Verbindung mit der Spurverfolgung die Bestimmung der Teilchenmasse und das elektromagnetische Kalorimeter (EMCal) erweitert die Möglichkeiten zur Messung von Elektronen, Photonen und, vor allem durch seine Triggerfähigkeiten, auch der kollimierten Jets aus Teilchen.

Die Spurverfolgungsalgorithmen verwandten einen Kalmanfilter zur Rekonstruktion der Teilchen. Lambda- als auch Photon-Kandidaten wurden über eine spezielle V^0 -Suche gefunden und das Gruppieren von Signalen der einzelnen Zellen des EMCals erlaubte es die Energie der elektromagnetischen Schauer zu erschließen. Am Ende eines mehrstufigen Prozesses der Datenreduktion standen die analyseorientierten Daten. Sie waren der Ausgangspunkt für die weiteren Betrachtungen innerhalb dieser Arbeit.

Die Untersuchungen erfolgten anhand des Pb-Pb-Datensatzes aus dem Jahr 2011. Für die Proton-Lambda-Korrelationen wurden die Ereignisse in drei Zentralitätsklassen, 0–10%, 10–30% und 30–50%, unterteilt.

Um die Beeinflussung des experimentell wiederhergestellten Impulses der Protonen durch die Assoziierung eines falschen Punktes zur Spurextrapolation zu vermeiden, wurde zur Impulsbestimmung ein Rekonstruktionsschema verwendet, das die Treffer im ITS ausließ, den mit Hilfe des ITS reproduzierten primären Vertex jedoch einschloss. Die dadurch erreichte

Impulsauflösung erlangte nicht vollständig aber in gutem Maße die Präzision eines Schemas, das die Spurpunkte im ITS vollends aufnahm. Die Identifikationsmethode der Protonen in der vorliegenden Analyse hing vom Impuls ab. Bis $0.75 \text{ GeV}/c$ erlaubte die TPC alleine eine eindeutige Zuordnung über den spezifischen Energieverlust. Im Bereich $0.75 \leq p \text{ (GeV}/c) < 1.0$ ergab sich eine Kombination aus TPC und TOF als beste Teilchenidentifikationsmethode; oberhalb dieses Bereiches und bis zu $p = 5.0 \text{ GeV}/c$ genügte die TOF-Information alleine zur akuraten Bestimmung der Spezies. Für alle untersuchte Zentralitäten und in allen differenziellen Impulsabschnitten ergab sich eine Protonreinheit $S/(S + B)$ besser als 99%; hierbei bezeichnet S das Signal bestehend aus Protonen, und B den Untergrund von anderen Teilchen. Die Bestimmung der Reinheit erfolgte direkt aus den Daten.

Bei einem nicht-vernachlässigbaren Anteil der Protonen handelte es sich um Produkte aus schwachen Zerfällen; dominant war dabei die Disintegration des Lambda-Hyperons mit einem $c\tau = 7.89 \text{ cm}$. Die hohe Auflösung des ITS' im Impaktparameter, d. h. des Abstandes der Spurextrapolation zum primären Vertex, erlaubte diese Kontamination aus schwachen Zerfällen sowie einen weiteren Beitrag von Protonen aus Materialwechselwirkungen zu unterdrücken und, durch Skalieren von Monte-Carlo-Verteilungen an die Distributionen aus realen Pb-Pb-Kollisionen, unter direkter Benutzung der Daten zu bestimmen. Die zweidimensionalen Selektionskriterien auf den Impaktparameter in der transversalen Ebene und der longitudinalen Richtung maximierten die Signifikanz der primären Protonen, die entscheidend für die Bestimmung des Quellenradius mit einem minimalen Fehler ist. Die Quantifizierung dieser Verunreinigungen wurde gleichzeitig differenziell im Transversalimpuls und der Rapidität der Teilchen und der Zentralität der Ereignisse, getrennt für Teilchen und Antiteilchen bestimmt. Der Anteil der nicht-primären Protonen war in jedem akzeptiertem Phasenraumbereich kleiner als 30%.

Eine eindeutige Identifikationsmethode einer Λ -Analyse ist durch die invariante Masse gegeben. Der Untergrund durch K_s^0 und zufällige Kombinationen von Spuren war hier jedoch so immens, dass bei der Inspektion aller V^0 -Vertizes sich leider kein sichtbares Signal bei der Masse des Λ von $1.115683 \text{ GeV}/c^2$ abzeichnete. Weitere, über die in der V^0 -Suche angewandte hinausgehende Selektionskriterien mussten angewandt werden. Aufgrund des beherrschenden Zerfallskanals der K_s^0 in zwei geladene Pionen und der generellen Dominanz der Pionen in hochenergetischen nuklearen Kollisionen lag die Identifikation der Zerfallstöchter nahe. In dieser Arbeit wurde dazu ein Schnitt auf die Abweichung des gemessenen und des erwarteten spezifischen Energieverlustes der Protontochter für den gegebenen Impuls durchgeführt. Am effektivsten zeigte sich hier diese Abweichung als Anzahl von Standardabweichungen N_σ^{TPC} zu quantifizieren; dies erlaubte eine einfache Handhabung dieser Selektion über den gesamten untersuchten Impulsbereich. Die Signifikanz des Λ -Signals als Funktion von N_σ^{TPC} der Protontochter saturierte wie erwartet bei circa drei Standardabweichungen, änderte sich nur marginal zwischen drei und fünf Standardabweichungen und hatte ein schwach ausgeprägtes Maximum

bei circa vier Standardabweichungen, welches als Selektionskriterium gewählt wurde. Weitere topologische Prüfungsmerkmale erwiesen sich als sinnvoll um die Signifikanz des Λ -Signals zu maximieren. Erwähneswert ist hierbei der Schnitt auf den Winkel zwischen dem Ortsvektor, der den V^0 -Zerfalls- mit dem primären Vertex verbindet, und dem rekonstruierten V^0 -Impulsvektor von weniger als 1° . Zu der Verbesserung des Λ -Signals unterdrückte diese Bedingung außerdem den Beitrag schwach zerfallender mehrfach seltsamer Hyperonen, dessen Bestimmung im Folgenden beschrieben wird.

Die mehrfach seltsamen Hyperonen Ξ^0, Ξ^- und Ω^- zerfallen mit einer Wahrscheinlichkeit von mehr als 99% in ein Λ , beim Ω^- passiert dies in circa 30% der Fälle über ein intermediäres Ξ . Die Messungen der Multiplizitäten der mehrfach seltsamen Hyperonen der ALICE-Kollaboration wurde mit einer Blast-Wave-Funktion parametrisiert um die ungemessenen Bereiche im transversalen Impuls zu beschreiben. Für die nicht rekonstruierten Ξ^0 wurde Isospinsymmetrie angenommen. Durch die Studie einer Monte-Carlo-Simulation wurden die Rekonstruktionseffizienzen als $p_T^Y \rightarrow (y^\Lambda, p_T^\Lambda)$, $Y = \Xi^-, \Xi^0, \Omega^-$ für die jeweiligen, betrachteten Zentralitäten bestimmt. Die Propagation der Hyperonspektren durch diese Rekonstruktionsmatrizen erlaubte es, den Beitrag durch schwache Zerfälle zur Λ -Auswahl differentiell in Rapidität, transversalem Impuls und Zentralität zu bestimmen.

Ein signifikanter Beitrag zur Λ -Selektion stammt von den elektromagnetischen Zerfällen $\Sigma^0 \rightarrow \Lambda\gamma$ mit einem Verzweigungsverhältnis von 100%. Experimentell kann der elektromagnetische Zerfallsvertex nicht vom primären Vertex getrennt werden, ein Λ aus dem Zerfall eines Σ^0 hat die gleiche Rekonstruktionswahrscheinlichkeit wie ein primäres Λ . Das Verhältnis von Σ^0 und Λ kann durch thermische Modelle abgeschätzt werden. Unter Einbeziehung hunderter, stark zerfallender Resonanzen geben verschiedene Gruppen konsistent einen Wert für $N_{\Sigma^0}/(N_\Lambda + N_{\Sigma^0})$ von etwas weniger als 30%.

Ein experimenteller Zugang zur Zweiteilchen-Korrelationsfunktion ist durch das Mischen von Ereignissen gegeben. Durch das Generieren von 14 Paaren aus gemischten Ereignissen pro Paar in echten Ereignissen konnte der Einfluss des statistischen Fehlers der gemischten Ereignisse auf die Unsicherheit der Korrelationsfunktion auf 3.5% des Beitrages aus echten Ereignissen reduziert werden.

Die wichtigsten experimentellen Zweiteilcheneffekte bei der Studie von Teilchenkorrelationen bei kleinen relativen Impulsen sind das Aufspalten und Verschmelzen von Spuren durch die limitierte Auflösung des Detektors und die begrenzte Präzision der Algorithmen. Ein Einfluß dieser auf die Korrelationsfunktion kann vermieden werden, indem gefordert wird, dass die Spuren im Ortsraum separiert sind. Hierzu wurden, aufbauend auf die bereits existierende Methode für zwei primäre Spuren, Methoden entwickelt, die auch erfolgreich Anwendung in anderen Analysen der ALICE-Kollaboration finden.

Die rohe Korrelationsfunktion wurde mit der Paarreinheit korrigiert. Die Paarreinheit setzt

sich dabei zusammen aus der Λ -Reinheit und dem Anteil der nichtprimären Protonen und Λ ; typischerweise ergibt sich eine Paarreinheit von leicht über 50%. Eine geringe Abhängigkeit der Paarreinheit von der Zentralität und der transversalen Masse wird hier durch den Beitrag aus schwachen Zerfällen und Materialwechselwirkungen zur Protonselektion verursacht, für Protonen (Antiprotonen) variiert dieser von 26% (16%) bis zu 15% (8%). Die so erhaltenen korrigierten Korrelationsfunktionen sind ein wesentliches Ergebnis dieser Arbeit, sie wurden auf mehreren internationalen Konferenzen präsentiert. Zum ersten Mal konnte dabei eine zentralitätsabhängige Studie von Proton-Lambda-Korrelationen durchgeführt werden. Die Korrelationsfunktionen zeigen das erwartete Verhalten, nämlich eine stärkere Korrelation für peripherere Ereignisse, was konsistent mit der Vorstellung eines grösseren geometrischen Überlapps und einer höheren anfänglichen Energiedichte für zentralere Ereignisse ist. Ebenfalls erstmals wurden Proton-Lambda-Korrelationen differentiell in transversaler Masse studiert, hier konnten bis zu vier unabhängige Auswahlen für die verschiedenen Zentralitätsselektionen erhalten werden. Es zeigt sich eine stärkere Korrelation für höhere transversale Massen. Dies entspricht dem erwarteten Einfluss der dynamischen Prozesse innerhalb des Mediums in einem hydrodynamischen Bild. Der studierte Bereich der transversalen Masse erstreckt sich hierbei über mehr als $0.9 \text{ GeV}/c^2$ in der mittleren transversalen Masse der Selektion und langt bis zuvor unerreicheten $2.18 \text{ GeV}/c^2$ in der mittleren transversalen Masse. Dies macht diese Analyse zu einem Test hydrodynamischer Modelle in zuvor unerkundeten dynamischen Bereichen.

Ein von R. Lednický and V.L. Lyuboshits entwickeltes Modell erlaubt es, eine theoretische Proton-Lambda-Korrelationsfunktion für einen gegebenen Radius einer Gaußförmigen Quelle analytisch zu berechnen. Für einen direkten Vergleich mit den experimentellen Korrelationsfunktion muss jedoch die endliche Impulsauflösung des Experimentes miteinbezogen werden. Die hierzu traditionell angewandte Methode unterliegt jedoch einer intrinsischen Schwäche: Die Korrektur ist von dem Ergebniss der Korrektur abhängig, nämlich dem Quellenradius. Das finale Ergebnis kann so nur in einer iterativen Prozedur gefunden werden, wobei eine Iteration in ALICE typischerweise eine Rechenzeit von 100 Tagen benötigt. Die benötigte Statistik in Monte-Carlo-Simulationen der traditionellen Methode macht diese für die hier untersuchten Proton-Lambda-Korrelationen nur bedingt anwendbar. Eine in dieser Dissertation entwickelte Methode überkommt diese Probleme und erlaubt zudem eine akkurate Bestimmung der Unsicherheit des Quellenradius der aus dem statistischen Fehler der Korrelationsfunktionen resultiert, welcher in der traditionellen Methode nur näherungsweise gegeben ist. Eine von A. Kisiel durchgeführte Studie ermöglicht die Berücksichtigung eines Effektes durch stark zerfallende Resonanzen.

Für die in dieser Arbeit experimentell bestimmten Quellenradien wurden extensive systematische Studien durchgeführt. Ein strikteres oder laxeres Kriterium bezüglich der invarianten Masse der Λ -Kandidaten veränderte die Reinheit der Λ -Selektion. Mit dieser veränderten Selektion von Λ -Teilchen und der entsprechend modifizierten, tabellierten Λ -Reinheit kon-

nten alternative, korrigierte Korrelationsfunktionen und Quellenradien gefunden werden. Die Abweichung zu den Quellenradien der Standardanalyse ergab einen Teil der systematischen Unsicherheit. Genauso ermöglichte ein verändertes Kriterium bezüglich des Abstandes der Spurextrapolation der Proton-Kandidaten zum primären Vertex einen veränderten Beitrag aus schwachen Zerfällen und Materialwechselwirkungen. Die Unsicherheit durch den Beitrag aus schwachen Zerfällen der mehrfach seltsamen Hyperonen wurde durch eine um 5% erhöht und erniedrigte Multiplizität der Spektren der mehrfach seltsamen Hyperonen abgeschätzt. Der systematische Fehler assoziiert mit dem elektromagnetischen Zerfall des Σ^0 konnte durch eine Evaluation verschiedener thermischer Modelle mit mehreren Variationen quantifiziert werden. Zahlreiche weitere Studien wurden durchgeführt, die hier nicht erwähnt werden sollen. Dominant erwies sich die Unsicherheit durch die limitierte Kenntniss der starken Wechselwirkung der Proton-Lambda-Paare, sie führt zu einer totalen systematischen Unsicherheit zu kleineren Radien von weniger als 5%, in etwa gleich der statistischen Unsicherheit. Hin zu größeren Quellenradien ist die statistische Unsicherheit dominant.

Die Bestimmung der Quellenradien aus Proton-Lambda-Korrelationen ist das Hauptergebnis dieser Arbeit. Der Vergleich der Radien mit Ergebnissen aus Pion-, Kaon-, und Proton-Korrelationen, ebenfalls mit ALICE gewonnen, offenbart sehr deutlich, dass ein Skalieren der Radien mit der transversalen Masse nicht gegeben ist. Während die Analyse der Kaon-Korrelationen für die 0–10% zentralsten Ereignisse bei einer transversalen Masse von etwa $1.3 \text{ GeV}/c^2$ einen Quellenradius von weniger als 4.5 fm mit einer totalen Unsicherheit von circa 0.2 fm zeigt, so ergibt sich aus den hier untersuchten Proton-Lambda-Korrelationen bei circa $1.3 \text{ GeV}/c^2$ transversaler Masse ein Quellenradius von mehr als 6 fm mit einer totalen Unsicherheit zu kleineren Werten von etwa 0.4 fm. In einer 3+1D hydrodynamischen Rechnung von A. Kisiel *et al.* wurde ein Skalieren der dreidimensionalen Radien in dem sich longitudinal mit dem Paar mitbewegenden Koordinatensystem gefunden. Dies impliziert das Fehlen des Skalierverhaltens im eindimensionalen Radius aufgrund des γ -Faktors zwischen den unterschiedlichen Referenzsystemen. Das Skalieren der theoretisch berechneten Radien konnte dort durch die Einführung eines phänomenologischen Faktors wiederhergestellt werden. Die Anwendung dieses phänomenologischen Faktors auf die vorläufigen Daten der ALICE-Kollaboration für Pionen, wie sie auf der Quark Matter 2012 Konferenz gezeigt wurden, der Aktualisierung der Kaon-Radien in der Dissertation von M. Steinpreis und den hier gewonnen Proton-Lambda-Radien verstärkt vor allem die Unterschiede zwischen den Pionen und Kaonen und verschlechtert in geringem Maße auch die Übereinstimmung der Proton-Lambda-Radien mit den Messungen der leichteren Teilchen. Das Auftragen der Radien als Funktion des transversalen Paarimpulses ergibt eine insgesamt bessere Übereinstimmung der Radien der verschiedenen Spezies bei gleichem transversalen Paarimpuls. Insbesondere im Zusammenhang mit den am RHIC durchgeführten Messungen der Pion- und Kaon-Radien ergibt sich ein Bild das eher ein Skalieren der Radien mit dem transversalen Paarimpuls unterstützt. Die bisherige Interpretation eines solchen Skalierens betont die Wichtigkeit der hadronischen

Phase. Detaillierte Modellstudien sind nötig um den Ursprung des beobachteten Verhaltens zu verstehen. Die in dieser Dissertation gewonnenen Ergebnisse sind dabei ein essentieller Baustein der konsistenten Beobachtung eines qualitativ neuen Paradigmas.

Zudem wurden in dieser Arbeit auch Photon-Photon-Korrelationen untersucht. Potentiell erlauben diese die Entschlüsselung des Photonrätsels, d. h. der bereits angedeuteten, gleichzeitigen Beobachtung einer hohen effektiven Temperatur in den Transversalimpulsspektren der Photonen einerseits und andererseits eines elliptischen Flusses der Photonen, der vergleichbar mit dem der Hadronen ist. In ALICE können Photonen über ihre Konversion in e^+e^- -Paare rekonstruiert oder direkt im EMCal nachgewiesen werden. Für die Selektion von Konversionsphotonen wurde auf die allgemeine Auswahl der Photonkandidaten der Konversionsgruppe in ALICE aufgebaut. Weitere Kriterien wurden angewandt um eine für eine Korrelationsmessung geeignete Selektion zu erhalten. So wurde beispielsweise auf eine gute Qualität der Impulsmessung Wert gelegt, ebenso wurden mögliche Kontaminationen durch zusätzliche Anforderungen bezüglich der Identifikation der Tochterelektronen unterdrückt. Um die Cluster der neutralen Photonen im EMCal zu selektieren, wurden Cluster, die gut mit der Spurextrapolation eines geladenen Teilchens zusammenpassen, verworfen. Außerdem erlaubte die Analyse der Form des Schauers im Kalorimeter, Hadronen zurückzuweisen.

Die Korrelationsfunktion für zwei Photonen, die im EMCal rekonstruiert wurden, geht für kleinste relative Impulse gegen null. Der Grund hierfür ist die limitierte Fähigkeit des Kalorimeters, zwei ortsnahe Cluster voneinander zu trennen. Die Korrelationsfunktion für zwei Konversionsphotonen ist ebenfalls durch die endliche Ortsauflösung der Spurverfolgungsdetektoren beeinflusst, jedoch ist hier die Depression der Korrelationsfunktion durch Zweispureffekte schwächer. Der Depression überlagert ist ein starkes, positives Korrelationssignal für relative Impulse kleiner als $10 \text{ MeV}/c$. Mit Hilfe einer einfachen Parametrisierung der Zweispureffekte ließ sich das positive Korrelationssignal quantitativ durch eine Gaußfunktion, die ihr Maximum bei verschwindenden relativen Impulsen hat, beschreiben. Die Höhe der Gaußfunktion nimmt dabei als Funktion des transversalen Paarimpulses stetig zu und erreicht für transversale Paarimpulse größer als $1.25 \text{ GeV}/c$ das Limit quantenstatistischer Korrelationen. Auch die Breite des Gauß' wächst von ungefähr $3 \text{ MeV}/c$ für transversale Paarimpulse zwischen 0.25 und $0.5 \text{ GeV}/c$ monoton auf etwa $7 \text{ MeV}/c$ Breite für transversale Paarimpulse größer als $1.25 \text{ GeV}/c$. Die Kombination von einem Konversionsphoton und einem im EMCal gemessenen Photon erlaubt, die Limitation der örtlichen Trennung der zwei Photonen zu überkommen. Wieder ergibt sich ein starkes, positives Korrelationssignal für relative Impulse kleiner als $20 \text{ MeV}/c$, das sich mit einer Gaußfunktion gut beschreiben lässt. Die solide Statistik erlaubte es, die Korrelationsfunktion in sechs unabhängige Gruppierungen bezüglich des transversalen Paarimpulses zu unterteilen. Fünf Selektionen erstrecken sich über den Bereich von 0.25 bis $1.5 \text{ GeV}/c$, eine weitere, nach oben offene schließt sich diesen an. Die Höhe des Korrelationssignals vergrößert sich dabei monoton um insgesamt mehr als ein Faktor zehn. Auch die Breite wächst um mehr als einen

Faktor zwei von etwa 6 auf circa 13 MeV.

Der Ursprung des stark positiven Korrelationssignals der Kombination eines Konversions- und eines Kalorimeter-Photons für kleine relative Impulse wurde mit Hilfe einer Monte-Carlo-Simulation untersucht. Es ergibt sich eine vernünftige Beschreibung sowohl der Höhe als auch der Breite des Signals in Daten durch die Simulation. Auch ohne das Evaluieren der Detektorantwort, jedoch unter Einschluß der Effekte durch das passierte Detektormaterial, ergibt sich für zwei mit der Monte-Carlo-Information identifizierte Photonen ein positives Korrelationssignal, das hier durch das Fehlen der experimentellen Auflösungseffekte ein sehr spitzes Maximum bei verschwindendem relativen Impuls hat. Die Höhe des Signals nimmt auch hier mit steigendem transversalem Paarimpuls stark zu. Da die standardmäßig verwendeten Generatoren keine quantenstatistischen Korrelationen beinhalten, muss zumindest ein Großteil des Signals aus anderen Quellen stammen. Denkbar wäre, dass hier die Korrelation zweier kollinear emittierter Photonen eines fragmentierenden Partons sichtbar wird. Andere Prozesse, in der zum Beispiel eine Art Autokorrelation aufgegriffen wird, wenn ein Konversionselektron eines Photons wieder ein Bremsstrahlungsphoton aussendet, sind jedoch nicht ausgeschlossen. Die schiere Menge an zu untersuchenden, möglichen Quellen überstieg den Umfang dieser Sondierungsstudie innerhalb dieser Dissertation. Das klare, beobachtete Signal, die gefundene Abhängigkeit der Korrelationsstärke vom Paarimpuls und die annehmbare Beschreibung des Signals durch die Simulation zeigen jedoch einen klaren Weg auf, um den Produktionsmechanismus der Photonen besser zu verstehen. Die hier vorliegende Arbeit bildet somit die Basis für weitergehende Studien zur Lösung des Photonrätsels.

Contents

1	The Quark-Gluon Plasma	1
1.1	The Phase Diagram of Strongly Interacting Matter	1
1.2	Early Experimental Access — The SPS Heavy-Ion Program	4
1.3	RHIC: The Strongly Coupled Liquid	11
1.4	The Physics Program of ALICE	15
2	Freeze-Out Radii	23
2.1	1+1D Ideal Hydrodynamics with Bjorken Flow and a 1st Order Phase Transition	23
2.2	Femtoscopy	25
2.3	Regions of Homogeneity	28
2.4	The RHIC HBT Puzzle and Viscosity Effects	31
2.5	Broken Pair Transverse Mass Scaling of Radii	34
2.6	Femtoscopic Radii in Pb-Pb Collisions at the LHC	37
2.7	Photon Sources	38
3	ALICE at the LHC	43
3.1	Coordinate Systems	44
3.2	The Inner Tracking System	45
3.3	The Time Projection Chamber	48
3.4	The Transition Radiation Detector	53
3.4.1	A Quality Assurance Framework for the ALICE TRD	59
3.5	The Time-Of-Flight Detector	61
3.6	The Electromagnetic Calorimeter	64
4	Data Reconstruction	67
4.1	Trigger and Centrality	67
4.2	Tracking	69
4.3	V^0 Selection	73

4.4	Clustering in the Calorimeters	75
4.5	AOD Filtering	77
4.5.1	Filtering Tracks	77
4.5.2	Filtering V^0	78
4.5.3	Creating Photon Conversion Candidates	80
5	pA Data Analysis: Event and Single-Particle Selection	85
5.1	Event Characteristics	85
5.2	Primary Proton Identification	86
5.2.1	Assuring Good Tracking	86
5.2.2	Proton PID at Low Momentum	88
5.2.3	Intermediate Momentum Proton Identification	90
5.2.4	Proton Selection for p from 1 up to 5 GeV/ c	92
5.2.5	Proton Feed-Down	94
5.3	Primary Λ Identification	98
5.3.1	Λ Selection	98
5.3.2	Feed-Down from Weak Decays	100
5.3.3	Feed-Down from Electromagnetic Decays	102
6	pA Data Analysis: Two-Particle Studies	107
6.1	Generalized Momentum Difference \tilde{q}	107
6.2	Event Mixing	108
6.3	Two-Track Resolution	110
6.3.1	Angular Distances ($\Delta\eta, \Delta\varphi^*$)	110
6.3.2	The Mean Distance	112
6.3.3	The Generalized Angular Distances ($\Delta\eta^*, \Delta\varphi^*$)	113
6.4	The Raw Correlation Function	115
6.5	Purity Correction	116
6.6	Corrected pA Correlation Functions	120
6.7	A Model for the Extraction of pA Radii	121
6.8	Momentum Resolution and Resonances	124
6.8.1	Experimental Momentum Resolution	124
6.8.2	Strongly Decaying Resonances	127
6.9	pA Systematic Uncertainties	129
6.10	Experimental pA Radii	137

7	Photon-Photon Correlations	143
7.1	Photon Conversion Candidate Selection	143
7.2	EMCal Photon Candidate Selection	145
7.2.1	Charged Particle Veto	145
7.2.2	Showar Shape Analysis	146
7.2.3	Energy Calibration of the ALICE EMCal	148
7.3	Photon-Photon Correlation Function	150
8	Summary	163
A	Lattice QCD: Extra Derivations	I
A.1	Wilson Loop	I
A.2	Polyakov Loop	VI
A.3	QCD Trace Anomaly	VI
B	Auxiliary Hydrodynamical Calculations with the MIT Bag Model	IX
C	Further Experimental Considerations	XVII
C.1	Medium Choice in Gaseous Detectors	XVII
C.2	Tail Cancellation and Baseline Filter	XIX
D	Additional Reconstruction Algorithms	XXI
D.1	Seeding for the Kalman Tracker	XXI
D.2	On-the-fly V^0 Finder	XXII
E	Λ Selection Supplements	XXV
E.1	On-The-Fly Criteria	XXV
E.2	Motivation for Differential Purity Estimates	XXVI
F	Adjunct Pair Observables	XXIX
F.1	Raw Correlation Functions	XXIX
F.2	Pair Statistics and Purity Fluctuations	XXXIII
F.3	Possible pK_s^0 Correlation	XXXVI
	Bibliography	XXXIX
	Curriculum Vitae	LXXI

Chapter 1

The Quark-Gluon Plasma

1.1 The Phase Diagram of Strongly Interacting Matter

The Quark-Gluon Plasma (QGP) is the deconfined state of Quantum Chromo Dynamics (QCD). Fig. 1.1 shows the phase diagram of strongly interacting matter as a function of baryon number density and temperature as it was first drawn in 1975 by N. Cabibbo and G. Parisi [1]. It shows two distinct phases of matter: hadrons for low temperatures and low baryon number density and deconfined quarks (and gluons) for high temperature and/or high baryon number density. Cabibbo and Parisi showed that the limiting Hagedorn temperature [2] is realized in ‘any model where hadronic matter has a second order phase transition.’

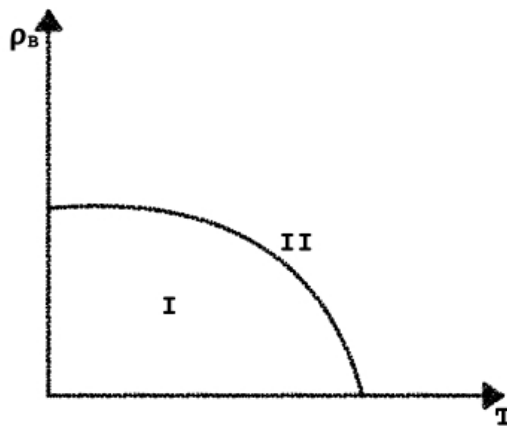


Figure 1.1: Schematic phase diagram of QCD. ρ_B denotes the baryon number density, T the temperature. In I the quarks are confined into hadrons, in II they are deconfined. According to [1].

D.J. Gross, F. Wilczek and H.D. Politzer proved in 1973, that a negative beta function — which leads to asymptotic freedom in QCD — is realized in a theory with self-interacting force-mediating particles [3,4]. This implies that for low momentum transfer Q , the strong running coupling α_s becomes large (as shown in Fig. 1.2) and perturbative techniques can not be applied anymore.

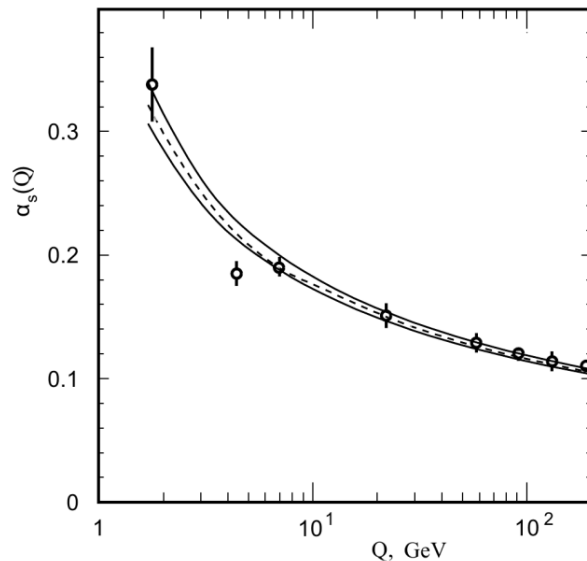


Figure 1.2: Running strong coupling α_s as a function of momentum transfer Q . We see the increase of α_s for low Q to values ~ 1 . Taken from [5].

An alternative approach in this non-perturbative regime of strong interactions is lattice QCD [6]. Three key ideas made the proposal a success [7]. a) The original problem resides in the Minkowski space with the metric $ds^2 = -(dt^2) + dx^2 + dy^2 + dz^2$. We see that the Minkowski metric is equivalent to the Euclidean metric $ds^2 = (d\tau^2) + dx^2 + dy^2 + dz^2$ with the substitution $t = -i\tau$. This Wick rotation [8] allows to solve the problem in Euclidean space time. b) Rather than in a continuous Euclidean space-time, the implementation is performed on a discrete Euclidean space-time grid with spacing a , which provides a non-perturbative regularization scheme by its UV cutoff at π/a . Physical values of quantities can be obtained by extrapolating $a \rightarrow 0$. c) To maintain local gauge invariance in the formulation of the fields and action on the lattice. This consideration leads to links between the different space-time points which are realized as the gluon potentials.

The lattice allows to calculate, e.g., the $q\bar{q}$ potential in QCD, which is implemented mathematically as a Wilson loop. In Section A.1 the Wilson loop on the lattice is derived. In [9] it is shown how to derive the result for the Wilson loop operator for different distances R . Fig. 1.3 (left) gives the result of the SESAM Collaboration [10]. One sees a familiar

Coulomb-like potential for small distances R and a linear term $\sim \sigma R$ for large R , leading to the confinement of quarks.

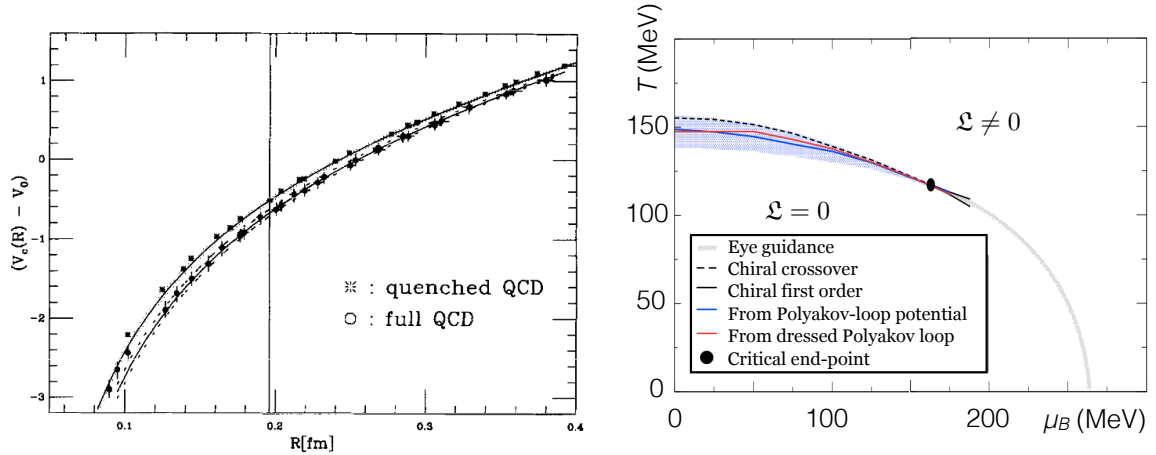


Figure 1.3: Left: Potential $V(R)$ for $q\bar{q}$ pair vs. the separation R of the pair as calculated by lattice QCD. Taken from [10]. Right: QCD phase diagram from Polyakov loop calculations at finite temperature and baryo-chemical potential. With an added gray line to guide the eye. Taken from [11].

In Section A.2 the Polyakov loop is discussed. It is related to the free energy of a single quark such that the Polyakov loop \mathcal{L} is zero in a confined state and non-zero in a deconfined plasma. This property makes it an order parameter of deconfinement. Recent developments allow to calculate the Polyakov loop at finite temperature and finite baryo-chemical potential. Fig. 1.3 (right) shows the results of [11], where the Polyakov loop calculations separate the two distinct phases within the plane of temperature and baryo-chemical potential. We recognize a similar dependence of the temperature of deconfinement on the baryo-chemical potential as in the Cabibbo and Parisi diagram, discussed in the beginning of this chapter (Fig. 1.1).

In the same way as the Polyakov loop is related to the center symmetry, the trace anomaly of QCD is connected to a scale transformation. In Section A.3 the connection between the trace of the energy momentum tensor and the QCD fields in a lattice QCD calculation is discussed. The trace of the energy momentum tensor Θ_μ^μ directly gives the equation of state

$$\Theta_\mu^\mu = \epsilon - 3P. \quad (1.1)$$

The results from the two leading lattice QCD groups — the Wuppertal-Budapest [12] and the HotQCD [13] Collaboration — are displayed in Fig. 1.4. We see the clear rise in the number of degrees of freedom, signaling the transition from a hadronic to a deconfined phase. The equation of state obtained from the lattice calculations is used in hydrodynamic calculations for the bulk matter created in heavy-ion collisions. As it is discussed in Chapter 2, the equation of

state is an essential ingredient to appropriately model the source dynamics; only an accurately determined equation of state leads to an agreement in the freeze-out radii of simulations and data from Pb-Pb collisions.

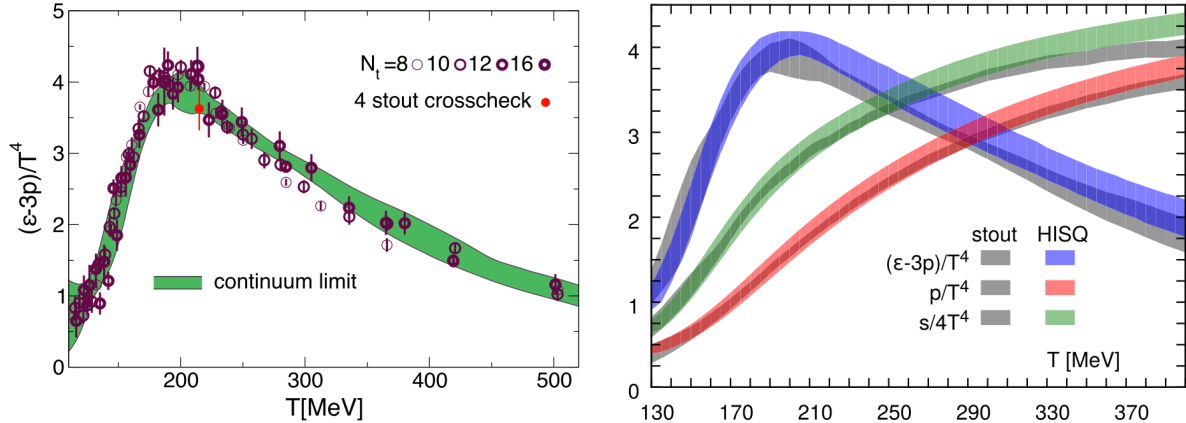


Figure 1.4: The equation of state in terms as $(\epsilon - 3p)/T^4$ derived from lattice QCD. Results from the Wuppertal-Budapest Collaboration [12] on the left and from the HotQCD Collaboration [13] on the right.

1.2 Early Experimental Access — The SPS Heavy-Ion Program

Ultra-relativistic heavy-ion collisions allow to examine the QGP phase in the laboratory. Powerful accelerators store kinetic energy in the beams of nuclei. By depositing a large fraction [14] of this energy in an transverse area following from the radius of, e. g., the Pb nucleus of $r \approx r_0 \cdot A^{1/3} \approx 7$ fm, energy densities — and therefore temperatures — are achieved, that surpass the phase boundary from hadrons to the state of liberated quarks and gluons. Although collisions with beams of protons generally provide a higher center of mass energy in the single nucleon-nucleon collision, the formation of a medium, that is a QGP, requires to exceed the threshold temperature over a minimum finite extent.

Hints for the QGP were experimentally first seen by the Super Proton Synchrotron (SPS) experiments at the European Organization for Nuclear Research (CERN). The excitement about the possible discovery culminated in a CERN press release [15] in the year 2000. The combined results of all the SPS experiments gave circumstantial evidence for the creation of a new state of matter as discussed in [16]. The heavy-ion community evolved much since then: new variables were proposed and measured; analysis techniques for already existing observables were refined. Still, some of the basis for today’s understanding was built by the SPS studies. In the following

a few key findings shall be briefly addressed.

The critical energy density ϵ for the phase transition to happen is believed to be ~ 2 GeV/fm³ (cf. [17]). Employing Bjorken's formula $\epsilon = (dE_T/d\eta)/\pi R^2\tau$ allows to extract the energy density created in heavy-ion collisions from transverse energy spectra [18]. The transverse energy at top SPS energy is mostly contained in charged and neutral pions. A direct measurement of the π^0 is experimentally inaccessible, but its decay photons can be observed with an electromagnetic calorimeter. Additionally measuring the strongly interacting part with, e.g., a hadronic calorimeter, allows for a good evaluation of the transverse energy distribution. The NA49 Collaboration measured this spectrum in central Pb-Pb collisions at $\sqrt{s_{NN}} = 17.3$ GeV and estimated the energy density to be 3.2 GeV/fm³, well above the critical energy density [19].

The slopes T of the single-particle $m_T - m_0$ spectra are related qualitatively to the kinetic freeze-out temperature T_{fo} , at which the interactions among the particles cease, and the possible average collective flow velocity $\langle\beta_T\rangle$ via $T = T_{fo} + m\langle\beta_T\rangle^2$. As we see from the preceding equation, measuring just one type of particle unfortunately can not discriminate between i) a scenario where particles are emitted at a high temperature without an imprint of a medium and ii) the much more interesting case of a limited temperature and a collective expansion of the matter. Measuring several species can lift this ambiguity. All seven big collaborations reported transverse-mass spectra for all kinds of particles, see e.g. [20–22]. The simultaneous description of all species with a single source by a hydrodynamic code, e.g. [23, 24], gives evidence of collective expansion. The similarity of the spectra, including strange particles and anti-matter, hints to particle production from a deconfined phase [25]. The extracted yields of the spectra indicate that a thermal equilibrium is reached with a freeze-out temperature which agrees with the expected phase boundary to a quark-gluon plasma [26, 27].

The collective expansion, or transverse flow, can also be seen in the anisotropy of transverse momentum distributions [28]. In non-central collisions, the reaction plane is defined by the direction of the beam and the impact parameter, and has an azimuthal angle Ψ in the transverse plane. The flow coefficients, v_1 for directed and v_2 for elliptic flow, follow from a Fourier decomposition of the particle spectra with respect to the reaction plane:

$$E \frac{d^3N}{d^3\vec{p}} = \frac{1}{2\pi} \frac{d^2N}{p_T dp_T dy} \left(1 + 2 \sum_{n=1}^{\infty} v_n \cos[n(\varphi - \Psi)] \right). \quad (1.2)$$

The v_1 and v_2 coefficients are easily accessible via:

$$v_n = \langle \cos[n(\varphi - \Psi)] \rangle, \quad (1.3)$$

where φ is the azimuthal angle of the particle and the angular brackets indicate averaging over all selected particles and events. Experimentally the reaction plane is inaccessible and only an event plane can be determined. In [29] the prescription is given for how the resolution effects in

the event plane determination can be corrected for.

NA49 measured the rapidity and transverse momentum dependence of directed and elliptic flow in [30]. The p_T -dependent v_1 and v_2 for protons and pions is shown in Fig. 1.5. A striking feature of the data is the mass ordering in the p_T -differential elliptic flow. The effect is caused by a common radial flow which pushes the heavier particles towards higher p_T [31]. The strong common flow field points to a high degree of thermalization of the particles. It was concluded that the observed flow pattern originates from the strong pressure gradients in the high density region, existing in the early phase during the evolution of the heavy-ion collision. The preservation of the momentum anisotropies until the final stage of the collision requires the viscosity of the medium to be not too high. The experimental data of Fig. 1.5 exemplify a typical weakness of the SPS era analyses. The statistics are scarce and the p_T range of the data is limited. Clearly this should be taken as a call for a detailed measurement with a better statistical precision and a more comprehensive investigation of the mass dependence by including other species. This call was answered by the RHIC experiments (see Section 1.3) and the LHC (see Section 1.4).

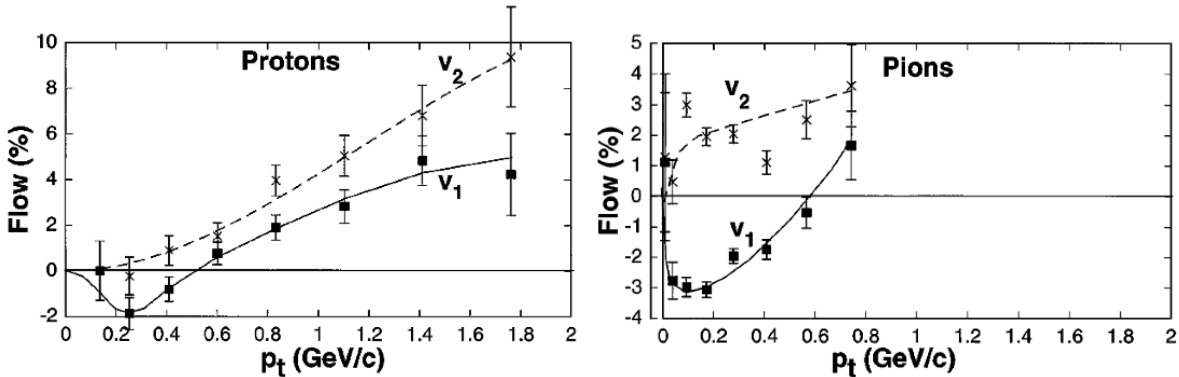


Figure 1.5: Directed and elliptic flow coefficients v_1 and v_2 for Pb-Pb collisions at $\sqrt{s_{NN}} = 17.3$ GeV as measured by NA49. The data show an imprint of the early hot and dense phase. Taken from [30].

In hadronic matter the production mechanism for strangeness that requires the least excess energy is



with a threshold of $E = m(K^+) + m(\Lambda) - m(p) \approx 670$ MeV; whereas in the QGP, the needed energy is only the mass of a $s\bar{s}$ pair, i. e., about 200 MeV [32]. The idea of studying strangeness production as a signature for a QGP formation was developed in 1982 [33]. Following this

proposal, WA97 measured the enhancement factor E ,

$$E = \left(\frac{\langle Y \rangle}{\langle N_{\text{part}} \rangle} \right)_{\text{Pb-Pb}} / \left(\frac{\langle Y \rangle}{\langle N_{\text{part}} \rangle} \right)_{\text{p-Pb}}, \quad (1.5)$$

i. e. the enhancement of the yield over the expected yield from N_{part} scaled p-Pb data; it is shown in Fig. 1.6 (left). The increase of the enhancement factor as a function of strangeness content of the particles contradicts the expectations for a hadron gas, where multi-strange particle production is obstructed by high thresholds. The observed enhancement is in line with equilibrated production of strange quarks in the QGP [34].

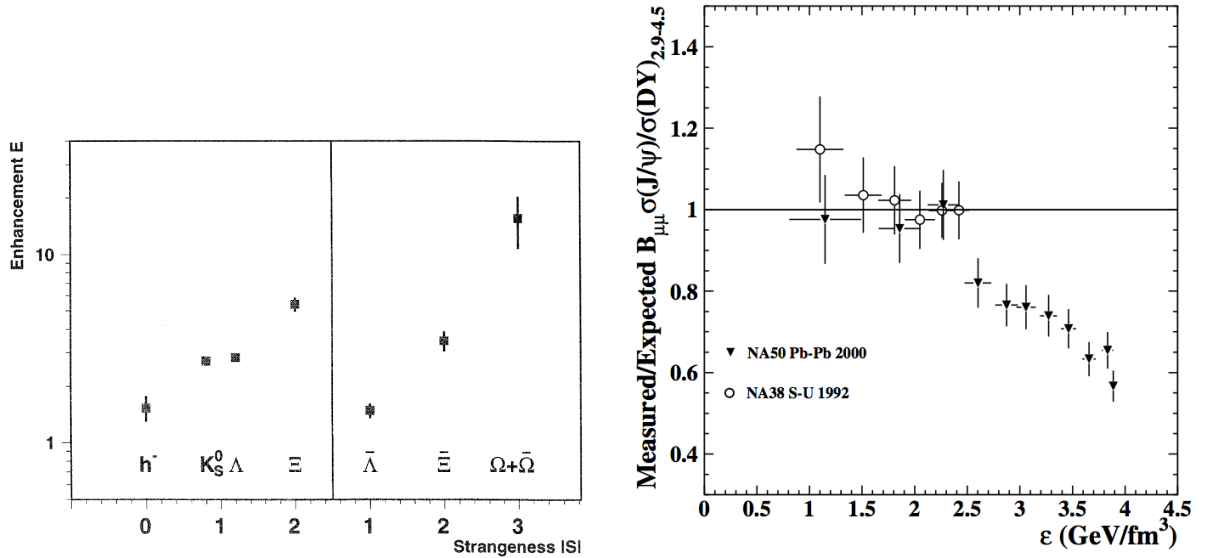


Figure 1.6: Left: Enhancement factor E (see Eq. 1.5) of Pb-Pb over N_{part} scaled p-Pb data for various particle species. The enhancement increases with the strangeness content of the particles. Taken from [34]. Right: J/ψ suppression in Pb-Pb collisions at $\sqrt{s_{\text{NN}}} = 17.3$ GeV as measured by the NA50 Collaboration. A suppression can be seen for high initial energy densities ϵ . Taken from [35].

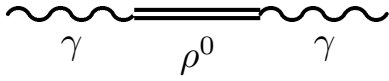
The NA50 Collaboration measured the J/ψ production in Pb-Pb collisions and observed a reduced yield for central events with high energy density as shown in Fig. 1.6 (right). The suppression is interpreted in the spirit of Matsui and Satz [36]. In vacuum the heavy $q\bar{q}$ pair is bound with a radius of less than a fm in the Coulomb-like part of the QCD potential shown before in Fig. 1.3 (left). The deconfinement of the quarks and gluons leads to a Debye-like [37] color charge screening. The different quarkonia states should be sequentially melted with rising temperature or energy density of the QGP [38].

Spectra of dileptons are studied because the leptons do not interact strongly and therefore

penetrate the hot and dense medium unscathed. Reconstructing the invariant mass of the pair

$$m_{\text{inv}} = \sqrt{P^2} = \sqrt{(P_1 + P_2)^2} \quad (1.6)$$

may show a signal from electromagnetic QGP radiation, created by $q\bar{q}$ annihilation, and gives access to the ρ^0 spectral function, which possibly is altered by chiral symmetry restoration [39].



The ρ^0 has the same quantum numbers as the photon:

$$\gamma : J^{PC} = 1^{--}, \quad \rho : J^{PC} = 1^{--}, \quad (1.7)$$

Figure 1.7: Vector meson dominance: The photon couples to the ρ^0 as both have quantum numbers $J^{PC} = 1^{--}$.

which in principle allows the process $\gamma \rightarrow \rho^0 \rightarrow \gamma$ depicted in Fig. 1.7. This hadronic dressing of the photon is described by the

Vector Meson Dominance (VMD) model, which arose from two paths. In 1960 Sakurai predicted vector mesons, coupled to the currents of isospin and hypercharge [40]. His idea was based on the theory by Yang and Mills [41] and was picked up by Gell-Mann in the course of his development of the Eightfold Way [42] in e. g. [43]. The other track was led by Nambu in 1957 [44], who interpreted the charge distributions of the neutron and proton obtained in electron scattering experiments as a possibility for the existence of a heavy neutral meson, the ρ^0 , which contributes to the form factor of the nucleon. Nambu's work was extended by Frazer and Fulco [45] who investigated the electromagnetic properties of the nucleon by means of the dispersion relation. They showed that the nucleon magnetic moment and radii can be reproduced with the inclusion of a $\pi\pi$ resonance, which leads to a peak in the pion form factor. This excursion to the history of the VMD model shows us that the ρ^0 plays a critical role in electromagnetic interactions with strongly interacting matter, like dilepton spectra emerging from the fireball created in heavy-ion collisions.

The e^+e^- spectrum measured by CERES/NA45 in p-Be and p-Au collisions is described by the decay cocktail of neutral mesons as shown in Fig. 1.8 (left) for the p-Be case. The biggest contributions arise from the Dalitz decays of π^0 , η , ω , η' , the direct decays of ρ^0 , ω , ϕ , and correlated charm decays. The cocktail was constrained by simultaneously measuring photons with the added TAPS calorimeter [46], and thus reconstructing the three-body Dalitz decays of the π^0 and η , which the cocktail was normalized to. The signal from semi-leptonic $D\bar{D}$ decays could be investigated using Pythia [47] simulations, which profited from input of measurements of charmed mesons [48, 49].

The measurement of the dilepton invariant mass spectrum in Pb-Au collisions by CERES/NA45 is shown in Fig. 1.8 (right) [50]. The most prominent feature is the enhancement of the experimental spectrum over the hadronic cocktail by up to an order of magnitude in the low mass range of $0.2 \text{ GeV}/c^2 < m_{\text{inv}} < 0.7 \text{ GeV}/c^2$.

CERES also presented that the enhancement is most pronounced for low pair transverse momentum p_T^{ee} and that the ratio a of the yield of e^+e^- pairs per charged particle yield $a = \frac{dN_{e^+e^-}}{d\eta} / \frac{dN_{\text{ch}}}{d\eta}$ increases linearly with the number of charged particles in the event $b = \frac{dN_{\text{ch}}}{d\eta}$ from p-Be and p-Au to more and more central Pb-Au collisions. For a single-particle decay as hadronic source of the excess, this ratio $a(b)$ would be constant. In contrast, a pair annihilation process like $\pi^+\pi^- \rightarrow \rho^0 \rightarrow e^+e^-$ exhibits the observed linear dependence in $a(b)$. Therefore $\pi^+\pi^-$ annihilation in the hot medium was considered to explain the observed excess in the CERES spectrum. It was found that — although the yield in e^+e^- pairs increases drastically — the shape of the experimental invariant mass spectrum is not reproduced by any of the various models by incorporating the $\pi^+\pi^-$ annihilation [51].

The models that described the excess in the low mass range can be separated into two groups, both of them involve a modification of the ρ^0 spectral function. The first approach does not involve a QGP phase, but just takes into account the broadening of the ρ^0 by collisions in the hot and dense hadronic phase. Its ρ^0 spectral function shows reminiscence to quark based calculations; the authors of [52] therefore mention a possible quark-hadron duality in the vicinity of the phase transition. Comparing the calculations of [53] shown in Fig. 1.9 (left), where only a hot meson gas was examined, with those of [52] shown in Fig. 1.9 (right), where also baryons were taken into account, reveals the importance of direct interactions $\rho N \rightarrow B$, $B = N, \Delta, N^*(1520), \dots$, and modifications via resonance-hole excitations. Contributions to the ρ^0 self-energy, namely the pion cloud and resonance-hole excitations, are shown in Fig. 1.10. Employing the modified ρ^0 spectral function also for the pion-pion annihilation process results in good agreement with the data.

A modification of the ρ^0 spectral function is also thought to occur when approaching the deconfined state where chiral symmetry should be restored; the mass of the ρ^0 is expected to drop. The phase transition of deconfinement and chiral symmetry restoration are presumed to be close to each other. In a scenario with a deconfinement temperature of $T_c = 207$ MeV and a chiral phase transition at $T_{\text{ch}} = 215$ MeV, R. Pisarski predicted a ρ^0 mass of 409 MeV at a temperature $T = 203$ MeV, slightly below deconfinement [54]. Dropping hadron masses were also predicted by G.E. Brown and M. Rho in [55] using effective chiral Lagrangians. A description of the dilepton spectra in proton-nucleus collisions without any medium modifications to the spectral functions and an implementation of the dropping mass scenario for central heavy-ion collisions, successfully reproducing the CERES dilepton spectra, was performed within a hadronic transport approach [56]. A calculation within a hydrodynamic framework [57] comes to the same conclusion that the data are not described with the vacuum masses, but are simulated with the reduced mass for the ρ^0 . Both works mention the constraint by single photon spectra [58].

Studying two-particle correlations at low relative momenta grants information about the size of the source. The two-particle correlations are influenced by the transverse expansion dynamics

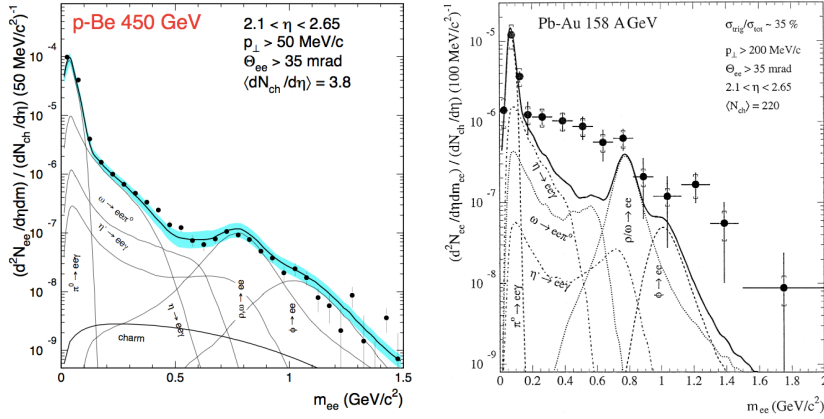


Figure 1.8: Dielectron spectra measured by CERES/NA45 in 450 GeV p-Be [59] (left) and 158A GeV Pb-Au [50] (right) collisions. While the hadronic decay cocktail describes the p-Be spectrum well, a vast excess over the cocktail is seen in the Pb-Au data.

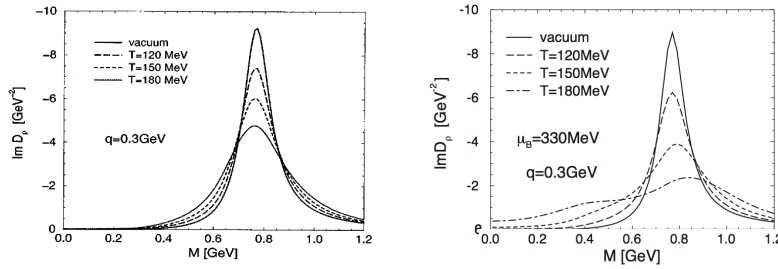


Figure 1.9: Spectral function of the ρ^0 in hot meson gas (left) [53] and a hot hadron gas with baryons included (right) [52]. The important effect of the baryons is seen especially around $M = 0.4$ GeV.

and are thus believed to be sensitive to a phase transition. Within the hydrodynamical model framework, the spatial and temporal components can be separated, thus allowing one to infer the components and infer the longitudinal and transverse expansion of the source [60]. A

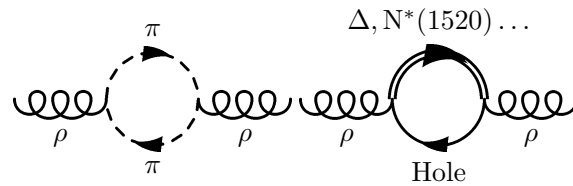


Figure 1.10: Contributions to the ρ^0 self-energy in nuclear matter: pion cloud (left) and resonance-hole excitations (right).

more detailed theoretical description is given in Chapter 2. Experimentally, the 3D pion and kaon radii measured by NA44 showed the predicted $1/\sqrt{m_T}$ dependence arising from collective flow [61]; the investigation by the NA49 Collaboration concluded that the system expands over $\tau = 8 \text{ fm}/c$ reaching a volume 14 times the initial size and the hadronic emission time is $\Delta\tau = 3.5 \text{ fm}/c$, i. e. finite and short, implying a QGP phase and disfavoring a first order phase transition without significant expansion in the partonic phase [62].

1.3 RHIC: The Strongly Coupled Liquid

The Relativistic Heavy Ion Collider (RHIC) at the Brookhaven National Laboratory (BNL) with its experiments Solenoidal Tracker At Rhic (STAR), Pioneering High Energy Nuclear Interaction eXperiment (PHENIX) and the smaller PHOBOS and Broad RAnge Hadron Magnetic Spectrometer (BRAHMS) took heavy-ion collisions to a new energy regime of up to $\sqrt{s_{NN}} = 200 \text{ GeV}$, while having the capability to also perform an energy scan to lower beam momenta. It collides Au+Au nuclei, and can also be fed with deuteron, helium, copper, uranium and (polarized) protons. Before the operation of RHIC, the QGP was thought of as a gaseous plasma of weakly interacting partons. However, RHIC ushered in the era of the strongly coupled QGP, the perfect liquid.

The measurement of the elliptic flow discussed in Section 1.2 was repeated at RHIC. The greater number of produced particles at high energies, along with the advances in detector technology paved the way for more differential and precise measurements, relative to the SPS. For example, the event plane resolution reported in the STAR measurement of 0.7 [63] exceeds the value of 0.27 reported by NA49 for the elliptic event plane at the SPS [30]. The p_T -integrated v_2 as a function of centrality at RHIC energies first measured by STAR [63] and confirmed by PHOBOS [64] and PHENIX [65], shows values of up to 6% for peripheral collisions. The large observed anisotropy is inconsistent with hadronic transport calculations by RQMD [66,67] or URQMD [68], which under-predict the data. Instead it shows agreement with hydrodynamic calculations [69]. The linear rise of the v_2 as a function of p_T is evidence for strong interaction. In a partonic transport calculation using pQCD cross-sections, gluon densities $dN_g/d\eta > 7000$ are required in order to match the data [70]. These first measurements of RHIC constrained the equation of state (EOS) used in the hydrodynamical code. When fixing the initial conditions by measured spectra, e. g. $dN^{\text{ch}}/d\eta$ measured over a wide pseudorapidity range by PHOBOS [71], an EOS involving a QGP phase is favored over a pure hadronic one and the freeze-out temperature is restricted [72]. Delaying thermalization from τ_0 by $\Delta\tau$ and assuming free streaming in between, leads to a reduction in the initial spatial eccentricity ϵ_x :

$$\frac{\epsilon_x(\tau_0 + \Delta\tau)}{\epsilon(\tau_0)} = \left[1 + \frac{(c\Delta\tau)^2}{\langle \vec{r}^2 \rangle_{\tau_0}} \right]^{-1} \quad (1.8)$$

where \vec{r} is the initial transverse radius and $\langle \dots \rangle_{\tau_0}$ denotes the azimuthal average at time τ_0 . The large observed anisotropic flow gives a stringent upper limit on the thermalization time τ_{equ} , insisting that thermalization must occur before $\tau_{\text{equ}} < 1.75 \text{ fm}/c$ [73]. A distinct feature of hydrodynamics is the mass dependence of the elliptic flow already mentioned in Section 1.2: for heavier particles the rise in $v_2(p_T)$ is shifted to higher p_T , due to the radial flow. This mass splitting was predicted for RHIC in [74] and today is considered a crucial test for the collectivity of a system [75]. The STAR Collaboration communicated the first measurement of identified particle elliptic flow at RHIC with the centrality dependent results of $v_2(p_T)$ for π^\pm , K^\pm , p and \bar{p} at $\sqrt{s_{\text{NN}}} = 130 \text{ GeV}$ in [76]. The data is completed with measurements of singly-strange neutral particles in [77]. The heavier particles are more affected by the flow field as their mass suppresses substantial thermal smearing of their momentum. Consequently their displayed elliptic flow is more sensitive to the EOS in a hydrodynamic framework. Fig. 1.11 shows the p_T -differential v_2 for pions and protons as measured in [76] with the predictions from [74] for an EOS of a hadron gas and one involving a phase transition. We see that the heavier protons show a much clearer deviation than the pions from the hadron gas EOS; making a stronger case for the scenario including a phase transition.

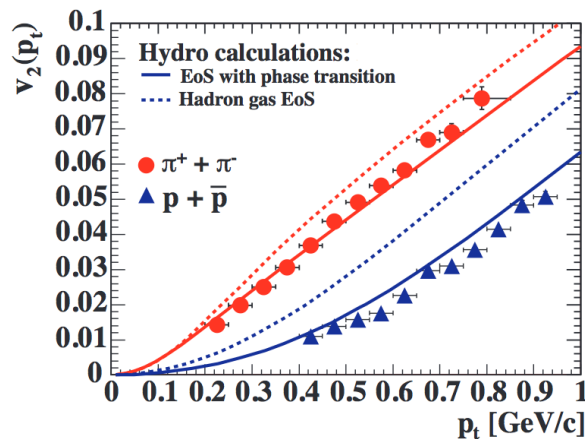


Figure 1.11: Elliptic flow v_2 as a function of p_T for pions and protons as measured by STAR in [76] together with the predictions of [74]. Picture taken from [78].

The hydrodynamic calculations carried out so far all did not include any viscous effects. One could only say from the good agreement of the ideal hydro predictions that it must be somewhat low. Being a property of the matter created in heavy-ion collisions, determination of the viscosity is of fundamental interest. It was soon realized that the ratio of the shear viscosity over the entropy density η/s has a substantial impact on the elliptic flow [79]. A conjecture from the correspondence between Anti-deSitter space and a limit of certain conformal field theories (AdS/CFT) [80] gives a lower limit on $\eta/s \geq \hbar/(4\pi k_B)$ [81]. It may be criticized that QCD is not supersymmetric Yang-Mills theory in the limit of large N_c and large t'Hooft coupling $g^2 N_c$, but a similar bound can be derived from Heisenberg's uncertainty principle alone, which

gives $\eta/s \geq \hbar/k_B$ [81]. A wealth of data on elliptic flow of unidentified and identified particles in $\sqrt{s_{NN}}=200$ GeV Au+Au collisions can be found in, e. g., [82, 83]. Fitting these data with a hydrodynamic code including shear viscosity, one arrives at the conclusion that indeed the shear viscosity is small, and depending on the initial conditions used, varies between one and two times the lower bound set by AdS/CFT [84].

The above quoted value for η/s should be thought of as an effective viscosity, averaged over the whole evolution of the collisions, with a non-negligible contribution from the hadronic phase. It is known that in general the viscosity depends on temperature. In [85] it was explored how sensitive the p_T -differential elliptic flow is to the viscosity of the hadron matter below and the QGP above the critical temperature by either assuming a realistic dependence of the viscosity on temperature [86, 87] with a minimum at the phase transition or setting it to the constant low value of $\hbar/(4\pi k_B)$. It turned out that with the heavy-ion collisions at RHIC, $v_2(p_T)$ is mostly sensitive to the properties of the hot hadron matter, but only slightly affected by the viscosity of the quark-gluonic state. The situation is different at the Large Hadron Collider (LHC), especially at its full energy of $\sqrt{s_{NN}}=5.5$ TeV where $v_2(p_T)$ is dominated by the transport coefficient of the QGP.

For reasons of causality the creation of a high- p_T parton pair should be unaffected by whether or not a QGP is formed in the nucleus-nucleus collision.¹ High- p_T particles can therefore probe the medium as they plow through it. Bjorken investigated the energy loss of such high- p_T partons in the QGP in [88] and derived the formula:

$$\frac{dE}{dx} \simeq \left(\frac{2}{3}\right)^{\pm 1} \epsilon^{1/2} \left(\log \frac{4ET}{M^2}\right) \cdot e^{-M/T} (1 + M/T) \text{ (GeV/c)}, \quad (1.9)$$

where the exponent -1 should be taken for gluons and +1 for quarks to account for the color factor (note the confusion on the sign of the exponent in Bjorken's work), ϵ is the energy density in GeV/fm³, E is the energy, T is the temperature, and M is the mass of the parton. Bjorken's formula reckons collisional energy loss only. He found that the mean loss in transverse momentum of a jet should be $\langle \Delta p_T \rangle \sim \left(\frac{dE_T}{dy}\right)^{1/2}$. This shows that for a highly dense plasma, a jet can be completely absorbed. The energy loss of jets was further explored in [89]. The possibility was raised that the deconfined phase could be signaled by a reduction of the collisional energy loss of partons and therefore an increased viscosity, both occurring only around the phase transition. Furthermore the radiative energy loss was examined and asserted to be at most comparable to the collisional one. A convenient way to quantify the energy loss by medium effects of high- p_T probes is the p_T -dependent nuclear modification factor:

$$R_{AA}(p_T) = \frac{d^2 N^{AA}/d\eta dp_T}{\langle T_{AA} \rangle d^2 \sigma^{PP}/d\eta dp_T}, \quad (1.10)$$

¹The parton is created before a medium forms.

where $\langle T_{AA} \rangle = \langle N_{\text{coll}} \rangle / \sigma_{\text{inel}}^{\text{NN}}$ is the nuclear overlap function. The dijet R_{AA} was calculated for $\sqrt{s_{\text{NN}}} = 200$ GeV. It turned out that even for zero energy loss in the QGP, the R_{AA} is below unity due to the hadronic phase. The amount of jet quenching is sensitive to the energy loss mechanisms. For central heavy-ion collisions with $\sqrt{s_{\text{NN}}} = 200$ GeV, at $p_{\text{T}} \sim 20$ GeV a reduction of the dijet yield of about a factor 10 is expected with a log-like rise as a function of p_{T} to smaller suppression factors of about 2 at $p_{\text{T}} \sim 80$ GeV. To allow for direct comparison with the experiments at RHIC, inclusive single particle spectra were examined with the HIJING MC generator [90] for their response on jet quenching in [91]. It became apparent that the p_{T} spectra in $\sqrt{s_{\text{NN}}} = 200$ GeV Au-Au collisions are modified by gluon shadowing and jet quenching, the former being easily accessible via p-Au collisions.

The suppression of single high- p_{T} particles was observed by PHENIX [92] and STAR [93]. Both collaborations showed that the $R_{AA}(p_{\text{T}})$ for $p_{\text{T}} \gtrsim 2$ GeV is about 0.5 for the 10% most central Au-Au collisions, while for peripheral ones it is consistent with a incoherent sum of single nucleon-nucleon collisions, i. e. $R_{AA} = 1$. The measurement confirms the substantial energy loss of the partons in the colored medium.

The quenching of dijets could be verified by p_{T} -triggered azimuthal correlations. In pp collisions, a strong back-to-back correlation exists in the dihadron data, which arises from the momentum conservation in the initial hard scattering of partons. This link persists in peripheral Au-Au events but is broken in central collisions. The effect can be quantified by defining an azimuthal pair distribution per trigger particle, corrected for efficiency ϵ :

$$D(\Delta\phi) = \frac{1}{N_{\text{trigger}}} \frac{1}{\epsilon} \int d(\Delta\eta) N(\Delta\phi, \Delta\eta). \quad (1.11)$$

Integrating the distribution over a certain angle, e. g. the away side, while subtracting the contribution from elliptic flow and constructing the ratio of Au-Au to pp collisions leads to the observable I_{AA} :

$$I_{AA}(\Delta\phi_1, \Delta\phi_2) = \frac{\int_{\Delta\phi_1}^{\Delta\phi_2} d(\Delta\phi) [D^{\text{Au-Au}} - B(1 + 2v_2^2 \cos(2\Delta\phi))]}{\int_{\Delta\phi_1}^{\Delta\phi_2} d(\Delta\phi) D^{\text{pp}}}. \quad (1.12)$$

When selecting the trigger particle to have a p_{T} between 4 and 6 GeV/ c , the I_{AA} for central events drops to about 0.1 for the away side $|\Delta\phi| > 2.24$, $\Delta\phi \in [-\pi, \pi]$. At the same time the per trigger yield on the near side $|\Delta\phi| < 0.75$ remains unmodified, i. e. $I_{AA} = 1$ [94]. The arising picture is that by triggering on a high- p_{T} particle in heavy-ion collisions, one creates a surface bias, i. e. the production point of the near-side jet is likely to be shifted into the trigger direction. The away-side jet therefore has to travel a long distance through the created medium suffering from severe energy loss up to complete absorption.

This picture is corroborated by d-Au collisions in which no QGP is believed to be formed. Fig. 1.12 shows the two discussed observables for jet quenching at $\sqrt{s_{\text{NN}}} = 200$ GeV. At this

energy the collaborations could take a complete dataset of pp, d-Au and Au-Au collisions. The $\langle N_{\text{bin}} \rangle$ -scaled ratio of p_T spectra, $R(p_T)$, for π^0 measured by PHENIX and depicted in Fig. 1.12 (right) exhibits no jet quenching in d-Au collisions. Consequently the strong stopping of high- p_T particles observed in Au-Au collisions is attributed to the violent interactions in the strongly coupled QGP. In Fig. 1.12 (left) dihadron correlations measured by STAR are superimposed for pp, d-Au and Au-Au collisions. It is apparent that the d-Au result resembles much the pp data with a distinct away-side peak at $\Delta\phi = \pi$, $\Delta\phi \in [-\frac{1}{2}\pi, \frac{3}{2}\pi]$. In the Au-Au data however, the away-side peak is absent and the jet completely absorbed by the medium.

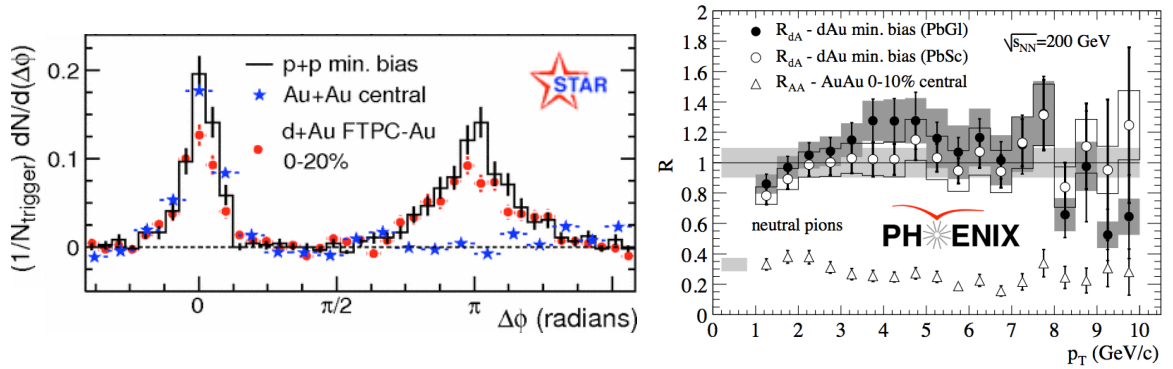


Figure 1.12: Evidence for jet quenching at RHIC. Left: Dihadron correlations in pp, d-Au and Au-Au collisions at $\sqrt{s_{NN}} = 200$ GeV by STAR [95]. The dijet away-side peak is clearly visible around $\Delta\phi = \pi$ in pp and d-Au collisions, but is extinct in Au-Au collisions. Right: Nuclear modification factor $R(p_T)$ for π^0 in d-Au and Au-Au collisions by PHENIX [96]. No modification by cold nuclear matter effects is seen in d-Au collisions, therefore the strong suppression observed in Au-Au collisions is a hot medium effect.

These most important RHIC measurements changed our image of the QGP. Instead of a weakly coupled gas, especially STAR and PHENIX proved it to be a liquid with fierce interactions.

1.4 The Physics Program of ALICE

After the discovery phase at the SPS and the more qualitative features we learned from RHIC about the QGP, the LHC with its dedicated heavy-ion apparatus A Large Ion Collider Experiment (ALICE) aims to quantify the properties of the state of liberated quarks and gluons. Several advantages over the RHIC setup will allow for that.

- The advances in technology result in an instrument allowing for high-precision measurements (see Chapter 3 for a discussion of the detectors of ALICE).

- The QGP lives longer at LHC energies. This makes the observables more sensitive to the QGP as, e. g., discussed already for the determination of the shear viscosity in Section 1.3.
- The multiplicities of particles, essential for any correlation measurement, and the cross sections for rare probes like J/ψ are much larger than at RHIC. Together with the high luminosity provided by the LHC this provides the rich statistics needed for differential analyses.

The first LHC publication was the measurement of $dN_{\text{ch}}/d\eta$ in pp collisions by the ALICE Collaboration [97]. For Pb-Pb collisions at $\sqrt{s_{\text{NN}}} = 2.76$ TeV, the ALICE measurement can be found in [98]. It is an experimentally more easily accessible variable as no particle identification or full momentum measurement is needed for it. Rather — to exaggerate the depiction — only straight line fits through detector hits are necessary. Nevertheless it is a major measurement constraining the theoretical models. Its importance can be grasped by looking at the theoretical predictions for $dN_{\text{ch}}/d\eta$ in the 5% most central collisions which — before the RHIC measurements were available — reached 8000 [99] and at the time of measurement at the LHC varied from about 1000 to 2200 [100–112]; the experimentally determined value amounts to $1584 \pm 4(\text{stat.}) \pm 76(\text{syst.})$. The resulting initial energy density at proper time $\tau_0 = 1$ fm/c is $\epsilon_0 = 10.7$ GeV/fm³ [113]. We will use a comparable value in Section 2.1 to calculate some dynamics of Pb-Pb collisions at the LHC.

ALICE not only repeated the measurement of charged particle density, but aims to study essentially all observables that were examined by the SPS and RHIC experiments with higher precision and more differentially [114]. To allow for this, ALICE unifies many detector technologies (see Chapter 3) which provide identification for all kinds of species over a wide range of momentum. For π , K, p this extends from $p \approx 100$ MeV/c [115] to $p_{\text{T}} \geq 20$ GeV [116]; for J/ψ the reach in p_{T} encloses $p_{\text{T}} = 0$ which makes ALICE unique at the LHC.

The low p_{T} reach for the J/ψ is particularly interesting. At lower energies like at the SPS and RHIC, the $c\bar{c}$ pair created in an initial hard scattering is thought to dissolve due to color screening (see Fig. 1.13 left). At the LHC a new production mechanism might be activated (see Fig. 1.13 right). Charm quarks produced in independent, initial hard scatterings could recombine on a statistical basis. This would lead to an enhancing component, which, taken together with the color screening, would result in a weaker suppression of the J/ψ , especially at mid-rapidity and low p_{T} [117]. Recent measurements of ALICE show an indication that a fraction of the J/ψ might indeed be produced via recombination [118, 119]. Fig. 1.13 (right) displays the possible room for a regeneration component at the LHC at low p_{T} , where less J/ψ suppression is observed in comparison to the PHENIX measurement at RHIC. In Section 3.4 a detector dedicated to providing an excellent electron identification at mid-rapidity needed for a precise measurement of the J/ψ is introduced.

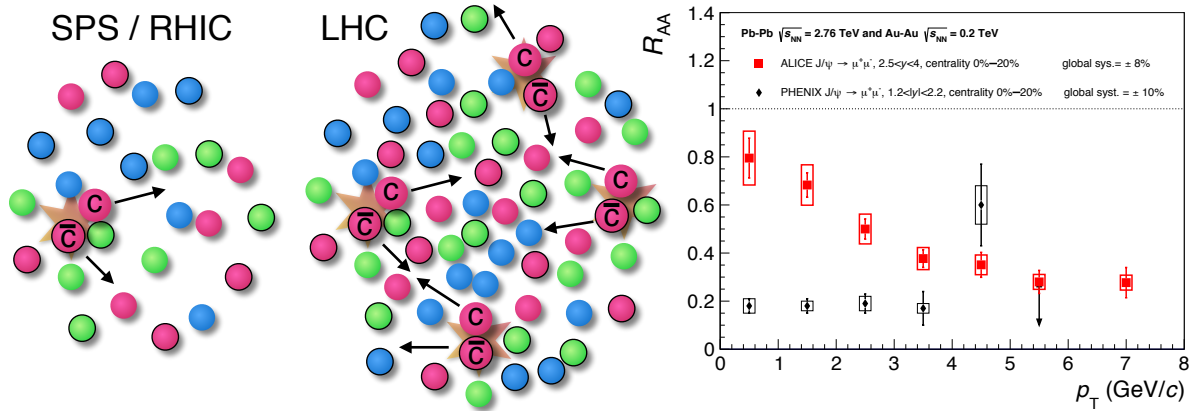


Figure 1.13: Medium effects in central heavy-ion collisions on J/ψ production at SPS and RHIC energies (left) and under LHC conditions (center). While at the SPS and RHIC the $c\bar{c}$ just dissolves into the medium owing to color screening, at the LHC independently produced $c\bar{c}$ can re-combine as a consequence of their abundant production. Right: Nuclear modification factor R_{AA} for J/ψ production at forward rapidities at the LHC (red squares) and at RHIC (black diamonds). At the LHC, less suppression compared to the RHIC measurement is seen for low p_T .

A new topic to study in heavy-ion collisions emerged in the LHC era: reconstructed jets. The R_{AA} and I_{AA} studied by STAR and PHENIX quantify the appearance of high- p_T hadrons. The object of interest though is the highly energetic parton and its energy loss in the dense medium. Jet finding algorithms provide a better approximation of the parton by grouping collimated sprays of particles to jets and reconstructing their energy. This provides the tool to study the energy loss in the QGP more differentially and try to track the radiated gluons. Fig. 1.14 shows the qualitatively two types of gluons: these radiated out of cone and those in cone. While the out-of-cone gluon will lead to less reconstructed energy within the cone, the in-cone radiated gluons will broaden the jet.

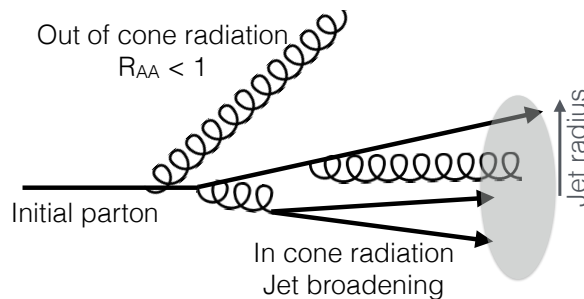


Figure 1.14: Partonic energy loss: a quark propagating through the medium. A gluon is emitted out of cone and together with the steeply falling spectrum leads to an $R_{AA} < 1$. Also shown is in-cone gluon radiation and gluon splitting which lead to a jet broadening.

One way of seeing the out-of-cone radiation is by looking at dijets. ATLAS [120] and CMS [121] with their 4π calorimetry coverage are particularly equipped for this. Fig. 1.15 (left) shows an event display of Pb-Pb collisions at 2.76 TeV by the CMS Collaboration [122]. The leading jet with $p_T = 205$ GeV/c is accompanied at $\Delta\phi \approx \pi$ by a jet of only 70 GeV/c. The subleading jet lost 2/3 of its energy by traversing the QGP. This dijet asymmetry $A_j = \frac{|E_1 - E_2|}{E_1 + E_2}$ was studied by ATLAS [123]. The distribution of A_j for the 0–10% most central events of Pb-Pb collisions at $\sqrt{s_{NN}} = 2.76$ TeV compared to the distribution in pp collisions and a Monte Carlo simulation can be seen in Fig. 1.15 (right). The distribution of A_j is peaked at 0.425, which corresponds to the subleading jet having lost 60% of its energy.

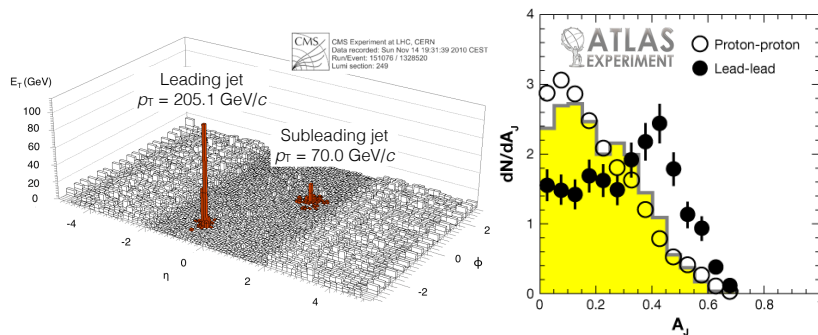


Figure 1.15: Dijets in Pb-Pb collisions at the LHC. Left: Event display by CMS showing two jets separated by $\Delta\phi = \pi$ peaking over a flat background. The subleading jet is stopped while traversing the medium and loses 2/3 of its transverse momentum. Figure from [122]. Right: Dijet asymmetry $A_j = \frac{|E_1 - E_2|}{E_1 + E_2}$ in 0–10% central Pb-Pb collisions at $\sqrt{s_{NN}} = 2.76$ TeV and pp data from $\sqrt{s} = 7$ TeV together with Hijing+Pythia calculations in the yellow filled histogram. The medium jet quenching appears as a shift of the distribution to higher asymmetries A_j . Figure from [123].

Scaling the single jet production cross-section with the nuclear overlap function T_{AA} which accounts for the changing number of initial hard scatterings [124], allows to study the evolution of jet production with system size. As the jet cross-section decreases rapidly with jet p_T , out-of-cone radiation will lead to a suppression in jet yield as a function of p_T . In [125], the ratio of jet yield in central (0–10%) to peripheral (50–80%) Pb-Pb collisions R_{CP} with fixed jet resolution parameter R was measured by ALICE. Consistent with ATLAS [126], a suppression by a factor of two in central collisions was found, as demonstrated in Fig. 1.16 (left). Before the start-up of the LHC, the lost energy of the jet was thought to be redistributed to small or moderate angles [127]. ALICE with its track transverse momentum coverage down to $p_T = 0.15$ GeV/c is well suited to study the fragments produced in the jet-medium interaction process. By looking at the ratio of the jet yield with a radius $R = 0.2$ to $R = 0.3$, one is sensitive to small or moderate angle radiation. Fig. 1.16 (right) shows this ratio in central Pb-Pb collisions and compares it to peripheral Pb-Pb collisions as well as the vacuum jet

fragmentation in Pythia. It is clear that within the uncertainties, no medium modification is visible in this observable. Taking the two measurements displayed in Fig. 1.16 together leads to the conclusion that the lost jet energy is dispersed to low- p_T particles appearing at large angles with respect to the jet axis.

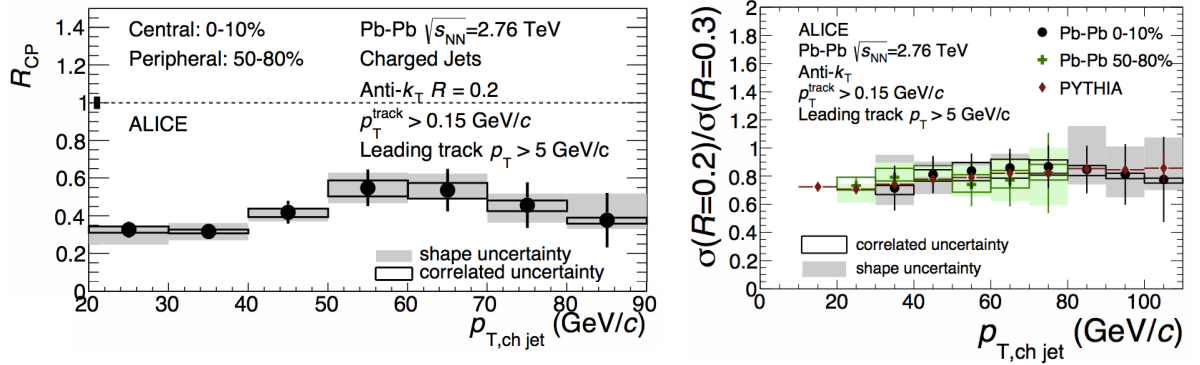


Figure 1.16: Study of the jet modification in Pb-Pb collisions. Left: Jet suppression in central Pb-Pb collisions quantified by R_{CP} , the ratio of the jet production cross-sections in central and peripheral collisions, scaled by the nuclear overlap functions. Right: Ratio of the jet production cross-section with a jet finder radius $R = 0.2$ and 0.3 studied in central and peripheral Pb-Pb collisions with ALICE compared to the vacuum fragmentation in a Pythia simulation. No impact of the medium modification on this ratio is observed. Both taken from [125].

A striking difference between pp and Pb-Pb collisions observed at the SPS [128] and RHIC was the baryon enhancement in nuclear collisions [129, 130]. Fig. 1.17 (left) shows the Λ/K_S^0 ratio in Pb-Pb collisions at $\sqrt{s_{NN}} = 2.76$ TeV measured by ALICE [131] together with the data obtained at RHIC and model calculations. The hydrodynamic calculation [132, 133, 133] follows the data only up to $p_T \approx 2$ GeV/c. A much better description is given by the EPOS model [134]. Within this approach based on parton ladders, a jet-medium interaction is essential to reproduce the ALICE data. The fragmenting jet picks up (anti-)quarks from the medium, such that the resulting hadrons bear a flavor and flow mark from the medium, but also carry high transverse momentum from the initial hard scattered parton.

A test of this imprint of the expansion and chemical composition of the bulk matter on the jet fragmentation was performed in [135]. The particle identification capabilities of ALICE allow to study the baryon enhancement in the jet and bulk region separately. Fig. 1.17 (right) shows that for central Pb-Pb collisions the proton to pion ratio in the jet is unaltered with regard to the vacuum fragmentation, i. e. pp collisions. Possibly, there is a strong surface bias introduced by approximating the jet with a high- p_T trigger particle, such that the fragmentation of the selected jets happens outside of the medium. At the LHC, jets are abundantly produced. Their interplay with the soft bulk has great potential to shed light on the strong interaction dynamics in the deconfined phase.

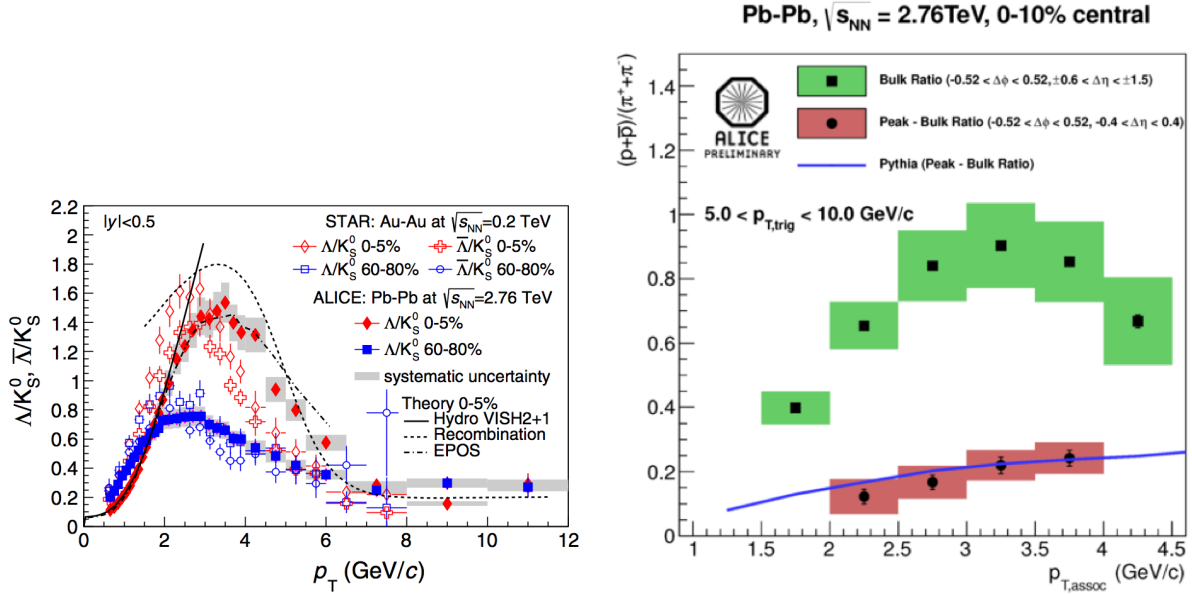


Figure 1.17: Left: Baryon enhancement in Pb-Pb collisions measured by ALICE with model comparison (see text). Taken from [131]. Right: Proton to pion ratio in the jet and bulk region with respect to a high- p_T trigger particle. Also shown is the proton to pion ratio in Pythia simulations of pp collisions. Taken from [135].

Fig. 1.18 presents the elliptic flow coefficient v_2 for identified particles in 20–30% most central Pb-Pb collisions, as measured in [136]. The wealth of data with low uncertainties allows to observe several features. At low $p_T < 3$ GeV/c, the particle species are ordered according to their mass. As mentioned in Section 1.2 and Section 1.3, this is caused by an interplay between the elliptic and the radial flow; the latter pushes the heavy particles to higher transverse momenta. Since the effect is stronger in-plane than out-of-plane, at low p_T it leads to a reduced v_2 of the heavy particles compared to the light species. At high $p_T > 3$ GeV/c, π^\pm , K^\pm , and K_S^0 on the one hand and p , Λ , Ξ , and Ω on the other hand seem to form a band with similar values of v_2 . This grouping into mesons and hadrons, when observed at RHIC, was taken as evidence of a number of constituent quark scaling originating in the partonic degrees of freedom in the QGP phase. The right panel of Fig. 1.18, evidences this scaling is only approximate at the LHC. The data is in fair agreement with a viscous hydrodynamical calculation coupled to a hadronic cascade code [137–139]. However, the model reverses the mass ordering for p and Λ which is not observed in data. In [136] it is stated that this discrepancy to data could indicate that the cross-sections in the transport code need further improvements.

A surprising result was the possibility of collective effects in p-Pb collisions. CMS presented a near-side ridge in high-multiplicity p-Pb collisions [140], and ALICE showed that by subtracting the away-side jet peak as it appears in low-multiplicity p-Pb events, a symmetric double-ridge structure is revealed [141]. The double ridge structure is either explained by hydrodynamics [142]

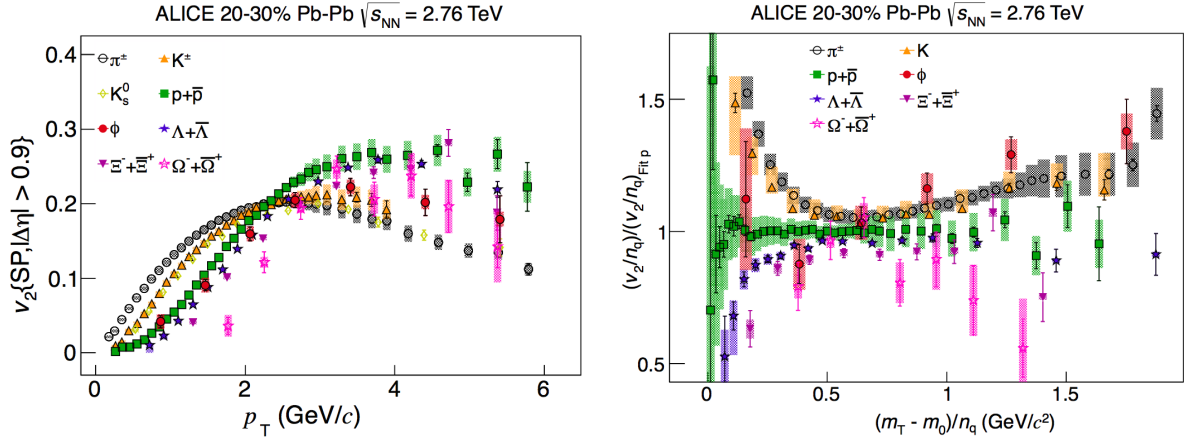


Figure 1.18: Left: Identified particle elliptic flow measured by ALICE. Right: Same data as on the left but here as v_2/n_q vs. $(m_T - m_0)/n_q$, where n_q is the number of constituent quarks. Both taken from [136].

or the color glass condensate (CGC) model [143]. In [144], the PID capabilities of ALICE were made use of to investigate the double ridge for each particle species separately. Fig. 1.19 (left) shows the second component of a Fourier decomposition of the double ridge for hadrons, pions, kaons, and protons. The pattern resembles the elliptic flow observed in A-A collisions, cf. Fig. 1.18. Various other studies of p-Pb collisions were triggered, e. g., the investigation of the Fourier component with the cumulant method [145] by the CMS Collaboration, and the study of three-pion correlations at small relative momenta [146] by ALICE. The main result of the latter is displayed in Fig. 1.19 (right), where the radius parameter in a Edgeworth expansion of the particle source is plotted as a function of the number of final-state charged particles. The radius parameter for both, two- and three-particle correlations, in p-Pb collisions appears more similar to pp than Pb-Pb collisions.

We note the potential of particle correlation measurements (at small relative momenta) to disclose the dynamics in strongly interacting systems.

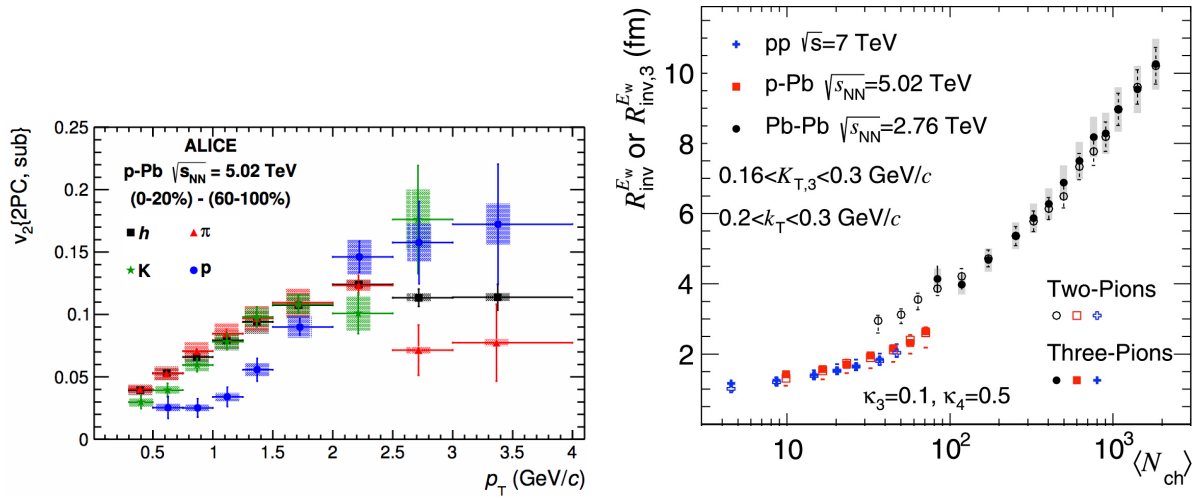


Figure 1.19: Left: Second Fourier coefficient v_2 for hadrons, pions, kaons, and protons in p-Pb collisions. Obtained by a subtraction procedure. Taken from [144]. Right: Source radii from two- and three-pion correlations in pp, p-Pb, and Pb-Pb collisions. Taken from [146].

Chapter 2

Freeze-Out Radii

2.1 1+1D Ideal Hydrodynamics with Bjorken Flow and a 1st Order Phase Transition

In Appendix B, a straight forward derivation of the evolution dynamics in 1+1D hydrodynamics with Bjorken flow and a 1st order phase transition according to the MIT bag model is given. It is based on the assumption of local thermal equilibrium, the conservation of energy and momentum, the different number of degrees of freedom in a confined and deconfined phase, and the bag constant B , where B describes the pressure of the vacuum.

The equation of state of the QGP phase within the MIT bag model, derived from Eqs. B.27 and B.28, reads $\mathcal{P}_s(\epsilon) = \frac{1}{3}(\epsilon - 4B)$, where \mathcal{P}_s is the hydrostatic pressure, ϵ is the energy density, and B is the bag constant. For the mixed phase, the pressure has a constant value of \mathcal{P}_c , and for the hadron phase $\mathcal{P}_s = \frac{1}{3}\epsilon$. Applying the proper time τ dependence of the energy density ϵ , Eq. B.53, grants

$$\text{QGP} \quad \partial_\tau \epsilon = -\frac{4}{3} \frac{\epsilon - B}{\tau} \quad \Rightarrow \quad \frac{\epsilon - B}{\epsilon_0 - B} = \left(\frac{\tau_0}{\tau}\right)^{\frac{4}{3}} \quad (2.1)$$

$$\text{MixedPhase} \quad \partial_\tau \epsilon = -\frac{\epsilon + \mathcal{P}_c}{\tau} \quad \Rightarrow \quad \frac{\epsilon + \mathcal{P}_c}{\epsilon_{\text{QGP}}(\mathcal{T}_c) + \mathcal{P}_c} = \frac{\tau_{\text{Q}}}{\tau} \quad (2.2)$$

$$\text{HadronGas} \quad \partial_\tau \epsilon = -\frac{4}{3} \frac{\epsilon}{\tau} \quad \Rightarrow \quad \frac{\epsilon}{\epsilon_\pi(\mathcal{T}_c)} = \left(\frac{\tau_{\text{H}}}{\tau}\right)^{\frac{4}{3}}. \quad (2.3)$$

Where τ_{Q} and τ_{H} are constants

$$\tau_{\text{Q}} = \tau_0 \left(\frac{\epsilon_0 - B}{\epsilon_{\text{QGP}}(\mathcal{T}_c) - B} \right)^{\frac{3}{4}}, \quad \tau_{\text{H}} = \tau_{\text{Q}} \left(\frac{\epsilon_{\text{QGP}}(\mathcal{T}_c) + \mathcal{P}_c}{\epsilon_\pi(\mathcal{T}_c) + \mathcal{P}_c} \right), \quad (2.4)$$

\mathcal{T}_c is the temperature of the phase transition, see Eq. B.29, and ϵ_0 is the initial energy density.

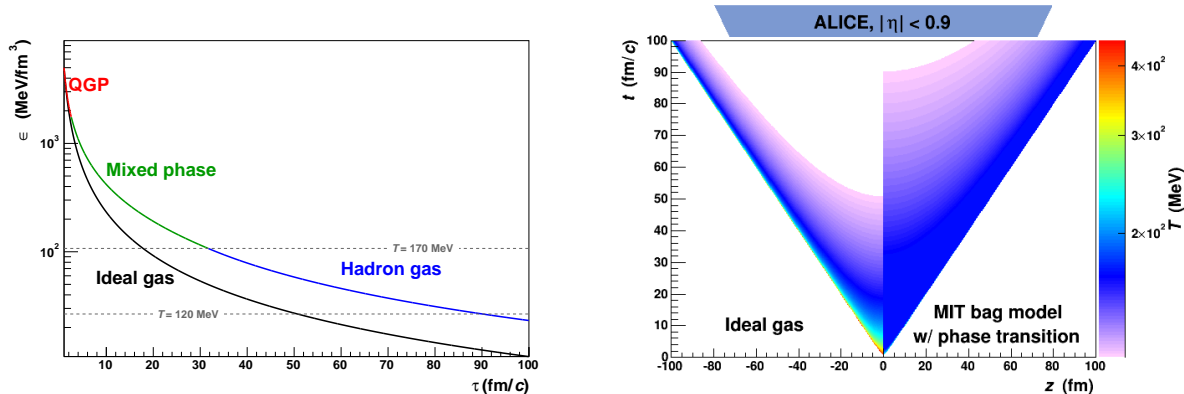


Figure 2.1: Ideal hydrodynamic evolution with $\epsilon_0 = 5 \text{ GeV/fm}^3$, $\tau_0 = 1 \text{ fm}/c$ for an ideal gas and an equation of state according to the MIT bag model with $B = (240 \text{ MeV})^4 \approx 0.4 \text{ GeV/fm}^3$. Left: energy density ϵ vs. proper time τ . Right: temperature vs. longitudinal z and time t for an ideal gas ($z < 0$) and the MIT bag model equation of state including a first order phase transition ($z > 0$). The minimum of the z axis was set to a temperature of 120 MeV, about the temperature of kinetic freeze-out.

This proper time evolution of the energy density for realistic initial conditions in central Au-Au collisions at RHIC [147], $\epsilon_0 = 5 \text{ GeV/fm}^3$ and $\tau_0 = 1 \text{ fm}/c$ together with the evolution for a pure ideal gas is shown in Fig. 2.1. These initial conditions are rather conservative estimates for the LHC, cf. $\epsilon_0 = 10.7 \text{ GeV/fm}^3$ at $\tau_0 = 1 \text{ fm}/c$ mentioned in Section 1.4. On the left side of Fig. 2.1 the development of the energy density ϵ as a function of proper time τ is displayed. The main feature is the decrease of the energy density with proper time that is slowed down with the bag model's equation of state. The evolution for the ideal gas and the hadron gas are the same, i. e., the difference is in the QGP and the mixed phase. In a double-log plot one sees the slopes of the ideal and the hadron gas are $-4/3$, while the slope of the QGP phase is significantly less steep and the mixed phase smoothly connects the two regimes. This implies that any higher initial energy density will increase the difference between the two scenarios. Therefore, this calculation should be seen as a lower limit for the impact of a phase transition on observables for heavy-ion collisions at the LHC. We note that a temperature of $\mathcal{T} = 120 \text{ MeV}$ — at which hadronic matter is believed to decouple and stream freely to the detectors — is reached at a proper time $\tau \approx 50 \text{ fm}/c$ for the ideal gas and $\tau \approx 90 \text{ fm}/c$ when the QGP phase is involved. This means that the source spraying out particles lives nearly twice as long when a QGP is produced.

On the right side of Fig. 2.1 the temperature dependence on the longitudinal space coordinate z and time t is presented for the ideal gas ($z < 0$) and the bag model ($z > 0$). Here, the mechanisms at work to cause the longevity of the medium become more evident. In the QGP

phase, the energy is absorbed by the liberation of the quarks and gluons rather than resulting in a higher thermal motion of the ideal pion gas. Over the whole duration of the mixed phase, the temperature stays constant and only at late proper times $\tau > 30$ fm/ c the cooling kicks in again. A temperature of $\mathcal{T} = 120$ MeV is color coded by the transition from light pink to white, indicating kinetic freeze-out; the particles interact only in the colored region. The matter moves on straight lines from the origin $(0, 0)$ in the (z, t) space, with blocks of matter at different rapidities not interfering with each other (remember Eq. B.60 $\partial_{\eta_s} \mathcal{P}_s = 0$). Therefore the acceptance of full tracking in the ALICE central barrel, corresponding to pseudorapidity $|\eta| < 0.9$, can be indicated by the trapezoid in the upper part of the figure. Connecting the edges of the trapezoid with the origin $(0, 0)$ tells us, which particles are being detected by the experiment. We see that for the ideal gas (IG) the interactions of detected particles cease at a time 50 fm/ $c \lesssim t \lesssim 70$ fm/ c . Taking a simple average, i. e. $t_{\text{fo}}^{\text{IG}} \approx 60$ fm/ c , tells us that the detected particles are extended over $2z_{\text{fo}}^{\text{IG}} \approx 80$ fm at the time of kinetic freeze-out. For the bag model (BM) scenario the same extent can not even be deduced graphically from Fig. 2.1 (right) as the particles at $z \gtrsim 45$ fm are still interacting for the maximal t displayed in the figure. It can however quickly be calculated. Taking $t_{\text{fo}}^{\text{BM}}(\eta_s = 0) \approx 90$ fm/ c gives $t_{\text{fo}}^{\text{BM}}(\eta_s = 0.9) = t_{\text{fo}}^{\text{BM}}(\eta_s = 0) \cosh(0.9) \approx 130$ fm/ c . Simple averaging yields $t_{\text{fo}}^{\text{BM}} = 110$ fm/ c , for which the particles within $|\eta_s| < 0.9$ are spread over $2z_{\text{fo}}^{\text{BM}} \approx 160$ fm. The particle emitting source is two times bigger in the scenario with a QGP than in the scheme without the parton phase.

Realistically, a (1+1)D expansion oversimplifies the problem. Also, the phase transition from a hadronic to a partonic medium was found to be a crossover rather than of first order [148, 149]. Alongside some experimental measurements, less idealized calculations will be discussed in the remainder of this chapter.

2.2 Femtoscopy

In 1956, R. Hanbury Brown and R.Q. Twiss used the interference of photons from Sirius to determine its angular size [150]. In Fig. 2.2 (left) their measurement of the correlation of photons in two detectors separated by the distance d is shown together with the expectation for a star with an angular size of $0.0063''$. This coined the term HBT for any source size determination via particle correlations at small relative momenta.

The first successful application of a similar technique in hadron collisions was done by Goldhaber, Goldhaber, Lee and Pais in 1960 [151]. They inferred a source size from particle correlations in high energy $p\bar{p}$ collisions and found that the angular correlation of pions in $p\bar{p}$ annihilation events is significantly modified by the quantum statistical symmetrization effects as shown in Fig. 2.2 (right), where the measured angular correlation of pions is compared to a calculation with no symmetrization effects (SM) and one including Bose-Einstein statistics for like sign pairs (like).

The radius ρ of the source could be constrained to about 0.75 ± 0.25 fm. The determination of such scales is referred to as femtoscopy and explicitly also includes measurements via particle correlations which are not (solely) of quantum statistical nature [152–154].

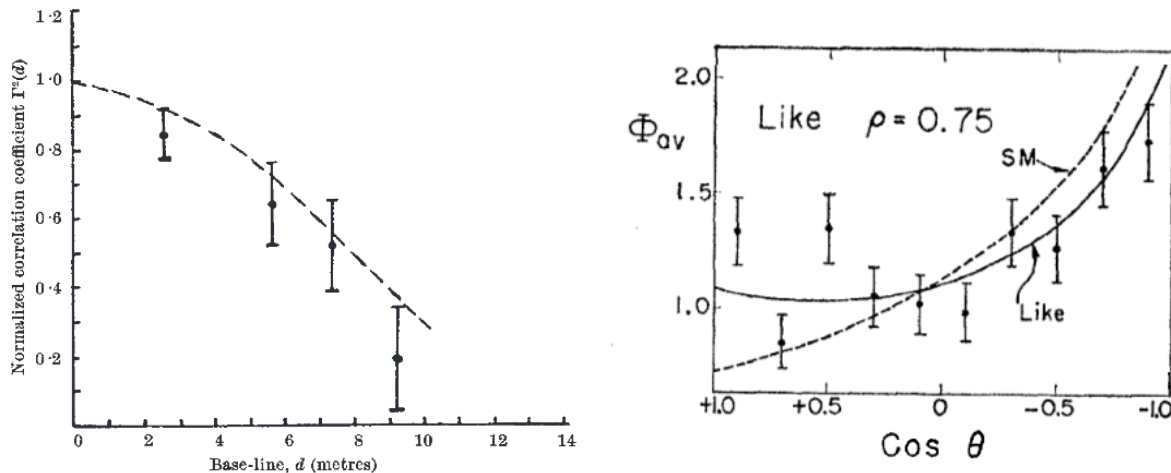


Figure 2.2: Left: Measured normalized correlation coefficient $\Gamma^2(d)$ as a function of d (data points) compared to the expectation for a star of angular size $0.0063''$ (dashed line) [150]. Right: Measured pion correlations Φ_{av} in $p\bar{p}$ annihilations as a function of the pair angle in the $p\bar{p}$ center of mass frame compared to the prediction by a statistical model (SM) and the additional inclusion of symmetrization effects for like sign pairs (like) for a Gaussian source. The parameter ρ is the radius of a similar sphere related to the Gaussian width σ via $\rho = 2.15\sigma$. The theoretically calculated Φ_{av} is averaged over events with four, five (dominant contribution), six or seven pions produced in the event [151].

While in [151] the interference pattern for four, five and six pion production was calculated explicitly, the case of many secondary particles was examined in [155] for evaporating, highly excited nuclei. The excited nucleus emits neutrons for which the detection probability is:

$$\langle \bar{P} \rangle \sim 1 - a \cos [\Delta \vec{p} \Delta \vec{x} / \hbar], \quad (2.5)$$

where $\Delta \vec{p}$ is the momentum difference and $\Delta \vec{x}$ is the difference in emission points of the two neutrons. The factor a in front of the \cos term equals $\frac{1}{2}$ for neutrons and arises from the concurrent occupation of the attractive singlet and the repulsive triplet states. In the same work it was proven that the same formalism can be applied to pion production in collisions of accelerated nuclei when each point of the illuminated region is regarded as an independent emitter. For identical spin-zero bosons like pions the factor a becomes $+1$.

The translation into measurable particle correlations in terms of two-particle production cross-sections which depend only on the size of the source and the pair momentum difference

was performed in [156] by integrating over the emission region. Similar work can also be found in [157], where it was shown that for particles with similar momenta, the extinction of states with odd orbital angular momentum occurs at $|\vec{p}_1 - \vec{p}_2|R < \hbar/R$, where R is the size of the field of particle generation. It was seen, that the dependence of the asymmetry coefficient in the angular distribution of the vector $\vec{p}_1 - \vec{p}_2$ (in the frame where $\vec{p}_1 + \vec{p}_2 = 0$) on the value of $|\vec{p}_1 - \vec{p}_2|$ allows to estimate the value of R .

In [158] the neutral kaon system was investigated. The situation here seems more complicated because of the $K^0\bar{K}^0$ mixing, but it could be shown that independently of the conditions under which the $K^0\bar{K}^0$ pair was created, two selected $K_s^0\bar{K}_s^0$ particles will exhibit Bose-Einstein enhancement. The experimentally reconstructed short-lived component is a superposition of states:

$$|K_s^0\bar{K}_s^0\rangle \sim |K^0K^0\rangle + |\bar{K}^0\bar{K}^0\rangle + |K^0\bar{K}^0\rangle + |\bar{K}^0K^0\rangle, \quad (2.6)$$

where the first two identical-boson doublets are symmetrized as well as the two last doublets because the $CP = +1$ state of the boson-antiboson pair is measured [159].

Two-proton correlations were studied theoretically in [160]. A large contribution from Coulomb and strong final-state interactions together with the Fermi-Dirac statistics result in a correlation function for small relative momenta with many features. Rather than obscuring the sensitivity of the correlation function through the quantum statistical interference to the size, velocity and lifetime of the system, the final-state interactions were found to boost the responsiveness for small systems ≤ 4 fm. While the authors of [160] solved the problem in non-relativistic quantum dynamics, relativistic effects and a finite emission time were included in [161].

The influence of coherence on the two-particle correlation function was investigated in [162]: The intercept of the identical-boson correlation function for zero momentum difference is two only for a fully chaotic source. Partial coherence will lower the height of the correlation function. This connects ““ any identical-particle measurement to the less explored possible phenomenon of coherent emission, making a full understanding of the experimentally observed correlation function more involved.

Finally, the proton-lambda system was suggested in [163]. The lambda is electrically neutral and the particles are non-identical, therefore the correlation results from the attractive strong final-state interaction only. Fig. 2.3 compares the $p\Lambda$ correlation function to the proton-proton one. The two-proton correlation function is depleted by Fermi-Dirac statistics and Coulomb repulsion for very small momentum differences $|\vec{p}_1 - \vec{p}_2|/2 = k < 10$ MeV/c, measured in the pair rest frame, and shows an enhancement above unity by the attractive strong potential around $k \approx 20$ MeV/c for small source radii ≤ 4 fm only. For larger radii the pp correlation function is in-discriminative between different radii. For the proton-lambda case, on the other

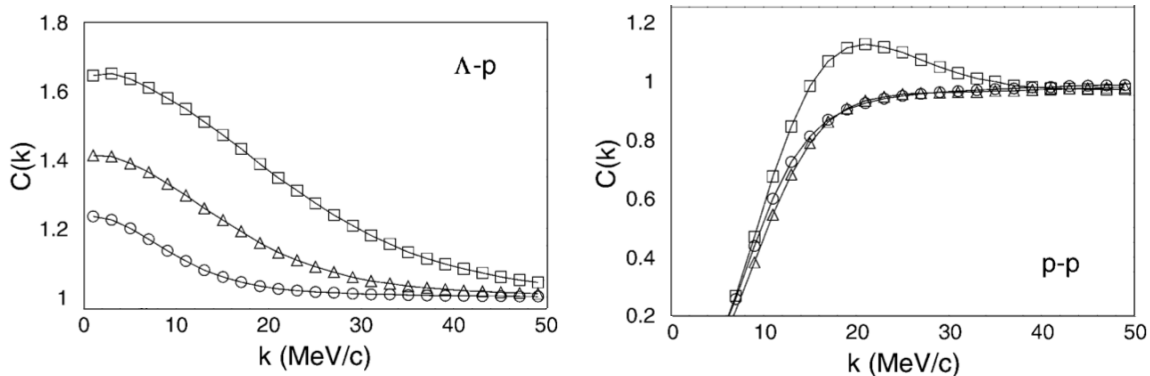


Figure 2.3: Two-particle correlation function $C(k)$ of pairs of protons and lambdas (left) and two protons (right) as a function of pair-momentum difference $k = |\vec{p}_1 - \vec{p}_2|/2$, measured in the pair rest frame, for Gaussian sources with various radii, specifically 4 fm (squares), 6 fm (triangles) and 10 fm (circles). Taken from [163].

hand, the excess at low relative momentum persists for greater extents and the sensitivity is maintained for widely varying source sizes. The correlation function is sensitive in height and shape to the dimensions of the emitter. Being non-identical particles, p Λ correlations empower one to determine whether both species are produced simultaneously [164,165] (although no attempt was made to pursue this experimentally within the scope of this thesis due to the limited amount of statistics). But even without measuring the emission asymmetry explicitly, p Λ correlations are susceptible to a possibly altered freeze-out of strange baryons for which there are hints from both theory and experiment [166].

2.3 Regions of Homogeneity

The Bevalac accelerator [167,168] provided beams of moderately heavy ^{12}C , ^{20}Ne and ^{36}Ar ions. In 1978, two-particle correlation measurements at small relative momenta for pion pairs produced in nucleus-nucleus collisions was carried out at a beam energy of 1.8 GeV/nucleon by the Riverside group [169] followed by W.A. Zajc *et al.* [170]. Going further, the Riverside group experimentally studied the dependence of the source radii on the transverse momentum of the selected pion pairs [171] and observed a decrease of radii with increasing pair momentum.

S. Pratt pointed out in [172] that introducing a common radial velocity β apparently reduces the region over which the particles are correlated. The thermal velocity, increasing with temperature T , competes with the collective flow resulting in an effective temperature $T_{\text{eff}} = T/(\gamma\beta)$. For a static source, this effective temperature is infinite and all particles will be correlated over the full source independent of pair momentum $K = |\vec{p}_1 + \vec{p}_2|$; the observed radius $R(K)$ is constant as a function of K . On the other hand, if significant expansion causes

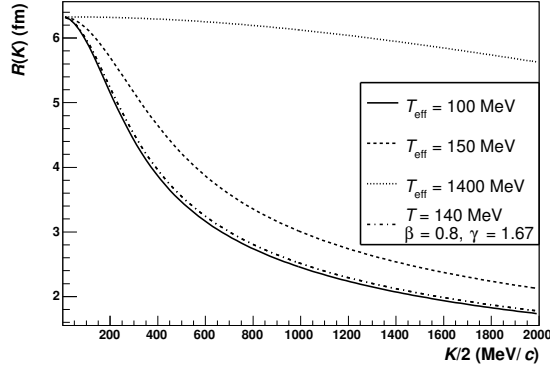


Figure 2.4: Impact of a collective velocity β on apparent radii as a function of pair momentum $K = |\vec{p}_1 + \vec{p}_2|$ for a sphere of radius $R = 7.75$ fm instantaneously emitting particles from its surface for various effective temperatures $T_{\text{eff}} = T/(\gamma\beta)$. According to [172].

the particles emitted from a certain region to have similar momenta, one will vice versa select particles from a specific, reduced space by looking at similar or small relative momenta as it is done in femtoscopy. The scenario investigated in [172] with its results depicted in Fig. 2.4 was a sphere emitting pions from its surface. For an instantaneous ejection of bosons, the extracted radius drops as a function of pair momentum like

$$R(K) = R [(y \tanh y)^{-1} - \sinh^{-2} y]^{1/2}, \quad (2.7)$$

where $y = \frac{1}{2}K/T_{\text{eff}}$ and $T_{\text{eff}} = T/(\gamma\beta)$. Fig. 2.4 reproduces the results presented in [172] for $T_{\text{eff}} = 100$ MeV with the solid line and further probes the sensitivity of the decrease with pair momentum of the experimentally obtained radius to this effective temperature. As can be seen, a moderate change in effective temperature does not change the qualitative dependence: $R(K)$ decreases with a similar shape from $K/2 = 0$ to 2 GeV/ c to 27% or 35% of the value for $T_{\text{eff}} = 100$ MeV or 150 MeV, respectively. Already at the SPS, flow velocities of $\frac{1}{2}c$ were observed [173] (corresponding to $T_{\text{eff}} \approx 240$ MeV). Therefore, an effective temperature of $T_{\text{eff}} = 1400$ MeV is unrealistic for any heavy-ion collision involving a QGP phase, but as can be seen in the figure, only such high effective temperatures exhibit a qualitatively different behavior and demonstrate only a small decrease of the source radii. Realistic values for the LHC, that will also be extracted from fits to particle spectra later within this thesis, of $T = 140$ MeV and $\beta = 0.8$, shown in Fig. 2.4 as the dash-dotted line, are barely distinguishable from the originally investigated scenario. This makes clear that the dependence of extracted femtosopic radii on pair transverse momentum is sensitive to the dynamics of the created fireball, even under the extreme conditions created by the LHC.

S.V. Akkelin and Yu.M. Sinyukov performed a deeper investigation of the influence of

relativistic flow on femtosopic radii in [174]. Analytical approximations of the momentum dependent behavior of extracted source sizes for different types of transversal expansion were studied. For the non-relativistic case, analytical solutions were found earlier by T. Csörgő *et al.* [175] or S. Chapman *et al.* [176]. A slight modification of the Gaussian transverse emission profile

$$\rho(r) = \exp[-\alpha(\cosh y_{\text{T}}(r) - 1)] \quad (2.8)$$

$$\approx \exp[-r^2/(2R_{\text{T}}^2)] \quad (2.9)$$

allows to analytically solve also the relativistic case. Here, $y_{\text{T}}(r)$ is the transverse rapidity and α accounts for a possible difference in the radius R_{ν} of the transverse flow profile (see Eqs. 2.16 and 2.17) and the azimuthally averaged, transverse extent of the emitting source: $\alpha = R_{\nu}^2/R_{\text{T}}^2$. Let us take the opportunity to introduce an experimentally accessible, three-dimensional coordinate system, referred to as the Bertsch-Pratt parametrization. As presented in Fig. 2.5, the pair momentum difference q can be separated into an out, side and long direction. The experimental, three-dimensionally decomposed, two-particle correlation function then allows to extract the characteristic radii R_{out} , R_{side} and R_{long} [177, 178]:

$$C(q_{\text{out}}, q_{\text{side}}, q_{\text{long}}) \approx 1 + \exp\left(-\frac{1}{2}R_{\text{out}}^2 q_{\text{out}}^2 - \frac{1}{2}R_{\text{side}}^2 q_{\text{side}}^2 - \frac{1}{2}R_{\text{long}}^2 q_{\text{long}}^2\right), \quad (2.10)$$

where we neglected the cross-term $R_{\text{out-long}}$ [179]. These experimentally observed radii were connected by Akkelin and Sinyukov [174] to the local length of homogeneity $\bar{\lambda}$:

$$R_{\text{out}}^2 = \bar{\lambda}_{\text{out}}^2 \left(1 + \frac{p_{\text{T}}}{m_{\text{T}}} \left|\frac{d\tau}{dr}\right|\right)^2 + \bar{\lambda}_{\text{long}}^2 \left(\frac{p_{\text{T}} \tanh \theta}{m_{\text{T}} \cosh \theta}\right)^2 \quad (2.11)$$

$$\stackrel{\theta=0}{=} \bar{\lambda}_{\text{out}}^2 \left(1 + \frac{p_{\text{T}}}{m_{\text{T}}} \left|\frac{d\tau}{dr}\right|\right)^2, \quad (2.12)$$

$$R_{\text{side}}^2 = \bar{\lambda}_{\text{side}}^2, \quad (2.13)$$

$$R_{\text{long}}^2 = \bar{\lambda}_{\text{long}}^2 \cosh^{-4} \theta \quad (2.14)$$

$$\stackrel{\theta=0}{=} \bar{\lambda}_{\text{long}}^2. \quad (2.15)$$

We see that for typical collider experiment geometries with vanishing longitudinal rapidity θ , the dimensions become independent and a direct relation between the experimental radii and the lengths of homogeneity is obtained. These lengths of homogeneity, introduced in Fig. 2.5 as brightly highlighted regions, describe over which extend of the source the momenta are similar so that the thermal velocity spectra of the particles are overlapping. The lengths of

homogeneity can as well be calculated by picking explicit transverse flow profiles:

$$\text{I: Hard flow} \quad y_{\text{T}}(r) = r/R_{\nu} \quad (2.16)$$

$$\text{II: Soft flow} \quad y_{\text{T}}(r) = \ln \frac{\sqrt{R_{\nu}^2 + r^2} + r}{R_{\nu}}. \quad (2.17)$$

The profiles are also visualized in Fig. 2.6, where it can be seen that for small transverse radii both schemes are equivalent. For large transverse radii, the hard flow retains its linear dependence and the soft flow manifests a more gradual rise.

The resulting radii can be found in Fig. 2.7. The R_{long} evolution with transverse momentum resembles the result from [172] with a strong impact of the transverse expansion, apparent as a Cauchy-like¹ reduction of radii. A universal response of R_{long} independent of the chosen transverse common velocity profile is found. This seems reasonable as the two directions, transverse and longitudinal, are defined perpendicular to each other. There is however a slight dependence of R_{long} on α . It appears that R_{long} is marginally sensitive to the amount of transverse flow, but not its structure. The case of $\alpha = \infty$ corresponds to no transverse expansion, and R_{long} decreases like $\sqrt{m_{\text{T}}}^{-1}$. Including a transverse component, i. e. α is finite, lets the radii decrease more steeply. This implies that measuring the m_{T} dependence of femtoscopic radii gives insight into the nature of the expansion dynamics of hot and dense matter. The R_{out} and R_{long} radii are additionally controlled by the structure of the transverse growth of flow. The common velocity competes with the thermal velocity, which in the hard flow scenario leads to a general reduction of radii with transverse momentum. The calculations show that the decrease is stronger for the side component. The situation changes for the out component when the soft flow pattern is applied. Then, the change of common velocity becomes more gradual going outwards in radius of the emitter. This means that the particles with a high p_{T} , emitted from large transverse radii, must evince correlation over larger extents, reflected in the rise of the out component with transverse momentum. These theoretical findings bring us in the comfortable position that the amount of expansion can be fixed by studying the longitudinal length of the source, and the out and side radii give us knowledge about the detailed flow profile. It is the m_{T} dependence of the radii that pins down the reaction dynamics of strongly interacting matter.

2.4 The RHIC HBT Puzzle and Viscosity Effects

Many few details were needed in hydrodynamic calculations to reproduce the experimental data in the soft sector [180], specifically the puzzling ratio of $R_{\text{out}}/R_{\text{side}} \approx 1$ observed by STAR [181] and confirmed later by PHENIX [182]. Initially, hydrodynamic models predicted a ratio $R_{\text{out}}/R_{\text{side}} \approx 1.6$, see Fig. 2.8 (left). Only the inclusion of several effects — all having

¹Standard Cauchy distribution: $f(x) = 1/[\pi(1+x^2)]$.

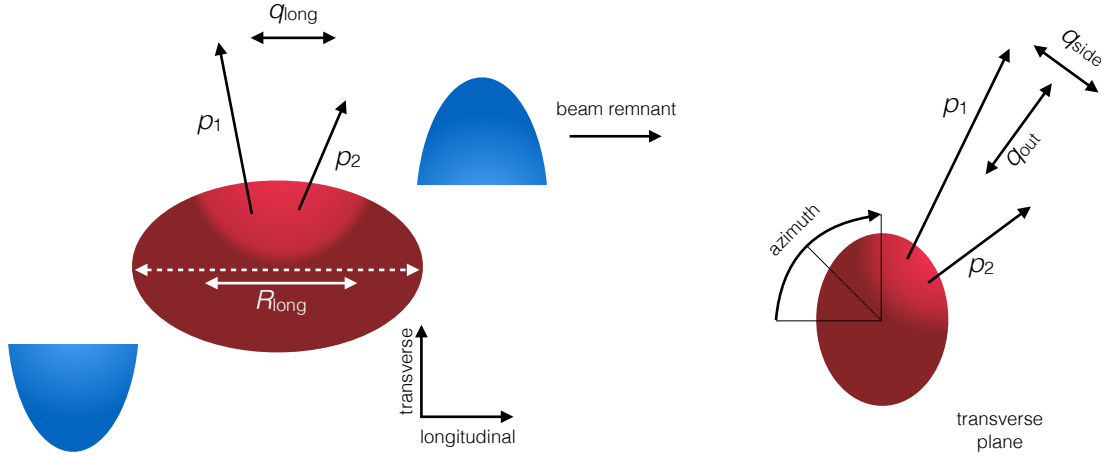


Figure 2.5: Experimentally accessible, three-dimensional decomposition of the two-particle momentum difference. Left: The longitudinal direction follows the beam axis. Although the full system extends further (red oval), only particles from regions with similar common flow will be correlated (bright highlight). The experimentally extracted, longitudinal size of the system will not correspond to the geometrical stretch (white, dashed double arrow) but characterizes the length of homogeneity R_{long} (white, solid double arrow). Right: The transverse plane is broken up into the out and side component along and perpendicular the total transverse pair-momentum, respectively.

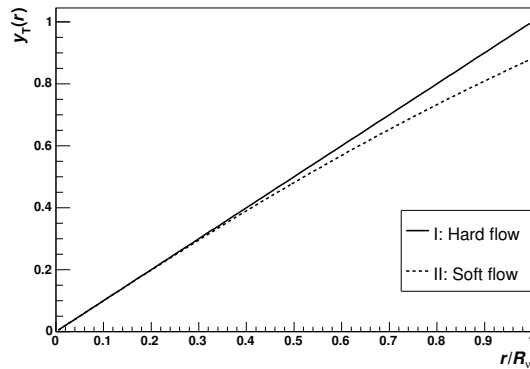


Figure 2.6: Two flow profiles as specified in Eqs. 2.16 and 2.17. The hard flow profile exhibits a simple linear dependence of the transverse rapidity y_T on the radius, whereas the soft flow profile includes a saturation of y_T for large radii.

only small impact on $R_{\text{out}}/R_{\text{side}}$, but consistently reducing the ratio — lead to an agreement between hydrodynamic calculations and data. The processes featured in Fig. 2.8 (left) are the inclusion of a initial, pre-equilibrium flow, a hard equation of state, viscosity, and a compact initial profile; the sum of these processes is considered crucial for the consistent description of

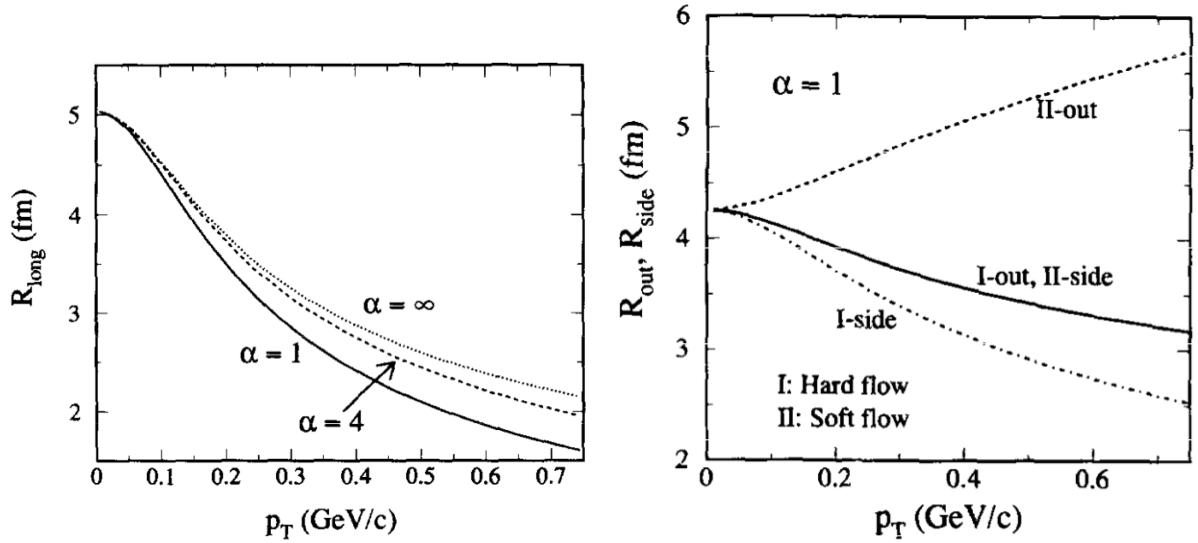


Figure 2.7: Left: Longitudinal radius R_{out} for different values of α (see Eq. 2.8) as a function of p_T . We see the universal decrease of R_{long} with p_T , independent of the assumed transverse flow profile, similar to what was observed in [172] for significant flow, displayed in Fig. 2.4. Right: R_{out} and R_{side} for hard and soft flow with $\alpha = 1$. The saturation of the flow profile for large transverse rapidities (see Eqs. 2.16 and 2.17 and Fig. 2.6) in the soft scenario I is reflected in the strong dependence of the R_{out} behavior on the assumed transverse flow shape, note the change of sign in slope. The side component shows a moderate subordination to the chosen flow scenario, in both cases a fair reduction of size with momentum is consequent. A different α , i. e. 4, yields the same trends, although the increase of the out radius with momentum is turned into a rather constant behavior, which is reasonable, as it can be seen in Fig. 2.6 that the saturation occurs mostly for large radii. Probing only the lower half of the flow profile (remember $R_{\nu}/R_T = \sqrt{\alpha}$) dilutes the effect. Both panels taken from [174].

the soft physics in heavy-ion collisions.

The impact of a finite viscosity on the $R_{\text{out}}/R_{\text{side}}$ ratio is indirect. Since the initial longitudinal flow is much larger than the transverse one in a Bjorken-like flow scenario, a finite viscosity will transfer some of the longitudinal expansion to a transverse velocity. Fig. 2.8 (right) shows the results of [183], where the effect of the inclusion of viscosity on HBT radii in a blast-wave scenario was investigated. We see the reduction of R_{out} — which is sensitive to the transverse flow — when viscosity is taken into account. R_{side} appears to be largely unaffected, leading to a decrease in the ratio $R_{\text{out}}/R_{\text{side}}$. The effect on the single radii might depend on the details of the hydrodynamic calculation. In a 3+1D calculation [184, 185], the introduction of viscosity affected R_{side} only a little and R_{out} got reduced by about 10%; taken together leading to a reduction of the $R_{\text{out}}/R_{\text{side}}$ ratio yielding better agreement with the data. Also in the 3+1D model, the HBT radii were found to be sensitive to the viscosity of the medium through the increased flow caused by the finite viscosity. The reduction of $R_{\text{out}}/R_{\text{side}}$ by a

finite viscosity through an increased transverse flow should be seen as a generic feature of hydrodynamic calculations.

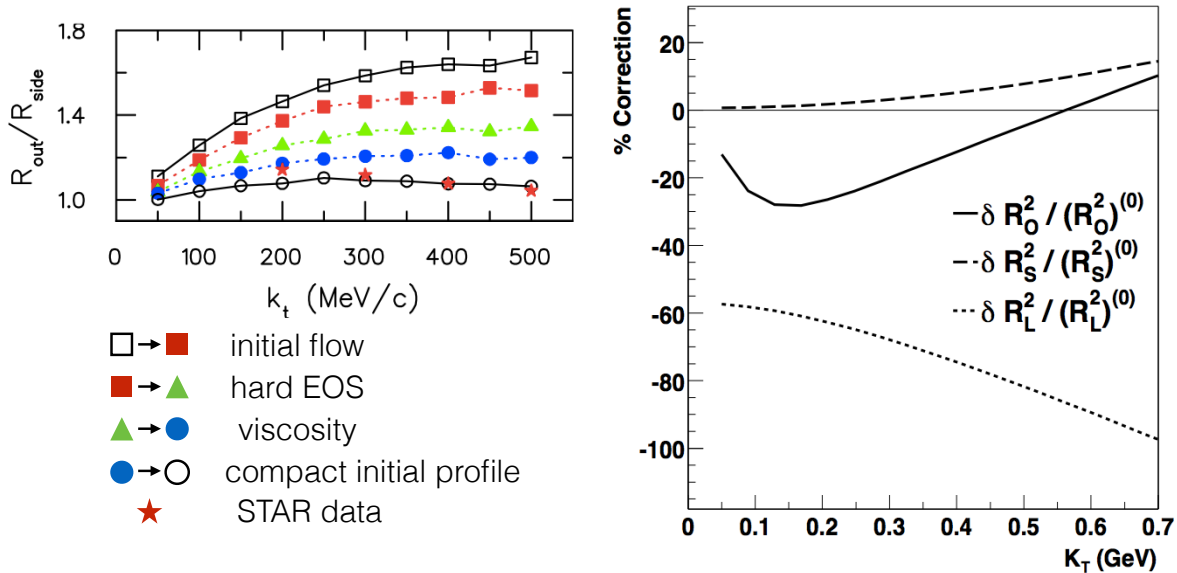


Figure 2.8: Left: Solution of the HBT puzzle, i. e. the small $R_{\text{out}}/R_{\text{side}}$ ratio in data, by the introduction of initial flow, a hard equation-of-state, viscosity, and a compact initial profile. Taken from [180]. Right: Effect of viscosity on HBT radii R_{out} , R_{side} , and R_{long} in terms of relative change with respect to the result without viscosity effects. Taken from [183].

Viscosity effects can also be taken into account phenomenologically, as done in the HKM model. The main effect of viscosity — an increased early transverse flow — can be incorporated in model calculations by increasing the initial, pre-thermal flow [186]. Practically, this means adjusting the parameter α in the transverse profile for the pre-thermal, initial transverse rapidity profile $y_T^{\text{init.}}$:

$$\text{Initial flow} \quad y_T^{\text{init.}}(r_T) = \alpha \frac{r_T}{\sqrt{\langle r_T^2 \rangle}}, \quad (2.18)$$

where r_T is the transverse radius.

2.5 Broken Pair Transverse Mass Scaling of Radii

The Buda-Lund model [187] is based on analytic solutions of the hydrodynamic equations with vanishing viscosity. Within the model, the experimentally reconstructed source radii are

obtained by azimuthally averaging over the principal transverse axes:

$$R_{\text{out}}^2 = (R_{*,x}^{-2} + R_{*,y}^{-2})^{-1} + \beta_{\text{out}}^2 \Delta\tau_*^2, \quad (2.19)$$

$$R_{\text{side}}^2 = (R_{*,x}^{-2} + R_{*,y}^{-2})^{-1}, \quad (2.20)$$

$$R_{\text{long}}^2 = R_{*,z}^2, \quad (2.21)$$

where the out direction shows the additional modification by the finite emission time and the asterisk indicates a modification from the collective expansion and temperature gradients

$$\frac{1}{\Delta\tau_*^2} = \frac{1}{\Delta\tau^2} + \frac{m_T d^2}{T_0 \tau_0^2}, \quad (2.22)$$

$$R_{*,x}^2 = X^2 \left(1 + m_T(a^2 + \dot{X}^2)/T_0\right)^{-1}, \quad (2.23)$$

and the y and z dimensions follow the x component analogously. Here, a and d are the spatial and time-like temperature gradients, respectively. These temperature gradients can mimic a pattern of collectivity: If the center of the fireball is hotter than the edges, it will emit particles with higher momenta. This gradient effect is showcased in Fig. 2.9, where it is seen that the spatial distribution of faster pions in an illustrative model without interactions has a smaller extent due to artificially large temperature gradients [188]. Let us consider any possible effect from a non-uniform freeze-out temperature, quantified as the parameter a in Eq. 2.23, as a minor modification to the strong expansion observed in heavy-ion collisions, introduced in Eq. 2.23 as \dot{X} . We then see that the m_T dependence of the observed radii is driven by the common flow velocity \dot{X} which competes with the thermal velocity $\sqrt{T_0/m_T}$. For a given collision system, only the m_T of the studied pair determines the radius. The strong claim of the Buda-Lund model is this m_T scaling of femtoscopic radii for all species.² An experimental effort was made to test this prediction. Recently, both STAR and PHENIX reported kaon radii [189] that deviate in the longitudinal direction at low m_T from the ideal hydro Buda-Lund model expectation but match the prediction of the hydro-kinetic model HKM [186]. The corresponding data together with the model predictions are shown in Fig. 2.10. It is clear from the graphic that there is a strong hint for the breaking of the m_T scaling, but further data is needed for convincing evidence. The LHC certainly is the place to study the effect in detail. In particular it will be interesting to see how the radii of other pairs of heavy particles behave as a function of m_T . Studying proton-lambda correlations at the LHC will certainly shed light on the reaction dynamics of relativistic heavy-ion collisions and therefore on the properties of strongly interacting matter in the non-perturbative regime of QCD.

²The scaling is predicted for the longitudinally co-moving system (LCMS). Radii obtained in the LCMS differ by a γ factor in the long direction to the radii obtained in the pair rest frame (PRF).

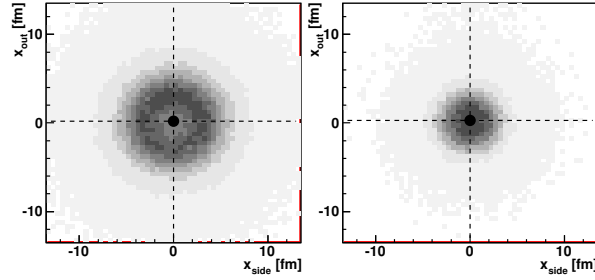


Figure 2.9: Impact of a temperature gradient on m_T dependent HBT radii. Shown are the freeze-out positions for simulated collisions with artificially large temperature gradients and no thermalizing interactions. The left panel shows all pions, while the spatial distribution on the right — which is clearly more confined — was obtained by selecting faster pions only. Taken from [188].

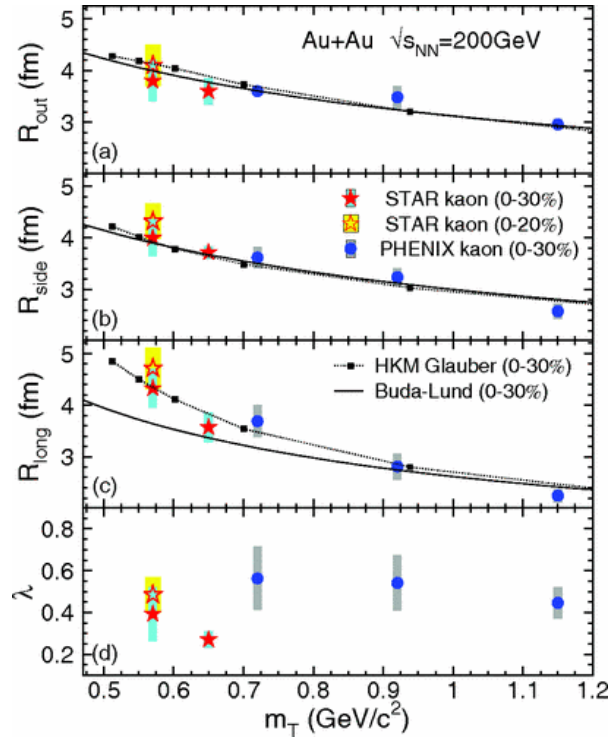


Figure 2.10: Three-dimensional freeze-out radii from femtoscopic charged-kaon correlations as a function of m_T . Shown are STAR data [189] together with PHENIX data [190] and model predictions from Buda-Lund [191] and HKM [186]. All data and model curves are consistent for R_{out} and R_{side} . For R_{long} however, HKM predicts a steeper rise of radii with decreasing m_T than Buda-Lund. The data from both STAR and PHENIX favor the HKM prediction. Taken from [189].

2.6 Femtoscopic Radii in Pb-Pb Collisions at the LHC

In addition to the already mentioned analysis of three-pion correlations, see Fig. 1.19 (right), several other analyses with the aim to determine a radius parameter of the particle emitting source were carried out at the LHC. All three collision systems provided by the LHC during Run 1 were investigated by CMS in [192]. An emphasis was put on comparing the p-Pb data with pp and peripheral Pb-Pb collisions. The data, exemplarily shown in Fig. 2.11 (left), lead to similar conclusions as already gained from the three-pion study by ALICE: p-Pb collisions seem to be more similar to pp than Pb-Pb collisions.

Data from $\pi\pi$ correlations for the 5% most central Pb-Pb collisions can be found in [193]. This paper was one of the first publications with Pb-Pb data from the LHC made publicly available in December 2010. One of its main findings was that the source at the LHC with $R_{\text{out}} \times R_{\text{side}} \times R_{\text{long}} \approx 300 \text{ fm}^3$ is much larger at the LHC than at the AGS, SPS, or at RHIC. The source also lives longer: $\tau \approx 11 \text{ fm}/c$ at the LHC compared to about $7 \text{ fm}/c$ for central collisions at RHIC. Additionally, the ratio of $R_{\text{out}}/R_{\text{side}}$ was investigated as a function of the pair transverse momentum. As discussed in Section 2.4, this ratio bears essential information about the source dynamics; it is shown in Fig. 2.11 (right). Similar to the situation at RHIC, models tend to over-predict the ratio. The best description of the ALICE data is given by the HKM model. The measurements of ALICE are extended by preliminary data on the centrality dependence of radius parameters extracted from $\pi\pi$ correlations [194].

The reach in pair transverse mass is expanded by the measurement of protons and charged and neutral kaons. Fig. 2.12 (left) shows the results presented in [195, 196]. These results will be put into context of the analysis carried out within this thesis in Section 6.10. The analyses test the scaling behavior of source radii with respect to different particle species. Additionally, it is clear that the source radii obtained from correlation measurements of heavier particles enhance the reach in pair transverse mass. The amplified m_T reach has two main reasons. First, the radial flow which — as, e.g., discussed in Section 1.4 — affects the heavier species more and pushes them to higher p_T . Second, the better PID capabilities which allow to identify massive particles more easily at higher momenta.

The right panel of Fig. 2.12 shows the final eccentricity of the source from experimental analyses at the AGS, SPS, RHIC, and the LHC. Experimentally, two-particle correlation functions were obtained differentially with respect to the event plane. From the observed oscillation of the radii vs. the azimuthal angle, a parametrization can be obtained:

$$R_{\mu}^2 = R_{\mu,0}^2 + 2R_{\mu,2}^2 \cos(2\Delta\varphi), \quad (2.24)$$

with $\mu = \text{out, side, long}$. From this, the final eccentricity can be quantified via the ratio $R_{\mu,2}^2/R_{\mu,0}^2$, which is represented by the magenta marker in Fig. 2.12 (right). Also shown in the

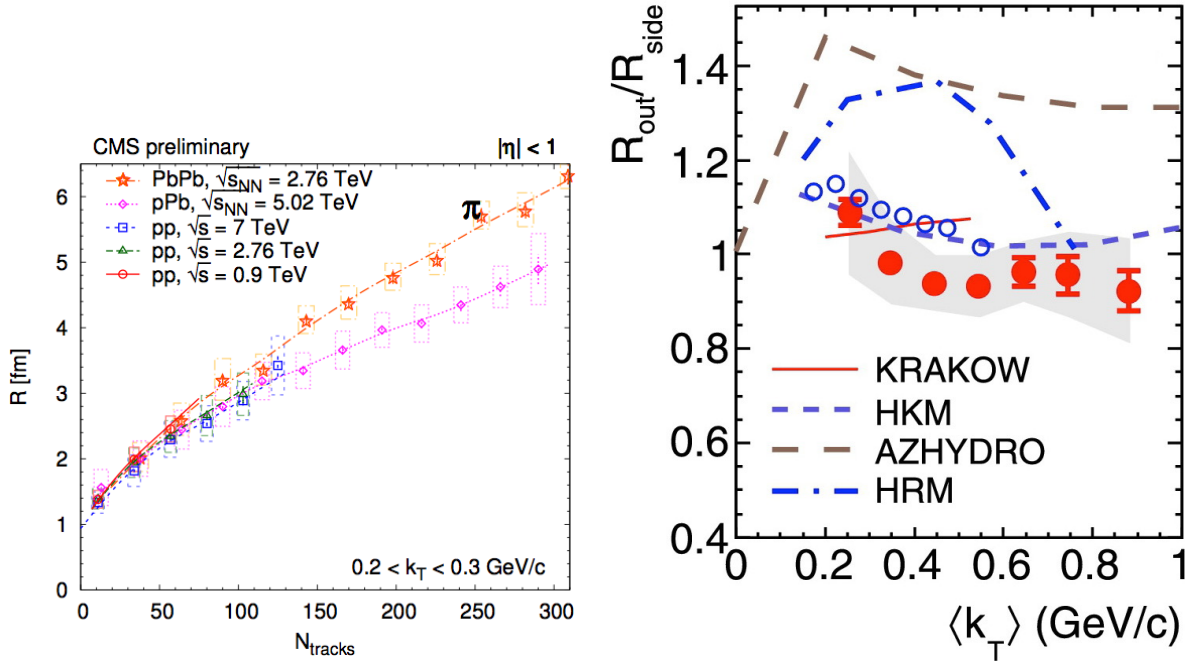


Figure 2.11: Left: Source radii from $\pi\pi$ correlations in pp, p-Pb, and peripheral Pb-Pb collisions measured by CMS [192]. Right: $R_{\text{out}}/R_{\text{side}}$ ratio in the 5% most central Pb-Pb collisions measured by ALICE [193].

figure are two hydrodynamical predictions which differ in their initialization in a blue and red curve; both significantly under-predict the final eccentricity at the LHC. The green curve, a study with the hadronic cascade UrQMD, describes the data well. This might be a hint towards the importance of a hadronic phase in model calculations.

2.7 Photon Sources

Kinetic freeze-out forms a frontier for momenta that cannot be looked past with strongly interacting probes. Only model comparisons let us indirectly infer properties of the deconfined phase. We are stuck with the paradox that we can study the strong interactions only after they have ceased. A salvation can be found in studying probes that do not interact strongly like leptons or photons. The solution to go back to the beginning of femtoscopy and study correlations of photons, like Hanbury Twiss and Brown did, is at hand. As the thermal emission rate in a thermodynamical equilibrium is proportional to the fourth power of the temperature, the hope exists that a photon-photon correlation study can provide an image of the fireball at earlier times than it is accessible with hadronic probes. Fig. 2.13 shows the photon yield as obtained from theory in [198] as a function of transverse energy for RHIC and LHC energies. One sees that in both cases, photons from the late, confined phase are most copious at low

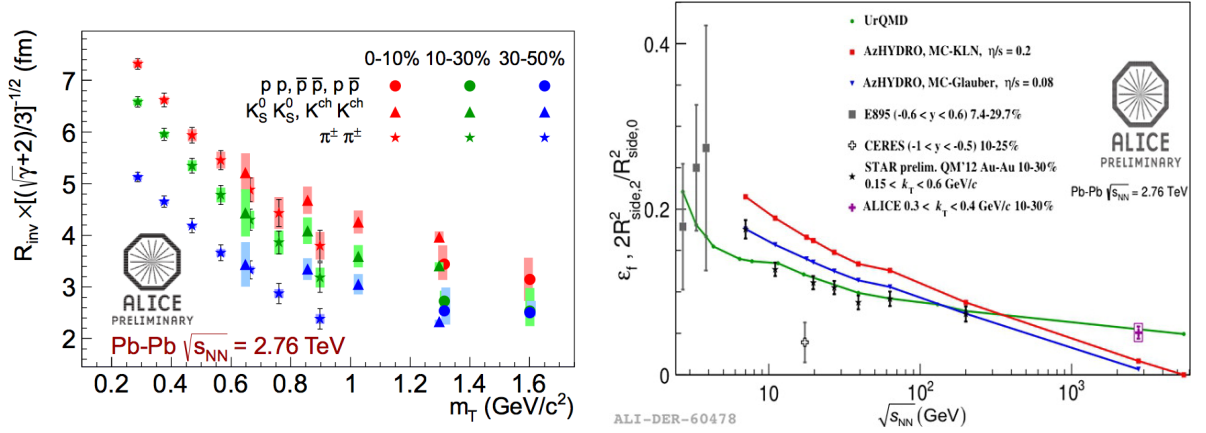


Figure 2.12: Left: One-dimensional radius parameters obtained from two-particle correlations of pions, neutral and charged kaons, and protons shown as a function of transverse mass [195, 196]. Right: Final state eccentricity from azimuthally sensitive $\pi\pi$ HBT as a function of energy. Taken from [197].

transverse energies less or equal 1 GeV. For higher photon energies, thermal radiation from the QGP phase is most abundant; at the LHC to more than 5 GeV, at RHIC up to about 3 GeV, where at RHIC hard, primordial γ rays are presiding. This means a sweet spot at RHIC for studying the deconfined medium between 1 to 3 GeV transverse photon energy and a broad range from 1 to more than 5 GeV at the LHC.

Two observations regarding photons are not easily understood theoretically and were consequently dubbed the photon puzzle. The PHENIX collaboration measured the direct photon yield and extracted an inverse slope parameter of the transverse momentum spectrum in central Au-Au collisions of $T = 221 \pm 19$ (stat.) ± 19 (syst.) MeV [199]. This inverse slope parameter can be interpreted as an effective temperature, since it is a time-integrated observable. Compared to the critical temperature of deconfinement of about 160 MeV, the inverse slope points to rather early production of the photons. Contrarily, the measurement of the direct photon elliptic flow [200], which yields values comparable to the flow of hadrons, suggests a late production. Although recently the evaluation of systematic uncertainties was criticized [201], the ALICE collaboration qualitatively sees the same patterns of a high effective temperature of $T = 304 \pm 51$ (syst. + stat.) MeV [202] and v_2 consistent with the one of hadrons [203]. An explanation for this puzzle could be that the photons are emitted at a later stage and the effective temperature has a significant contribution from flow [204]. In Fig. 2.14 this possible blue shift by radial flow for photons is displayed. The calculations show that the temperature of the medium drops rapidly as a function of proper time τ and that a temperature of $T = 221$ MeV at RHIC exists only as early as $\tau \lesssim 1$ fm/c and similarly at the LHC $T = 304$ MeV is only reached even earlier. The experimental slope however corresponds to the effective temperature, which carries a large imprint from the expansion. To be consistent with the experimental

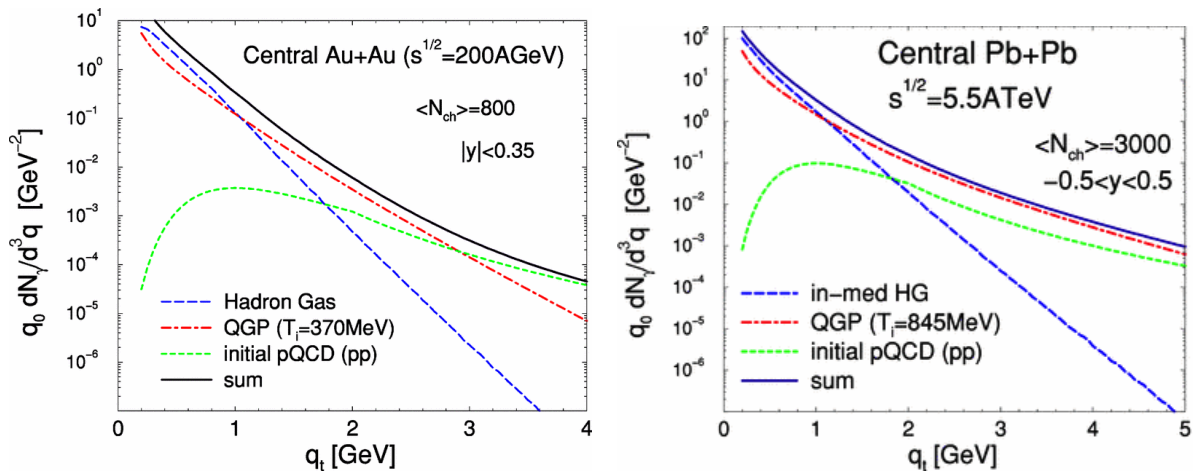


Figure 2.13: Photon yields from different sources as a function of transverse energy of the photon for central collisions of Au-Au at RHIC (left) and Pb-Pb at the LHC (right). For RHIC one sees that up to a transverse energy of about 1 GeV, the contribution from the late hadron gas is dominant. In an intermediate range from 1 to 3 GeV, the thermal photons from the QGP prevail; for higher energies the direct photons from initial, hard pQCD processes are governing the total spectrum. At the full LHC energy of $\sqrt{s_{\text{NN}}} = 5.5 \text{ TeV}$, the majority of photons comes from hadronic sources up to about 1 GeV, but the reign of thermal photons is much extended towards higher transverse energies as compared to RHIC of more than 5 GeV. Taken from [198].

inverse-slope measurements, the photons in the model could be instantaneously ejected as late as $\tau = 10 \text{ fm}/c$ both at RHIC and the LHC.

The problem however is that models do not show such a late production and subsequently fail to describe the v_2 and/or do not yield enough photons to reproduce the p_T spectra. Fig. 2.15 evidences the deviation between data and an exemplary calculation [205]; various other models fail to reproduce the photon data as well [206–208]. An HBT measurement of photons could unveil the origin of these gauge bosons, resolving the puzzle. Such a measurement was already carried out successfully by the WA98 Collaboration [209] at the SPS, presented in Fig. 2.16. Within the study, both photons were reconstructed with the electromagnetic calorimeter of WA98. While the data for $Q_{\text{inv}} \lesssim 20 \text{ MeV}/c$ were found to be affected by detector resolution effects, the excess seen for intermediate relative momenta up to $Q_{\text{inv}} \lesssim 90 \text{ MeV}/c$ was observed to be stable against all variations of the selection criteria. It was thus attributed to the quantum statistical correlation of primary photons. The hope for such a measurement with ALICE at the LHC would be to extract a radius of the photon source. A large radius would then reveal a late hadronic production mechanism of the photon excess and a small size prove the early photon genesis.

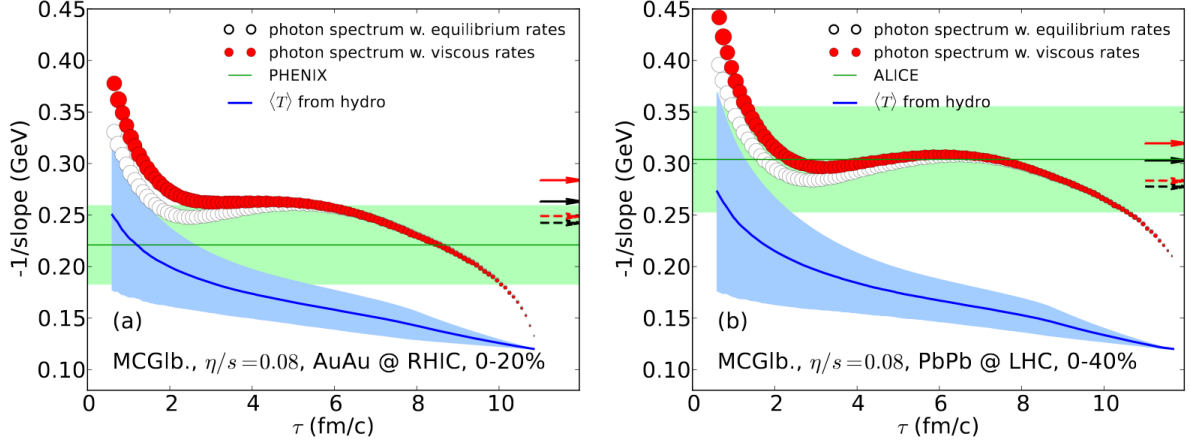


Figure 2.14: Blue shift of photons at RHIC (left) and LHC (right) in a hydrodynamic calculation [204]. Shown is the average temperature as a blue line and the apparent, effective temperature, i. e. the inverse slope parameter of the photon p_T spectrum, without viscous corrections as white dots and including viscous effects as red dots together with the experimental, integrated value as green line. We see that although the temperature drops monotonically with proper time τ , the effective temperature stalls for $2 \lesssim \tau$ (fm/c) $\lesssim 8$. The temperature agrees in numbers with the experimental inverse slope for proper times of ~ 1 fm/c, but the effective temperature is still consistent as late as $\tau \approx 10$ fm/c. Taken from [204].

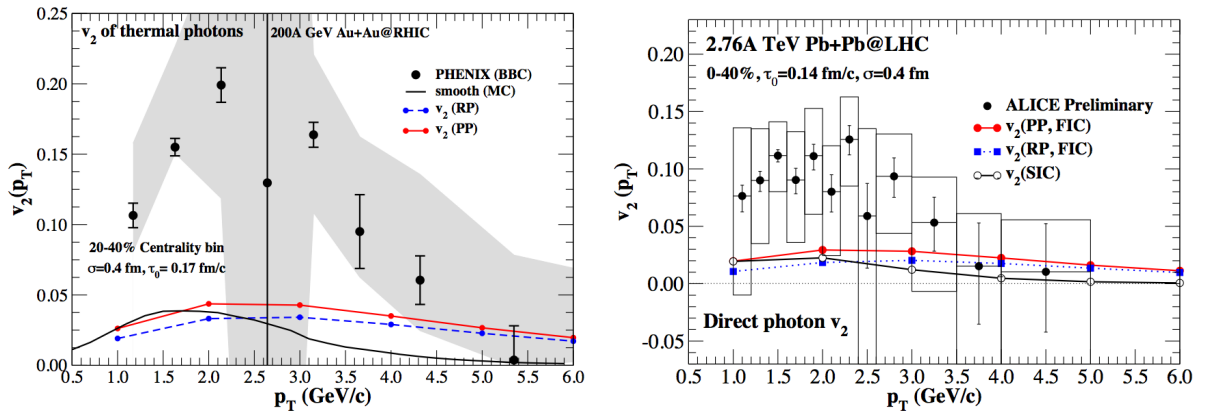


Figure 2.15: Elliptic flow of direct photons as a function of transverse momentum as measured by PHENIX [200] at RHIC (left) and ALICE [203] at the LHC (right) compared to a hydrodynamical, event-by-event calculation [205]. The discrepancy, called the photon puzzle, is obvious. Taken from [205].

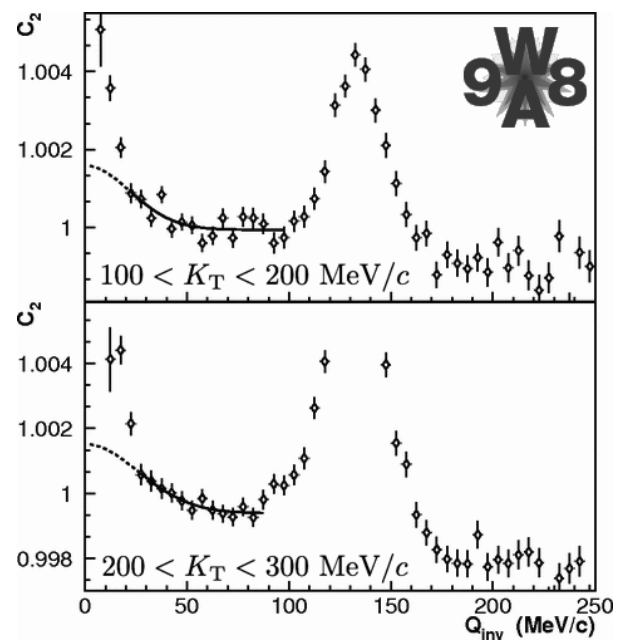


Figure 2.16: $\gamma\gamma$ correlation measurement by WA98 [209].

Chapter 3

ALICE at the LHC

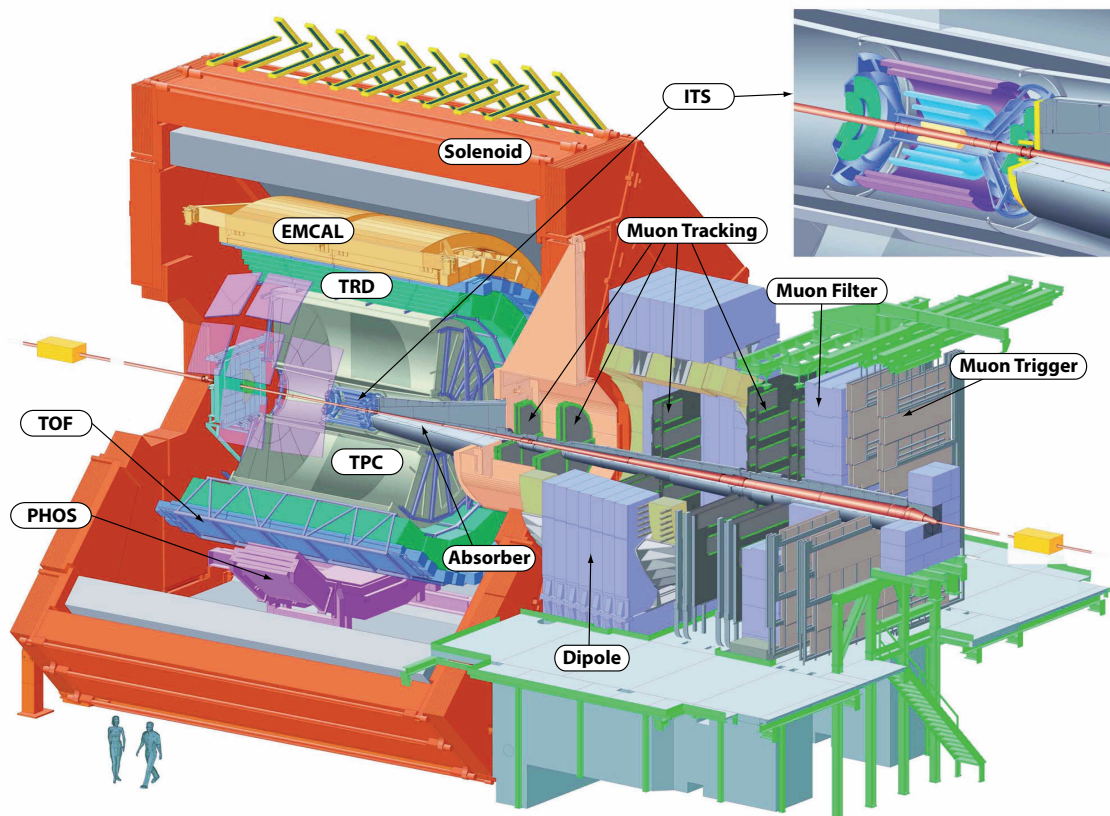


Figure 3.1: Setup of A Large Ion Collider Experiment

ALICE — A Large Ion Collider Experiment — is located at the second interaction point (Point 2) of the Large Hadron Collider (LHC). The ALICE setup [99] is shown in Fig. 3.1. The LHC was built into the existing tunnel of the Large Electron Positron Collider (LEP),

and ALICE inherited its main magnet from the LEP L3 experiment, which was located at the same interaction point as ALICE now is. The magnet was modified for ALICE to improve the uniformity of the magnetic field by adding plugs to the octagonal shaped opening of the yokes of the magnet [210]. It is one of the largest non-super-conducting magnets. The magnetic field of 0.5 T is at the upper limit of the 6000 A current which the magnet can hold. While for low- p_T observables a lower magnetic field of ~ 0.2 T would be desirable [114], the strong field gives better resolution for high- p_T observables which generally have low statistics. The interaction point is surrounded by a beam pipe. Its outer diameter amounts to 60 mm; it is 800 μm thin.

A significant part of ALICE consists of the muon arm depicted on the right hand side of Fig. 3.1. However, the studies performed within this thesis do not comprise any analysis of muons. The muon setup is therefore not covered here; for details see e. g. [211, 212].

3.1 Coordinate Systems

The global ALICE coordinate system is a right-handed and Cartesian one with the origin $x = y = z = 0$ at the nominal interaction point. The z axis follows the beam direction, the muon arm is at negative z . The x axis is aligned horizontally, perpendicular to the z axis and points towards the center of the LHC ring. The y axis is perpendicular to the other two and points upwards. The azimuthal angle φ is zero at the positive x axis and increases from there towards the positive y axis. The polar angle θ is zero at the positive z axis, $\pi/2$ in the (x, y) plane and π at the negative z axis [213]. Within the ALICE software, coordinate values are usually in cm. Unless specified differently, the global coordinate system is used. Especially for tracking the particles through the detectors, a local coordinate system exists. It is also Cartesian and right-handed, and even the z axis agrees with the global coordinate system, but the local system is rotated around the z axis by an angle α with respect to the global system. The definition of α changes with the radius $r = \sqrt{x^2 + y^2}$. For $r < 45$ cm, i. e. within the ITS, the rotation is such that the x axis points in the direction of the projection of the momentum vector of the particle on the transverse plane. For $r \geq 45$ cm, the azimuth is segmented 18-fold with the zeroth segment starting at $\varphi = 0$. Here the rotation α is the angle of the center of the segment in which the point (x, y, z) lies. The segments correspond to the azimuthal TPC sectors and TRD supermodules. This brings the advantage that all azimuthal TPC sectors and TRD supermodules have the same coordinates in the local coordinate system, simplifying the tracking codes.

3.2 The Inner Tracking System

The Inner Tracking System (ITS) consists of three silicon detectors using different techniques, namely the Silicon Pixel Detector (SPD), the Silicon Drift Detector (SDD), and the Silicon Strip Detector (SSD). Each silicon detector is made of two layers. Their radial position and longitudinal extent is tabulated in Table 3.1. Each layer is designed such that it has a guaranteed acceptance in pseudorapidity of at least ± 0.9 for a primary interaction vertex within $\pm 1\sigma$, i. e. an expected $\pm 5.4 \text{ cm}^1$ for both pp and Pb-Pb interactions, in z direction around the nominal interaction point at $(0, 0, 0)$ in the ALICE global coordinate system. (See Section 3.1 for details on the coordinate system.) The SPD has an extended range in pseudorapidity in order to provide a stand-alone multiplicity measurement called SPD clusters or SPD tracklets, see Section 4.1 for a discussion of the centrality determination in ALICE.

By correlating hits in the SPD, the z position of the primary vertex can be determined in a highly efficient way with a precision of $10 \mu\text{m}$ in Pb-Pb events and $90 \mu\text{m}$ in pp events [214]. Roughly the same resolution in z and an additional reconstruction of the x and y coordinate can be achieved with a 3D version of this vertexer with a degradation in efficiency for very low multiplicity pp events. This SPD vertex can later be superseded using reconstructed tracks resulting in an improved resolution. The efficiencies for the two versions of the SPD vertexer can be seen in the left panel of Fig. 3.2, and a comparison of their resolutions in the z direction in the right panel. The resolution for the 3D SPD vertexer in all dimensions is shown in the left panel of Fig. 3.3, while in the right panel the comparison in terms of resolution to the vertexing with reconstructed tracks is made. During reconstruction all three vertexers are run after each other and the best vertex is taken. Fig. 3.4 shows on the left the z component (z_{vtx}) and on the right the x and y component (x_{vtx} and y_{vtx}) of the reconstructed primary vertex position for the 10% most central events in a subset of good runs². In addition, a Gaussian was fit to the z_{vtx} distribution. The resulting width of 7.26 cm is slightly higher than the originally expected value. The x and y components are offset from zero by a few mm and peak with an RMS of about $40 \mu\text{m}$.

The ITS improves the tracking capabilities of ALICE. The main tracking device, the Time Projection Chamber (TPC, see Section 3.3), can not cope with the high track densities in central Pb-Pb collisions at radial distances from the interaction point smaller than $\sim 85 \text{ cm}$. It is here where the ITS takes over the tracking. The radial positions of the layers were optimized for efficient track finding and impact parameter resolution. Specifically, the position of the sixth layer of the ITS is dictated by the track matching capabilities with the TPC, while the

¹For a Gaussian bunch size in z direction of $\sigma_z^{\text{beam}} = 7.7 \text{ cm}$ [114], the z position of the primary vertices will have a Gaussian distribution with $\sigma_z^{\text{vtx}} = \sigma_z^{\text{beam}}/\sqrt{2} = 5.4 \text{ cm}$.

²Run numbers: 170027, 169858, 169855, 169846, 169838, 169837, 169417, 169415, 169411, 169094, 169091, 169035, 168992, 168988, 168826, 168777, 168512, 168511, 168467, 168464, 168362, 168361, 168342, 168341, 168325, 168311, 168310, 168115, 168108, 168107, 168105, 168069, 167988, 167987, 167920, 167915.

Layer	type	radial position (cm)	longitudinal extent $\pm z$ (cm)
1	pixel	4	16.5
2	pixel	7	16.5
3	drift	14.9	22.2
4	drift	23.8	29.7
5	strip	39.1	45.1
6	strip	43.6	50.8

Table 3.1: Dimensions of the ITS, see [214]

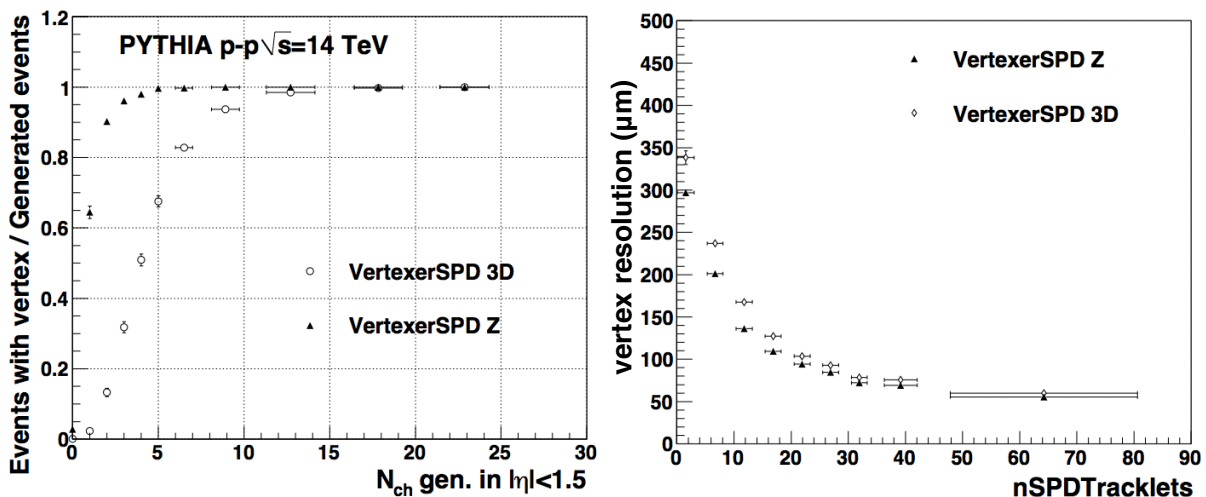


Figure 3.2: Left: Efficiency of primary vertex reconstruction for the two versions of the SPD vertexer as a function of event multiplicity. Right: Comparison of resolutions in z direction of the two SPD vertexers as a function of reconstructed SPD tracklets. Both obtained from Pythia simulations for pp collisions at $\sqrt{s} = 14$ TeV and taken from [215].

first layer is as close to the interaction point as the beam pipe permits.

The improved impact parameter resolution of the ITS enables ALICE to perform measurements in the charm sector (see Fig. 3.5). The Solenoidal Tracker At RHIC (STAR) collaboration showed that D mesons can be reconstructed with only a TPC as tracking detector in d-Au [217], pp [218], and Au-Au [219] collisions. A full D meson reconstruction — including the reconstruction of the secondary vertex — requires the impact parameter resolution to be of the order of the decay length of the D meson ($c\tau = 122.9 \mu\text{m}$) in order to discriminate between primary tracks and daughters of D meson decays. STAR achieved a pointing resolution with the help of its Inner Silicon Tracker of a few hundred μm at a transverse momentum p_T of 1 GeV/c [220]. This allowed the STAR collaboration to perform for the first time a full D meson reconstruction

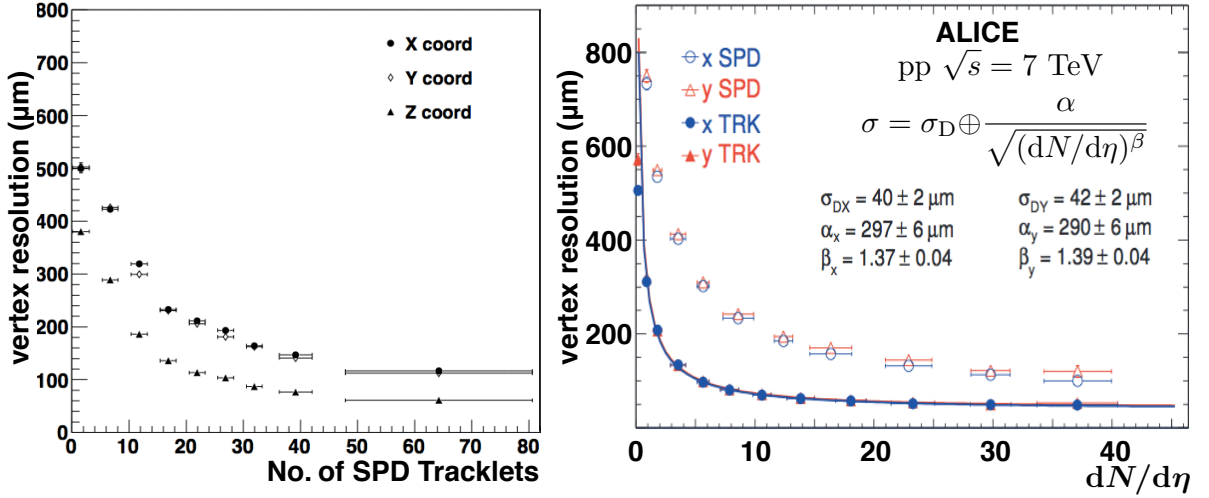


Figure 3.3: Left: Resolution in all components of the 3D SPD vertexer. Obtained from Pythia simulations for pp collisions at $\sqrt{s} = 14$ TeV. Taken from [215]. Right: Comparison of resolutions of the 3D SPD vertexer and a vertexer using reconstructed tracks, including tracking information from other detectors than just the SPD. Obtained from 7 TeV pp collisions data. Taken from [216].

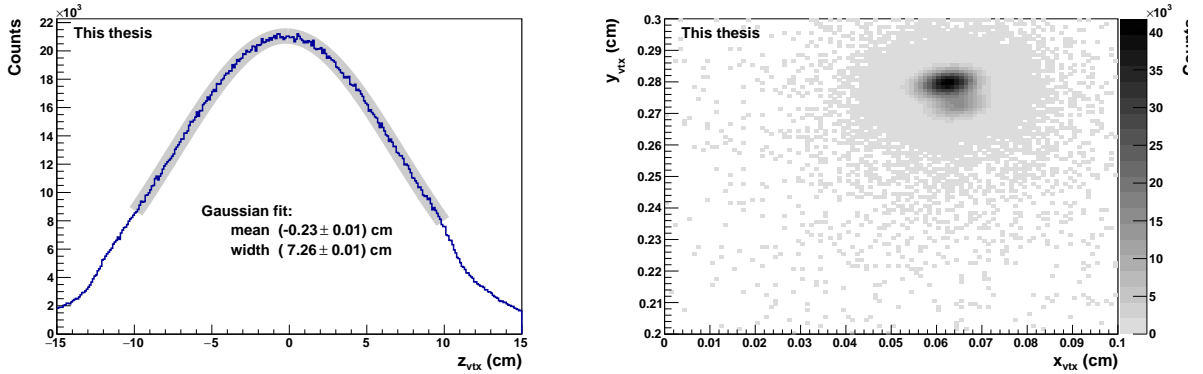


Figure 3.4: Left: Distribution of the z component of the primary vertex for a subset of good runs (see footnote 2) in the blue histogram with a Gaussian fit as a gray band in the background and the fit result. Right: Two-dimensional distribution of the x and y component of the primary vertex for the same subsample as in the left panel. One can spot two merging peaks. They stem from slightly different accelerator set-ups which adjust for the changing running conditions.

in heavy-ion collisions [221]. ALICE achieves a transverse impact parameter resolution $d_{0,xy}$ of about $60 \mu\text{m}$ at $p_T = 1$ GeV/ c (see left panel of Fig. 3.6). The main advantage of the secondary vertex reconstruction is, that it allows to use topological selection criteria (see Section 4.3 for a detailed discussion of such criteria) on the decay vertices. The effect of two such criteria can be seen in the right panel of Fig. 3.6. The selection criteria were: a) on the decay length of the D

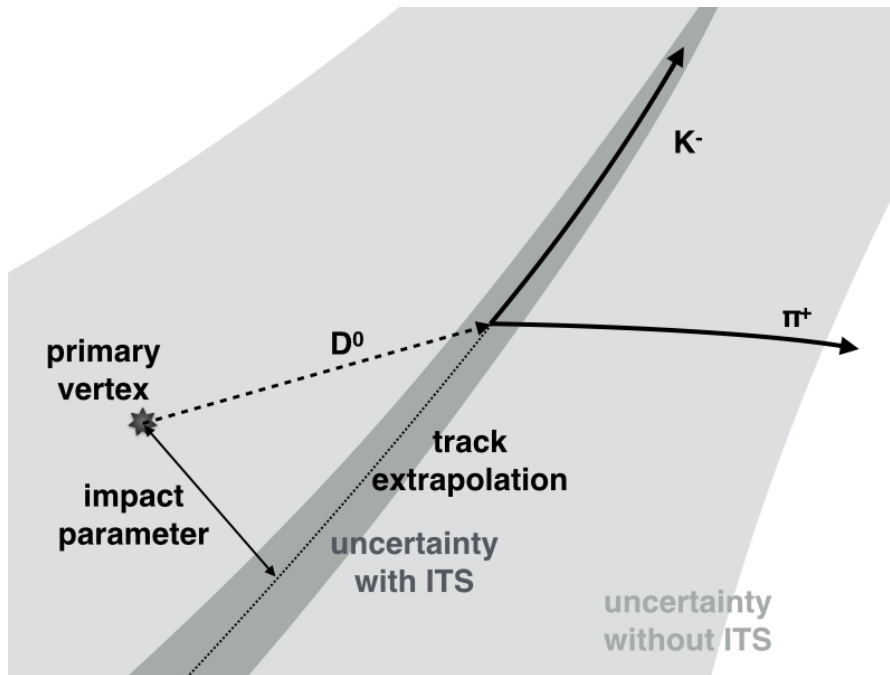


Figure 3.5: Sketch of a $D^0 \rightarrow K^- \pi^+$ decay depicting the improvement of the impact parameter resolution by the ITS.

meson candidate and b) on the angle between the reconstructed momentum of the D meson candidate and the vector connecting the secondary and primary vertex. The vast improvement due to the background rejection is obvious.

Although the ITS was designed to specifically accommodate the needs of charm reconstruction, all the qualities of the ITS, which were discussed so far, are equally beneficial to a measurement of strange lambda particles as done in this thesis. The ITS also provides particle identification via the measurement of the energy loss. This feature was not exploited in the scope of this thesis. See Section 3.3 for a general discussion of the concept of an energy loss measurement.

3.3 The Time Projection Chamber

The Time Projection Chamber (TPC) is read out by a multi-wire proportional chamber (MWPC) and extends in the transverse direction from $85 < r \text{ (cm)} < 247$ with a 88 m^3 gas volume. The basic principle in gaseous detectors like the TPC is to detect charged particles via their ionization of the gas medium. With an applied electrical field, the produced ions and electrons drift in opposite directions. After amplifying the electron charge, the particle's position in the plane perpendicular to the drift direction is obtained by detecting the charge in spatially segmented pads, while the time of the charge's arrival on the pad plane is used to

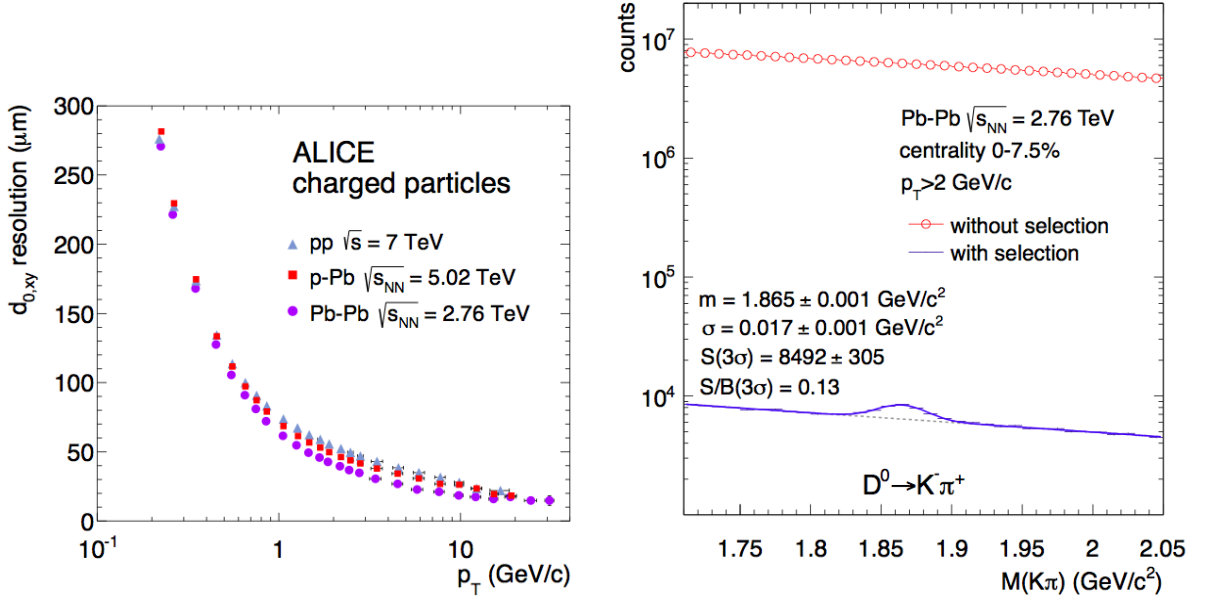


Figure 3.6: Left: Transverse impact parameter resolution for different collision systems in ALICE. Right: Effect of two topological selection criteria (see text) on the invariant mass spectrum of the D meson candidates. Taken from [216].

derive the position of the gas-traversing particle in the drift direction. The electrons should drift through the gas fast to provide a good event-rate capability of the detector and with low diffusion to give a good spatial resolution of the reconstructed track. In addition, the detector should have a good energy loss resolution to allow for particle identification. The intrinsic low material budget of a gaseous detector is beneficial for the momentum and impact parameter resolution of low p_T particles, for which the resolution is dominated by multiple scattering in the material [114]. A low material budget also reduces the production of secondary particles. A comprehensive, general write-up on particle detection including TPCs can be found in [222]. ALICE specific details can be found in the technical design report of the TPC [223] and e.g. [224]. Some considerations concerning the gas mixture are discussed in Section C.1. A few basics are communicated here.

In ALICE the choice was made to use NeCO_2N_2 with a mixture of 90 : 10 : 5, i.e. 85.7% Ne, 9.5% CO_2 , and 4.8% N_2 , which was changed to 90% Ne and 10% CO_2 in the beginning of 2011 [124]. For ALICE, Ne is used as the noble gas in order to reduce the material budget: the density of Ne (0.9 g/L @ 0°C , normal pressure) is half the one of argon (1.8 g/L @ 0°C , normal pressure). Another gas property is the ion mobility. It depends slightly on the ratio E/N , where E is the electrical field and N is the neutral gas number density. For an ideal gas, i.e. $6 \cdot 10^{23}$ particles occupying 24 l at ambient conditions, the number density is $2.5 \cdot 10^{19} \text{ cm}^{-3}$. With the drift field $E = 400 \text{ V/cm}$, this results in a typical $E/N = 1.6 \times 10^{-17} \text{ V cm}^2 = 1.6 \text{ Td}$.

Under these conditions, the mobility of Ne^+ ions in a Ne gas is about $4.1 \frac{\text{cm}}{\text{s}} / \frac{\text{V}}{\text{cm}}$ while the one of Ar^+ in an Ar gas is only around $1.5 \frac{\text{cm}}{\text{s}} / \frac{\text{V}}{\text{cm}}$ [225]. (The same result is given in [226].) The TPC gas is called a cold gas as its diffusion is close to the thermal limit. Fig. 3.7 shows a comparison of the transverse (on the left) and longitudinal (on the right) diffusion coefficients of NeCO_2 with other gases. The addition of N_2 does not change the diffusion. The diffusion of the TPC gas for both the transverse and longitudinal direction is $220 \mu\text{m}/\sqrt{\text{cm}}$, which results in a spread over the maximum drift distance (2.5 m) of 3.4 mm laterally and 120 ns in the time direction. The dependence of the drift velocity on the temperature of about $0.05 \frac{\text{cm}}{\mu\text{s}} \frac{1}{\text{K}}$ is steep which makes temperature control to the 0.1 K level crucial [224].

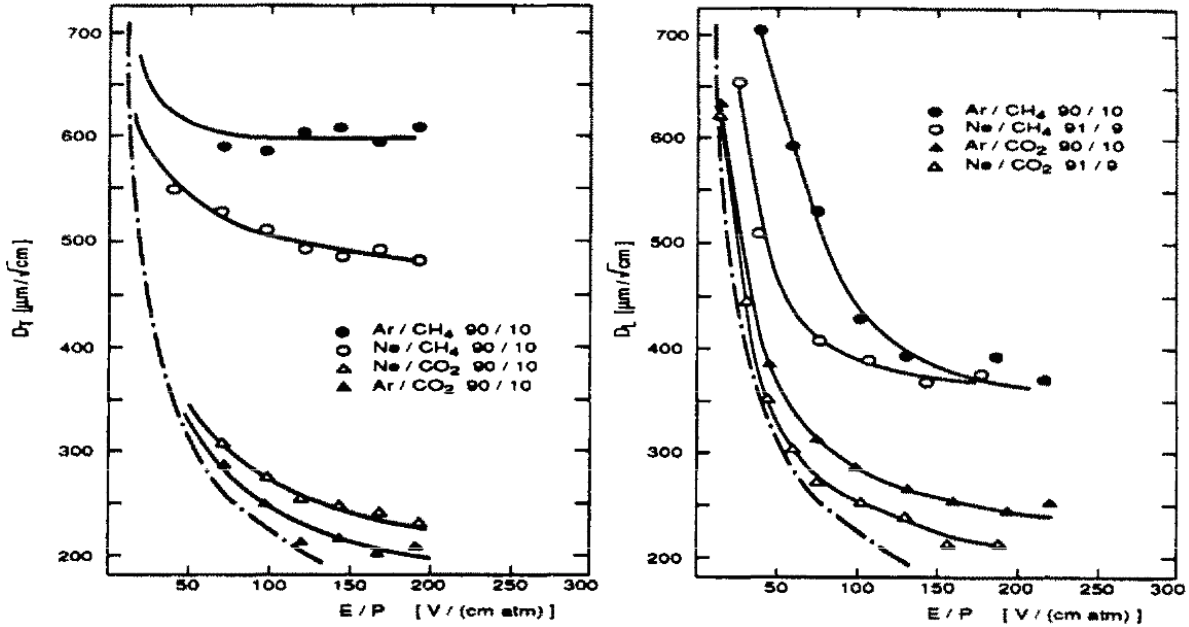


Figure 3.7: Transverse (left) and longitudinal (right) diffusion coefficients for several gas mixtures as a function of electrical field E over pressure P . Also shown is a dotted line for the thermal limit. Taken from [227].

The gas also meets the needs of the amplification process. The primary ionization produced by a charged particle traversing the TPC gas is only about 43 electron-ion pairs.³ As this charge is too small to be detectable by electronic devices, an internal gas amplification is used. A sketch can be found in Fig. 3.8 (left). The drifting electrons created by an ionizing particle follow the electrical field lines. The uniform drift field of $E = 400 \text{ V/cm}$ in z direction is created between the central electrode and the cathode. Here, the electrons move with a constant drift velocity, $v_D = 2.83 \text{ cm}/\mu\text{s}$, and the number of electrons stays approximately constant. The gating grid can be open or closed. When closed, it has an alternating voltage of $V_G \pm \Delta V$ and

³The energy loss of a minimum ionizing particle in Ne is 1.56 keV/cm [228]. The energy lost per created electron-ion pair, which amounts to 36 eV for Ne [229], is larger than the ionization energy since a significant part will be transferred to gas excitations. This means 43 electron-ion pairs are created per cm.

acts as the anode for the electrons: all the drift field lines end on the positively biased gating grid wires. Therefore, all drifting electrons get absorbed by the gating grid; no read out takes place. In the open state the voltage is V_G for all wires, which was chosen such that the grid is completely transparent for the electrons, and they drift undisturbed to the cathode. The gating grid is usually closed and only opens for 100 μs upon a trigger. The opening time matches the maximum drift time for electrons of $\frac{2.5 \text{ m}}{2.83 \text{ cm}\cdot\mu\text{s}^{-1}} = 88 \mu\text{s}$. The main purpose of the gating grid is to prevent the positively charged ions from drifting back into the gas volume. Such an ion back flow would result in large distortions caused by the space charge of the ions. At the anode, the electrical field strength increases dramatically and the drifting electrons start a cascade amplifying the number of electron-ion pairs by a factor $\sim 2 \cdot 10^4$. The dependence on the applied high voltage of the gain factors for the two operating gas mixtures in the ALICE TPC are shown in Fig. 3.8 (right). Adding N_2 to the Ne-CO_2 mixture allows for a higher gas gain, but demands an increased amplification voltage. In other words: the removal of N_2 from the $\text{Ne-CO}_2\text{-N}_2$ can prove favorable if the high voltage has to be reduced. The vast majority of the electron-ion pairs will be produced directly at the anode, where the highly mobile electrons will quickly be absorbed. The ions in contrast, which are a factor of 10^3 slower⁴, induce an image charge on the pad plane. The height of the pad signal is proportional to the generated charge [223]. Two signal processing methods that potentially improve the detector performance are discussed in Section C.2.

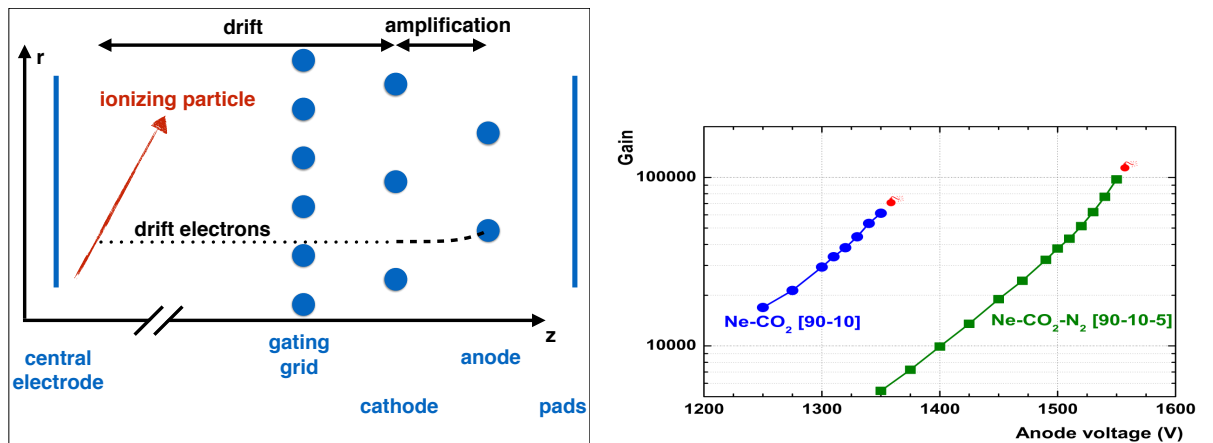


Figure 3.8: Left: Sketch of the path of drifting electrons from an ionizing particle in the transverse (r) and longitudinal (z) plane. Details see text. Right: Gas gain for the two gases utilized before and after beginning of 2011. One observes that the addition of N_2 allows for a higher gas gain, though the applied high voltage must be significantly increased to achieve it. Taken from [230].

The energy loss of a given particle with an energy typical for a heavy-ion collision experiment

⁴Compare the ion mobility of $1.1 \frac{\text{cm}}{\text{s}} / \frac{\text{V}}{\text{cm}}$ multiplied by the electrical drift field of $400 \frac{\text{V}}{\text{cm}}$ resulting in an ion drift velocity of $0.44 \cdot 10^{-3} \frac{\text{cm}}{\mu\text{s}}$ to the electron drift velocity of $2.83 \frac{\text{cm}}{\mu\text{s}}$.

can be parametrized with the Bethe formula [32]:

$$\langle -dE/dx \rangle = Kz^2 \frac{Z}{A} \frac{1}{\beta^2} \left[\frac{1}{2} \ln \left(\frac{2m_e c^2 \beta^2 \gamma^2 T_{\max}}{I^2} \right) - \beta^2 - \frac{\delta(\beta\gamma)}{2} \right], \quad (3.1)$$

with the variables defined in Table 3.2. The Bethe-Bloch formula results from the Bethe formula with the approximation $I \approx Z \cdot 10$ eV. Today, this approximation is often replaced by more accurate measurements. Nevertheless, the name Bethe-Bloch formula prevails. Data from muons on copper together with various parametrizations, including the Bethe formula, are shown in Fig. 3.9. One distinguishes mainly between the $1/\beta^2$ region which extends from the beginning of the validity of the Bethe formula (the grey vertical band at $\beta\gamma \sim 0.05$) to $\beta\gamma \approx 1$ (a function $f(x) \sim 1/x^2$ is linear in a double-log plot), the region of minimum ionization, and the relativistic rise following this minimum. Particles with different masses will appear as separate bands in a $\langle dE/dx \rangle$ vs. momentum plot. This feature is exploited for particle identification.

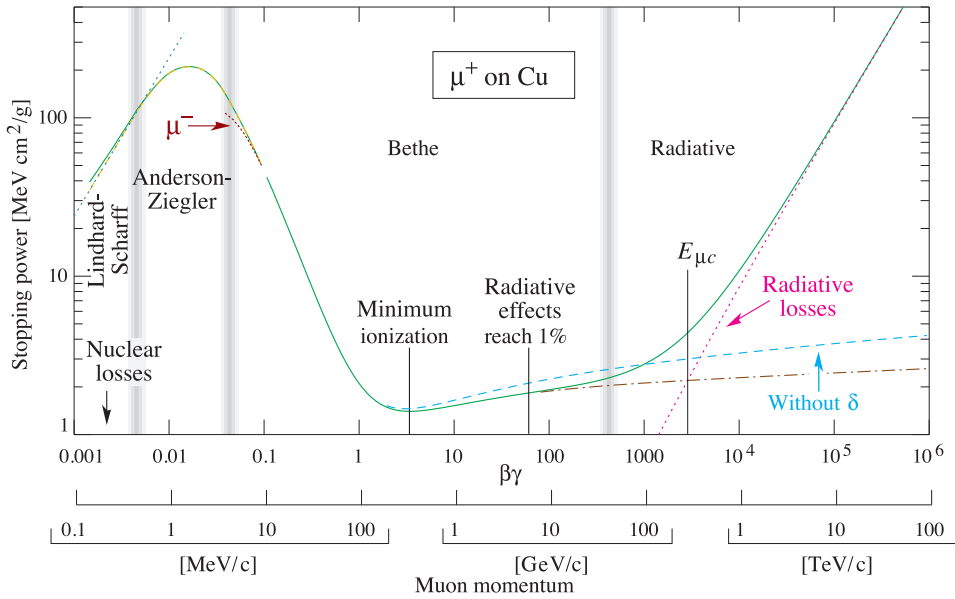


Figure 3.9: Stopping power ($= \langle -dE/dx \rangle$) for μ on Cu. Taken from [32].

The collisional energy loss of a particle in a gas theoretically follows a Landau distribution [231]:

$$L(\zeta) = \frac{1}{\pi} \int_0^{\infty} e^{t \ln t - \zeta t} \sin(\pi t) dt, \quad (3.2)$$

$$L(\zeta) \approx M(\zeta) = \frac{1}{2\pi} \exp \left(-\frac{1}{2} (\zeta + e^{-\zeta}) \right), \quad (3.3)$$

$$\zeta = (x - \bar{x})/\sigma \quad (3.4)$$

Symbol	Definition
K	$4\pi N_A r_e^2 m_e c^2$
N_A	Avogadro's number
r_e	Classical electron radius: $e^2/(4\pi\epsilon_0 m_e c^2)$
I	Mean excitation energy, $\approx 10 \text{ eV}/Z$
$\delta(\beta\gamma)$	Density effect correction
T_{\max}	Maximum kinetic energy which can be transferred to a free electron in a single collision

Table 3.2: Definition of variables used in the Bethe formula Eq. 3.1

The Moyal distribution [232] introduced in Eq. 3.3 as $M(\zeta)$ can approximate the Landau distribution. The most probable value \bar{x} and the width σ are incorporated with the variable substitution in Eq. 3.4. When exploiting the collisional energy loss of a particle for identification, one usually performs several measurements and rejects a certain fraction of clusters with the highest amplitudes. One thus gets rid of large fluctuations in the so called Landau tails. This is depicted in Fig. 3.10, where on the left a Landau distribution is shown for a most probable value of five and a width of two together with 20 random draws from the distribution representing 20 dE/dx measurements, i. e. clusters, for a given track. The 60% lowest clusters are inked in gray. The mean of the full distribution of cluster energies is very sensitive to the unlikely occurrences of high cluster energies. The right panel of Fig. 3.10 shows the mean and truncated mean for 100 000 randomly drawn distributions of 20 clusters according to the left panel. One sees that the truncated mean shows less fluctuations resulting in a smaller relative width. It is a small relative width that is desirable to distinguish different particle species via the measurements of the specific energy loss. Although being a finite statistics effect, the truncation even improves the resolution for 100, 1000 and 100 000 clusters per track. Looking at the distributions for 100 000 clusters per track, the statistical fluctuations at the high end of the tail are still evident. For how the $\langle dE/dx_{\text{trunc.}} \rangle$ was used for particle identification in this analysis see Chapter 5.

3.4 The Transition Radiation Detector

A significant part of the physics program of ALICE involves the measurement of electrons in the central barrel, see Section 1.4. The electron identification in the TPC is limited when the pions fully enter the relativistic rise of the Bethe formula (Eq. 3.1) and the energy loss is proportional to $\ln(\beta\gamma)$, i. e. for momenta above 1–3 GeV/c. It is this momentum range where another effect can be exploited. Transition Radiation (TR) happens when charged particles with high γ traverse an in-homogenous region, e. g. the interface of two media with different

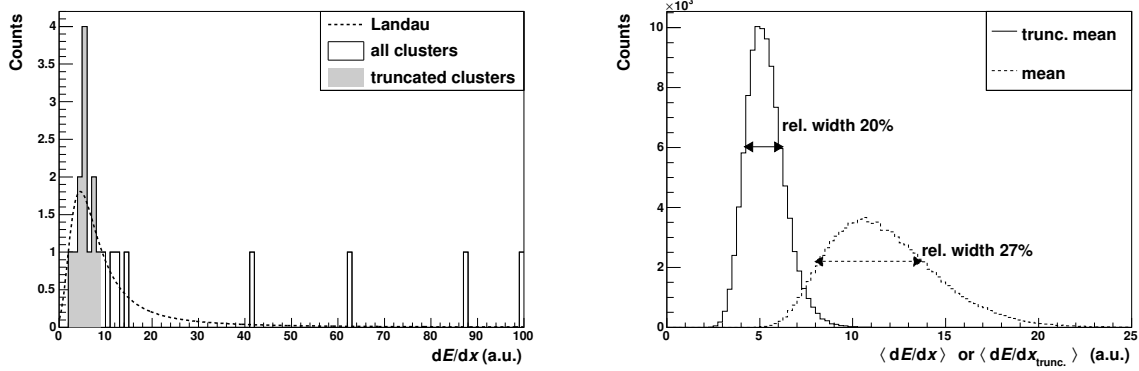


Figure 3.10: Left: Landau distribution with the integral being normalized to 20 counts in the dashed line. 20 random values drawn from the Landau distribution representing measured clusters of a track as histogram with the 60% lowest clusters filled in gray. Right: Distribution of 100 000 sampled means and truncated means according to the distributions shown on the left with their relative widths.

dielectric constants. TR or *perechodnoje islutschenije* was first considered by V.L. Ginzburg and I.M. Frank in 1945 [233]. A comprehensive derivation of the spectral properties of the TR emitted by entering a medium extended in $z > 0$ with a dielectrical constant ϵ can be found in [234]; here only a result is given. The intensity I of the TR with a frequency ω emitted into the solid angle element $d\Omega$ for a particle of charge ae travelling with velocity v in z direction is:

$$\frac{d^2I}{d\omega d\Omega} = \frac{c}{32\pi^3} \left(\frac{\omega_p}{c}\right)^4 \left| \vec{\epsilon}_a \frac{2\sqrt{2\pi} ae \sin \theta \left(k \cos \theta - \frac{\omega}{v\gamma^2}\right)}{v \left(\frac{\omega}{v} - k \cos \theta\right) \left(\frac{\omega^2}{\gamma^2 v^2} + k^2 \sin^2 \theta\right)} \right|^2, \quad (3.5)$$

where the dielectrical constant was approximated as $1 - \frac{\omega_p^2}{\omega^2}$, ω_p being the plasma frequency, $\vec{\epsilon}_a$ is the polarization vector perpendicular to the wave vector \vec{k} and the y axis, and the wave vector itself is perpendicular to the y axis and inclined by the angle θ to the z axis with the length $|\vec{k}| = n(\omega)\frac{\omega}{c}$. A graphical representation of Eq. 3.5 can be seen in Fig. 3.11. The figure shows three characteristic electron velocities. First, a non-relativistic scenario ($\gamma = 1, \beta = 0.10$) where the electron induces an image charge in the medium and standard dipole radiation is emitted. In the relativistic case ($\gamma = 1, \beta = 0.55$) the dipole radiation is bent away from the medium and TR can already be spotted in the forward region $\theta < 45^\circ$. The right panel reveals the radiation of ultra-relativistic particles ($\gamma = 707, \beta = 1.0$), it is very peaked in the forward direction. (On the right panel the x axis is zoomed by a factor 100.) In contrast to Cherenkov radiation, which is only emitted if the velocity of the particle is higher than the speed of light in the medium, TR has no threshold behavior. Integrating Eq. 3.5 yields a dependence of the total intensity proportional to γ . Because of this correspondance, TR was originally thought to give access to a direct measurement of γ in a kinematic region where other techniques face

substantial difficulties. Today, TR detectors are used for the identification of ultra-relativistic electrons.

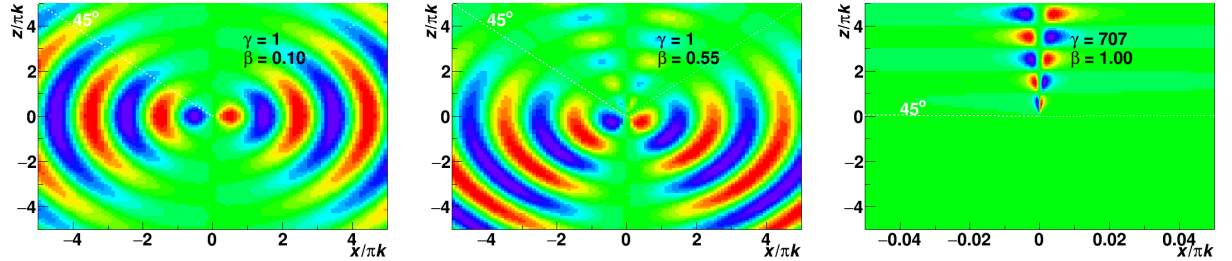


Figure 3.11: Electromagnetic radiation of frequency $\omega = \gamma\omega_p$ of a relativistically moving electron entering a medium at $(x = 0, z = 0)$ after Eq. 3.5. The medium is extended over $z > 0$ and its properties are an electron density of $6 \cdot 10^{23} \text{ cm}^{-3}$ and a refractive index of 1.6. The different panels show increasing electron velocities from left to right. Note the zoom by a factor 100 on the x axis in the right most panel; for orientation a line at $\theta = 45^\circ$ is drawn. Left: The electron creates an image charge in the medium and a standard dipole radiation is seen. Center: Relativistic effects start to kick in. The dipole radiation is bent away from the medium and a hint of transition radiation can be seen for $\theta < 45^\circ$. Compare with the calculations in [235], which show the same relativistic effect on the dipole radiation. Right: The very forward peaked transition radiation is dominant.

The Transition Radiation Detector (TRD) is located radially outwards of the TPC at a position of $2.9 < r < 3.7$ m and is segmented in φ into 18 supermodules, covering the full azimuth. Each supermodule spans over the central barrel acceptance $-0.9 < \eta < 0.9$, and is divided in η into 5 stacks. Each stack consists of 6 radial layers with one chamber each, making up a total of $18 \cdot 5 \cdot 6 = 540$ possible chambers. In order to reduce the material budget in front of the PHOS detector, no chambers were installed there, resulting in a total number of 510 chambers. A chamber is in radial direction composed of a radiator, a small drift volume and the amplification region. For the radiator, a sandwich structure of Rohacell foam and polypropylene fibers was chosen. The foam provides mechanical stability and shows a quite good yield in transition radiation. The majority of the transition radiation is produced in the fibers. The material was chosen following a test-beam campaign, where several options were investigated [236].

The TR created in the radiator ionizes the gas filling the chamber. Although being expensive, Xenon was chosen due to its high Z leading to a high conversion probability of the TR photons. An averaged pulse-height spectrum versus the drift time for electrons and pions from test-beam data can be seen in Fig. 3.12. The shape of the pion signal can easily be understood if one takes into account that the particles are traversing the amplification region: the peak at $0.6 \mu\text{s}$ appears as charge from both sides of the sense wire (radially outwards and inwards) is

collected. The second peak in the electron spectrum at $2.2\ \mu\text{s}$ stems from the TR, which is preferentially absorbed close to the radiator leading to long drift times. Currently, four methods for an effective electron-pion discrimination are available within ALICE: i) truncated mean ii) one-dimensional and iii) two-dimensional likelihood probabilities on the integrated charge, and iv) a neural network.

It was found in [237] that a Landau distribution is describing the energy loss including the TR. The implementation of a truncated mean following the description given in Section 3.3 thus is straight forward. The advantage of the truncated mean is that it not only provides an electron-pion discrimination, but also allows to generally identify hadrons with the TRD. The TR of electrons just increases the truncated mean for high- γ electrons.

The one-dimensional probability, also called LQ1D, uses reference distributions for electrons, pions and protons of the integrated charge deposit in the TRD from clean samples. The clean samples were obtained from V^0 decays, i. e. π from K_S^0 , p from Λ and e from γ conversions. Although the method was implemented in the scope of [238], only a poor description can be found therein. A better report exists in [239]. Fig. 3.13 shows the energy-loss distributions for electrons (in black) and pions (in red) normalized to unity. The likelihood of a particle to be an electron with a given energy-loss measurement $Q = dQ'/dl$ is defined as:

$$L(e|Q) = \frac{P(Q|e)}{P(Q|e) + P(Q|\pi)}, \quad (3.6)$$

where $P(Q|k)$, $k = e, \pi$ are the energy-loss distributions shown in Fig. 3.13. The radially stacked chambers produce up to six energy loss measurements ${}_iQ = d_iQ'/dl$, d_iQ'/dl is the specific energy loss in the i th stack. The measurements are to a good degree independent, thus the six probabilities $P({}_iQ|k)$ factorize. It is shown in [216] that the LQ1D method is out-performing the truncated mean. This is reasonable as the LQ1D approach takes into account the full shape of $P(Q|k)$ and not just its (truncated) mean.

The two-dimensional LQ2D approach developed in [239] further refines the particle identification with the likelihood method by slicing the pulse-height signal into two time bins such that the charge Q_0 integrated over the first half includes the signal from the amplification peak and the charge Q_1 integrates over the times where TR typically occurs for electrons. It is obvious from Fig. 3.12 that a particle with a high Q_0 and Q_1 , is likely to be an electron. Whereas a particle with a statistically fluctuating higher charge deposit in the first part, but only a small signal in the second half, is more likely to be a pion. The two-dimensional probabilities for electrons and pions $P(Q_0, Q_1|k)$, $k = \pi, e$ which were obtained with clean samples from V^0 decays, are stored within the AliRoot software framework⁵ and can be looked up to calculate the likelihood following Eq. 3.6.

A neural network approach is also available for electron identification in the TRD. It theoretically can exploit the full information of the measured pulse-height spectrum. In the realized

⁵<http://git.cern.ch/pubweb/AliRoot.git>

approach [240], the pulse-height spectrum is divided into eight time bins. The network needs to be trained with reference distributions. One reason to limit the input to eight time bins was that the training takes longer the more complicated the network is. The neural network outperforms all other approaches discussed here.

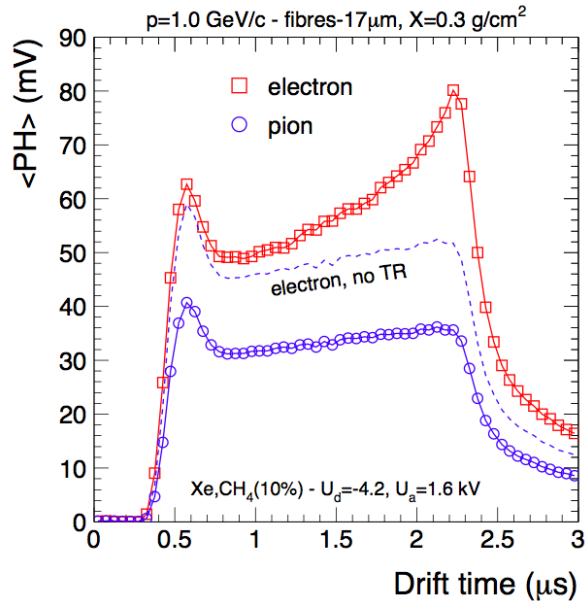


Figure 3.12: TRD pulse height versus the drift time for electrons in red and pions in blue and the expected signal for electrons without TR in the dashed blue line for a momentum of 1 GeV/ c . The TR signal is manifest as the difference between the red and the dashed blue line. Taken from [236].

The TRD provides online tracking and particle identification within 7.7 μs after the primary interaction of the LHC beams and thus allows for a versatile triggering scheme. The pads collecting the deposited charges of the traversing tracks are segmented only coarsely (pad length ~ 80 mm) along the beam axis. This allows for a fine pitch (pad width ~ 7 mm) in the bending direction of the track in the magnetic field. In the offline reconstruction, the z position can be recovered as the pads in the different layers are alternately tilted by $\pm 2^\circ$. Online, the z coordinate is of lesser importance and the high granularity in the bending direction enables the TRD to perform a reasonably good p_T determination. Compared with the p_T as determined offline using the TPC, a resolution of 20% is achieved in the studied range from one up to circa ten GeV/ c of transverse momentum [241]. The drift region extends over 3 cm, and the drift velocity is about $1.5 \frac{\text{cm}}{\mu\text{s}}$, which spans the signal over 2 μs . The signal is read out with a sampling frequency of 10 MHz resulting in 20 time bins, each representing the energy deposited over ~ 1.5 mm. In analogy to the TPC, the possibility to employ a baseline adjustment and ion-tail cancelation exists (see the discussion in Sec. 3.3).

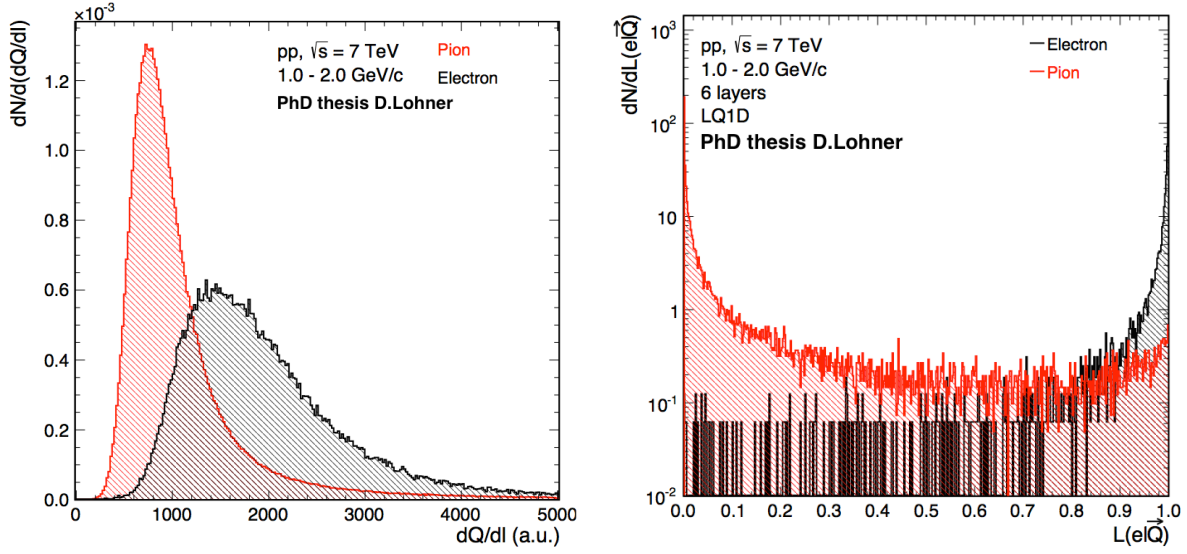


Figure 3.13: Left: Charge deposit dQ per length dl in the TRD for electrons (black) and pions (red). Right: Electron likelihood for electrons and pions selected via V^0 decays $K_s^0 \rightarrow \pi^+\pi^-$ and $\gamma \rightarrow e^+e^-$. Both taken from [239].

Pad-by-pad gain variations are corrected for by utilizing online gain tables. The gain tables were acquired by placing the solid ^{83}Rb in the TRD gas system; the TPC makes use of the equivalent procedure. The radioactive ^{83}Rb transforms via a beta decay to the gaseous, meta stable ^{m83}Kr with a lifetime of $\tau = 1.83 \text{ h}$ (half life $t_{1/2} = \ln(2) \cdot \tau = 2.64 \text{ h}$), which disperses into the chambers of the TRD. A reference spectrum for the decay of the ^{m83}Kr was obtained by the analysis of a single chamber which showed good statistics and healthy behavior.⁶ Fitting the single-pad response with the reference, as shown in Fig. 3.14 (left), allows to obtain the relative gain factor for each read-out pad. The up to four individually reconstructed ^{m83}Kr peaks on the chamber level also allow to test the electronics for a linear behavior. The resulting relative gain factors for an exemplary chamber are showcased in Fig. 3.14 (right). The impact of the chamber geometry is apparent. The resulting gain uniformity on the pad level is better than 1% [242].

In the standard reconstruction, a cluster is formed for each time bin taking into account the pad response function. Instead of employing a center of gravity method using a Mathieson fit⁷ [244], look-up tables for the amplitudes of the maximal charge and the two nearest neighbors are used. The resolution of the cluster in the bending direction depends on the inclination of the track with regard to the pad surface. For high- p_T tracks, a single cluster resolution of $303 \pm 2 \mu\text{m}$ was found in [245]. With up to 120 clusters per track, this allows the TRD to trigger

⁶The chosen reference chamber was super module 0, stack 0, layer 0.

⁷E. Mathieson provided an empirical formula to take into account the angular position of the avalanche at the anode wire, which strongly influences the distribution of the induced pad charge. See also [243].

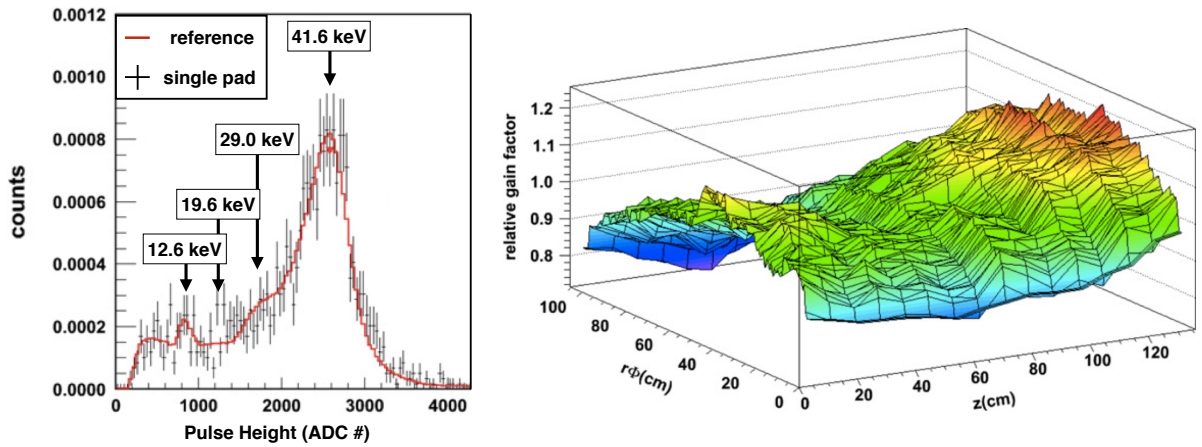


Figure 3.14: Krypton Gain Calibration. Left: ^{38}Kr single pad spectrum in black markers with a fit by a reference spectrum in red. Right: Pad-by-pad gain factors relative to the reference spectrum for one chamber. Both taken from [242]

on rare high- p_T probes. Currently, a jet trigger looking for many high- p_T tracks close by, and a high- p_T single and di-electron trigger, exploiting the online PID capabilities, are in place.

3.4.1 A Quality Assurance Framework for the ALICE TRD

Many errors at the online stage can not be corrected for during offline reconstruction: an interesting event that is not triggered on is lost. The ALICE data reconstruction happens in stages (passes), first reconstructing a smaller subset for calibration. Thus, errors that can be corrected need immediate action to, e. g., avoid wasting valuable computing time. It is therefore crucial to constantly monitor the performance of the TRD. In the scope of this thesis, an automated quality assurance (QA) framework with easy usability was developed.

At the beginning of this task, a few visual collections of histograms with key observables for the TRD were collected at <http://www-alice.gsi.de/trd/beam09/>. The histograms are created centrally when reconstructing the data. For each run, the file containing the histograms had to be downloaded to a local machine where the representations were created. These had to be copied to the common ALICE account at GSI, and a link added by hand to the html document at the above specified link. Data for different data taking periods were scattered across several places and the webpage did not allow for an easy comparison of, e. g., different runs. The newly developed webpage can be reached at <http://www-alice.gsi.de/trd/monitoring/>. It contains the QA information for all data taken with the TRD since the start-up of the LHC in 2009 to the present day. For this vast amount of data, a good organization is important. The page starts with a table giving an overview on the different data-taking periods and the different passes, giving links which lead to the section on the page where all available plots for each run

is linked. Clicking on the desired plot opens a pop-up window showing the plot. The pop-up window has buttons for browsing through, e. g., the different runs, easing the comparison of the plots and facilitating it to spot irregularities. Comparing two specific plots is also possible by clicking on the main page on a different link. Changes are most evident by going back and forth between two representations with the ‘back’ button on the pop-up window. The information about the last viewed frame is stored on the main page with hidden input fields and sent to the pop-up window via the browsing address. The navigation is performed with java scripts, which are aware of the available content.

Emphasis should be put on the fact that the front-end page is entirely and continuously rewritten by a permanently running process. The process checks the Worldwide LHC Computing Grid⁸ for new ALICE data, generates the aforementioned pictures, stores them on the GSI web server and then writes the java script and html page. This makes the TRD QA framework essentially maintenance free, as no links have to be added by hand to the webpage and no plotting macros have to be started. It has the additional, important advantage of always being up to date, allowing for short reaction times upon problems.

The framework was extended by J. Book in the course of [246] to also monitor the run-wise TRD calibration objects in the Offline Conditions Database (OCDB). Fig. 3.15 shows the mean TRD chamber drift velocity as a function of run number for the data taking period LHC12f as an example for one of the calibration parameters. This picture can also be found at http://www-alice.gsi.de/trd/trending/#LHC12f_Mean_ChamberVdrift.png. Run 187047 clearly shows abnormal behavior in this variable. As can be seen from the Run Condition Table (RCT)⁹ or the logbook¹⁰, this was a test run for the TRD, not intended for regular data analysis. The power of such a trending plot, where the value of a characteristic observable is shown as a function of time, is that a whole data taking period can be checked within a glimpse. This led to the decision to not only provide such trending plots for the calibration factors in the OCDB, but also for the most important quantities for the TRD which are accessible during reconstruction. Currently the matching efficiencies with the adjacent TPC and TOF detectors and some more TRD track quality parameters are monitored run by run at <http://www-alice.gsi.de/trd/trendingQA>.

Available at <http://www-alice.gsi.de/trd/monitoring/TTreeIndex.html> are TTrees¹¹ for each data taking period with the run-by-run quantities from the reconstruction QA and the OCDB trending and a few more of which the luminosity proved to be very useful already. The luminosity in ALICE can be determined in two ways. First by the Beam Rate from Neutrals (BRAN) system of the LHC and second by ALICE itself via dedicated triggers. The BRAN system detects energy from neutral particles produced in the collision of the two beams in the

⁸<http://wlcg.web.cern.ch/>

⁹<http://alimonitor.cern.ch/configuration/>

¹⁰<https://alice-logbook.cern.ch>

¹¹<http://root.cern.ch/root/html/TTree.html>

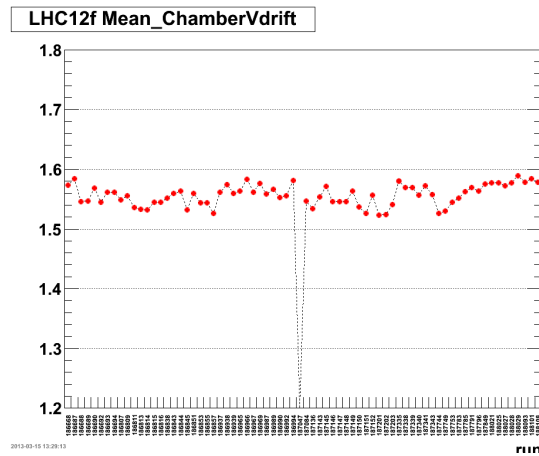


Figure 3.15: Mean TRD chamber drift velocity for the LHC12f data taking period as a function of run number. The outlier run 187047 can easily be spotted.

forward direction [247,248]. The BRAN luminosity can be retrieved for pp collisions in intervals of one second from the LHC data entry, which is stored as a Global Run Parameter (GRP) in the OCDB. ALICE has a dedicated luminosity monitor trigger called `C0VTX`. At the end of 2012, ALICE was running with beam-satellite pp collisions [216], resulting in the full trigger name `C0TVX-S-NOPF-ALLNOTRD`. In all other data taking periods beam-beam collisions were recorded, thus the trigger name is `C0TVX-B-NOPF-ALLNOTRD`. One divides the level zero trigger counts before any veto (`L0b`) by the difference of the time stamps of the trigger recording of the Central Trigger Processor (CTP). To calculate the luminosity, one has to divide the trigger rate by a conversion factor. This conversion factor is $0.75 \cdot 2$ for PbPb and pPb collisions, and 25 or 28 for pp collisions in the year 2011 or 2012, respectively. Plotting the most probable value of the total charge deposited by a particle of 1 GeV/c in the TRD vs. the luminosity as it is done in Fig. 3.16, reveals a strong dependence (closed symbols) on luminosity. After rejecting tracks from pile-up events in the TRD calibration code (open symbols), this dependence is gone. The bias by pile-up events of the TRD calibration was only found with the powerful QA machinery developed in this work. Quickly after the problem in the TRD calibration was found, the TPC used the TRD QA TTrees, and also spotted a similar dependence.

3.5 The Time-Of-Flight Detector

The Time-Of-Flight (TOF) detector is located radially outwards from the TRD. It covers the full azimuth and the pseudorapidity region $|\eta| < 0.9$. As the TPC and TRD, it is segmented into 18 azimuthal sectors, each consisting of several strips. The strips are made of 10-gap double-stack Multigap Resistive Plate Chambers (MRPCs) as shown in Fig. 3.17. A stack is produced by putting six glass plates on top of each other; the gas gaps are generated by

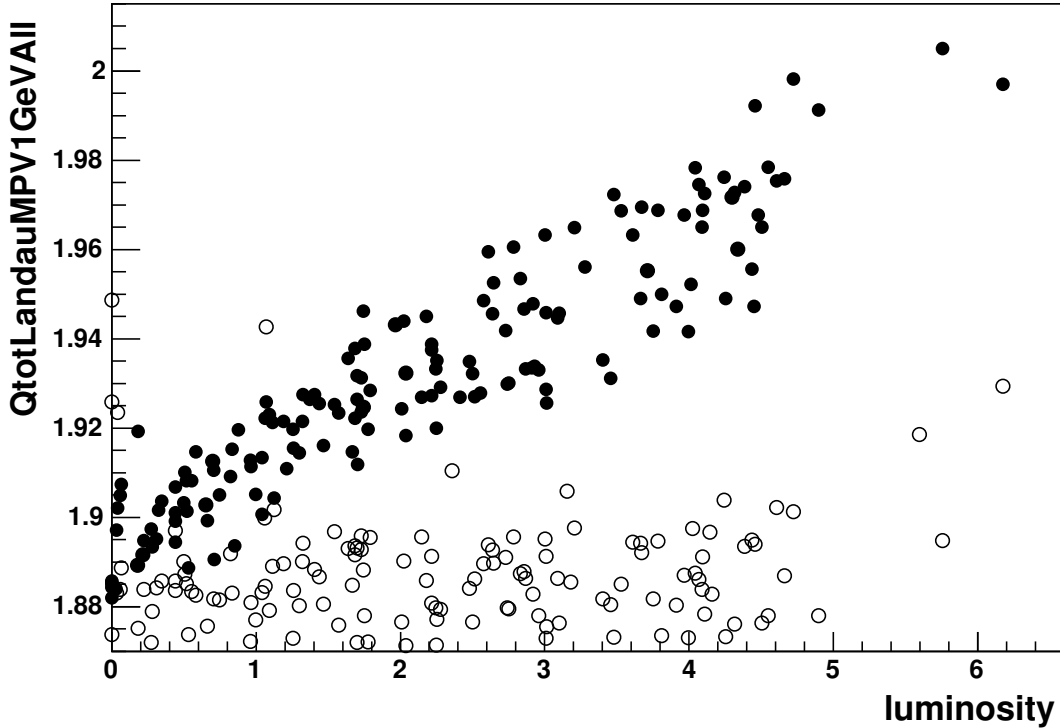


Figure 3.16: Luminosity dependence of the most probable value of the total deposited charge for a particle of 1 GeV/ c before (closed symbols) and after (open symbols) a fix in the TRD calibration code.

placing a spacer in between the glass plates. The spacer used here is a fishing line that is laid in a zig-zag across the plates along the 1220 mm long strip. The bottom and top glass plates are coated with acrylic paint loaded with metal oxides to form a resistive layer and a high voltage of typically 12 kV over the stack is applied. This high voltage will cause an avalanche if a charged particle traverses the detector. The inner glass plates are electrically floating. It was argued in [249] that the system is self stabilizing and no voltage has to be applied to the internal plates. If by any reason the voltage of a glass plate deviates from the nominal value, the next avalanche will produce more charge in one of the two adjacent gaps and less in the other, equalizing the voltage. The electrons drift only across short distances, which makes the detector very fast. The jitter in the time signal is dominated by statistical fluctuations in the avalanche. The advantage of the Multigap RPC to a traditional wide gap RPC is that the glass plates stop the avalanche, but are transparent to the signal that is being created on the pick-up pads by the movement of the avalanche electrons. This is shown in Fig. 3.18: the fluctuations in the wide gap RPC grow more and more on the avalanche's way to the anode. The spatial spread of the signal is large; consequently, the spread in time will be large too. Stopping the avalanche in the MRPC reduces the fluctuations of the time signal. The small gap size leads to

a precise time measurement with an intrinsic time resolution of better than 40 ps. Several gaps are used to reach a high efficiency of close to 100% [114] even at atmospheric pressure.

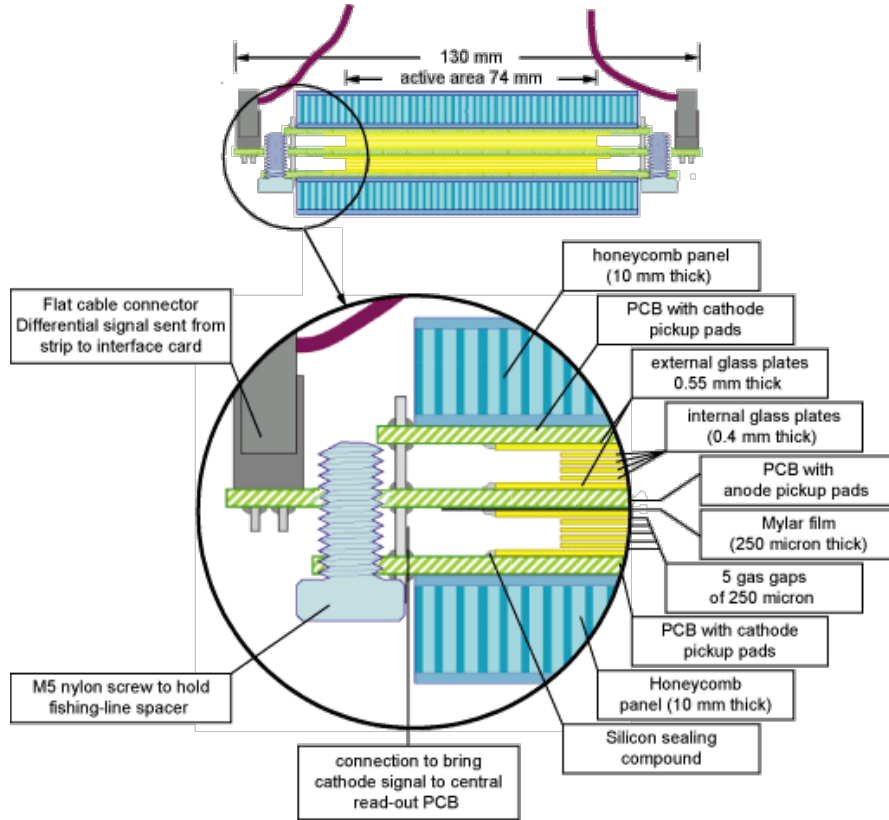


Figure 3.17: Cross section of the ALICE double-stack 10-gap TOF MRPC strip. The strip consists of two stacks symmetrically arranged around the Printed Circuit Board (PCB) with the anode pads in the center. Taken from <http://aliceinfo.cern.ch>, cf. [114].

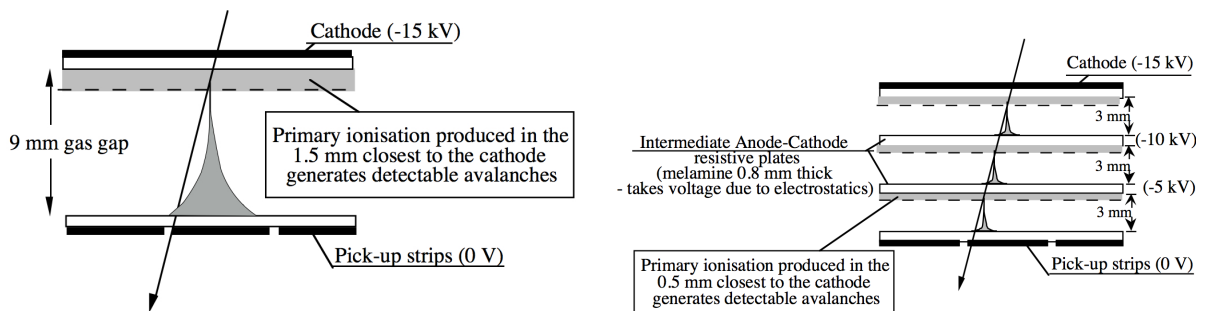


Figure 3.18: Comparison of the avalanche evolution in a wide gap RPC (left) and a Multigap RPC (right); here a three-gap MRPC is shown. The small gap size in the MRPC improves the time resolution. Taken from [249].

A start time with a resolution of 50 ps is provided by the T0 detector [250]. It consists of

two Photo Multiplier Tube (PMT) arrays behind Cherenkov radiators, which they are optically coupled to, on either side of the interaction point close to the beam pipe. Taking into account the path length from the primary interaction to the TOF detector L and the track momentum p , as reconstructed by the tracking detectors, one can calculate the expected time of arrival t_{exp} at the TOF detector for a given particle mass m :

$$t_{\text{exp}} = \frac{L}{\beta \cdot c}, \quad (3.7)$$

$$\beta = p/E = 1/\sqrt{1 + \frac{m^2}{p^2}} \quad (3.8)$$

The difference of the expected time to the measured time can easily be exploited for PID purposes (see Chapter 5). For high-multiplicity events an even better resolution of the start time can be achieved by the TOF detector itself. After the track reconstruction, the start time is obtained by a χ^2 minimization procedure in a self-consistent way. For a p-Pb event sample with more than 20 matched tracks, a start time resolution of less than 30 ps was achieved in [251].

3.6 The Electromagnetic Calorimeter

The ElectroMagnetic Calorimeter (EMCal) is located behind the TOF detector with its front face at a radius of ~ 4.5 m from the interaction point. It spans 107° in φ and extends over $|\eta| < 0.7$, a six-fold larger acceptance than the Photon Spectrometer (PHOS). The EMCal apparatus is segmented into 12 288 towers, each having a size of $\Delta\varphi \times \Delta\eta = 0.0143 \times 0.0143$ [252]. It is a sandwich calorimeter made of Pb and polystyrene. The Pb with its high density and high Z provides the necessary opaqueness for incident electromagnetically interacting particles, triggering the showering of these. The use of polystyrene for the scintillator base has the advantage that it can be manufactured easily and it is cheap. The plastic itself does not provide enough scintillation light yield and cannot transmit its own light, but adding a primary fluorescent emitter makes it much brighter and a wavelength shifter can provide the needed transparency. Examples for these additives can be found in [253].

The general strength of calorimeters is their improved precision at higher energies. The number of particles and detectable scintillation light generated in a fully absorbed shower is directly proportional to the incident particle energy. Therefore the relative error on the measurement decreases with increasing energy — in contrast to a gaseous detector like the TPC measuring the momentum:

$$\text{EMCal} \quad \frac{\sigma_E}{E} \sim \frac{1}{\sqrt{E}}, \quad \text{TPC} \quad \frac{\sigma_p}{p} \sim p \quad (3.9)$$

The predominant process for high-energy electrons to lose energy is bremsstrahlung, for high-energy photons it is e^+e^- pair creation. A measure of the electromagnetic thickness of an object is the radiation length X_0 . One radiation length is equivalent to the length an electron has to travel to lose all but $1/e$ of its energy by bremsstrahlung or $7/9$ of the mean free path for pair production of a photon [254]. In order to contain the full cascade of produced particles within the calorimeter, it is a design objective that the total detector material gives many radiation lengths. As the EMCal detector was added at a late stage to the ALICE proposal [255], its design is constrained by the integration volume: it has to fit in between the L3 magnet and the other detectors. By choosing a volume ratio of Pb to scintillator of 1 : 1.22, an effective radiation length of 12 mm is achieved. With an active detector depth of 24 cm, this results in 20 radiation lengths. Simulations of the EMCal design showed that the energy resolution of a 100 GeV photon is dominated by shower leakage. With the chosen setup this leakage is limited and the resolution is as good as 2.5% [252]. The simulations were verified with test beam results [256]. The energy resolution becomes better the higher the sampling frequency of the Pb and scintillator is. For practical reasons like the assembly labor, it was limited to 77 layers of Pb and scintillator each [255].

The light generated in the scintillator is transmitted to Avalanche Photodiodes (APDs) by wavelength shifting, doubly cladded fibers which pierce through the Pb and scintillator like a shashlik stick. Cladding is the process of surrounding the high refractive index core with lower refractive index material. It is a standard procedure for real-world applications of fibers. Without cladding any drop of oil or water on or contact between the fibers would change their optical properties. Here, the $n_D = 1.59$ polystyrene (PS) core was enclosed with a layer of $n_D = 1.49$ polymethylmethacrylate (PMMA) and a coating of $n_D = 1.42$ fluorinated polymer (FP). To maximize their light output to the APDs, an aluminum mirror is added to the front face of the fibers.

Chapter 4

Data Reconstruction

In this chapter, the data preparation provided by the common framework is discussed. A general write-up of the utilized software can be found in [257].

4.1 Trigger and Centrality

The LHC provides beams in bunches. During the Pb-Pb runs of the LHC in 2010 and 2011, bunches were set up to collide at the second interaction point, where ALICE is located.¹ Synchronizing the experiment with the LHC clock, data was only taken, if a beam-beam bunch crossing was expected.² The different triggers are grouped according to their latency, i. e. the time difference between the interaction and the trigger decision, into levels from zero (L0) to three (L3), with latencies of $0.9\ \mu\text{s}$, $6.5\ \mu\text{s}$, and $100\ \mu\text{s}$ for the zeroth to second level; the last stage L3 is implemented in a computing farm as the High Level Trigger (HLT). The L2 latency matches the drift time of the TPC, making a past-future protection possible: events can be rejected if another event from a different bunch crossing is noticed.³ The ALICE physics program is dedicated to studying the soft bulk, present in each and every inelastic event, which gives an online event reduction less importance than for, e. g., Higgs physics. There are however certain means of purifying the event sample by fast, dedicated detectors.

The V0 scintillators suppress elastic events when a signal in both the A side detector (V0A) and C side array (V0C) is required. Together with the beam-beam bunch crossing, this condition constituted the minimum-bias trigger for the 2011 heavy-ion campaign (MB_{and}). In the 2010 Pb-Pb run, also a less pure trigger $\text{MB}_{2\text{-out-of-3}}$ was used, that only requires two

¹Cf. the beam-satellite collisions mentioned in Section 3.4.1.

²Such a beam-beam trigger condition is indicated by B in the trigger name after the first hyphen [258].

³An enabled past-future protection is indicated in the trigger name by a PF after the second hyphen. During Run 1 of the LHC from 2009 until 2013, no such a past-future protection was in place; all used triggers have a NOPF in their name.

out of the following three conditions: (i) two hit pixel chips in the outer layer of the SPD, (ii) a signal in VZERO-A, (iii) a signal in VZERO-C. With the increasing interaction rate at the end of the 2010 Pb-Pb campaign, the $MB_{2-out-of-3}$ was replaced by $MB_{3-out-of-3}$, where a coincidence of all three conditions was required [259]. In the second year of heavy-ion operation, the LHC could provide beams with much higher luminosity as compared to the first year. The bottleneck being now more and more the bandwidth available to write data, a purification of the 2011 dataset by additionally requiring a signal in both zero degree calorimeters (ZDCs) and thus subduing electromagnetic interactions of the high Z Pb nuclei makes sense. Imposing the ZDC condition on the minimum-bias trigger MB_{and} results in a trigger called MBZ. The V0 signals are available at L0 and proportional to the energy deposited by produced particles, which enables the experiment to acquire only specific centralities. The CENT and SEMI trigger classes require a signal threshold corresponding to 10% and 50% most central events in each of the two V0 detectors separately and a coincidence of the trigger from both sides. With the higher luminosity, the recorded statistics could be enhanced from 56M registered MB events in 2010 to 72M events in the MBZ, SEMI and CENT classes written to disc in 2011 [216]. Any correlation analyses, like the ones discussed in this document, profit statistics-wise from the centrality selection. The number of particle pairs is roughly given by the product of the number of events times the square of the event multiplicity, which increased by the online impact parameter selection with the V0 detector. Only 12% of the 2011 Pb-Pb sample consist of the MBZ class. Events from the CENT and SEMI trigger, picking nuclear collisions with an online centrality from 0–10% and 0–50%, make up 40% and 48% of the 2011 sample, respectively [216].

The standard offline centrality determination is done via the mean of the two V0 amplitudes (V0M) [124]. Other measures exist as well, like the energy deposited in the zero degree calorimeters or the track multiplicity in the central barrel. In general good agreement between the different estimators is found; this is demonstrated in Fig. 4.1, where the correlation between the track multiplicity in the barrel (TRK) and the mean V0 signal (V0M) is displayed.

The T0 quartz arrays are located in both hemispheres (A side and C side) of the nominal interaction point and provide a fast timing signal at L0 and give a wake-up call to the TRD even before that.⁴ The good resolution of the interaction time provided by the T0 makes it a precise start time for the time-of-flight measurement of the particles used for particle identification. By requiring the difference of the time signals provided by T0A and T0C to be below a certain threshold, the T0 detector effectively restricts the longitudinal position of the event vertex z_{vtx} . The limit on $|z_{vtx}|$ helps ensuring a uniform acceptance of the central barrel detectors. Due to the limited amount of produced particles in 90% central collisions, only about 35% of these events have signals from both halves of the T0 detector. This fraction increases steeply, so that at 70% centrality all events have the necessary information. Therefore, the vertex constraint by the T0 could be employed for the SEMI and CENT trigger class in the 2011

⁴Triggers with the TRD wake-up are appended a WU to their descriptor.

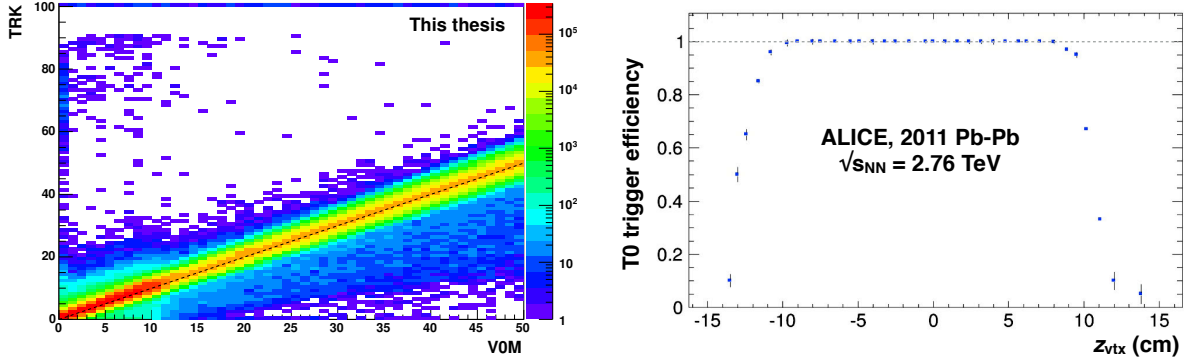


Figure 4.1: Left: Correlation for two different centrality estimators: VOM, the mean V0 amplitude, on the x-axis and TRK, the number of tracks in the central barrel, on the y-axis. The dashed line indicates the diagonal of a one-to-one correlation. Good agreement between the two estimators is seen, note the log-scale on the z-axis. Right: T0 trigger efficiency as a function of the longitudinal vertex position. One sees that for $|z_{vtx}| < 10$ cm the efficiency is close to 100% and quickly drops to zero for $|z_{vtx}| \gtrsim 12.5$ cm. The trigger efficiency was obtained for the SEMI and CENT event class, corresponding to 0-50% most central events. Taken from [260].

campaign [261]. Conservatively, about half of the SEMI and CENT events was taken without the T0 requirement. The effect of the T0 trigger on the ALICE data sample is shown in Fig. 4.1 (right). Displayed is the trigger efficiency of the T0 vertex position trigger (0TVX) as a function of z_{vtx} . We see how the trigger is fully efficient for $|z_{vtx}| \lesssim 10$ cm and nicely rejects events with $|z_{vtx}| > 10$ cm, thus effectively increasing the available amount of data for a physics analysis.

4.2 Tracking

ALICE uses a Kalman filter for tracking [262]. A Kalman filter [263] starts at time step t_0 with an input guess for the state vector \vec{x}_0 that has an uncertainty in form of a covariance matrix Σ_0 . Confronted at time step t_1 with a measurement \vec{y}_1 that itself has a limited precision, the guess is updated using Bayes' theorem to \vec{x}_1 . Using an underlying, e. g. physics, model, the guess can now be propagated to time step t_2 to predict the next measurement. Here, not only the errors on the old guess \vec{x}_1 are evolved, but also the propagation process itself adds another uncertainty on the successive observation. An appropriate example in the context of high-energy particle or heavy-ion physics is a scattering process on detector material. The Kalman filter is aware of the possibility for such a distortion and incorporates it into the expected measurement. This is a qualitatively new and important feature.

Fig. 4.2 shows an example of a Kalman filtering. A particle moves in a generic (x, y) space

from $(0.0, 1.0)$ on a circle with the circle's center in $(0.0, 0.0)$. The particle's path is indicated by the red, solid line. The Kalman filter was provided an initial guess $(-0.2, 0.8)$ with an uncorrelated uncertainty of 0.3 in each x and y , shown as a pale blue ellipse in the background. As the particle moves in (x, y) space, it is measured at finite time steps. The true position of the particle at the different time steps is indicated with a black diamond; this however is hidden to the Kalman filter and only the measurement (indicated by a red diamond) is provided to the algorithm. The chosen uncertainty on the measurement is an uncorrelated, Gaussian one with a standard deviation of 0.05 in both dimensions, visualized by the red, transparent ellipses. The predictions of the Kalman filter for the measurements are shown with the dark blue ellipses. The error ellipses represent the full covariance matrix: the axes of the ellipses point into the direction of the eigenvectors of the covariance matrix; the length of the axes in the predictions correspond to the square root of the eigenvalues of the matrix. As expected from the chosen, uncorrelated measurement precisions, the uncertainties in this example are independent down to the given, limited numerical precision. Although being simple in its equations, the filter is very powerful through the underlying mathematics. We see that its prediction nicely converges towards the true position of the particle with appropriate uncertainty estimations as more and more dynamic measurements are provided. We also see the bias towards the provided guess in the first predictions. This illustrates, that a suitable initial seed is crucial for a successful and effective running of the Kalman tracking program. Kalman filters are very popular and widely used. Not only was Kalman awarded the 2008 Charles Stark Draper Prize for their development [264]; they are also, e. g., one of the tools for interpreting macroeconomic data that the 2011 Nobel Prize in economics was awarded for [265]. Using economists' language, i. e. *shock* for *measurement*, Kalman filtering is discussed at length in the 2011 announcement ceremony [266–268].

In ALICE, the central barrel tracking starts at the outer radius of the TPC, where the track density is low. As we have seen in the above paragraph, appropriate seeding is important in case a Kalman filter is invoked for tracking. Consequently, a thorough analysis of the best seeding practice was carried out with the result of 36 consecutive seedings. The seeding is discussed in Section D.1.

The Kalman filter propagates the information given by the seeds inwards in radius from the TPC via the ITS to the primary interaction vertex. Bridging the gap between two detectors is one of the strengths of a Kalman filter, as its estimate is always local. A global fit might describe well the average momentum of a particle in, e. g., the TPC. Yet what is important when extrapolating the track is the momentum at the edge of the detector. The tracker is divided into detector specific software modules, where, e. g., the relevant geometries are implemented. Each package is responsible for the track prolongation within the volume of the detector. Additional detector hits, also from the ITS at small radii, are associated to the track if they happen to lie on a road, i. e., within a certain distance of the expected position.

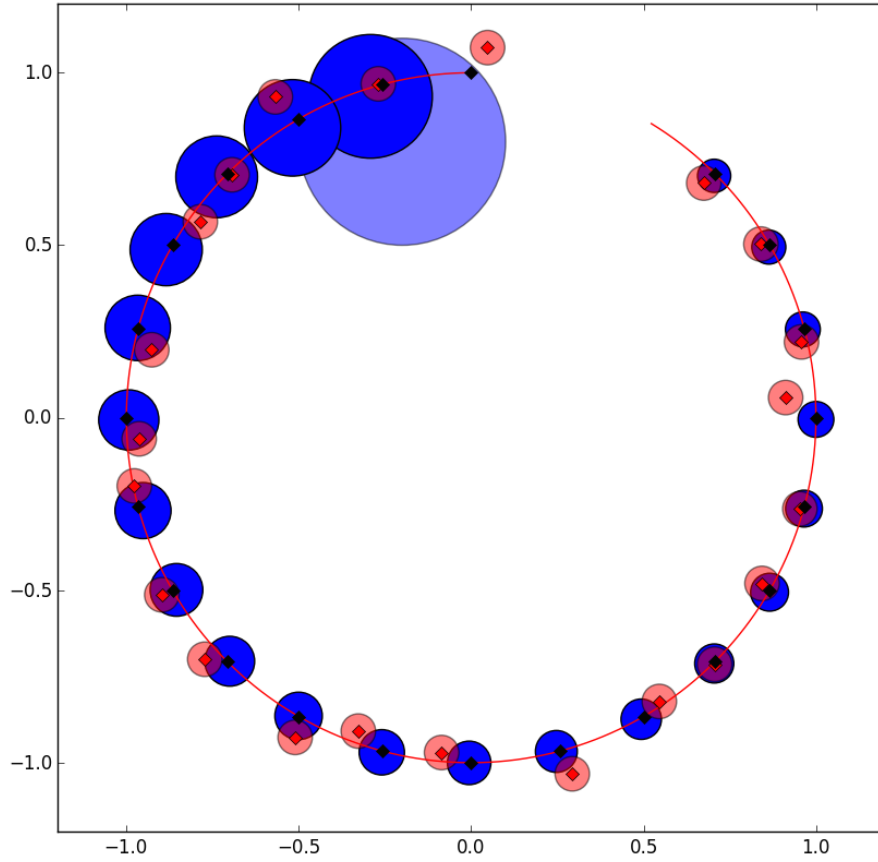


Figure 4.2: Simple Kalman filter. A particle moves counter-clockwise on a circle (red line). At finite time steps (the particle's true position is indicated by black diamonds), its position is measured (red diamonds) with a finite precision (red transparent ellipses). The Kalman filter's guess (blue ellipses) is subsequently updated with the measurements. For details see text.

After the inward propagation of the TPC seeds is concluded, a local mode in the ITS, the ITS standalone tracking, is started. The acceptance down to low p_T of the TPC is limited by its geometrical extent and the strength of the magnetic field. With $B = 0.5$ T and the minimal radius of the TPC of $\rho = 0.85$ m the softest reconstructed primary particles have a p_T of

$$\text{TPC} \quad p_{T,\min} \approx 0.3 \cdot B \cdot \rho \frac{\text{GeV}/c}{\text{T m}} \approx 130 \text{ MeV}/c. \quad (4.1)$$

Putting into this equation parameters for the ITS, i. e. $\rho = 7.6$ cm at the second SPD layer, the benefit of such a ITS standalone mode becomes clear:

$$\text{ITS} \quad p_{T,\min} \approx 10 \text{ MeV}/c. \quad (4.2)$$

At such low momenta, the energy loss of the particles is significant and distorts the tracks, such that the position of the reconstructed point at a given layer deviates significantly from

the expected position without distortions. Since a limit on the window for associating clusters is mandatory to suppress fake tracks, the efficiency of the tracking algorithm drops below 40% for momenta smaller than $100\text{MeV}/c$ [269] and lifts the limit for track reconstruction to $p_T \gtrsim 90\text{ MeV}/c$ [270]. The ITS standalone method not only provides additional acceptance at low p_T but also fills gaps in φ at the TPC sector boundaries.

In a second tracking step, the direction of propagation is reversed and extended to the outer central barrel detectors covering full azimuth, i. e. TRD and TOF, and also those with partial coverage in φ , i. e. EMCAL, HMPID, and PHOS. After propagating the particles through the TRD, tracks are prepared for matching them with hits in the TOF detector. To avoid fake combinations of a track and a TOF hit, each TOF cluster is only assigned once. Since the precision on the knowledge of the particle's spatial position is increased for straight high-momentum tracks, they are sorted according to their transverse momentum such that the association to TOF clusters starts with high- p_T tracks. In a first matching round, all tracks are extrapolated through TOF and are linked to a time signal if the read-out pad they traverse fired. In a second round, tracks are assigned the closest TOF pulse within a radius of 3 cm.⁵ Fig. 4.3 shows the fraction of mismatched TOF hits for protons as obtained with a simulation [271]. It can be seen that the contamination from tracks which did not create a TOF signal reaches a quite high level of more than 80% at $p \lesssim 0.4\text{ GeV}/c$. This impurity drops to a moderate 25% for $p > 0.75\text{ GeV}/c$ and further decreases for higher momenta. Additionally, the constant effort by the collaboration to improve the data quality resulted in a much better situation regarding the mismatch for the Pb-Pb data taken during Run 1: the mismatch could be reduced to around 6.5% for tracks with $p > 1\text{ GeV}/c$ [216]. We will see in Section 5.2 how even this lower mismatch can be further suppressed by applying surprisingly simple selection criteria.

A local estimate of the track parameters as provided by the Kalman filter becomes critical when physics processes like multiple scattering happen. Such an energy loss correlates the measurements, which in a global fit approach would lead to matrices as large as $n \times n$, where n is the number of measurements. With up to 159 clusters in the ALICE TPC alone, this becomes computationally too expensive. Based on the local estimate, the Kalman filter also allows to reject a cluster that was previously associated to the track via the method of roads. The inward fit where the track parameters are finally determined concludes the tracking in the third step. Local snapshots of the track parameters are stored in the Event Summary Data (ESD) track class. This comes in handy when the energy loss in the time projection chamber is exploited for PID for which the local velocity of the particle in the TPC is the determining factor. This velocity certainly differs from the speed at the primary vertex as a significant amount of material in which the particle will loose energy was placed in between these two

⁵The value is 3 cm for the Pb-Pb data reconstruction only. In the low multiplicity environment of pp collisions, a looser restriction of 6 cm can be applied.

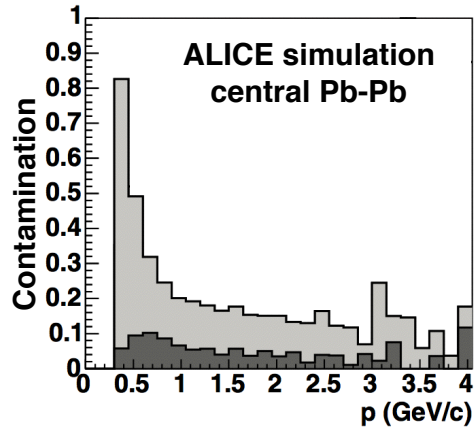


Figure 4.3: Contamination of a proton sample with wrongly associated TOF hits. The dark and light-shaded histograms show the contamination from tracks which did and did not create a TOF signal, respectively. Taken from [271]. Cf. [216] for a more recent study without differential values given.

locations. Also available is a series of parameters where information from the TPC but not from the ITS was used in the fit process; we will discuss the usage of such a set in Chapter 5. In total, each track has five sets of track parameters. These are

1. the global track parameters, to which generally all detectors contribute,
2. global constrained parameters, where the global parameters were updated with the additional measurement of the primary vertex,
3. parameters at the inner wall of the TPC, which are essential for TPC PID purposes,
4. TPC-only parameters, with only the TPC contributing to the measurement, and
5. parameters at the outermost reconstructed cluster of the track.

During the different reconstruction steps, bits are set to be able to, e. g., only select tracks where the refit was successful. Fig. 4.4 illustrates the three tracking phases in ALICE and the associated flags of the tracks.

4.3 V^0 Selection

In ALICE, the uncharged lambda particle can only be reconstructed indirectly via its charged decay $\Lambda \rightarrow p\pi^-$, and similarly $\bar{\Lambda} \rightarrow \bar{p}\pi^+$. This weak process, with a $c\tau(\Lambda) = 7.89$ cm, leaves a distinct V^0 topology in the charged particle detectors, alike to the decay of the K_s^0 in a pair of oppositely charged pions. Two algorithms exist in ALICE to find these electrically neutral

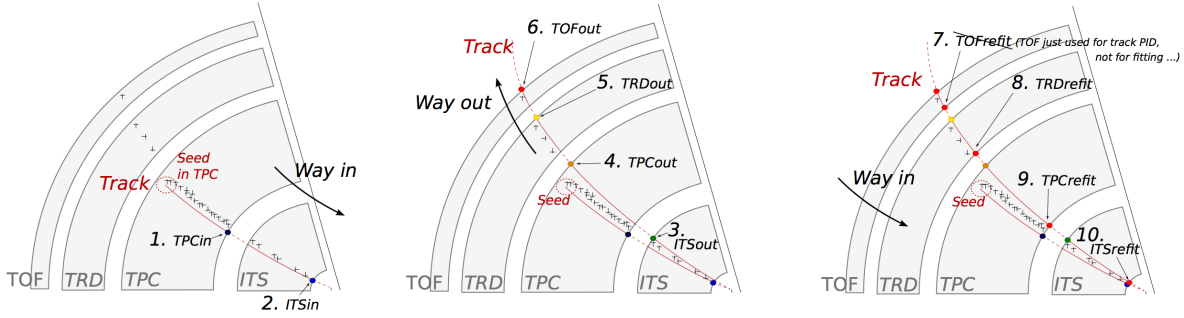


Figure 4.4: Bits set during the reconstruction which — as described in the text in detail — starts with seeds at the outer TPC, propagates the track inwards, subsequently outwards and finally refits the track. The `kDETin`, `kDETout` and `kDETrefit` bits — where `DET` should be replaced with the appropriate detector acronym — are set if the detector’s hits are used in the track propagation in the inward, outward or refit step, respectively. Taken from [272].

carriers of strangeness: the offline and the on-the-fly finder. The offline finder is described here; the slightly more complicated on-the-fly finder is discussed in Section D.2.

The offline finder runs after the charged particle tracking has succeeded. The code itself can (currently) be found in `$ALICE_ROOT/STEER/ESD/ALiV0vertexer.cxx`. The V^0 s are constructed from the tracks which pass the final refit inwards step of the global tracking. Mostly due to the magnetic field and the finite decay length, the products generally do not point back to the primary vertex; see Fig. 4.5, also for the following discussed selection criteria. To reduce the computational effort for the subsequent pairing step, tracks with a small impact parameter (b^+ and b^- in the figure) are discarded from further consideration. The rejection criteria at this stage are very loose in order to not discard any vertices that are useful for a physics analysis. The standard value together with the stricter version for Pb-Pb data taking of the impact parameter cut (and the further selections) can be found in Table 4.1. From the reduced sample, all oppositely charged tracks are paired. For each combination, they are propagated to the point of their mutual closest approach. The chosen criterion is d :

$$d^2 = \frac{(\Delta x)^2}{\sigma_y^2} + \frac{(\Delta y)^2}{\sigma_y^2} + \frac{(\Delta z)^2}{\sigma_z^2}, \quad (4.3)$$

$$\sigma_y^2 = \sigma_{y,1}^2 + \sigma_{y,2}^2, \quad (4.4)$$

$$\sigma_z^2 = \sigma_{z,1}^2 + \sigma_{z,2}^2, \quad (4.5)$$

which is minimized in a parabolic iteration. Here, $\sigma_{y,1}^2$ and $\sigma_{y,2}^2$ are the squared uncertainties of the position in the y direction in the local coordinate system of the first and second track, respectively; analogously the same holds for the longitudinal component. Note that no uncertainty exists in the direction of propagation, therefore the uncertainty in y direction, σ_y ,

also appears in the term proportional to Δx . Neglecting any track parameter correlation, the squared uncertainties are approximated by the diagonal elements of the full covariance matrix. If the track's weighted distance of closest approach $\sqrt{d^2 \sqrt{\sigma_y^2 \sigma_z^2}}$, which corresponds to a naïve distance in the case of $\sigma_y = \sigma_z$, is smaller than the maximally allowed value, it is checked whether the vertex lies in a fiducial volume (represented by the long-dashed lines in Fig. 4.5). The fiducial volume cut is introduced as most of the background still originates from primary particles making up random combinations with other tracks. This combinatorial contribution is suppressed if a minimum transverse distance of the secondary vertex from the primary vertex is required. Furthermore, a maximal transverse distance ensures a good quality of the tracks. The three-momentum of the V^0 candidate \vec{p} is calculated from the daughter tracks, its angle θ with the vector connecting the decay vertex with the primary vertex \vec{r} is called the pointing angle and provides an estimate whether the V^0 was a well reconstructed primary particle. The condition $\cos(\theta) > 0.9$, corresponding to an angle θ smaller than 25° , is a good compromise of rejecting fake V^0 and keeping secondary particles like Λ from Ξ decays. References to the daughter tracks are stored. To indicate the reconstruction by the offline finder, a boolean is set and the V^0 is written as a `AliESDv0` to the event.

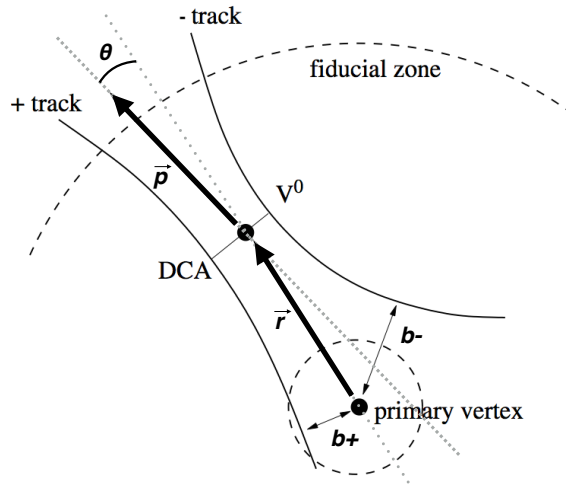


Figure 4.5: V^0 decay topology in the transverse plane and selection criteria for the offline V^0 finder. For details see text. Based on [271].

4.4 Clustering in the Calorimeters

One tower or cell in the EMCal extends over $6\text{ cm} \times 6\text{ cm}$. The transverse extent of an electromagnetic shower is characterized by the Moliere radius, within which 90% of the energy is deposited. For the material used in the EMCal, the Moliere radius amounts to 3.2 cm [273].

Cut variable	Cut value
Min. track impact parameter	0.05 cm
Max. weighted DCA daughters	1.5 cm
Min. cosine of V0 pointing angle	0.9
Min. fiducial radius	0.2 cm
Max. fiducial radius	200 cm

Table 4.1: Selection criteria with cut values of the offline V0 finder.

This implies that an electromagnetic shower will typically spread over a few adjacent towers and clustering, i. e. combining the energy over several cells, becomes necessary. Multiple algorithms exist to perform this task, two of which are illustrated in Fig. 4.6. The baseline procedure, called V1 and depicted on the left of Fig. 4.6, starts from a seed, i. e. a cell in which the energy exceeds an energy E_{seed} , and simply adds neighboring cells with energies above noise levels. A downside of this V1 algorithm is that two hits from close particles get merged into one cluster. Such a merging occurs for π^0 with $p_T > 6.0$ GeV/ c [216] and generally in the high-density environment of Pb-Pb collisions. Other algorithms avoid such a merging. One of them, named V2 and depicted on the right of Fig. 4.6, stops adding cells to a cluster when the energy of the next cell is larger than the current one. The V2 clusterizer is the standard algorithm for clusterization in the ALICE EMcal and was used within this thesis.

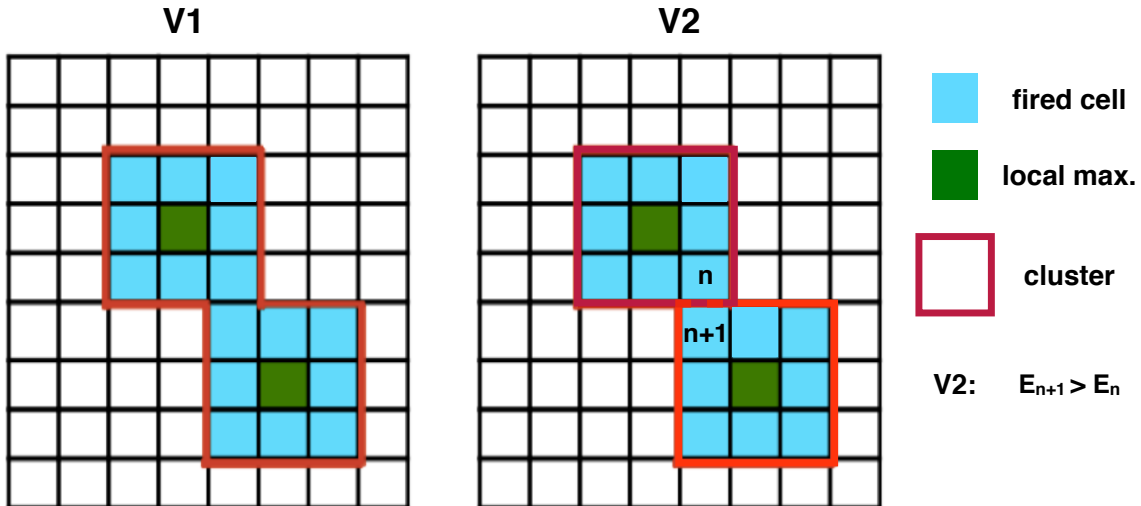


Figure 4.6: Illustration for two algorithms to group cells into a cluster; V1 on the left and V2 on the right. Taken from [274].

4.5 AOD Filtering

Reconstructing the raw detector signals as Event Summary Data (ESD), during which mainly the reduction from detector hits to tracks occurs, decreases the size already considerably from 11 380 kB/event for raw data by almost a factor of ten to 1710 kB/event in the ESDs. Following this strategy and further restricting the written information to the one needed for analysis results in the analysis oriented data (AOD). Here, another reduction in disc space by a factor of five to 365 kB/event could be achieved [275]. The AOD filtering also allows to execute minor calibration tasks and common, basic analysis steps. The employed filtering procedure from the ESDs to the AODs is allowed to change and each modification in the method results in a different AOD specifier, typically an increasing integer. In this analysis, the AOD 115 of the LHC 11h data taking period in the second reconstruction pass are used. The filtering macros are kept in a common place on alien, for this case in `/alice/cern.ch/user/a/alidaq/AOD/AOD115/`. The `.jdl` file in this folder specifies that AliRoot v5-02-Rev-31 was used. Keeping track of the software revision is beneficial, as the algorithms are continuously developed.

4.5.1 Filtering Tracks

In the AODs the concept of several sets of parameters within one track structure — as it exists in the ESDs — is given up and tracks are duplicated when a new set of parameters is stored. Duplicate tracks are assigned a negative unique identifier: $ID' = -ID - 1$. Only tracks that fulfill certain minimal criteria are written to the AOD files. For each fulfilled criterion, a filter bit is set. A twiki⁶ nicely documents all applied selections. The requirements for the most commonly used filter bits are summarized in Table 4.2 and 4.3. For the seventh bit — TPC-only tracks constrained to the primary vertex —, first a good quality of the track in the TPC is asked for by selecting only tracks with at least 50 clusters in the TPC and requiring a maximum $\chi^2/\text{n.d.f.}$ of two.⁷ Furthermore, a loose picking of primary tracks is done by rejecting daughter tracks of kink-topology vertices and applying a two-dimensional selection on the DCA to the primary vertex with the long (short) axis of the ellipse being 3.2 cm (2.4 cm) in the longitudinal (transverse) direction. Then the TPC-only parameters of the ESDs are constrained to the global primary vertex measurement. Within the Kalman tracking approach, this reduces to providing the primary vertex position as an additional measured point for the track. With the decomposition of the spread of the primary vertex position into the width of the luminous region σ_D and the resolution of the vertexing algorithm given in Fig. 3.3 (right), one arrives at a uncertainty of the primary vertex position of less than $2\ \mu\text{m}$ at a $\langle dN/d\eta \rangle$ of 1584 [98] for central Pb-Pb collisions. This is small compared to effective cluster resolution

⁶See <https://twiki.cern.ch/twiki/bin/viewauth/ALICE/PWGPPAODTrackCuts>.

⁷A $\chi^2/\text{n.d.f.}$ of two corresponds to a χ^2 per TPC cluster of four, as each TPC cluster has two degrees of freedom.

of the TPC which can be approximated as $\sigma_{C1}/N_{C1} \approx 80 \mu\text{m}$, where $\sigma_{C1} \approx 0.1 \text{ cm}$ is the single cluster resolution [276] and $N_{C1} = 159$ is the number of clusters. Therefore, constraining the tracks has a significant impact on the track parameters, as we will see in Section 5.2.

Name	Description	Comprehensive Requirements
Standard TPC cuts	Assure good track quality in the TPC.	SetMinNClustersTPC(50) SetMaxChi2PerClusterTPC(4) SetAcceptKinkDaughters(kFALSE) SetMaxDCAToVertexZ(3.2) SetMaxDCAToVertexXY(2.4) SetDCAToVertex2D(kTRUE)
Common ITS + TPC cuts	Certify track reconstruction by the TPC and ITS	SetMaxChi2PerClusterTPC(4) SetMinNCrossedRowsTPC(70) SetMinRatioCrossedRowsOverFindableClustersTPC(0.8) SetAcceptKinkDaughters(kFALSE) SetRequireTPCRefit(kTRUE) SetRequireITSRefit(kTRUE) SetMaxChi2TPCConstrainedGlobal(36) SetMaxDCAToVertexZ(2) SetDCAToVertex2D(kFALSE) SetMaxChi2PerClusterITS(36)

Table 4.2: Common cuts used in the AOD filtering process, see Table 4.3.

4.5.2 Filtering V^0

Similarly, the V^0 sample is reduced in the ESD to AOD filtering procedure by applying some loose selection criteria. The same criteria currently are applied to V^0 vertices from both, the offline and on-the-fly, V^0 finder. The cuts were chosen according to a study of offline V^0 vertices. However, an analysis of V^0 vertices from ESDs for the Pb-Pb data of the year 2010 performed within this thesis showed that for the on-the-fly V^0 finder some applied selections are too strict while others could be tighter. The best values alongside the used quantities are documented in Table 4.4. The used cuts result in signal loss and increased data volumes by unnecessarily written background. These findings are visually supported by distributions from a toy model together with the best and used selection criteria in Fig. 4.7. The on-the-fly V^0 finder exhibits an improved resolution with respect to the offline finder. This allows for a more stringent handling of vertices, namely a) the selection of true V^0 and b) the rejection of fake background vertices. Case a) is depicted on the left of Fig. 4.7, where the DCA of the two daughters is shown for a peaked signal (representing the on-the-fly finder) in blue, a smeared

Filter Bit	Description	Comprehensive Requirements
Bit 0 (001)	Global tracks	Standard TPC cuts
Bit 1 (002)	ITS stand-alone tracks	SetRequireITSSstandAlone(kTRUE)
Bit 2 (004)	Global tracks with SPD hit	Bit 0 SetClusterRequirementITS(AliESDtrackCuts::kSPD, AliESDtrackCuts::kAny)
Bit 3 (008)	Global tracks with SPD hit and Electron PID	Bit 2 SetTPCnSigmaCut(AliPID::kElectron, 3.5)
Bit 4 (016)	ITS + TPC tracks with SPD hit and loose DCA selection	Common ITS + TPC cuts SetClusterRequirementITS(AliESDtrackCuts::kSPD, AliESDtrackCuts::kAny) SetMaxDCAToVertexXY(2.4) SetMaxDCAToVertexZ(3.2) SetDCAToVertex2D(kTRUE)
Bit 5 (032)	ITS + TPC tracks with tight DCA selection and SPD hit	Common ITS + TPC cuts SetMaxDCAToVertexXYPtDep("0.0105+0.0350/pt^1.1") SetClusterRequirementITS(AliESDtrackCuts::kSPD, AliESDtrackCuts::kAny)
Bit 6 (064)	ITS + TPC tracks with tight DCA selection, no hit on SPD and hit on first SDD layer	Common ITS + TPC cuts SetMaxDCAToVertexXYPtDep("0.0105+0.0350/pt^1.1") SetClusterRequirementITS(AliESDtrackCuts::kSPD, AliESDtrackCuts::kNone) SetClusterRequirementITS(AliESDtrackCuts::kSDD, AliESDtrackCuts::kFirst)
Bit 7 (128)	TPC-only tracks constrained to primary vertex	Standard TPC cuts

Table 4.3: Incomplete list of filter bits in AOD 115 (bit 8–10 missing) with their requirements. See Table 4.2 for the commonly used cuts.

signal (symbolizing the offline finder) in cyan and a flat background in red. As shown, the used cut of 1.5 cm (dotted line) might be appropriate for the offline finder, yet the augmented performance of the on-the-fly algorithm would allow for a cut as strict as 0.2 cm (dashed line). The consequence in this case is not dramatic, as the used cut still keeps all the on-the-fly signal and the only negative impact is an increased size of the AODs as unnecessarily background is

stored. The more unpleasant case b) is depicted on the right of Fig. 4.7, where the DCA of the (anti-)proton daughter to the primary vertex is shown. A flat signal is drawn in blue; a peaked background, reflecting the superior resolution of the on-the-fly reconstruction, is displayed in red; a smeared background for the offline version is sketched in orange. It is clear that — for the scenario with the inferior resolving power — the used cut of 0.05 cm nicely rejects the region, where the background is dominant. It also appears that this used cut avoidably excludes a region where the signal presides over the peaked background and valuable statistics are lost. The author of this thesis tried to change the filtering procedure in May 2012 but got stuck due to the missing feed-back of other V^0 analyses. Mentioning the issue here should be seen as another call for action with the benefit of improved statistics for V^0 analyses.

Cut variable	Applied cut 10h&11h	Best cut 10h
Minimum V^0 radius	0.2 cm	n/a
Maximum V^0 radius	200 cm	not studied
Min. DCA (anti-)proton daughter	0.05 cm	0.02 cm
Min. DCA pion daughter	0.05 cm	0.05 cm
Max. DCA V^0 daughters	1.5 cm	0.2 cm
Min. $\cos(\theta)$	0.99	0.9999

Table 4.4: Selection criteria on V^0 as applied in the AOD filtering for the 2010 (10h) and 2011 (11h) Pb-Pb data and the best criteria for the on-the-fly finder for 10h from an ESD study. For the 10h dataset, a cut on the minimum radius of the the on-the-fly V^0 of 0.5 cm was already applied on the reconstruction level.

4.5.3 Creating Photon Conversion Candidates

An example for a basic analysis step in the AOD filtering is the creation of photon candidates from conversions into e^+e^- pairs that are then commonly used in ALICE. The individual selection criteria in the photon conversion method framework are steered via a string⁸. Each character in the string stands for a specific criterion and the value of the digit determines the cut value. This allows to adjust the framework to the particular conditions of, e. g., the different collision systems. In the following the applied filtering for the AOD 115 used in this analysis is discussed.

For events with a longitudinal position of the vertex $|z_{\text{vtx}}| < 10$ cm, the V^0 candidates of the on-the-fly finder are inspected. The on-the-fly finder exhibits a higher efficiency and better momentum resolution for reconstructing photons when compared to the offline finder [277].

⁸For the AOD 115 filtering this string is “900177009350113211200001000000000”.

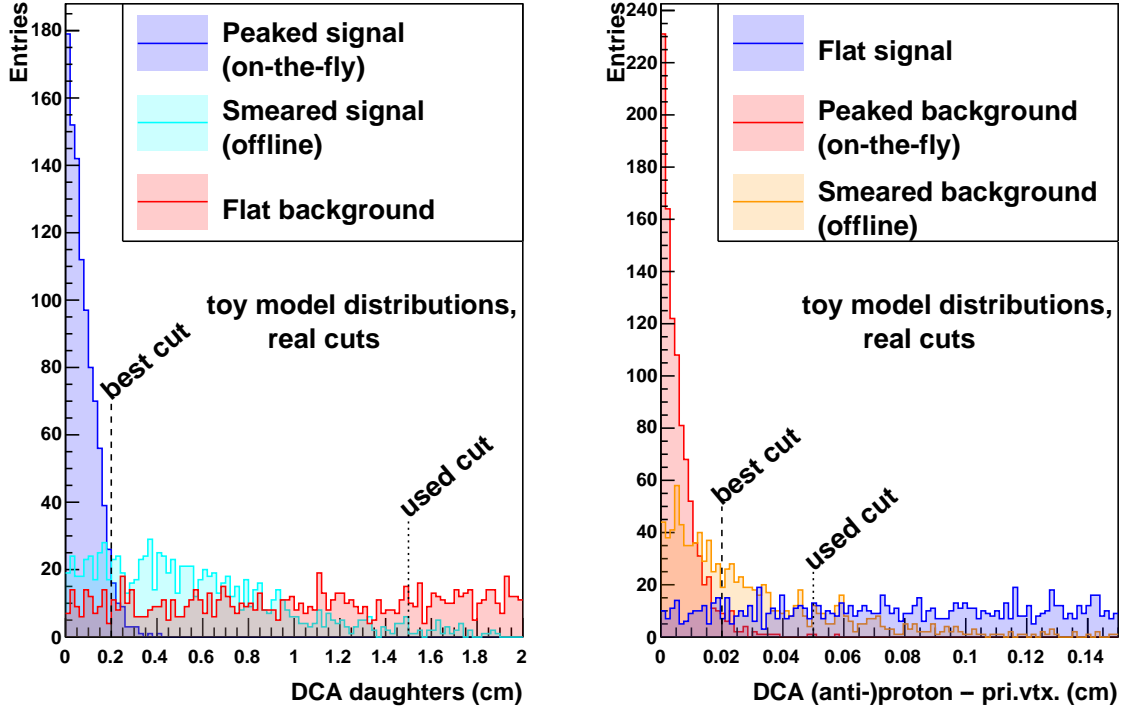


Figure 4.7: Resolution effects on cuts for signal selection (left) and background rejection (right). See text.

Both daughter tracks are required to fall into a pseudorapidity window of $|\eta| < 0.8$. For larger pseudorapidities, the distribution of detector material is known to not be perfectly described in the Geant detector model. Intrinsicly, this has a larger impact on the simulations of photon conversions, which result from an interaction with the material, than hadrons. A continuous effort is made to improve this by, e. g., accounting for detector support like cooling, gas and low and high voltage. For the time being, it is safer to exclude large pseudorapidities in order to ensure a good correspondance of the Monte Carlo to the data taken. A minimum p_T of 50 MeV/c for both daughters is mandatory; tracks with a kink topology are rejected; and the TPC refit bit — which can be acquired in the third pass of the tracking, see Section 4.2 — is asked for. The PID capabilities of ALICE allow to suppress the vast hadronic background by a $\pm 5\sigma$ inclusion around the expected dE/dx from a Bethe-Bloch parametrization for electrons. Between $0.4 < p$ (GeV/c) < 5.0 , also all particles which fall below a 3.5σ deviation in the positive direction of the expected dE/dx value for pions are rejected. For all remaining vertices, a Kalman package for V^0 reconstruction [278] is invoked. It puts a hard constraint of zero mass and obliges the photon candidate to stem from the primary vertex. The Kalman package incorporates the restrictions into a χ^2 per number of degrees of freedom measure. Candidates which exceed the value of 100 in this observable are discarded. The zero mass of the photon

furthermore implies that the two helix approximations of the decay daughters ideally intersect in one point in the transverse (R, φ) plane with the daughter momenta parallelly aligned. This allows to recalculate the decay vertex position as described in [279] — improving the secondary vertex resolution [280].

A powerful tool for studying V^0 particles is the Armenteros-Podolanski plot [281]. Fig. 4.8 (left) shows a typical example in ALICE. The Armenteros-Podolanski plot shows the momentum of one decay daughter transverse to the V^0 flight direction $p_T^{\text{Arm.}}$ vs. the asymmetry α of the decay

$$p_T^{\text{Arm.}} = |\vec{p}^+| \sin(\vartheta^+) = |\vec{p}^-| \sin(\vartheta^-), \quad (4.6)$$

$$\alpha = \frac{p_{\parallel}^+ - p_{\parallel}^-}{p_{\parallel}^+ + p_{\parallel}^-}, \quad (4.7)$$

where \vec{p}^+ (\vec{p}^-) is the three-momentum of the positive (negative) daughter, ϑ^+ (ϑ^-) is the angle of the momentum of the positive (negative) daughter and the momentum of the V^0 , and p_{\parallel}^+ and p_{\parallel}^- are the momenta of the daughters parallel to the flight direction of the V^0 . The strength of an Armenteros-Podolanski plot is that the different species can be spotted immediately and picking specific particles is straightforward: a selection of $p_T^{\text{Arm.}} < 0.1 \text{ GeV}/c$ allows to reject non-photons. The cut is especially effective against a contamination from K_s^0 with their relatively high momentum released in the decay of $206 \text{ MeV}/c$. This is demonstrated in Fig. 4.8 (right) where it can be seen that the distribution of the Armenteros transverse momentum $p_T^{\text{Arm.}}$ is very peaked at the maximal possible value and rejecting V^0 particles with a $p_T^{\text{Arm.}}$ above a certain threshold effectively reduces the contamination from V^0 with a large momentum release during their decay like K_s^0 .

Fig. 4.9 (left) shows the transverse spatial distribution of photon decay vertices in pp collisions from 2010 together with a Monte Carlo simulation. It can be seen from the figure, that the number of conversions approaches zero for $R \rightarrow 180 \text{ cm}$. Removing vertices with $R > 180 \text{ cm}$ ensures a good leverage arm of the TPC for the decay leptons. Also requiring a minimum R of 5 cm further reduces the contamination from K_s^0 ($c\tau = 2.68 \text{ cm}$) and Λ ($c\tau = 7.68 \text{ cm}$) and combinatorial background while — as can be seen from Fig. 4.9 (left) — rejecting only a small fraction of photons.

With the improved constraints, the spatial vertex position is (re-)checked to fall into a volume analogous to the aforementioned pseudorapidity window. A minimum of 60% of reconstructed over findable clusters for both daughters starting from the photon conversion vertex radially outwards certifies a good resolution and a cut on the Ψ_{pair} further selects conversions. Ψ_{pair} describes the angle between the plane formed by the two daughter tracks and the magnetic field. As no momentum is released in the photon conversion, the decay plane is always normal to the magnetic field — in contrast to other two-particle sources — as visualized in Fig. 4.9.

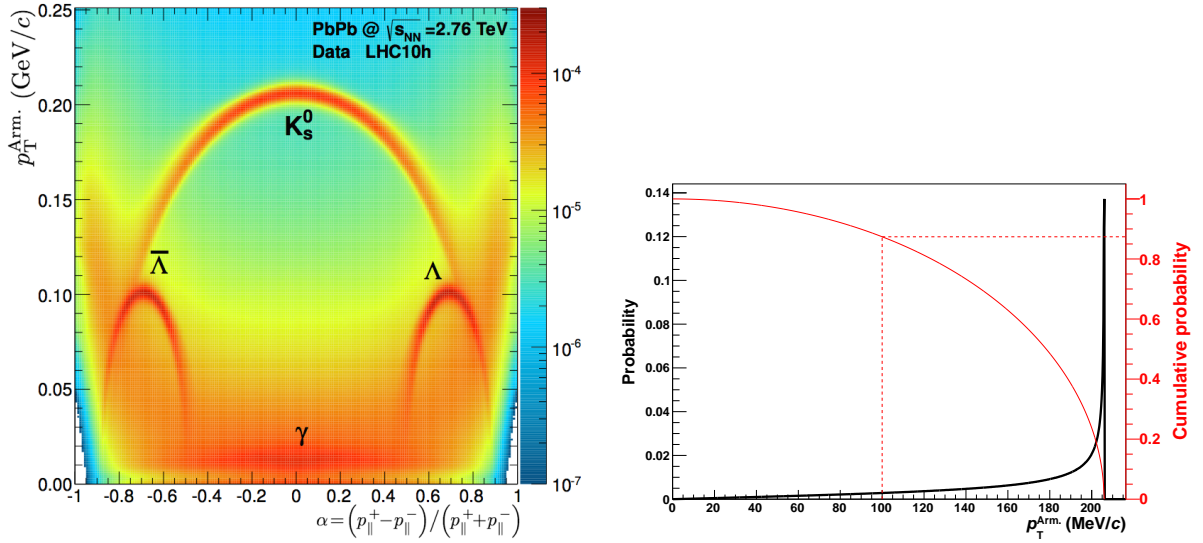


Figure 4.8: Left: A typical Armenteros-Podolanski plot of V^0 particles in ALICE for Pb-Pb collisions. Taken from [282]. Right: Probability distribution of the Armenteros transverse momentum $p_T^{\text{Arm.}}$ for a K_s^0 decay into two charged pions in black. One sees that the $p_T^{\text{Arm.}}$ distribution peaks at the maximal possible $p_T^{\text{Arm.}}$ of 206 MeV/c. Apart from the position of the maximum, the shape of the distribution is fully given by the projection of the three-dimensional shell of the daughter momenta in the decay rest frame onto $p_T^{\text{Arm.}}$. Cumulative probability distribution in red. A selection on $p_T^{\text{Arm.}} < 100$ MeV/c rejects about 90% of all K_s^0 .

Finally, only candidates whose pointing angle (see Section 4.3) fulfills the condition $\cos(\theta) > \pi$ are written as `AliAODConversionPhoton` to the delta AOD file `AliAODGammaConversion.root`. The stored photon candidates have a decent purity and good quality, so that a basic analysis can immediately follow without further restrictions on the sample; the imposed criteria are loose enough to accommodate the needs of any general photon analysis.

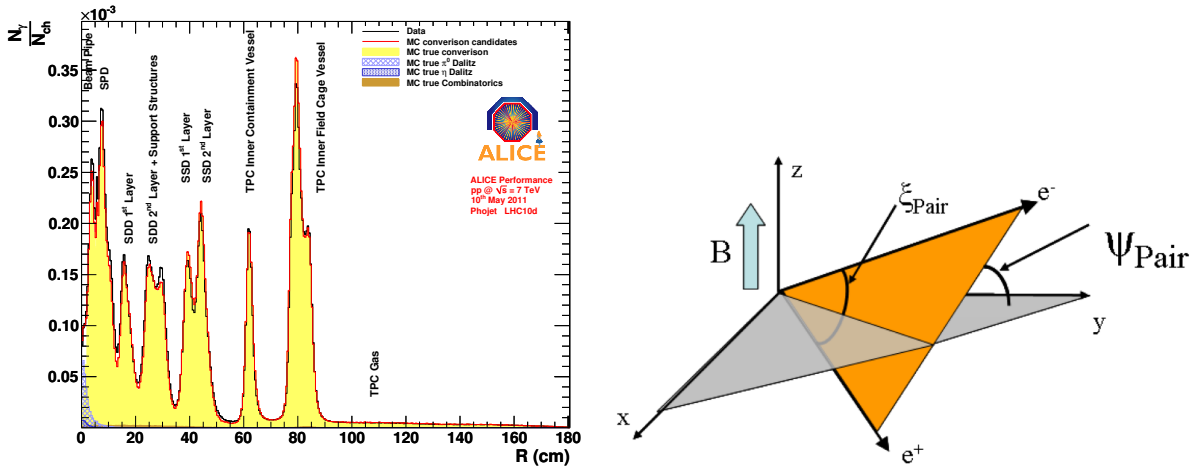


Figure 4.9: Left: Transverse radius R distribution of photon decay vertices in data compared to a simulation with the Monte Carlo generator PHOJET [283, 284]. The Monte Carlo allows for the separation of the different photon sources. Right: Visualization of the angle Ψ_{pair} which is formed by the plane perpendicular to the magnetic field and the one formed by the two daughter tracks. Taken from [285].

Chapter 5

p Λ Data Analysis: Event and Single-Particle Selection

5.1 Event Characteristics

Within this thesis, the second reconstruction pass of the 2011 Pb-Pb data, denoted by ALICE internally as ‘LHC11h’, are analyzed. Unless explicitly stated otherwise, all distributions are obtained with the AOD 115 dataset.

The Run Condition Table (RCT)¹ easily lets the user select proper runs by choosing a good global quality.² Restricting the analysis to events with the longitudinal position of the primary vertex $|z_{\text{vtx}}| < 10$ cm ensures a uniform acceptance in pseudorapidity. Events are grouped according to their centrality; the standard estimator V0M (see Section 4.1) is used for this. The common centrality framework also flags events which show an abnormal correlation between different centrality estimators. Although the centrality framework was asked to reject outliers in, e. g., the correlation of the TRK and the V0M estimator by accepting only events with the quality flag of the centrality task equal to zero³, it appears from Fig. 4.1 (left) that this tagging should be re-checked within the centrality framework. Nevertheless, the agreement between different centrality estimators is good, as previously stated in Section 4.1.

¹See <http://alimonitor.cern.ch/configuration/>.

²In the RCT, a good quality is represented by the value one.

³See <https://twiki.cern.ch/twiki/bin/viewauth/ALICE/CentStudies>.

5.2 Primary Proton Identification

5.2.1 Assuring Good Tracking

The ALICE reconstruction code allows cluster sharing. It was quickly seen in the first Pb-Pb data that two close tracks can get assigned the same cluster in the ITS and an artificial bias on the two-track momentum difference is introduced [286]. This leads to the creation of fake, yet similar track parameters and is confirmed within this thesis as demonstrated in Fig. 5.1, where the angular distance (calculated as the squared mean of the azimuthal and polar angle) between two tracks using only the TPC (y axis) versus the angular distance of the same two tracks using their global parameters (x axis) is shown for real (left panel) and mixed (right panel) events. In the AODs, no set of track properties with only the TPC contributing and without a vertex constraint are available. Therefore, this correlation was obtained from the ESD tracks using their TPC-only parametrization (see Section 4.2). The right panel with the mixed events exhibits the expected behavior of a diagonal, one-to-one correlation with a finite resolution. However, the real events in the left panel show an additional excess for small angular distances in the global (ITS+TPC) tracking scheme, indicated by the black ellipse. To circumvent this two-particle detector effect, the current ALICE strategy for particle correlations at small relative momenta in the high-multiplicity Pb-Pb environment is to avoid the global (ITS+TPC) tracking for the momentum determination [287].

The left panel of Fig. 5.2 shows that the vast improvement of the momentum resolution gained by incorporating the ITS in the Kalman filtering process — when compared to a TPC-only determination — can be recovered to a large extent by constraining the tracks to the primary vertex. Such a set of track parameters is conveniently available in the AODs with the filter bit $1 \ll 7 = 128$, where \ll is the bit shift operator. The momentum, as obtained with the filter bit 128 procedure, fulfills both main requirements by this analysis on the tracking scheme to obtain good resolution and no two-track bias. Thus, it was chosen here for the primary proton sample.

In order to not duplicate information and to save disc space, the PID information is not stored for the TPC-only tracks. This makes it mandatory to find the corresponding global track for a given TPC-only track; the two are related by their unique identifier (see Section 4.5). A simple search implemented as a loop over all tracks until the unique identifier matches works, but embeds another particle loop for each particle that is analyzed and hence is highly CPU expensive in the high-multiplicity environment in Pb-Pb collisions at the LHC. A smarter solution is the usage of an identifier map that was chosen for this work. The identifier map is an array of pointers to the tracks. At the beginning of each event, this array is reset and then each pointer to a global track is stored at the array position of the track's unique identifier. This reduces the problem of retrieving the global track for all TPC-only tracks of an event from

$\mathcal{O}(N \times N)$ to $\mathcal{O}(2N)$, where N typically is 10 000.

When creating the identifier map, it is apparent that more than one global track with the same unique identifier exists. Usually, only one of these tracks has a filter bit set and a non-empty TPC fit map⁴ from which the number of TPC clusters is obtained. The other track did not acquire the TPC refit bit in the third reconstruction step and can, e.g., stem from the on-the-fly V^0 finder. The problem was followed up⁵. In the future, there will still be more than one global track for a given unique identifier, but at least all will have the TPC fit map properly filled. The fix requires another reconstruction from raw data. For the time being, a practical solution for the identifier map is to not overwrite already existing pointers with tracks that show no TPC clusters.

A document by the TPC group experts [288] gives the recommendation to remove fake tracks by requiring a minimum number of crossed rows and a minimum ratio of the number of crossed rows over findable clusters in the TPC. The same document also provides an explanation of the used quantities and defines a findable cluster as a space-point which can be geometrically assigned to the track by taking into account boundaries between the chambers and the limited coverage in pseudorapidity. The number of crossed rows n_{eff} quantifies the leverage arm — which is decisive for the p_T resolution — as $n_{\text{eff}} = n_{\text{cl}} + n_{\text{miss}}$. Here, n_{cl} is the number of TPC clusters and n_{miss} is the number of missing clusters. A cluster is counted as missing, if the track has an associated space-point on any of the total four (two outwards and two inwards) neighboring pad-rows. The standard cut values within ALICE for the two selections are 70 crossed rows and 0.8 for the ratio of crossed rows over findable clusters, as can be checked in the `AliESDtrackCuts.cxx`. These standard selections were also taken for this analysis.

Shared TPC clusters have the same potential impact on a two-particle observable as the bias from cluster sharing in the ITS, which was discussed at the beginning of this section. Part of the problem is that two tracks from different events can not share clusters. As we will use the event mixing technique (see Appendix 6), special care must be taken so that the mixed events can accurately separate the unique two-particle correlation from the shape of the two-particle momentum-difference distribution introduced by phase-space. Based on these considerations, it is beneficial to reject tracks that have shared clusters. The right panel of Fig. 5.2 shows the differential (cumulative) distribution of the number of clusters for each track in black (red). One sees from the black differential distribution, that the majority of tracks have zero shared clusters; however the details of the distribution are hidden in this depiction. A better representation is given by the cumulative distribution, which easily quantifies that about 95% of the tracks are not sharing any detector signal. It was consequently decided to reject tracks with shared clusters.

⁴The TPC fit map consists of 159 bits. The bit at position i should be `true`, if the track has a cluster on pad row i which was used in the determination of the track's momentum in the reconstruction. Otherwise the bit should be `false`.

⁵See <http://savannah.cern.ch/bugs/?97544>.

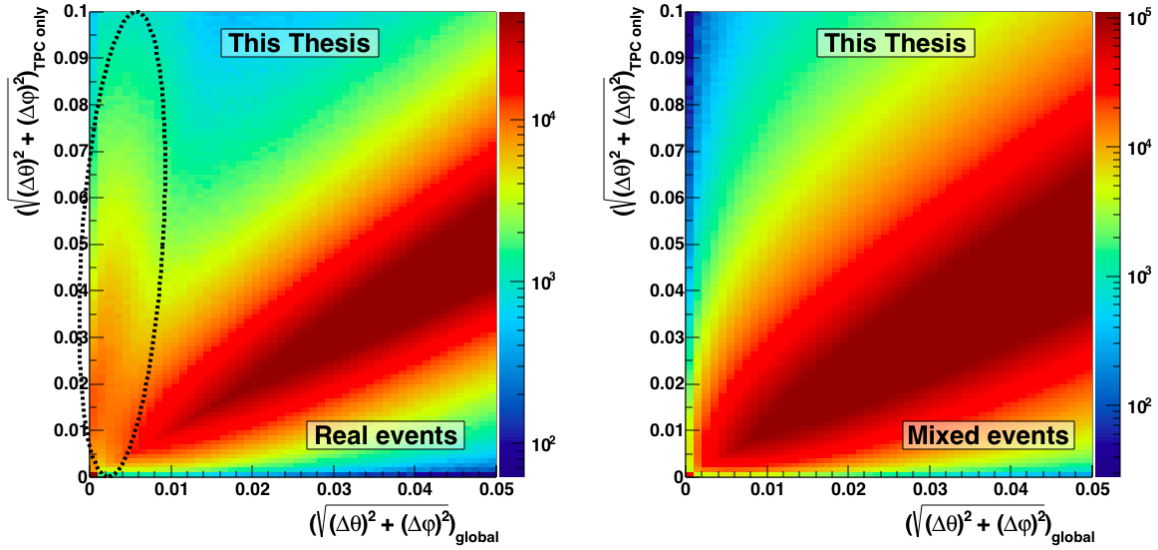


Figure 5.1: Bias from wrongly associated SPD clusters. See text.

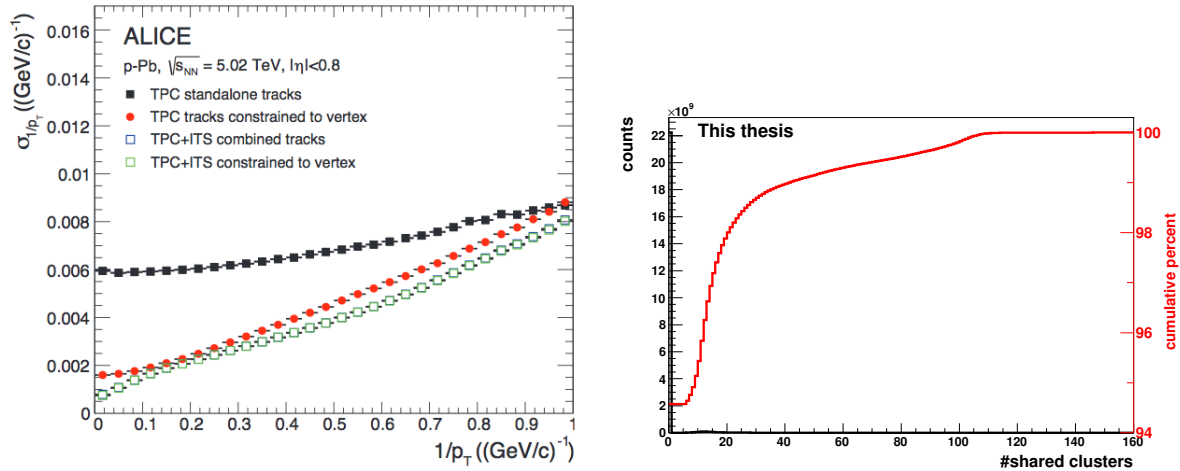


Figure 5.2: Left: Momentum resolution for four different track classes. Taken from [216]. Right: Number of shared TPC clusters of each track; differential distribution in black. The differential distribution does not allow to visually gauge the impact of a selection on the number of shared clusters. Therefore, also the cumulative distribution is shown in red, which readily represents the features of the data.

5.2.2 Proton PID at Low Momentum

As thoroughly discussed in Appendix 3, various detectors of ALICE offer PID capabilities. The performance of the different techniques highly depends on the momentum of the particles due to the underlying exploited physics processes. Ergo, momentum-specific selection procedures were applied in this analysis.

The specific energy loss of the particles in the ALICE TPC provides good identification capabilities, especially for low momentum in the $1/\beta^2$ region (see Section 3.3). For the calculation of the dE/dx , detector hits shared between tracks are not used; it was also found that instead of taking the total charge of a cluster, it is beneficial to employ the amplitude at the local maximum of the cluster charge, which is less sensitive to overlapping clusters in the high-multiplicity environment of Pb-Pb collisions at the LHC [271]. For the description of the specific energy loss in the ALICE TPC, it is useful to replace the Bethe-Bloch formula (Eq. 3.1) by a parametrization. Doing so, one substitutes, e. g., the mean excitation energy of the medium with a fit parameter. This has the advantage, that a detailed, a priori knowledge of the medium is not necessary. Many effects, like the stronger binding of electrons in a molecule when compared to the binding in a single atom, make it anyway necessary to determine the coefficients of the Bethe-Bloch equation for the specific medium. Or as the authors of [289] put it: ‘Neither the theory of Bethe, Bloch, and Sternheimer nor the model of Allison and Cobb offer a closed mathematical form⁶.’ The ALEPH parametrization [289]

$$f(\beta, \gamma) = \frac{P_1}{\beta^{P_4}} \left(P_2 - \beta^{P_4} - \ln\left(P_3 + \frac{1}{(\beta\gamma)^{P_5}}\right) \right) \quad (5.1)$$

provides a good description of the ionizing power of particles in a medium with five parameters that are determined by fits to the energy-loss spectra. Fig. 5.3 (left) shows such a parametrization representing the energy loss of electrons, pions, kaons, and protons in the ALICE TPC for central Pb-Pb collisions in blue, gold, green, and red, respectively. Together with the mean value as a solid line, one and three sigma bands for a realistic resolution of 6% (cf. [216]) are shown as dashed and dotted lines. It is apparent that below a momentum of 0.75 GeV/ c , the proton line is separated by more than two times three sigma from any other species. In the region $0.75 < p$ (GeV/ c) < 1.0 , the proton band overlaps with the electrons, but is however isolated — again by at least two times three sigma — from the other hadrons. This proves that the ALICE TPC can provide a standalone proton identification on a track by track level up to a momentum of 0.75 GeV/ c and can assist in recognizing the charged nucleon by rejecting the other hadrons and heavier particles up to 1 GeV/ c .

The approach outlined in the preceding paragraph was followed within this thesis. For $p < 0.75$ GeV/ c , a dE/dx selection based on a second ALEPH parametrization was used to select the (anti-)protons, its coefficients can be found in Table 5.1. The values were obtained (not by this author) during the work carried out for the first publication of ALICE with data from the LHC above injection energy [290]. Within this thesis, the parametrization was compared to the Pb-Pb data taken in the years 2010 and 2011. It was found that the curves do not describe the mean values of the energy losses in Pb-Pb collisions, but rather represent the lower ends of the Gaussian distributions of dE/dx in a given momentum slice for the 2010 Pb-Pb data. For the changed settings and thus slightly reduced gain in 2011, the same could

⁶A closed mathematical form is an expression that can be evaluated with a finite number of operations.

be achieved by multiplying the value returned by the ALEPH parametrization with a factor 0.95. Although obsolete for newer productions⁷, the `kTPCpid` bit still certifies for the inspected dataset that a dE/dx signal is present. A `kTPCpid` bit unequal to zero is equivalent to either a set `kTPCin` or a true `kTPCout` flag (see Appendix 4). Additionally, it requires the TPC signal to be smaller than a 5σ deviation to the higher end of the expected signal of any of e, μ, π, K, p . It was ensured that the bit was set for each examined track.

P_1	P_2	P_3	P_4	P_5
2.83086e-02	2.63394e+01	5.04114e-11	2.12543	4.88663

Table 5.1: ALEPH parametrization coefficients for describing the lower ends of the distributions in dE/dx of the 2010 Pb-Pb data.

Fig. 5.3 (right) shows the truncated mean dE/dx of charged tracks in the TPC for momenta of the tracks $0.74 < p \text{ (GeV}/c) < 0.75$. The prominent feature of the plot is the clear separation of the different particle species with the proton distribution peaking at $\langle dE/dx \rangle \approx 105$. Also shown is a fit. It consists of four components representing pions, kaons, electrons and protons, which are displayed in red, green, magenta, and blue, respectively. The sum of these elements can be seen in the figure as a gray line, which nicely describes the data. The functional description allows for the quantitative decomposition of the contributions. The quality of the selection can be characterized by the purity of the proton-candidate sample

$$\text{pur}_p = \frac{S}{S + B}, \quad (5.2)$$

where the signal S is the number of protons, and B is the background (here other particles). With the aforementioned chosen selection criterion based on the ALEPH parametrization, which appears as a red line in Fig. 5.3 (right) at $\langle dE/dx \rangle \approx 90$, a purity of the sample of more than 99% is achieved for this specific momentum bin. The reader should note that the separation in dE/dx of the charged nucleon from the other particles is even better at lower momenta.

5.2.3 Intermediate Momentum Proton Identification

The Time-Of-Flight detector has a slightly higher intrinsic cut-off in p_T than the TPC (cf. Eq. 4.1) due to the cylindrical geometry of the instrument with a radius of 3.7 m [292]:

$$\text{TOF } p_{T,\text{min}} \approx 0.3 \cdot B \cdot \rho \frac{\text{GeV}/c}{\text{T m}} \approx 0.56 \text{ GeV}/c. \quad (5.3)$$

⁷The PID group recommends to use the methods provided by the `AliPIDResponse` instead, see https://twiki.cern.ch/twiki/bin/viewauth/ALICE/PIDInAnalysis#Checking_PID_status.

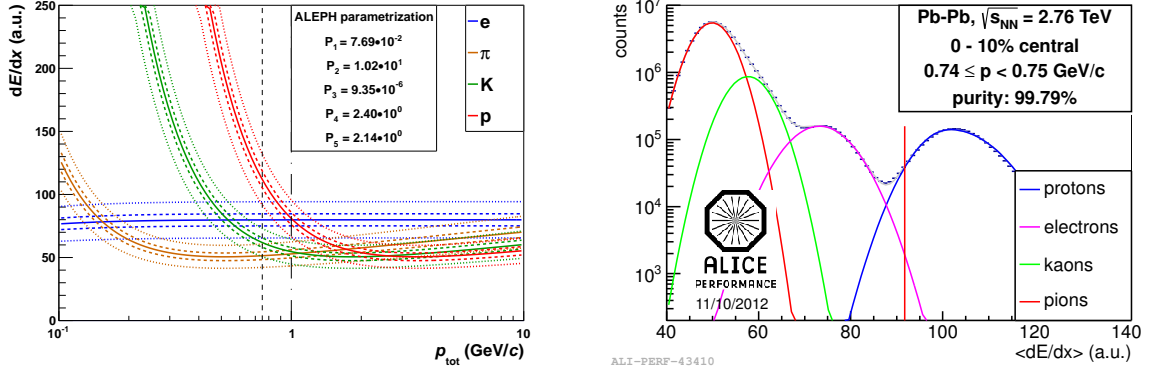


Figure 5.3: Left: ALEPH parametrization of the specific energy loss of electrons, pions, kaons, and protons in the TPC shown as blue, gold, green, and red solid curves. The indicated parameters were taken from a study of central Pb-Pb collisions [291]. Around the expected values in solid curves are also shown the one and three sigma bands in dashed and dotted curves, respectively. A resolution of 6% is displayed, cf. [216]. Right: Exemplary dE/dx spectrum for $0.74 < p$ (GeV/c) < 0.75 with a fit decomposing the different species. Also shown is the proton selection criterion for this momentum slice as a red vertical line.

This lower limit for TOF in transverse momentum of $p_T = 0.56$ GeV/c corresponds to a total momentum of $p = 0.7490$ GeV/c at a pseudorapidity of $\eta = 0.8$. By design, it matches the upper limit of the TPC for the unambiguous proton identification of 0.75 GeV/c. Therefore, the TOF system can provide the track-by-track particle recognition, in the momentum region where the TPC capability becomes quite limited. Also the `kTOFpid` indicator is obsolete, i. e. no longer set, for productions since October 2014. Before that, it is equivalent to requiring the `kTOFout`, `kTIME`, and — since the LHC11d period — `kITSin` tags and rejecting light nuclei with a time exceeding 5σ of the proton expectation⁸. In this analysis, it was used as a convenient and meaningful way of assuring a usable TOF signal for PID purposes. Again, the PID group advises to use the function `AliPIDResponse::CheckPIDStatus` for the future; note that in the `AliPIDResponse` the ITS matching is no longer required⁹. Fig. 5.4 (left) shows the time-of-flight spectrum for charged particles with a momentum of $0.75 < p$ (GeV/c) < 1.0 with the `kTOFpid` bit set. On the x axis, the expected travel time for protons stemming from the particles' tracked path and momentum was already subtracted from the measured signal; the protons clearly stick out around zero. The lighter particles, e. g. pions and kaons, lead to the peaks at $t - t_{\text{exp}}^{(p)} < -3$ ns. The protons can be reasonably selected with $-1 \text{ ns} < t - t_{\text{exp}}^{(p)} < 1.25 \text{ ns}$, indicated by the red lines. Doing so, one realizes that the distributions from pions or kaons are confined below -3 ns and do not contaminate the proton candidates. However, a linear pattern

⁸See <https://twiki.cern.ch/twiki/bin/viewauth/ALICE/TOF> and the AliRoot function `MakeTOFPID` in the `AliESDpid` class.

⁹See `AliPIDResponse::GetTOFPIDStatus`.

with a slight negative slope can be made out. This structure originates from mismatched tracks. Mismatch occurs when a track gets associated to a TOF hit that originates from a different particle. (See also the discussion in Section 4.2.) As a result, the expected time according to the path of the track $t_{\text{exp}}^{\text{p}}$ is unrelated to the time of the TOF hit t and the difference will be more or less randomly distributed, resulting in the linear background observed. Fitting the distribution allows one to quantify the purity (see Eq. 5.2). For the sample $-1 \text{ ns} < t - t_{\text{exp}}^{\text{p}} < 1.25 \text{ ns}$ the mismatch degrades the purity to only 92.6%.

What kind of particles constitute the mismatch? Given the charged-particle ratios in Pb-Pb collisions at the LHC of $K/\pi \approx 0.15$ and $p/\pi \approx 0.05$ [293], the mismatch will primarily originate from pions (and some kaons) being assigned a random TOF hit. This characteristic can be exploited to further purify the proton candidate sample. As discussed earlier in Section 5.2.2, in the intermediate momentum region of $0.75 < p \text{ (GeV}/c) < 1.0$ the dE/dx measurement in the TPC allows to discriminate between protons and the abundant pions and kaons. Removing tracks that show a TPC signal consistent with the expectation for pions or kaons will remove a significant amount of tracks that are mismatched in TOF. Since the energy loss of protons and electrons is similar in this kinematic region, see Fig. 5.3 (left), such a selection is given by

$$dE/dx > \text{BB}(e) \cdot a, \quad a = \begin{cases} 1.0, & p \leq 0.85 \text{ GeV}/c \\ 0.9, & p > 0.85 \text{ GeV}/c \end{cases}, \quad (5.4)$$

where $\text{BB}(e)$ is the Bethe-Bloch parametrization for electrons with the parameters of Table 5.1. Fig. 5.4 (right) shows the effect on the TOF spectrum. In the background, the original distribution with its fit is indicated in light gray and pale blue for comparison. The foreground, in black, shows the data with the TPC pre-selection, forcing the `kTPCpid` bit to be present. Also drawn is the fit to the data in blue with the background component (which mostly falls on top of the x axis) as a black line. It can be seen that the TPC pre-selection gives essentially no loss in signal. Within the TOF selection window represented by the red lines, the purity of the proton candidate sample is above 99%.

5.2.4 Proton Selection for p from 1 up to 5 GeV/ c

As explained in Section 4.2, the problem of mismatch in the TOF detector lessens for higher momentum tracks, which follow a more straight trajectory. Therefore, only the `kTOFpid` bit was required for $p \geq 1 \text{ GeV}/c$. For the momentum range $1.0 \leq p \text{ (GeV}/c) < 1.25$, a significant mismatch component is still needed to describe the data with a fit. However, the magnitude of the mismatch is much lower. Consequently, the `kTPCpid` was not forced to be present and a

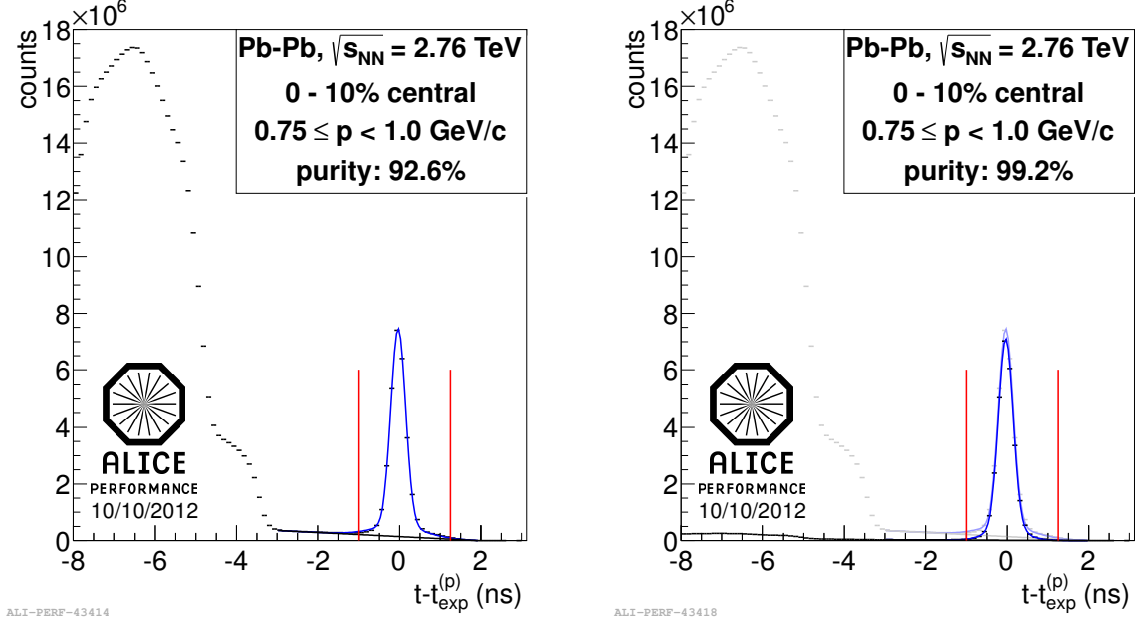


Figure 5.4: TOF signal for $0.75 \leq p$ (GeV/c) < 1.0. Left: Without any other requirements. Right: With an additional pre-selection via the specific energy loss in the TPC.

selection on the dE/dx was performed only if the signal was present anyway. The used criterion

$$dE/dx > BB(p) - 10 - 35 \cdot (p \text{ (GeV/c)} - 1), \quad (5.5)$$

where $BB(p)$ is the expected energy loss for protons according to the parameters given in Table 5.1. This selection could again suppress the mismatch. It follows the lower end of the Gaussian component representing the protons in the fit to the dE/dx data. At the high end of this momentum bin, barely any particle gets rejected by the cut. At the low end, where mismatch is more important, all pions and kaons are discarded. Fig. 5.5 (left) shows that the mismatch drastically decreases for higher momenta. This feature is further corroborated by Fig. 5.5 (right) where it can be seen that the TOF spectrum for $1.75 \leq p$ (GeV/c) < 2.00 is well described by three Gaussians for the different particle species without the need of a mismatch component.

The bands of the particles in the TOF spectrum, displayed in Fig. 5.5 (left), approach each other as momentum increases. Although the proton stripe can be distinguished up to $p = 5$ GeV/c, it starts to significantly overlap with the other species above a momentum of 3 GeV/c. This requires a momentum-dependent TOF selection window; the extent of the chosen intervals within this thesis can be found in Table 5.2. An exemplary momentum bin is showcased in Fig. 5.5 (right) where the TOF spectrum is decomposed by a fit — consisting of

three Gaussians representing pions, kaons, and protons — which allows to calculate the purity. Also shown is the lower selection threshold as a red line, for this bin at $t - t_{\text{exp}}^{(\text{p})} = -500$ ps. The change of the lower threshold with momentum is driven by two effects. Firstly, the proton peak width decreases with increasing momentum. This is explained by the lower uncertainty on the travelled particle's path for straighter tracks. Secondly, the peak from pions and kaons contaminates the tails to lower times of the proton peak at high momentum. The selection consequently becomes more restrictive; starting from $p \approx 3$ GeV/ c , a certain fraction of good protons is rejected. In the limit of $4.75 \leq p$ (GeV/ c) < 5.00 , 50% of the protons are discarded. Tracks with a momentum of more than 5 GeV/ c are rejected. As a result, a purity better than 99% is maintained over the full momentum range. The analysis profits greatly from this strategy, since no possible kaon-lambda or pion-lambda correlation has to be considered¹⁰ and no correction on the proton purity is necessary.

Momentum (GeV/ c)	TOF selection window (ps)
$1.00 \leq p < 2.00$	$-500 \leq t - t_{\text{exp}}^{(\text{p})} < 500$
$2.00 \leq p < 2.25$	$-350 \leq t - t_{\text{exp}}^{(\text{p})} < 500$
$2.25 \leq p < 2.50$	$-300 \leq t - t_{\text{exp}}^{(\text{p})} < 500$
$2.50 \leq p < 2.75$	$-250 \leq t - t_{\text{exp}}^{(\text{p})} < 500$
$2.75 \leq p < 3.00$	$-200 \leq t - t_{\text{exp}}^{(\text{p})} < 500$
$3.00 \leq p < 3.75$	$-150 \leq t - t_{\text{exp}}^{(\text{p})} < 500$
$3.75 \leq p < 4.25$	$-100 \leq t - t_{\text{exp}}^{(\text{p})} < 500$
$4.25 \leq p < 4.50$	$-50 \leq t - t_{\text{exp}}^{(\text{p})} < 500$
$4.50 \leq p < 5.00$	$0 \leq t - t_{\text{exp}}^{(\text{p})} < 500$

Table 5.2: Momentum dependent TOF selection window.

5.2.5 Proton Feed-Down

A large fraction of the selected primary proton candidates emanates not from the fireball itself but is a product from the weak decays of (mostly) lambda particles. Two efforts concerning the contamination by feed-down are carried out within this thesis. Firstly, its contribution should be suppressed in order to enhance the significance of the signal from pairs of primary protons and Λ in the correlation function and secondly, it should be quantified so that it can be corrected for (see Section 6.5). Both can be achieved with the Distance of Closest Approach (DCA) of the track extrapolation to the primary vertex, see Fig. 3.5 for a sketch of the DCA.

¹⁰It was shown by the NA49 Collaboration that within the uncertainties of their data, no kaon-lambda or pion-lambda correlation is present [294,295].

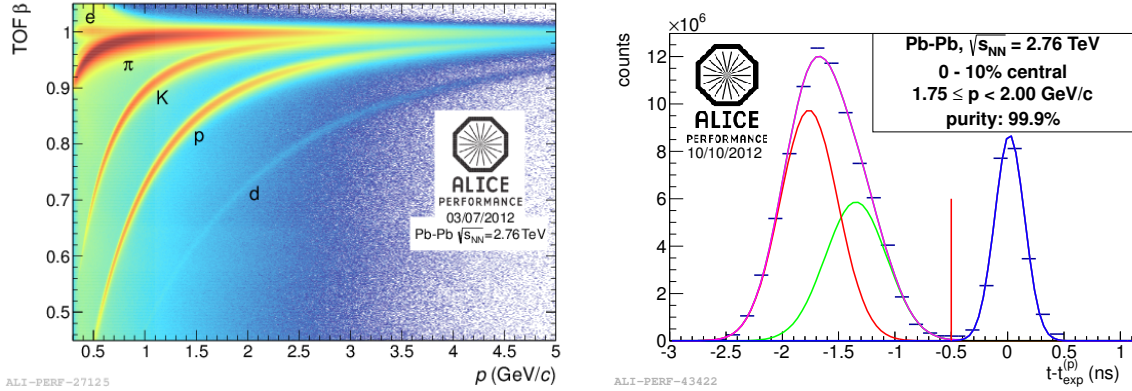


Figure 5.5: Left: Measured TOF β for the 2011 Pb-Pb run, calculated as follows from Eq. 3.7. The bands for the different species get closer as the momentum increases, but the protons appear separated up to $p = 5.0$ GeV/ c . The mismatch decreases drastically with increasing momentum. Right: Exemplary TOF spectrum with the expected time for protons $t_{\text{exp}}^{(p)}$ subtracted from the measured time t for the momentum bin $1.75 \leq p$ (GeV/ c) < 2.0 with a fit decomposing the different contributions.

The DCA generally is the length of a three-dimensional vector. Due to the rotational symmetry in azimuth of ALICE it simplifies the analysis to reduce the x and y components to a single transverse element DCA_{xy} . It is a common approach in ALICE to only study this transverse component [290] since it alone provides enough separation power to distinguish between primary protons,¹¹ protons from weak decays, and protons from an interaction with the detector material. In this thesis, an additional effort was made to not only employ the transverse DCA_{xy} but also make use of the longitudinal DCA_z . The two-dimensional DCA of protons was obtained for three centrality classes, 0–10%, 10–30%, and 30–50% most central events, differential in rapidity and transverse momentum and separately for the particles and anti-particles. In Fig. 5.6 (left) the two-dimensional ($\text{DCA}_{xy}, \text{DCA}_z$) distribution of protons relative to the primary vertex for an exemplary phase space bin is projected on the DCA_{xy} component. The data, shown in black, are well described by a fit (magenta) consisting of Monte-Carlo templates for primary protons (red), protons from weak decays (green), and protons from material (blue); the symbols for the Monte-Carlo distributions are connected with lines for better visualization. The templates were obtained by analyzing simulated Hijing events, anchored to the Pb-Pb data taken in 2011.¹² The same track selection criteria were applied to the Monte-Carlo samples as on the Pb-Pb data, only the particle identification was performed with the information from the event generator. The single components all display a distinct shape in DCA, which is almost flat for the contribution from material, shows broad shoulders for the weak decays and is very peaked for the primary protons. Visible for the contribution

¹¹Note that according to an ALICE definition, primary particles include particles from decays, except weak decays of light flavor (u, d, s) hadrons and muons.

¹²All periods from LHC12a17a_fix to LHC12a17i_fix were analyzed.

from material interactions is a peaked structure for $DCA_{xy} < 0.1$ cm. It was found in [296] (see the discussion in Section 3.2.3 therein), that it originates in the fake association of a SPD cluster from a primary track to the trajectory of the secondary particle. In the two-dimensional fit to the data, only three parameters in each bin are left free, which are the scaling factors of the MC templates. The progressive binning in the DCA variables, e. g. bin widths of 0.2 cm in DCA_{xy} for $|DCA_{xy}| > 2.0$ cm down to widths of 0.02 cm for $|DCA_{xy}| < 0.1$ cm, allowed for an additional sensitivity in the interesting region of small distances while keeping the data structures small enough to handle them effectively.

When deciding on a cut value in DCA, an objective criterion for the determination of the best cut value is beneficial. Let us consider the background in the proton sample to be uncorrelated with the lambda particles (this assumption will be verified in Section 5.2.5). Then, the height of the correlation function above one, H , is proportional to the purity of the sample: $H \sim \text{pur} = S/(S + B)$. The number of pairs found in real events $N_{\text{pair}}^{\text{real}}$ is proportional to the number of selected protons $N_{\text{pair}}^{\text{real}} \sim N_{\text{p}} = S + B$. Its uncertainty is driven by Poisson statistics, since we are still just counting pairs, hence $\Delta N_{\text{pair}}^{\text{real}} = \sqrt{N_{\text{pair}}^{\text{real}}} \sim \sqrt{S + B}$. When utilizing the event mixing technique, the uncertainty on the ratio of real over mixed events is usually dominated by the uncertainty of the real events as the mixed events typically have a factor of ten more statistics:

$$\Delta \left(\frac{N_{\text{pair}}^{\text{real}}}{N_{\text{pair}}^{\text{mixed}}} \right) / \left(\frac{N_{\text{pair}}^{\text{real}}}{N_{\text{pair}}^{\text{mixed}}} \right) = \sqrt{\left(\Delta(N_{\text{pair}}^{\text{real}})/N_{\text{pair}}^{\text{real}} \right)^2 + \left(\Delta(N_{\text{pair}}^{\text{mixed}})/N_{\text{pair}}^{\text{mixed}} \right)^2} \quad (5.6)$$

$$= \sqrt{1 + 0.1} \cdot 1 / \sqrt{N_{\text{pair}}^{\text{real}}} \approx 1 / \sqrt{N_{\text{pair}}^{\text{real}}}. \quad (5.7)$$

We see that the uncertainty on the correlation function E consequently is $E \sim 1/\sqrt{N_{\text{pair}}^{\text{real}}} \sim 1/\sqrt{S + B}$. Therefore, the ratio of the correlation function above one to the uncertainty of the correlation function is:

$$H/E \sim \frac{S}{S + B} \sqrt{S + B} = \frac{S}{\sqrt{S + B}} := \zeta, \quad (5.8)$$

where ζ is the commonly used significance of the single-particle sample. In order to obtain the most accurate measurement, the single-particle significance ζ has to be maximized.

Fig. 5.6 (right) shows the significance ζ as a function of the cut value in $|DCA_{xy}|$ and $|DCA_z|$. One sees that a selection on the $|DCA_{xy}|$ and/or $|DCA_z|$ on the order of 0.5 cm provides a good significance. It is important to note that a too strict selection should be avoided, as the significance drops rapidly for $|DCA_{xy}|$ and/or $|DCA_z|$ smaller than on the order of 0.01 cm. It turns out that a maximum exists in the distribution of ζ , according to which the selection was chosen to be $|DCA_{xy}| \leq 0.1$ cm and $|DCA_z| \leq 0.15$ cm for protons. For the anti-protons, the contribution from material interactions does not play a role, therefore a slightly looser selection

of $|DCA_{xy}| \leq 0.15$ cm and $|DCA_z| \leq 0.20$ cm was applied, yielding a maximum ζ .

The feed-down fraction in the proton sample f_p should be defined as the number of particles from material interactions and weak decays over the number of all particles and is thus a measure of the uncorrelated background. The DCA fits allow to obtain f_p within the aforementioned selection windows in DCA. For the example shown in Fig. 5.6 (left), the feed-down fraction f_p amounts to 15%, where the main feed-down contributors are from weak decays, with less than 1% of f_p coming from interactions with detector material.

The feed-down fraction exhibits a dependence on phase space, which is shown in Fig. 5.7 for protons in the 0–10% most central events. The most prominent feature of the distribution is the increased feed-down at central rapidity $|y| < 0.5$ and low transverse momentum $p_T < 0.5$ GeV/c. This contribution arises from protons which were knocked-out from the detector. This conclusion emerging from the DCA fits is confirmed by the fact that the anti-protons do not show such a behavior. Due to the significant amount of feed-down, protons, but not anti-protons, with $|y| < 0.5$ and $p_T < 0.5$ GeV/c are rejected from the sample as indicated by the hatched overlay in the figure. Loading such a histogram in the analysis to look up the feed-down fraction for each single particle allows to correct the correlation function for the uncorrelated background in a later stage, see Section 6.5. The selection on the DCA concludes the proton selection.

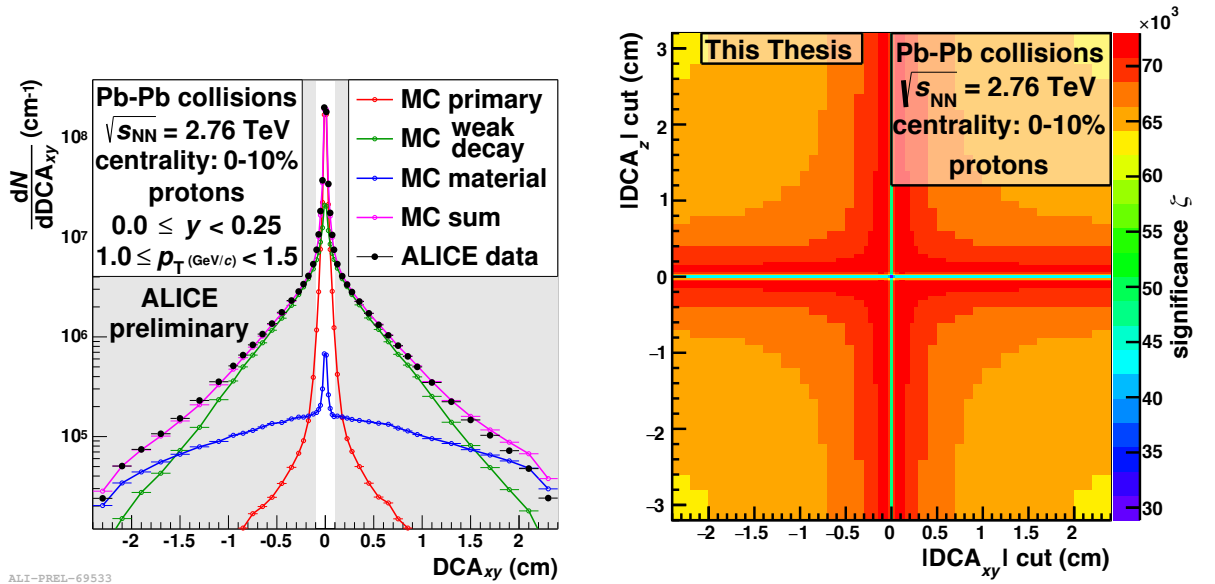


Figure 5.6: Left: Transverse DCA distribution of protons in an exemplary phase space bin for the 0–10% most central events with a fit using Monte-Carlo templates. See text for the discussion. Right: Significance ζ as a function of the cut values in DCA_{xy} and DCA_z for protons in 0–10% most central events. Mirrored around $(0,0)$. A maximum in ζ exists for $|DCA_{xy}| \leq 0.1$ cm and $|DCA_z| \leq 0.15$ cm.

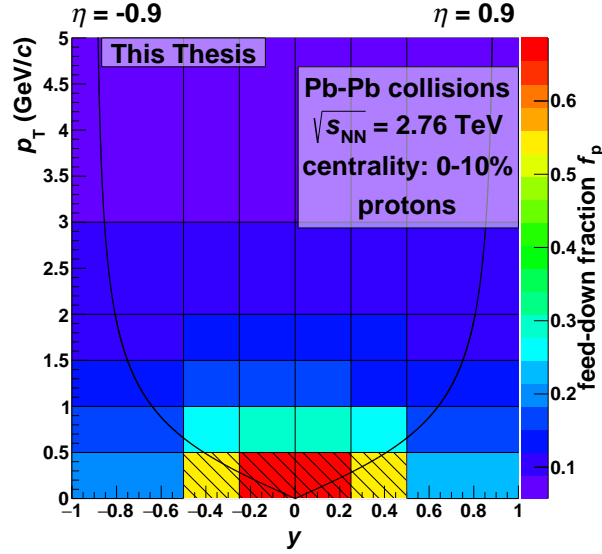


Figure 5.7: Evolution of the feed-down fraction f_p as determined by DCA fits with phase space.

5.3 Primary Λ Identification

5.3.1 Λ Selection

K_s^0 are much more abundantly produced in heavy-ion collisions at the LHC than Λ . Therefore, it is necessary to identify the Λ from all V^0 vertices. For such a selection, a highly discriminating variable is the invariant mass of the vertex. However, when simply looking at the distribution of the invariant mass assuming a Λ decay of all V^0 vertices of the on-the-fly V^0 finder, no peak is visible at the PDG mass of the Λ of 1.115683 ± 0.000006 GeV/ c^2 [32]. It is necessary to make use of additional information to obtain a highly significant Λ signal.

The standard analysis uses vertices from the on-the-fly V^0 finder; the V^0 of the offline finder were only invoked for a systematic study, see Section 6.9. The selection makes use of topological criteria and the particle identification provided by the experiment. An exemplary measurement that can be used to purify the Λ sample is the energy loss measurement in the TPC. By fitting the bands of the energy loss curves in the TPC with a Gaussian parametrization in dE/dx for each particle, one can obtain a degree of consistency of the measurement with a certain particle species by the comparison of the measured dE/dx to the expected dE/dx in terms of standard deviations of the measurement; this variable is referred to as N_σ^{TPC} . The main advantage of this method is its simplicity, as only one parameter is needed to select a certain species over the full kinematic range. Another benefit is the intuitiveness of the procedure. If all dependencies of the expected dE/dx signal, e.g. on the η of the track, are incorporated, a

three sigma selection will contain 99.73% of the particles. Fig. 5.8 (right) shows the results of a detailed study which reveals that indeed the significance $\zeta = S/\sqrt{S+B}$ saturates for a cut value of about three. A closer look, see the inlay of Fig. 5.8 (right), demonstrates that the maximum significance is reached for cut values of about 3.5 to 4.1. This hints to, e. g., a slight variation of the mean energy loss with some observable which is not yet accounted for. Maximizing the significance for each cut variable results in the Λ selection criteria listed in Section E.1.

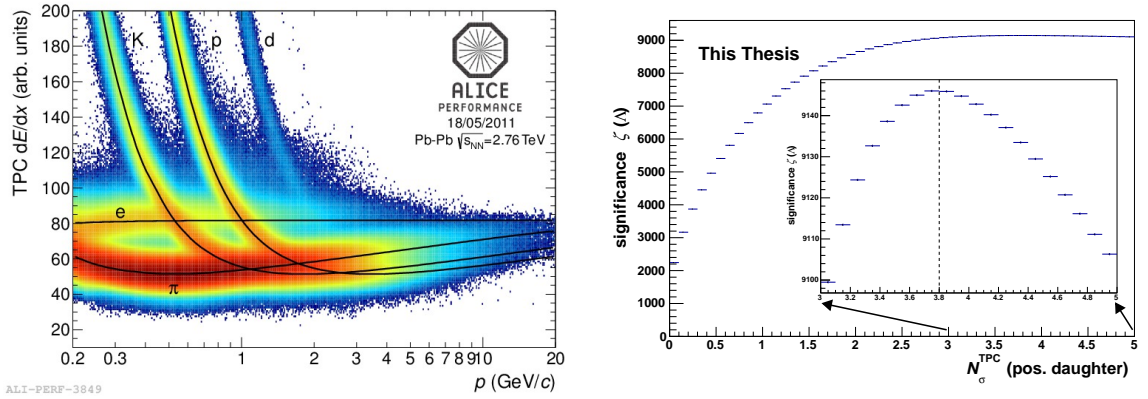


Figure 5.8: Left: dE/dx vs. p as measured with the TPC. Right: Significance ζ of Λ as function of the cut value on the number of standard deviations in dE/dx of the positive daughter; errors are correlated.

The invariant mass spectrum, after the selection criteria have been applied, is shown in Fig. 5.9 (left) for 0–10% most central events in an exemplary region in phase space, specifically $0.5 < |y| < 0.6$ and $1.0 \leq p_T$ (GeV/c) < 1.5 . This kinematic region yields a high number of V^0 vertices and is a representative example. The signal peaks at the PDG mass of $m_{\text{PDG}} = 1.115683$ GeV/ c^2 . A parametrization allows to disentangle the contributions from real Λ and combinatorial background or, e. g., falsely selected K_s^0 . Taking the signal shape from a Monte-Carlo simulation gives an edge over a Gaussian or Lorentzian representation. The simple functional descriptions can not fully account for the detailed structures of the peak, which are intrinsically linked to the specific dependence of the detector resolution on, e. g., the possibility of the occurrence of multiple scattering. Knowledge about the material budget and an accurate map of the magnetic field are necessary to reproduce the signal shape. The Monte-Carlo template gives a better description of the data and reduces the number of fit parameters. The good momentum resolution of the detector confines the bulk of the signal to ± 4 MeV/ c^2 . This gives the additional advantage that the background in the fit is well constrained. The background also is rather flat, cf. the situation at the SPS [297]. Together, all of these points lead to fact that the parametrization is very reliable. Within the selection window of $m_{\text{PDG}} \pm 4$ MeV/ c^2 , the purity $\text{pur}_{\Lambda} = \frac{S}{S+B}$ in this phase-space region is 91%.

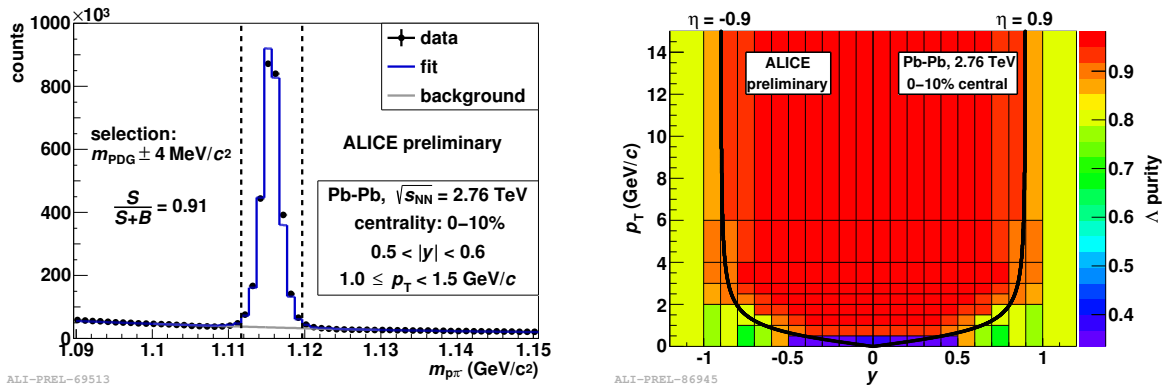


Figure 5.9: Left: Λ m_{inv} spectrum for an exemplary phase-space bin in the 0–10% most central events with a fit employing a Monte-Carlo template. Right: Phase-space dependence of the Λ purity pur_Λ for the 0–10% most central events.

In Section E.2 the motivation is given to determine the single-particle purities differential in phase space in order to gain accurate information on the average pair-purity. Using a toy model it can be shown that a binned single-particle purity determination precisely reproduces the true pair purity, even under highly unfavorable conditions. The right side of Fig. 5.9 exhibits the phase-space dependence of the Λ purity for the 0–10% most central events. The high statistics together with the discussed advanced conditions for the fitting procedure allow for a finely grained purity determination. For central rapidities $|y| < 0.5$ and low transverse momentum $p_T < 0.5 \text{ GeV}/c$ a degraded purity of only about 40% can be spotted. A significant amount of protons from material interactions, which resemble secondary tracks from weak-decay vertices, contributes here. We conclude on the origin of these vertices based on the shape in invariant mass of the additional background and the non-observation of the effect for $\bar{\Lambda}$, which is consistent the findings for the DCA of protons in Section 5.2.5. Consequently, Λ but not $\bar{\Lambda}$ with $p_T < 0.5 \text{ GeV}/c$ are rejected. For p_T higher than $0.5 \text{ GeV}/c$, the contribution from material interactions perishes. For large rapidities $|y| > 1.0$, the purity is 81%; within pseudo-rapidities $|\eta| \leq 0.9$, the sample has a purity above 90%.

5.3.2 Feed-Down from Weak Decays

The collection of Λ is contaminated with products from weak decays. The main contamination originates from cascades and omega baryons which decompose with a high branching ratio (BR) into states containing a Λ . The dominantly contributing decays are $\Xi^0 \rightarrow \Lambda\pi^0$ (BR 99.5%), $\Xi^- \rightarrow \Lambda\pi^-$ (BR 99.9%), $\Omega^- \rightarrow \Lambda K^-$ (BR 67.8%), and $\Omega^- \rightarrow \Xi(\rightarrow \Lambda\pi)\pi^-$ (BR 32.2%). The measurement of multi-strange baryons in Pb-Pb collisions at $\sqrt{s_{\text{NN}}} = 2.76 \text{ TeV}$ by the ALICE Collaboration [298] poses a great advantage for this analysis. There, p_T -differential yields were obtained in five centrality classes for Ξ^- , $\bar{\Xi}^+$, Ω^- , and $\bar{\Omega}^+$. These results allow

to obtain the feed-down contribution in the Λ sample by propagating the spectra through reconstruction-efficiency matrices obtained from Monte-Carlo simulations.

The multi-strange spectra range from $0.5 \leq p_T$ (GeV/ c) < 8.0 for Ξ and $1.2 \leq p_T$ (GeV/ c) < 7.0 for Ω , making it necessary to find a parametrization that allows for an extrapolation to the unmeasured regions. A good description of the data is provided by fits with a blast-wave parametrization [298, 299]. The blast-wave function assumes an underlying flow field with a transverse velocity β_r , which has a profile in transverse radius r of

$$\beta_r(r) = \beta_{\max} \left(\frac{r}{R} \right)^n. \quad (5.9)$$

This leads to the m_T distribution

$$\frac{dN}{m_T dm_T} \propto \int_0^R r dr m_T I_0 \left(\frac{p_T \sinh \rho}{T} \right) K_1 \left(\frac{m_T \rho}{T} \right), \quad (5.10)$$

where T is the temperature and $\rho = \tanh^{-1} \beta_r$ is the transverse boost of each single thermal source cell. $I_0(z) = (2\pi)^{-1} \int_0^{2\pi} e^{z \cos \varphi} d\varphi$ and $K_1(z) = \int_0^\infty \cosh y e^{-z \cosh y} dy$ are modified Bessel functions. Two blast-wave fits to the data are shown for Ξ^- in Fig. 5.10. The blast-wave fit with a fixed exponent $n = 1$ for the flow profile of Eq. 5.9 is shown black. The shift of the maximum of the spectrum by the radial flow towards higher p_T is slightly under-predicted. A better description of the data is given by leaving the exponent n as a free parameter. The fit, shown as a red line, gives $n = 0.41$ as indicated in the figure and describes the data reasonably well. The blast-wave with the fitted exponent was chosen for parametrizing the data. Also shown are the Monte-Carlo spectra for Ξ^- and Ξ^0 . At high p_T one sees the artificially added constant component to enhance the statistics for high p_T particles. On top of the constant component sits the p_T spectrum of the Hijing generator. The Hijing spectra for Ξ^- and Ξ^0 are almost identical, justifying the assumption of isospin symmetry for the unmeasured Ξ^0 . The discrepancy of the Hijing simulation to the data is evident, making a strong case for the usage of the measured spectra. For the unmeasured Ξ^0 and Ξ^+ , isospin symmetry is assumed.

The tiny statistical uncertainties of the simulated data shown in Fig. 5.10 allow to obtain multi-differential reconstruction efficiencies with high accuracy. Fig. 5.11 displays such an efficiency matrix for $p_T^{\Xi^-} \rightarrow (y^\Lambda, p_T^\Lambda)$. The matrix exhibits the familiar acceptance, which is maximal only for pseudo-rapidity $|\eta| \leq 0.9$. Also visible is the linear correlation between the generated transverse momentum of the mother and the reconstructed one of the daughter, proof of the good experimental transverse momentum resolution. Such matrices were created for Ξ^- , Ξ^+ , Ξ^0 , Ξ^+ , Ω^- , and $\bar{\Omega}^+$ following the centrality binning of [298], i. e. 0–10%, 10–20%, 20–40%, and 40–60%.

Propagating the measured spectra with their blast-wave parametrization through the efficiency matrices yields the feed-down from Ξ^- , Ξ^+ , Ξ^0 , Ξ^+ , Ω^- , and $\bar{\Omega}^+$ differential in centrality

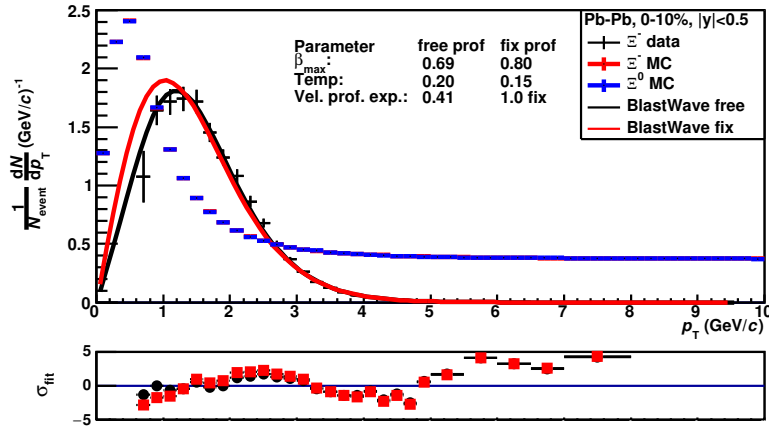


Figure 5.10: ALICE data from [298] for Ξ^- in 0–10% most central Pb-Pb collisions at $\sqrt{s_{\text{NN}}} = 2.76$ TeV together with two blast-wave fits and a Hijing simulation with injected signals for Ξ^- and Ξ^0 .

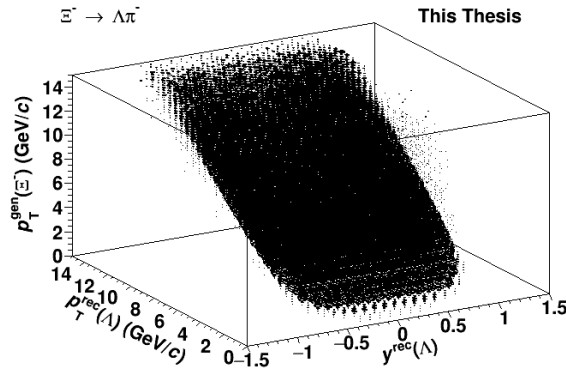


Figure 5.11: Reconstruction efficiency for the decay $\Xi^- \rightarrow \Lambda\pi^-$ multi-differential in $p_{\text{T}}^{\text{gen}}(\Xi^-) \rightarrow (y^{\text{rec}}(\Lambda), p_{\text{T}}^{\text{rec}}(\Lambda))$. 0–10% most central Pb-Pb collisions at $\sqrt{s_{\text{NN}}} = 2.76$ TeV.

and (y, p_{T}) , as displayed for the 0–10% most central events in Fig. 5.12. These histograms quantify the raw amount of uncorrelated feed-down from weak decays in the Λ sample and allow to correct the measured correlation function for the dilution in a following step.

5.3.3 Feed-Down from Electromagnetic Decays

A significant fraction of the selected Λ particles are daughters of the electromagnetic decay of the Σ^0 . Experimentally resolving the $c\tau = 22.2$ pm of the disintegration $\Sigma^0 \rightarrow \Lambda\gamma$ with a branching ratio of 100% is not possible with ALICE. The similar mass of the singly strange baryons gives comparable thermal production rates. Therefore, Λ from Σ^0 constitute the most

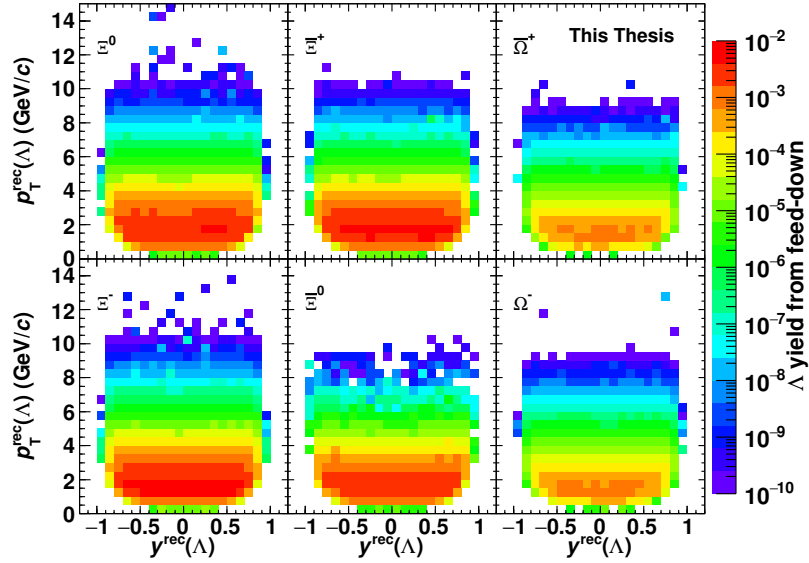


Figure 5.12: Feed-down contribution as raw yield to the Λ sample from the various multi-strange hyperons exemplary for 0–10% most central Pb-Pb events at $\sqrt{s_{\text{NN}}} = 2.76$ TeV. Note the z scale of eight orders of magnitude.

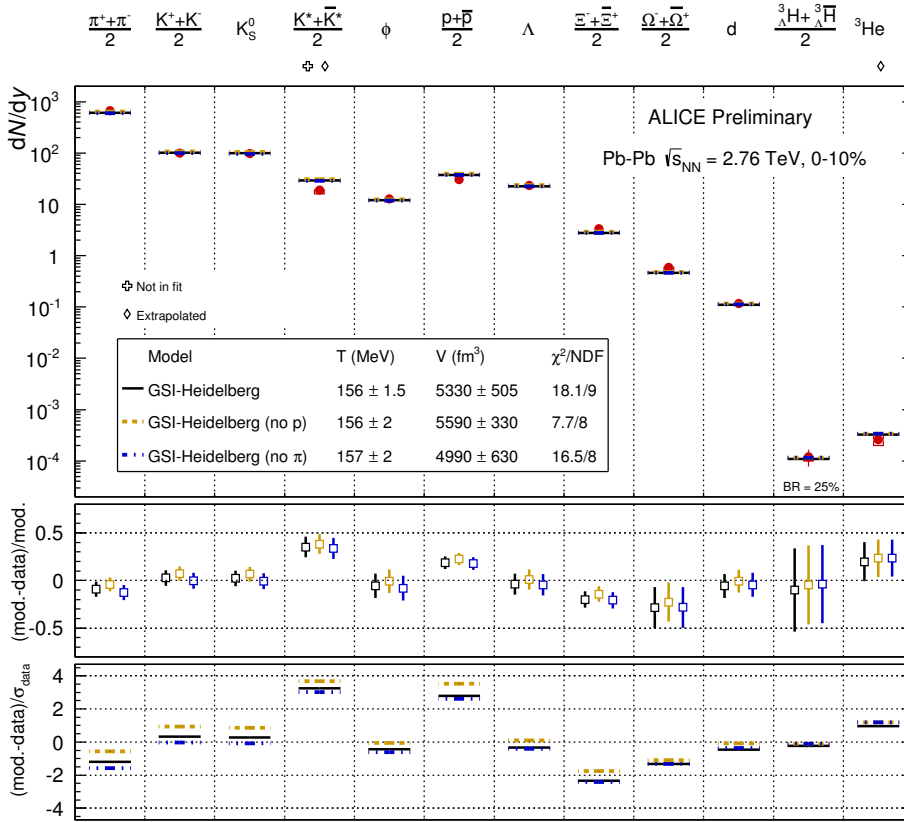
abundant contamination of the samples.

Thermal model calculations describe well the particle production in Pb-Pb collisions at the LHC, as illustrated in Fig. 5.13. The momentum distribution of primary baryons — excluding any decays from, e. g., resonances and without collective flow — obeys Fermi statistics and the appropriate phase-space factor:

$$\frac{dN}{dp} \propto \frac{p^2}{\exp[(E - \mu_{\text{eff}})/T] + 1}, \quad (5.11)$$

where E is the particle’s energy, p its momentum, and $\mu_{\text{eff}} = \mu_B \cdot B + \mu_S \cdot S$ is the chemical potential. Plugging the mass of the Λ and Σ^0 into Eq. 5.11 and taking $\mu_B = 1$ MeV, $\mu_S = 0$ MeV, and $T = 164$ MeV for LHC conditions [300] gives the momentum distributions shown in Fig. 5.14 (left). Integrating these distributions results in the relation of the yields $N_{\Sigma^0}/(N_{\Lambda} + N_{\Sigma^0}) = 0.405$. However, this number can not be taken as a description of the measured particle multiplicities in ALICE, since resonance production significantly alters the numerical value. Especially at the high temperatures reached at the LHC, higher mass states are abundantly populated. The effect is illustrated in Fig. 5.14 (right). Resonances typically have higher branching ratios to the Λ state than to the Σ^0 , one reason being the bigger phase space for the decay to the lowest lying strange baryon level. Thus, the relation of the yields evolves to $N_{\Sigma^0}/(N_{\Lambda} + N_{\Sigma^0}) \approx 0.30$ when the Σ^* is included. State-of-the art thermal models incorporate resonances up to masses of several GeV/c^2 . Let us now consider in detail the decay of a Ξ^* resonance, specifically $\Xi^*(1530) \xrightarrow{\text{strong}} \Xi(\xrightarrow{\text{weak}} \Lambda\pi)\pi$, where the strong decay has a branching ratio

of 100%. The strong feed-down from the $\Xi^*(1530)$ is already included in the measured Ξ spectra by ALICE [298], which were used to determine the contamination of the Λ sample by weak-decays. When accounting for resonances, decay chains involving a weak decay have therefore to be excluded. For this analysis the ratio $N_{\Sigma^0}/(N_{\Lambda} + N_{\Sigma^0}) \approx 0.27$ from Therminator [301] was used, while systematically other models [302,303] were consulted, see Section 6.9. Assuming that all Λ products which underwent strong decays are correlated with primary protons and that products from Λ which decayed electromagnetically are independent, the correlation function can be corrected for the uncorrelated contributions.



ALI-PREL-74473

Figure 5.13: Published data from ALICE for π , K, and p [304], K_s^0 and Λ [131], Ξ and Ω [298], and ϕ and K^* [305] together with preliminary ALICE data [306] and thermal model calculations [307].

The weak (discussed in Section 5.3.2) and electromagnetic decay products in the Λ sample are united in the feed-down fraction f_{Λ} , which shall be defined as the ratio of the number of Λ baryons from weak and electromagnetic decays to the number of all Λ . This feed-down fraction will be used to correct the pA correlation function for the contamination in the Λ sample in Section 6.5.

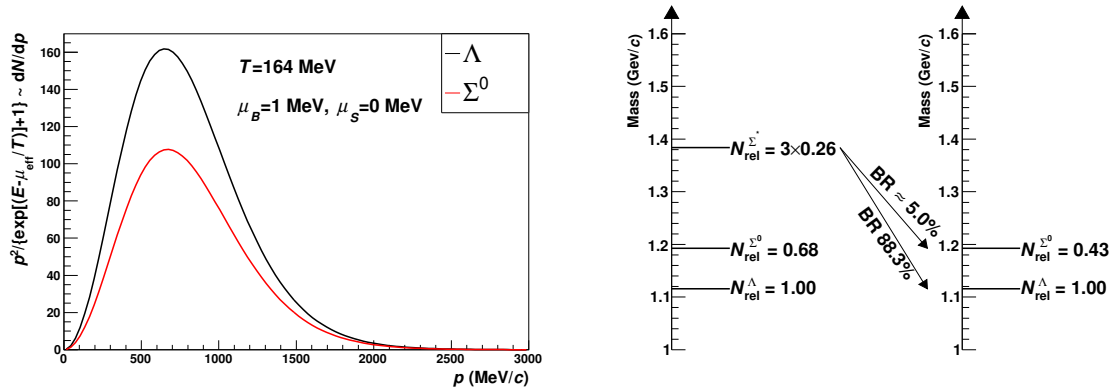


Figure 5.14: Left: Thermal momentum distribution of Λ and Σ^0 not taking into account decays from resonances and without collective flow. Right: The effect of resonances on the relative yields of Λ and Σ^0 . The three Σ^* states have a higher branching ratio to the Λ and change the relative yields N_{rel} away from the naïve thermal values.

Chapter 6

p Λ Data Analysis: Two-Particle Studies

6.1 Generalized Momentum Difference \tilde{q}

When dealing with correlations of non-identical particles, it is useful to not restrict oneself to the Pair Rest Frame (PRF), but to generalize the momentum difference to any frame as done in [308] by R. Lednicky:

$$\tilde{q} = |q - P(qP)/P^2|, \quad (6.1)$$

$$q = p_1 - p_2, \quad P = p_1 + p_2, \quad (6.2)$$

where p_1 and p_2 are the four-momenta of the particles. In the PRF, where the three-momenta cancel (i.e. $\vec{P} = 0$), the generalized momentum difference \tilde{q} coincides with the relative momenta of the particles \vec{k}^* multiplied by the trivial factor of two:

$$\text{PRF : } \quad \tilde{q} = (0, 2\vec{k}^*). \quad (6.3)$$

In the following, the generalized momentum difference is used throughout and the tilde is omitted for simplicity.

6.2 Event Mixing

The experimental access to the two-particle correlation function is given by the event mixing technique

$$C_2(p_1, p_2) = \frac{N(p_1, p_2)}{N(p_1) \cdot N(p_2)} = \frac{A(q, m_T)}{B(q, m_T)}, \quad (6.4)$$

where $A(q, m_T)$ is the two-particle distribution in real events and $B(q, m_T)$ is obtained from mixed events.

As already touched on in Appendix 5, it must be certified that the correlation function is not biased by experimental detector effects. For example a changing acceptance can introduce such an undesired outcome. Fig. 6.1 (left) showcases a study with a simplistic toy model, where 1k events with 100 tracks each were generated. The tracks are simulated in a two-dimensional momentum space with a constant transverse momentum of 1 GeV/ c and a flat distribution in azimuth. The correlation function is obtained as a function of the momentum difference $\Delta p = \sqrt{(\Delta p_x)^2 + (\Delta p_y)^2}$. Two event classes were populated equally by assigning events subsequently to class one and two. Three scenarios were investigated: a) a full detector acceptance in both classes; b) full acceptance in the first set and an acceptance hole in $0 \leq \varphi < \pi/2$ in the second category of events; c) an acceptance hole in both groups. The resulting momentum distributions in (p_x, p_y) space for the two event classes can be seen as an inlay in the top right for a) in green (top), b) in blue (center), and c) in red (bottom). The corresponding correlation functions share the same color code. We see that without an acceptance gap (green circles) the correlation function is flat at unity. In the case where only one class of events had an acceptance hole (blue squares), the correlation function shows an excess for momentum differences $\Delta p < 1.4$ GeV/ c . The effect is a non-trivial consequence of the pairing process with the acceptance gap spanning from $(p_x = 0, p_y = 1$ GeV/ c) to $(p_x = 1$ GeV/ $c, p_y = 0)$, i. e. a $\Delta p = \sqrt{(\Delta p_x)^2 + (\Delta p_y)^2} = 1.4$ GeV/ c . If both sets showed the acceptance gap (red crosses), the correlation function is again flat at unity. We see that a changing acceptance easily mimics a correlation signal from physics effects, e. g. mini-jets, as measured by the CMS Collaboration and shown on the right of Fig. 6.1. This is not meant as a critique of the CMS results — the resemblance of the correlation functions is coincidental —, but rather should show how important an appropriate event mixing is. In order to combine only similar events within this thesis, event mixing was performed within 10% wide centrality groups and 5 cm wide classes of the longitudinal vertex position within the selection of ± 10 cm; correlation functions were obtained separately for the two possible orientations of the solenoidal magnetic field as well as independently for pairs of particles and anti-particles.

The event mixing technique gives the opportunity to sample many more mixed events than real collisions were recorded. Here, the minimum desired number of pairs from mixed

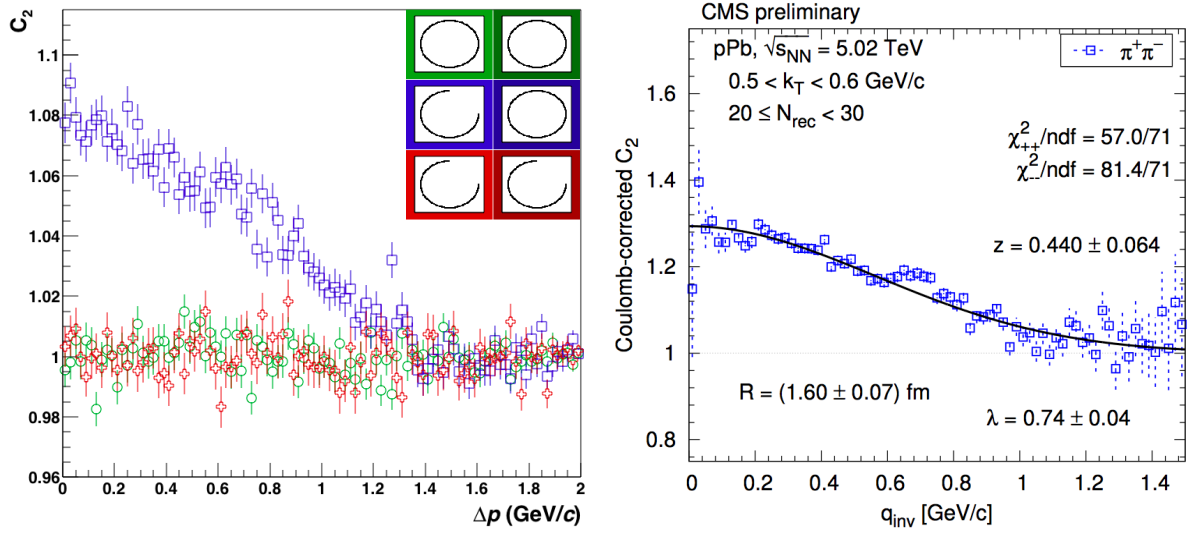


Figure 6.1: Left: Effect of an acceptance gap on the two-particle correlation function C_2 in a simplistic toy model. See text. Right: Coulomb-corrected two-particle correlation function C_2 for pairs of oppositely charged pions in p-Pb collisions as measured by CMS. Taken from [309].

events per pair in real events is estimated. Since the pairs in real and mixed events are statistically independent, the error calculation of the correlation function is straight forward. We approximate the number of pairs in mixed events B as a simple product of the number of pairs in real events A times a constant N_{mix} . It then follows

$$\frac{\Delta C_2}{C_2} = \sqrt{\left(\frac{\Delta A}{A}\right)^2 + \left(\frac{\Delta B}{B}\right)^2} \quad (6.5)$$

$$\stackrel{B=A \cdot N_{\text{mix}}}{=} \frac{\Delta A}{A} \sqrt{1 + \frac{1}{N_{\text{mix}}}}. \quad (6.6)$$

We see that ten times more pairs in mixed events lead to a relative statistical uncertainty on the correlation function that is less than 5% larger than the relative uncertainty of the distribution in real events. By mixing all Λ from the current event with all protons from the buffered events and all protons from the current event with all Λ from the buffered events, 14 times more pairs in mixed events than in real events¹ could be obtained while retaining only 7 events for mixing in memory. Applying Eq. 6.6, the resulting contribution to the statistical uncertainty of the correlation function from mixed events relative to the uncertainty from real events is as small as 3.5%.

¹The ratio of mixed event pairs to real event pairs was determined in the region $0.2 < q$ (GeV/c) < 0.3 .

6.3 Two-Track Resolution

Even with a perfect event mixing procedure, one is typically left with the finite two-track resolution of the detector, especially in the high-multiplicity environment of Pb-Pb collisions. Two tracks close in space can get reconstructed as one track. As the effect is more likely to occur if the particles have similar momenta and is absent in mixed events, the finite two-track resolution generally leads to a depression in the correlation function at small relative momenta. In the course of this work, a systematic investigation extending over several particle species and multiple cut variables was carried out. The findings resulting from this study are the base of several publications of the ALICE Collaboration.

6.3.1 Angular Distances ($\Delta\eta, \Delta\varphi^*$)

A previous study of the two-track resolution effects in ALICE can be found in [310]. There, through an examination of Monte-Carlo simulations of central Pb-Pb collisions, the two-dimensional angular distances ($\Delta\eta, \Delta\varphi^*$) of two tracks at a fixed transverse radius $R = 1.2$ m were identified as variables that efficiently separate the region which is affected by the finite detector resolution. The angular distances can be calculated according to

$$\Delta\eta = \eta_1 - \eta_2, \quad (6.7)$$

$$\Delta\varphi^* = \varphi_1 - \varphi_2 + \arcsin(a_1) - \arcsin(a_2), \quad (6.8)$$

$$a_i = \frac{0.3 R B z_i}{2 p_{T,i}} \frac{1}{\text{Tm}}, \quad (6.9)$$

where for particle $i = 1, 2$ the pseudorapidity is denoted by η_i , φ_i is the azimuthal angle at the primary vertex, z_i is the charge in units of the elementary charge e , and $p_{T,i}$ is the transverse momentum. R is the transverse radius where the distance is evaluated, here $R = 1.2$ m, and B is the magnetic field, $B = \pm 0.5$ T in ALICE. The angular separation was previously employed successfully by the CERES Collaboration [311]. Cutting out a region around $(0, 0)$ in $(\Delta\eta, \Delta\varphi^*)$, i. e. requiring a minimum angular distance of each pair, makes the correlation function insusceptible to the finite detector resolution.

Within this thesis, real data from Pb-Pb collisions registered by ALICE were studied. Distributions in $(\Delta\eta, \Delta\varphi^*)$ at a radius $R = 1.2$ m were obtained differentially in transverse pair momentum $k_T = |\vec{p}_{T,1} + \vec{p}_{T,2}|$ for tracks going in separate halves of the TPC or not for charged particles, pions, kaons, and protons; centrality dependent for 0–10, 10–30, and 30–50% most central events; as function of the track quality quantified by the number of TPC clusters; and for tracks with a large and small DCA_{xy} [312, 313]. The results can easily be summarized. The merging for primary tracks is very confined in $\Delta\eta$, restricted to $|\Delta\eta| \lesssim 0.01$. The suppression in $\Delta\varphi^*$ is nicely described with a Gaussian centered at zero. Its width and depth is independent

of centrality and independent on the number of TPC space-points in the studied range of 50–90 clusters. The merging qualitatively exists also for tracks going in different halves of the TPC, i. e. pairs of tracks with a pseudo-rapidity of unequal sign. The merging strongly depends on the pair transverse momentum k_T . The width of the Gaussian suppression in $\Delta\varphi^*$ decreases from 0.02 for $0.1 \leq k_T$ (GeV/c) < 0.4 to 0.01 for $1.3 \text{ GeV/c} \geq k_T$. Simultaneously the depth of the C_2 , where C_2 is normalized to unity for large angular distances, increases from 0.07 to 0.6 for pions and kaons and from 0.06 to 0.3 in the previously mentioned ranges in k_T . A two-track efficiency of 99% for primary tracks can be retained throughout by rejection the region where both $|\Delta\varphi^*| \lesssim 0.04$ and $|\Delta\eta| \lesssim 0.01$.

Another variable was put forward in [310], namely the minimum azimuthal distance within the TPC $\Delta\varphi_{\min}^*$. Here it was found that the way of calculating $\Delta\varphi_{\min}^*$ in [310] is too CPU expensive; $\Delta\varphi_{\min}^*$ is almost zero for most pairs; and the mixed event technique can not reproduce the very peaked distribution in $\Delta\varphi_{\min}^*$.

For secondary particles the variables $\Delta\eta$ and $\Delta\varphi^*$ with their proposed derivation are ill-defined. The idea behind the suggested observables is that the spatial distance at the center of the TPC is a good proxy for the overall spatial distance of the tracks within the main tracking device. Due to the longitudinal direction of the magnetic field, the angular distance in the polar direction of two primary tracks simply equals the difference in pseudo-rapidity and does not change as the particles fly through the detector. This is not true if secondary tracks are involved as they originate from a production vertex which is displaced from the primary vertex by tens of centimeters. The problem is illustrated in Fig. 6.2. Remembering that this set of variables was just meant to approximate the distance of the tracks, we can easily come up with a remedy.

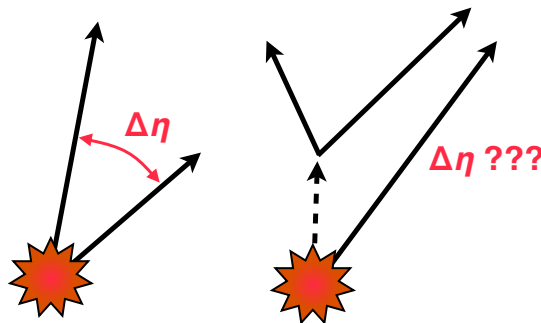


Figure 6.2: $\Delta\eta$ for a pair of two primary tracks and a pair involving a secondary particle. While $\Delta\eta$ describes the spatial separation of the pair of primaries, it does not reflect a particular distance when a secondary particle is involved.

6.3.2 The Mean Distance

In past analyses [294,314–316], the mean distance of two tracks proved to be a handy tool to reject pairs of too close particles. An algorithm which propagates the tracks through the TPC and obtains the mean distance of pairs was developed within this thesis and is successfully used in the analysis of $\Lambda\Lambda$ correlations [317] and $K_s^0 K_s^0$ femtoscopy [159]. In the case of $\Lambda\Lambda$ correlations the track merging is confined to mean distances of less than 3 cm, as shown on the left of Fig. 6.3. This value equals the findings of the pA analysis by the NA49 experiment. For the $K_s^0 K_s^0$ daughters the merging dip is present for mean distances smaller than 5 cm, which still allows to retain enough statistics. However, the combination of a primary proton and a daughter of a Λ decay exhibits track merging out to distances of at least 13 cm as shown on the right of Fig. 6.3 for a study of $p\bar{\Lambda}$ correlations [318]. The same holds true for pairs of $p\Lambda$, visualized in Fig. 6.4 (left). The observation of the effect in two independent analyses makes it unlikely that this observation is not indeed reflecting a detector effect. The found behavior is problematic for two reasons. Firstly, the value of 13 cm is larger than expected and such a wide cut can reject a considerable amount of $p\Lambda$ pairs with small relative momenta, possibly hindering an analysis with high statistical significance. Secondly, no sharp transition to a region which is unaffected by track merging can be located; it is therefore uncertain whether the cut should be placed at 13 cm or more like 17 cm.

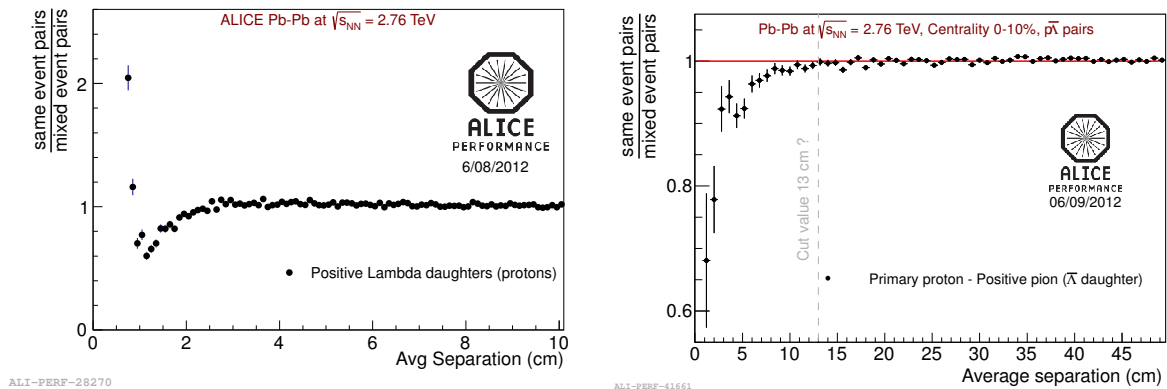


Figure 6.3: Finite two-track resolution visible as a depression below unity in the C_2 . Left: Pairs of $\Lambda\Lambda$. The dip is visible for mean distances of the positively charged daughters smaller than 3 cm [317]. Right: Pairs of $p\bar{\Lambda}$. The drop in two-track efficiency for the proton and the positively charged daughter of the $\bar{\Lambda}$ extends to about 13 cm (marked by the dashed, vertical line) or even further [318].

The effectiveness of the two-track resolution cut can be studied, to some limited detail, with the correlation function vs. the relative momentum $C_2(q)$. Fig. 6.4 shows the $p\Lambda$ correlation function without a cut on the mean distance of the primary and the decay proton in black circles and with the aforementioned rejection of $p\Lambda$ pairs when the two protons were on average

separated by less than 13 cm in red squares. The dip around $q \approx 0.1$ GeV/ c present in the data without cut is a typical signature for track merging. No anti-correlation, i. e. $C_2 < 1$, is expected for the p Λ system in the absence of detector effects, since no repulsive interaction is present in the p Λ final-state. We see that for the data with the cut on the mean distance in red, the depression is lifted a tad, but still the data is not consistent with unity. It can only be concluded that a cut of 13 cm is not sufficient to handle the finite two-track resolution in ALICE.

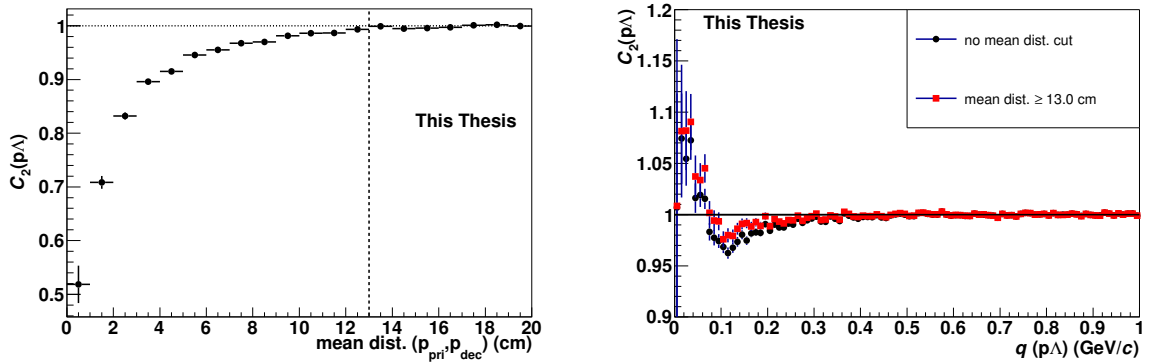


Figure 6.4: Left: p Λ correlation as a function of the mean distance of the primary proton and the decay proton of the Λ . A very broad merging out to distances of about 13 cm is visible. Right: $C_2(q)$ for p Λ pairs without (black circles) and with (red squares) mean distance cut on the two protons. Track merging is apparent as a depletion below unity at $q \approx 0.1$ GeV/ c for both cases.

6.3.3 The Generalized Angular Distances ($\Delta\eta^*$, $\Delta\varphi^*$)

The good experience with the angular distances ($\Delta\eta$, $\Delta\varphi^*$) lead to the decision to generalize them to also be applicable for secondary particles. Instead of simply calculating the angular positions at $R = 1.2$ m from the momenta of the tracks (as proposed in [310]), an algorithm was developed that propagates the tracks taking also into account their spatial positions, i. e. their origin from the secondary vertex, both for the polar and azimuthal position. The advantage of using only a momentum based observable is that one does not have to take into account a changing primary vertex position; the effect was investigated, e. g., for the E877 forward spectrometer at the AGS in [319]. In addition to the event mixing in bins of the longitudinal position of the primary vertex, all event vertices were shifted to $(0, 0, 0)$ to counteract the additional correlation² stemming from the common point of origin in real but not in mixed events. To signify that the angular distance in the polar direction no longer merely equals the

²A linear excess structure was seen in the two-dimensional correlation function vs. the minimum and mean distance of the two protons when not shifting the primary vertex. It vanished as the event vertex was moved.

difference in pseudo-rapidity, an asterisk is added, resulting in the variable names $(\Delta\eta^*, \Delta\varphi^*)$. Using subscript notation to indicate the first or second track of the pair, $\Delta\eta^*$ and $\Delta\varphi^*$ are calculated as

$$\Delta\eta^* = \eta_1^* - \eta_2^*, \quad (6.10)$$

$$\eta^* = -\ln(\tan(\theta^*/2)), \quad (6.11)$$

$$\theta^* = \pi/2 - \arctan(z'/R), \quad (6.12)$$

$$z'_i = z_i - z_i^{\text{vtx}}, \quad (6.13)$$

$$\Delta\varphi^* = 2 \cdot \arctan\left(\frac{\sqrt{(\Delta x')^2 + (\Delta y')^2}}{2R}\right), \quad (6.14)$$

$$\Delta x' = x'_1 - x'_2, \quad (6.15)$$

$$\Delta y' = y'_1 - y'_2, \quad (6.16)$$

$$x'_i = x_i - x_i^{\text{vtx}}, \quad (6.17)$$

$$y'_i = y_i - y_i^{\text{vtx}}, \quad (6.18)$$

where x_i, y_i , and z_i are the position of the track $i = 1, 2$ when it was propagated to the global, transverse radius R ; the position of the primary interaction vertex of the event which contains the track $i = 1, 2$ is denoted by $x_i^{\text{vtx}}, y_i^{\text{vtx}}$, and z_i^{vtx} .

The two-dimensional correlation as a function of $(|\Delta\eta^*|, |\Delta\varphi^*|)$ of the primary proton and the decay proton of the Λ is pictured in Fig. 6.5. The distribution was obtained differentially in centrality and pair transverse momentum, but the shape of the depression proved to be independent of these observables. The depth of the indent around $(0, 0)$ depends on k_T . In order to preserve a 99% two-track efficiency, an ellipsoidal rejection was performed with the axes extending to $|\Delta\eta^*| = 0.14$ and $|\Delta\varphi^*| = 0.03$ as indicated in the figure by the red dashed line. A systematic study regarding the exact values of the two-track resolution cut is included in Section 6.9. The most important finding is, that the merging dip is very asymmetric with a much larger extent in the longitudinal direction. The magnitude in the longitudinal direction $\Delta\eta = 0.14 \xrightarrow{\eta \approx 0} \Delta\theta \approx 0.14 \xrightarrow{R=1.25\text{m}} \Delta z \approx 17.5\text{ cm}$ explains the wide merging structure in the study of the mean distance. The vast asymmetry of the extent of the merging structure in the polar and azimuthal direction gives the two-dimensional rejection criterion an advantage over any one-dimensional measure which does not weight the two scales properly. Two tracks with the same pseudorapidity, separated by $\Delta\varphi^* = 0.04 \xrightarrow{R=1.25\text{m}} \sqrt{(\Delta x)^2 + (\Delta y)^2} \approx 5\text{ cm}$ would be rejected by a cut on the three-dimensional spatial distance of 17.5 cm although the pair is unaffected by merging. Judging by the two-dimensional test, preserves high pair statistics and effectively deals with the two-track resolution.

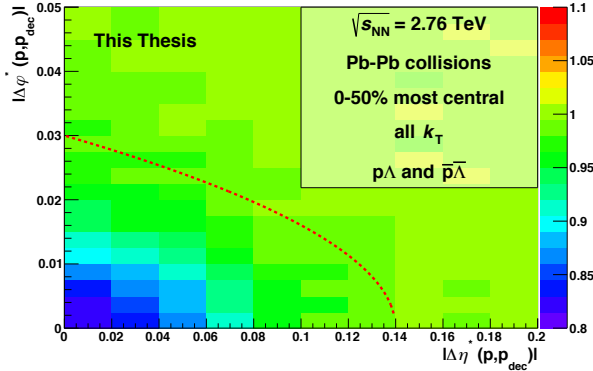


Figure 6.5: Dependence of the correlation function of the selected $p\Lambda$ pairs on the two-dimensional angular distance $(|\Delta\eta^*|, |\Delta\varphi^*|)$ at $R = 1.25$ m of the primary proton and the decay proton of the Λ . Track merging is apparent around $(0, 0)$.

6.4 The Raw Correlation Function

As discussed in Section 6.2, mixed events can only reproduce the real events if the particle distributions are not altered from event to event by acceptance effects. The same argumentation forbids to add particles and anti-particles on the level of real and mixed events (which one is tempted to do due to the simpler algorithmic implementation of the wrong procedure). Rather, only the correlation functions should be merged. This is also true for the two different orientations of the solenoidal magnetic field. The merging of the correlation functions was done following the recipe of the Particle Data Group [32], an error-weighted average:

$$\langle x \rangle \pm \delta \langle x \rangle = \frac{\sum_i w_i x_i}{\sum_i w_i} \pm \left(\sum_i w_i \right)^{-1/2}, \quad (6.19)$$

where the weights are the inverse squared uncertainty of the single measurement

$$w_i = 1 / (\delta x_i)^2. \quad (6.20)$$

Raw $p\Lambda$ and $\bar{p}\bar{\Lambda}$ correlation functions were obtained for three centrality classes, 0–10, 10–30, and 30–50%, differential in transverse mass m_T :

$$m_T = \sqrt{\left(\frac{m_p + m_\Lambda}{2} \right)^2 + k_T^2}, \quad (6.21)$$

$$k_T = \frac{1}{2} |\vec{p}_T^p + \vec{p}_T^\Lambda|. \quad (6.22)$$

The raw correlation functions for pairs of $p\Lambda$ and $\bar{p}\bar{\Lambda}$, merged over the different field orientations, are shown in Section F.1.

6.5 Purity Correction

As discussed in Section 2.2, we want to exploit the correlation between protons and lambda particles which originates from the strong interaction and is consequently limited in its range to a few fm [320].

As mentioned in Section 5.2.5, a significant amount of the selected primary proton candidates originates from feed-down of (dominantly) lambda particles. The decay $\Lambda \rightarrow p + \pi^-$ has a $c\tau$ of 7.89 cm [32], hence these daughter protons will not interact with other particles and therefore will not contribute on their own to a correlation.

A topic of current interest is residual correlations in correlation functions [321, 322]. The correlation of a pair of mother particles can survive their decay and thus feed-down to another system. The issue is discussed in many occasions for pp correlations in Au-Au collisions registered with STAR [323–326]. Also the measurement of pp correlations by ALICE [195] makes an effort to take the remanent correlation from p Λ pairs into account. The effect was discussed already in 1999 by F. Wang in [327]. Fig. 6.6 (left) shows the correlation of p Λ pairs when the momentum difference of the primary proton and the proton of the lambda decay $\Lambda \rightarrow p_{\text{dec}}\pi$ is studied. We see that the peak of the p Λ correlation at a momentum difference of the proton lambda pair $q(\text{p}\Lambda) \approx 0$ is still present in the pp $_{\text{dec}}$ system. However, it is shifted to $q(\text{pp}_{\text{dec}}) \approx 80$ MeV/ c . This shift is explained by two effects. The main reason for the peak displacement is the momentum released in the decay of the Λ of $p = 101$ MeV/ c [32]. As pictured in Fig. 6.6 (right) this release directly translates itself into the pp $_{\text{dec}}$ relative momentum. Ignoring any other influences, we simply expect a peak in the pp $_{\text{dec}}$ correlation function at $q = 101$ MeV/ c . The reason why the peak in Fig. 6.6 (left) appears at a lower momentum difference of about $q(\text{pp}_{\text{dec}}) \approx 80$ MeV/ c can be understood by phase-space considerations, which give a q^2 dependence for the number of pairs. The more abundant high- q pairs dilute the signal, which moves the peak to slightly lower momentum differences, ending up at $q \approx 80$ MeV/ c . Using the same argumentation we can explain the second feature of Fig. 6.6 (left), namely the lowering of the maximum of the correlation function from the p Λ to the pp $_{\text{dec}}$ system by more than a factor of ten. The few pp $_{\text{dec}}$ pairs originating from $q(\text{p}\Lambda)$ equal to about 0 to 20 MeV/ c , which show a value in $C_2 \approx 1.7$ in the example, are diluted by the increase in the number of pairs with q^2 , for which the pairs are less and less correlated.

A significant number of p Λ pairs stem from $\Lambda\Lambda$ pairs, where one partner decayed via $\Lambda \rightarrow p_{\text{dec}}\pi$ and the decay proton is selected, thus forming a p $_{\text{dec}}\Lambda$ pair. The measurement of $\Lambda\Lambda$ pairs by STAR, presented at the Quark Matter Conference 2012 [328], shows no correlation. Consequently, the feed-down from Λ hyperons was considered an uncorrelated background in the proton sample. The update from the STAR collaboration [329] and the preliminary measurement by ALICE [317], both appearing at the end of 2014, show a slight anti-correlation. Keeping in mind the dilution by the decay momentum of about a factor of ten, the assumption

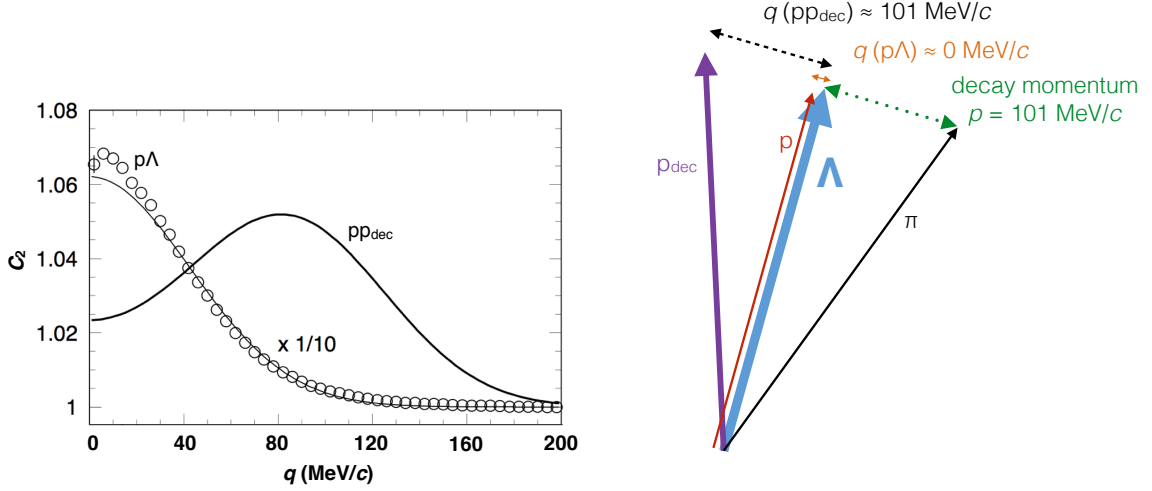


Figure 6.6: Left: Residual $p\Lambda$ correlation in the pp system. Taken from [327]. Right: Kinematics of the decay $\Lambda \rightarrow p_{dec}\pi$ with its consequence on the pp_{dec} system.

of an uncorrelated background for protons from weak decays is a good approximation.

The interest in associated strangeness production near threshold yields a rich set of data for the reaction $pp \rightarrow p\Lambda K^+$ and $pp \rightarrow p\Sigma^0 K^+$ [330–332]. Fig. 6.7 (left) shows the enhancement of the cross-section for the Λ production over the one for the Σ^0 . The clear increase of the ratio from 2.2 for an excess energy ϵ of more than 700 MeV towards small excess energies, where the ratio reaches a value of about 30 is interpreted as an absence of a considerable final-state interaction in the $p\Sigma^0$ system. As shown on the right in Fig. 6.7, the absolute cross-section with the $p\Lambda$ in the final state can not be described by pure phase-space effects, i. e. a quadratic dependence on the excess energy $\sigma \propto a \cdot \epsilon^2$, where a is a constant. However, the $p\Sigma^0$ system perfectly agrees with such a description. This implies that $p\Sigma^0$ pairs will not be correlated.

It was elaborated in Section 5.2 that the contamination of the proton sample from misidentified particles is negligible; in Section 5.3.1 it was discussed that and Section E.2 it was discussed that by looking up the differential single-particle purity and/or feed-down fraction, the pair purity can be obtained. While the value of the pair purity can be gained straight forward by dividing the purity-weighted pair distribution by the non-weighted counts, the calculation of the fluctuation of the pair purity is a little more involved. Calculating this fluctuation is desirable in order to give a good graphical representation of the pair purity, get a good understanding of the applied pair purity correction, and test possible systematic variations of the pair purity with, e. g., relative pair momentum. In Section F.2 it is shown, that within the root framework neither the standard error calculation, nor a binomial error, nor variations of it are applicable,

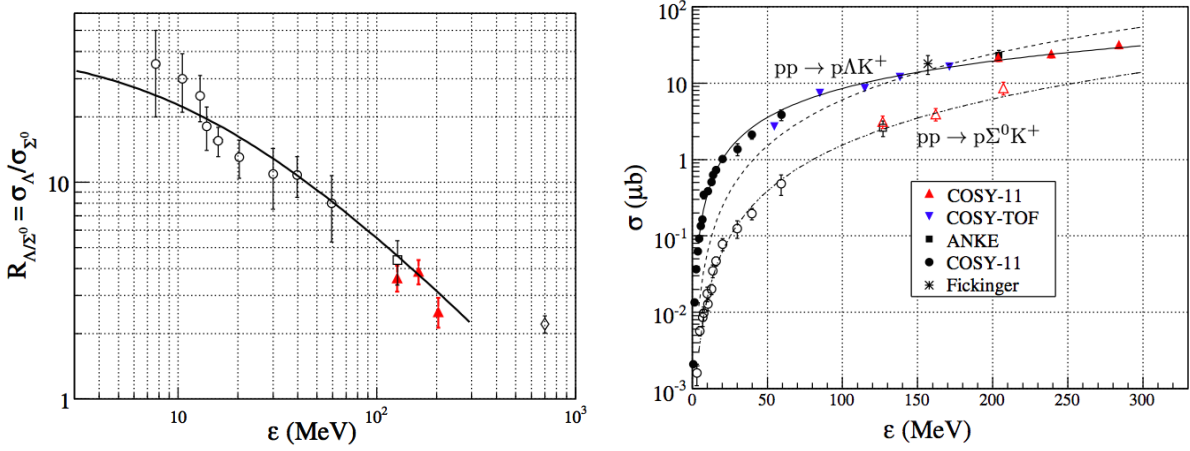


Figure 6.7: Left: Enhancement of $\sigma_{pp \rightarrow p\Lambda K^+}$ over $\sigma_{pp \rightarrow p\Sigma^0 K^+}$ vs. the excess energy ϵ of the system. The ratio increases from about 2.2 at high excess energy towards about 30 at low excess energy. Right: Absolute cross section for the reaction $pp \rightarrow p\Lambda K^+$ (closed symbols) and $pp \rightarrow p\Sigma^0 K^+$ (open symbols). Expectation from pure phase space as dashed lines. Both taken from [332].

and only the central limit theorem appropriately describes the fluctuations. In order to apply the central limit theorem, see Eq. F.1, knowledge of the purity fluctuations is necessary. While the single-particle Λ purity varies by about 0.25 in the accepted region of phase space (see the right panel of Fig. 5.9), the fluctuations of the lambda pair-purity are reduced, since most Λ forming a pair stem from the high-purity region $|\eta| < 0.9$. As shown in Fig. 6.8, the root mean square of the lambda pair-purity distribution is only 0.010. The effect is presented in a bit more detailed way but with slightly different particle selection criteria in [333].

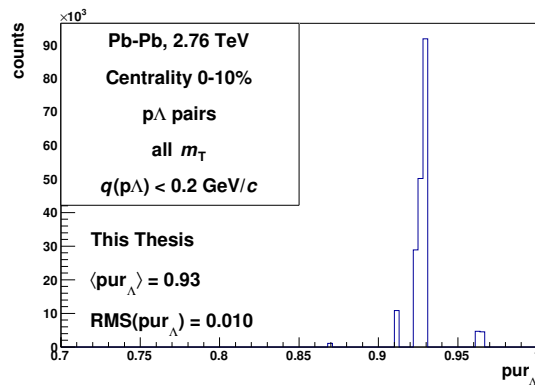


Figure 6.8: Fluctuation of the lambda purity in 0–10% most central events for pairs of p Λ with any m_T and $q(p\Lambda) < 0.2 \text{ GeV}/c$.

Fig. 6.9 shows the Λ pair-purity $\text{pur}_{\Lambda}(q, m_T)$ for the 0–10% most central events and

$m_T \geq 1.9 \text{ GeV}/c^2$. The bigger fluctuations with decreasing relative momentum q are described by the derived vertical error bars. The pair purity is very high, above 95%, and shows no or only a very weak dependence on q , note the scale of ± 0.01 of the y axis. Shown as a red line in the figure is a fit of the pair purity with a constant in the region $q < 0.15 \text{ GeV}/c$. The good description of the data by the constant confirms that for low q the Λ pair purity can be regarded as independent of q . In the current implementation, the fit value is used to correct the data.

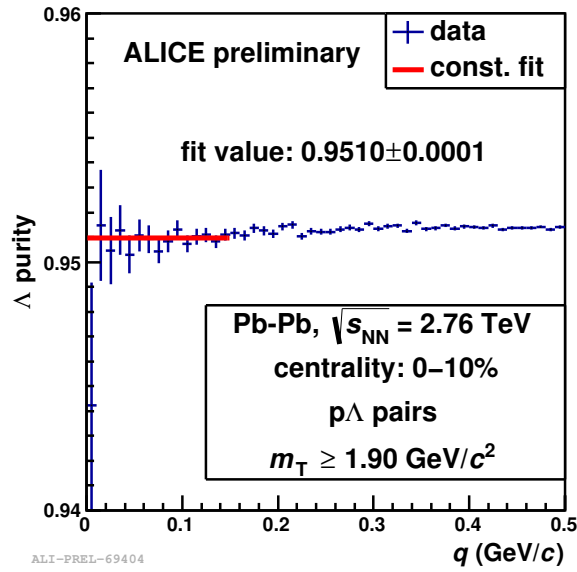


Figure 6.9: Λ pair-purity for the 0–10% most central events and pairs with $m_T \geq 1.9 \text{ GeV}/c^2$. Obtained by looking up for each pair the single particle purity, see Fig. 5.9 (right).

Similar to the Λ pair-purity, the pair fraction of protons and Λ from feed-down is obtained. The overall purity, which includes the Λ purity (pur_Λ) and the feed-down fraction for the sample of Λ (f_Λ) and protons (f_p), factorizes according to

$$\left\langle \text{pur}(q, m_T) \right\rangle_{\text{pair}} = \left\langle \text{pur}_\Lambda(q, m_T) \cdot (1 - f_p(q, m_T)) \cdot (1 - f_\Lambda(q, m_T)) \right\rangle_{\text{pair}} \quad (6.23)$$

$$\approx \left\langle \text{pur}_\Lambda(q, m_T) \right\rangle_{\text{pair}} \cdot \left\langle (1 - f_p(q, m_T)) \right\rangle_{\text{pair}} \cdot \left\langle (1 - f_\Lambda(q, m_T)) \right\rangle_{\text{pair}}, \quad (6.24)$$

where the brackets denote averaging over pairs. The approximation of Eq. 6.24 is valid, since the variation of the purities and feed-down fractions in phase space, i. e. (y, p_T) , is small and only partially correlated. The numerical values for the variables of Eq. 6.24 are cataloged for all centrality classes and m_T selections in Table 6.1. With this, the unique $p\Lambda$ and $\bar{p}\bar{\Lambda}$ correlation

function $C_2^{\text{corr.}}$ can be recovered via the correction

$$C_2^{\text{corr.}}(q, m_T) = \left(\frac{1}{\langle \text{pur}(q, m_T) \rangle_{\text{pair}}} \cdot (C_2^{\text{raw}}(q, m_T) - 1) \right) + 1. \quad (6.25)$$

No difference in the corrected correlation functions between pairs of particles and pairs of anti-particles were found. Therefore, they were combined following the procedure by the PDG (see Eq. 6.19). The following discussion applies to the correlation functions merged over matter and anti-matter.

centrality (%)	m_T (GeV/ c^2)	pair	$\langle \text{pur}_\Lambda \rangle_{\text{pair}}$	$\langle f_\Lambda \rangle_{\text{pair}}$	$\langle f_p \rangle_{\text{pair}}$	$\langle \text{pur} \rangle_{\text{pair}}$
0.0-10.0	1.0–1.4	p Λ	0.928	0.328	0.256	0.464
0.0-10.0	1.0–1.4	$\bar{p}\bar{\Lambda}$	0.955	0.320	0.156	0.548
0.0-10.0	1.4–1.6	p Λ	0.948	0.323	0.220	0.500
0.0-10.0	1.4–1.6	$\bar{p}\bar{\Lambda}$	0.944	0.318	0.147	0.549
0.0-10.0	1.6–1.9	p Λ	0.943	0.325	0.217	0.499
0.0-10.0	1.6–1.9	$\bar{p}\bar{\Lambda}$	0.939	0.321	0.149	0.542
0.0-10.0	1.9– ∞	p Λ	0.951	0.331	0.214	0.500
0.0-10.0	1.9– ∞	$\bar{p}\bar{\Lambda}$	0.947	0.327	0.151	0.542
10.0-30.0	1.0–1.6	p Λ	0.962	0.323	0.208	0.516
10.0-30.0	1.0–1.6	$\bar{p}\bar{\Lambda}$	0.970	0.317	0.117	0.585
10.0-30.0	1.6– ∞	p Λ	0.964	0.323	0.186	0.531
10.0-30.0	1.6– ∞	$\bar{p}\bar{\Lambda}$	0.960	0.318	0.116	0.579
30.0-50.0	1.0– ∞	p Λ	0.979	0.316	0.149	0.570
30.0-50.0	1.0– ∞	$\bar{p}\bar{\Lambda}$	0.981	0.310	0.081	0.621

Table 6.1: Purities used to correct the raw correlation function for uncorrelated contaminations. They were obtained from constant fits for low relative momenta $q < 0.15$ GeV/ c .

6.6 Corrected p Λ Correlation Functions

For the 30–50% most central events, grouping all p Λ pairs resulted in a $\langle m_T \rangle = 1.55$ GeV/ c^2 ; the experimental uncertainty on all reported $\langle m_T \rangle$ is $\mathcal{O}(10^{-5})$ GeV/ c^2 . The higher particle multiplicities for the 10–30% most central events allowed to split up the p Λ sample in half at a transverse mass of 1.6 GeV/ c^2 , giving a mean transverse mass of 1.37 and 1.93 GeV/ c^2 for the two selections. The 0–10% centrality class additionally profited from the dedicated trigger on central collisions, thus four m_T selections could be obtained with good statistics, namely up to

1.4, 1.4–1.6, 1.6–1.9, and more than 1.9 GeV/ c^2 ; the resulting $\langle m_T \rangle$ are 1.27, 1.50, 1.74, and 2.18 GeV/ c^2 . Note that this span in $\langle m_T \rangle$ extends over more than 0.9 GeV/ c^2 . The $\langle m_T \rangle$ of 2.18 GeV/ c^2 for the 0–10% most central data is the largest of any femtoscopic measurement from the SPS [294], RHIC [314, 323] or the LHC [195, 196]. This makes the present study a test for hydrodynamic calculations over unprecedented scales.

Two sets of corrected correlation functions are shown in Fig. 6.10 — with the centrality dependence in the top panel and the m_T dependence in the bottom pad — as first publicly presented at the Quark Matter Conference 2014 [334]. The shown systematic uncertainties are discussed in Section 6.9. In order to disentangle the dependence of the correlation function on the two observables, the top panel displays two correlation functions where the transverse mass coincides to $\langle m_T \rangle = 1.5$ GeV/ c^2 ; the data for the 0–10% most central Pb-Pb collisions are shown in red markers and for the 30–50% most central events in blue. The data for the more central events clearly show less correlation than the data for more peripheral events, evident of a larger source for more central collisions. This meets the expectations from a initial larger geometrical extent and higher energy densities for more central collisions. In the bottom panel, the m_T dependence for 0–10% most central collisions is conveyed. Pairs of p Λ with $1.0 \leq m_T$ (GeV/ c^2) < 1.4 are shown in green markers and pairs with $m_T \geq 1.9$ GeV/ c^2 are shown in gold. The data for the higher m_T shows more correlation than the set for lower m_T . In a hydrodynamical interpretation this increase of correlation is caused by the strong flow at LHC energies. In the centrality-dependent examination, the mean number of participants for the two sets differ by a factor of three [124]. It is remarkable that the m_T -differential study exhibits a difference in the correlation functions similar to the one observed for the varied centrality selection at such high m_T . It is clear from the correlation functions — without invoking any model — that we do not see a saturation of flow effects.

6.7 A Model for the Extraction of p Λ Radii

In the analytic model by R. Lednický and V.L. Lyuboshits [161, 308], the source is described by single emitters which are small compared to the full extent of the fireball. Furthermore, the density of particles in momentum space is assumed to be sufficiently small, so that multi-particle contributions in the final-state interaction can be neglected.

The strong interaction is described as a distortion to the production amplitude in case of non-interacting particles:

$$T^{S,\mu}(p_1, p_2) = T_0^{S,\mu}(p_1, p_2) + \Delta T^{S,\mu}(p_1, p_2), \quad (6.26)$$

$$\Delta T^{S,\mu}(p_1, p_2) = \frac{\sqrt{P^2}}{2\pi^3 i} \sum_{S', \mu'} \int d^4 \kappa \frac{T_0^{S', \mu'}(\kappa, P - \kappa) f^{S, \mu; S', \mu'}(p_1, p_2; \kappa, P - \kappa)}{(\kappa^2 - m_1^2 + i0) [(P - \kappa)^2 - m_2^2 + i0]}, \quad (6.27)$$

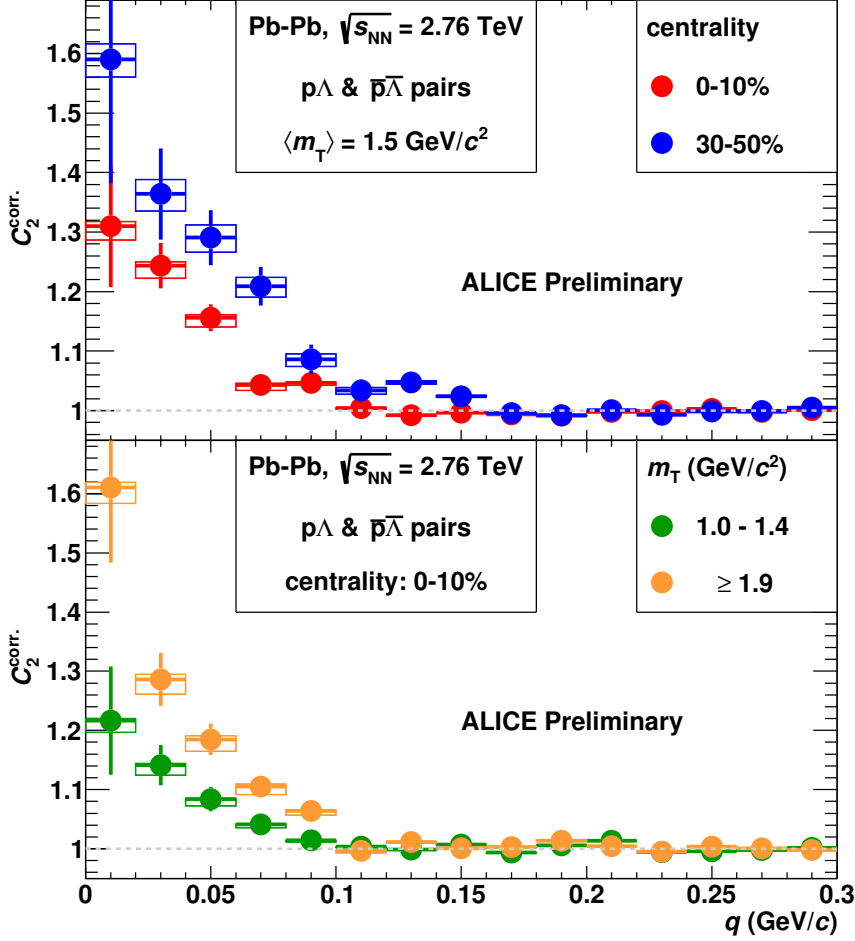


Figure 6.10: Exemplary p Λ and $\bar{p}\bar{\Lambda}$ correlation functions corrected for weak and electromagnetic decays. Centrality dependence at the top, m_T dependence at the bottom. First shown at Quark Matter 2014 [334].

where S is the total spin of pair and μ its projection, p_1 and p_2 are the observed momenta of the single particles, $P = p_1 + p_2$ is the sum of these momenta, κ and $P - \kappa$ are the momenta before the scattering, and f is the scattering amplitude. We recognize the simple structure of Eq. 6.27: two particles with momenta κ and $P - \kappa$ are produced with spin S' and projection μ' as if there was no interaction, they move according to their propagators appearing in the denominator and finally scatter according to f to their final states p_1 and p_2 . The decomposition is visualized in Fig. 6.11.

The problem is solved with the Bethe-Salpeter [336] amplitude

$$\Psi_{p_1, p_2}^S(x_1, x_2) = e^{PX} \left[e^{iq(x_1 - x_2)/2} + \varphi_{p_1, p_2}^S(x) \right], \quad (6.28)$$

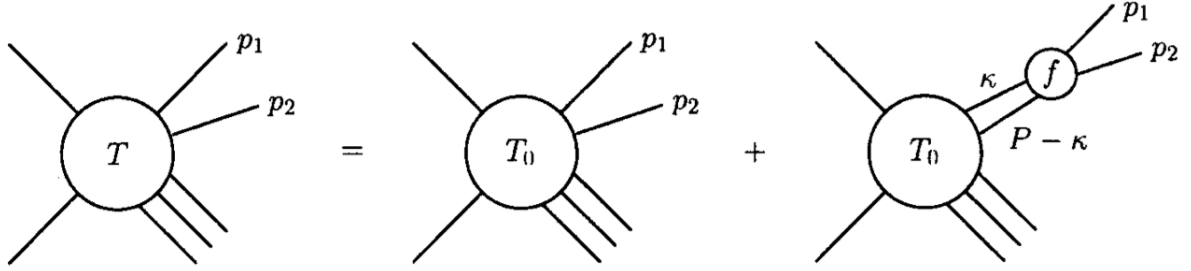


Figure 6.11: Scattering diagram of the final-state interaction. Taken from [335].

where $X = \frac{1}{2} [x_1 + x_2 + (x_1 - x_2)(qP)/P^2]$ is the appropriate four-vector sum of the coordinates x_i , $i = 1, 2$ of the particles. Assuming s-wave dominance reduces the dependence of f^S and thus lets φ^S factorize

$$\varphi_{p_1, p_2}^S(x) = \frac{f^S(k^*)}{2\pi^2} \int \frac{d^3\kappa \exp(-i\kappa r^*)}{\kappa^2 - k^{*2} - i0} F(\kappa^2, t^*), \quad (6.29)$$

where r^* is the distance of the two emitter, and k^* is the three-vector relative momentum in the pair rest frame $q \stackrel{\text{PRF}}{=} \{0, 2k^*\}$. The bracketed part of Eq. 6.28 is a generalization of the text-book solution $\Psi_{\vec{k}}^+$ from Sec. 137 of [337].

The equal time approximation, i. e. the assumption that both particles of the pair are emitted simultaneously, is justified [153, 308] when the difference in emission time of the p and Λ in the pair rest frame Δt^* is small compared to the product of the mass of the particles and the squared radial position r^* of the emitter. For scattering momenta that are small compared to the reduced mass $1/m_{\text{red}} = 1/m_1 + 1/m_2$, it holds that [335]

$$F(\kappa^2, t^*) \simeq \exp\left(-i \frac{\kappa^2 - k^{*2}}{2m(t^*)}\right). \quad (6.30)$$

The solution then takes the form

$$\varphi_{p_1, p_2}^S(x) = f^S(k^*) e^{ik^* r^*} / r^*. \quad (6.31)$$

A common parametrization of the scattering amplitude f^S is given by the effective range approximation

$$f^S(k^*) = \left(\frac{1}{f_0^S} + \frac{1}{2} d_0^S k^{*2} - ik^* \right), \quad (6.32)$$

see, e. g., Sec. 11.2.2 of [338] for a derivation. The Bethe-Salpeter amplitude is then averaged over the space-time points of the emitters. Utilizing a Gaussian distribution for the single-particle

source

$$\propto \exp\left(-\frac{x^2 + y^2 + z^2}{2R_G^2}\right) \quad (6.33)$$

results in the distribution for the distance r^* of the emitters

$$\propto \exp\left(-\frac{r^{*2}}{4R_G^2}\right). \quad (6.34)$$

The Gaussian shape for the source yields an analytical solution for the theoretical two-particle correlation function

$$C_2^{\text{th.}}(k^*) = 1 + \lambda \cdot \sum_S \rho_S \left[\frac{1}{2} |f_0^S(k^*)|^2 \left(1 - \frac{d_0^S}{2\sqrt{\pi}R_G}\right) + \frac{2\Re f^S(k^*)}{\sqrt{\pi}} F_1(2k^* R_G) - \frac{\Im f^S(k^*)}{R_G} F_2(2k^* R_G) \right], \quad (6.35)$$

where $F_1(\zeta) = \int_0^\zeta d\xi \exp(\xi^2 - \zeta^2)/\zeta$, $F_2(\zeta) = (1 - \exp(-\zeta^2))/\zeta$, and ρ_S is the spin density. Following [294, 314, 339, 340] it is assumed that pairs are produced unpolarized, i. e. $\rho_0 = 1/4$ and $\rho_1 = 3/4$ for the singlet $S = 0$ and triplet $S = 1$ respectively; the λ parameter is introduced to accommodate for a possible non-Gaussian shape of the correlation function by strongly decaying resonances (see Section 6.8.2) and allow for a cross-check of the purity correction procedure performed via Eq. 6.25.

As the pA interaction parameters are sufficiently well known (see the systematic evaluation in Section 6.9), Eq. 6.35 directly links the correlation function to the source radius. To facilitate the comparison with other experiments [294, 314, 339, 340], we stick to the commonly used parametrization given in [163].

6.8 Momentum Resolution and Resonances

Two additional effects inhibit the direct comparison of Eq. 6.35 with the experimental correlation functions of Fig. 6.10. They are the experimental momentum resolution and the non-Gaussian shape of the source, which is introduced by the strongly decaying resonances.

6.8.1 Experimental Momentum Resolution

The usual way of taking into account the finite momentum resolution of the detector is to correct the experimental correlation function with a Monte Carlo simulation. Since there is no straight-forward way of including symmetrization effects on the particle production level

for Monte-Carlo generators, any after-burner [301, 341, 342] operates with weights to account for Coulomb and strong final-state interaction and quantum statistical effects. The standard way [287, 343–346] of studying detector resolution effects on the correlation function thus is to assign each pair a weight according to its generated relative momentum and compare it to the recreated weights as a function of the reconstructed relative momentum. The problem with this method is, that a source radius has to be plugged into the analysis of the Monte-Carlo sample. The experimental radius from Pb-Pb data can then only be determined in an iterative procedure, since the correction of the data depends on the outcome of the analysis of the corrected data. An additional, more fundamental problem is that the uncertainty evaluated by the fit procedure can conceptually only be wrong. To retrieve the uncertainty, the fit parameter, i. e. the radius, is varied and compared to the data. However, the momentum-resolution correction on the data is no longer valid for the varied fit parameter. Within this thesis, an improved method was developed that avoids both the iterative procedure and the inaccurate uncertainties by means of a response matrix. It has the additional advantage of a possible parametrization yielding practically infinite statistics for the response matrix whereas the traditional approach severely suffers from the limited statistics available in Monte-Carlo simulations.³

Fig. 6.12 shows the momentum resolution in form of a Monte-Carlo response matrix. The axes represent the diagonal and the perpendicular to it of a q_{rec} vs. q_{sim} graphic. The slightly less intuitive variables $(q_{\text{rec}} - q_{\text{gen}})/\sqrt{2}$ vs. $(q_{\text{rec}} + q_{\text{gen}})/2$ were decided on since they illustrate more clearly a feature of the matrix, namely the independence of the momentum resolution on q in the studied region $q \lesssim 0.3$ GeV/ c . Since both q_{rec} and q_{gen} can only be bigger than zero, the small region indicated by the black lines in Fig. 6.12 can not be populated. Taking this into account, no variation of the momentum resolution, i. e. the spread in $(q_{\text{rec}} - q_{\text{gen}})/\sqrt{2}$, can be observed. This allows us to determine a q -integrated momentum resolution correction.

Fig. 6.13 shows the momentum resolution $(q_{\text{rec}} - q_{\text{gen}})/\sqrt{2}$ integrated over $0.0 \leq (q_{\text{rec}} + q_{\text{gen}})/2$ (GeV/ c) < 0.1 for the three centrality bins investigated within this work. Also shown is a Gaussian fit to each of the datasets, which quantifies the momentum resolution to be about 7 MeV/ c in $(q_{\text{rec}} - q_{\text{gen}})/\sqrt{2}$ for all centrality classes. The centrality dependence shows only a very mild degradation of less than 2% towards more central events.

The pair statistics as a function of $(q_{\text{rec}} + q_{\text{gen}})/2$ were described by a polynomial fit. Taking into account the increase of the number of pairs with increasing q is equally important since — with a finite momentum resolution — the less correlated pairs at high q will dilute the femtoscopic effect at low q even more when they are more abundant. Fig. 6.14 shows the momentum resolution matrices $M_{q_{\text{rec}}}^{q_{\text{gen}}}$ generated from the aforementioned parametrization for 0–10, 10–30, and 30–50% most central events. Generating pairs from a flat distribution in $(q_{\text{rec}} + q_{\text{gen}})/2$ and using the pairs statistics as a weight when obtaining the matrices, allows

³The traditional approach is impossible for this pA study. Only a centrality and m_{T} integrated correction factor could have been obtained. The situation is of course better for highly abundant particles like pions.

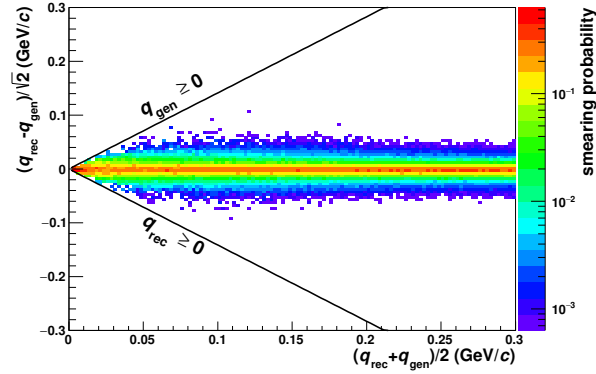


Figure 6.12: Momentum resolution as obtained from a Hijing Monte-Carlo simulation. The histogram was normalized such that the sum over one column in y direction equals one. The axes were chosen due to the symmetry in a q_{rec} vs. q_{sim} representation, they are the diagonal and the perpendicular to the diagonal in the q_{rec} vs. q_{sim} histogram.

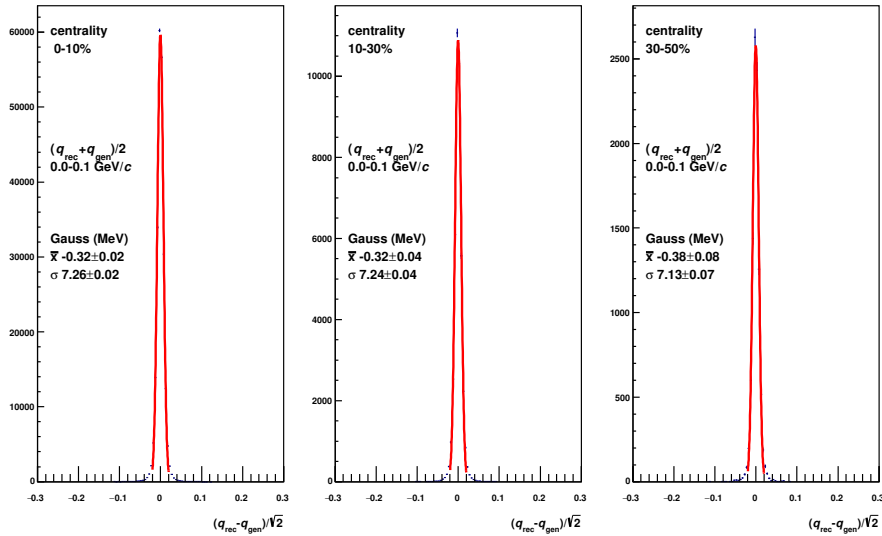


Figure 6.13: Momentum difference distribution integrated over $(q_{\text{rec}} + q_{\text{gen}})/2 \in [0.0, 0.1]$ GeV/c for the three centrality ranges investigated with in this thesis.

to significantly reduce the statistical fluctuations in the low q region and obtain the high granularity shown in Fig. 6.14. The matrices $M_{q_{\text{rec}}}^{q_{\text{gen}}}$ allow to properly translate the theoretical $C_2^{\text{th.}}(q_{\text{gen}})$ of Eq. 6.35 into a correlation as a function of the reconstructed momentum $C_2^{\text{th.}}(q_{\text{rec}})$ via a simple sum

$$C_2^{\text{th.}}(q_{\text{rec}}) = \sum_{q_{\text{gen}}} M_{q_{\text{rec}}}^{q_{\text{gen}}} C_2^{\text{th.}}(q_{\text{gen}}) \quad (6.36)$$

and thus allows to directly compare to the measured correlation function. By performing the sum of Eq. 6.36 during the fitting procedure, appropriate uncertainties are obtained. The standard approach of correcting the correlation function [287, 343–346] needs an analysis of the full Monte-Carlo sample to alter the source radius used in the momentum resolution correction; this has a typical timescale of 100 days of running time. The procedure developed here only needs ~ 1 second, corresponding to a speed-up factor of about 10^9 .

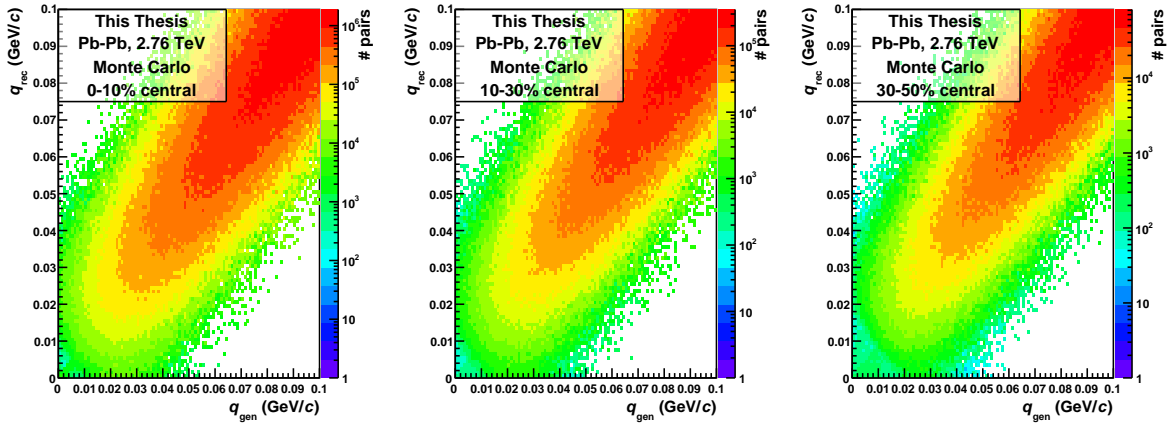


Figure 6.14: Momentum resolution matrix generated from a parametrization of a Monte-Carlo study for 0–10, 10–30, and 30–50%.

6.8.2 Strongly Decaying Resonances

A λ parameter (see Eq. 6.35) below unity is expected from the contribution of strongly decaying resonances [347, 348]. The source size at the LHC for primary particles, excluding strong decay products, is about 12 fm, see [349] for a set of $\sqrt{s_{\text{NN}}}$ -dependent emission functions. The $\Delta(1232)$ has a width of about 117 MeV [32] and thus a $c\tau$ of 1.69 fm. This decay length is roughly 10% of the just mentioned source size. The protons coming from decays of $\Delta(1232)$ resonances will therefore be offset relative to the truly primary protons, which leads to non-Gaussian shape of the source; specifically long non-Gaussian tails develop [350]. Fig. 6.15 shows correlation functions obtained from Fourier transformations of a source with the shape of a Gaussian (left), a Lorentzian (center), and a mix of the two (right). Pairs were sampled according to a q^2 functional for the phase-space dependence and the Fourier transformations were used as weights for these pairs. An equivalent for mixed events was formed by generating 15 times more pairs following the q^2 dependence but without the weights. In order to avoid a bias, the same random pair distributions were used for the Gaussian, Lorentzian, and mixed source. The correlation functions resulted from the division of the weighted set by the unweighted one; therefore, the correlation functions appropriately display the feature of larger statistical fluctuations for small

relative momentum q . Also shown in the panels of the figure is a Gaussian fit to the correlation functions, where the height and width were left as free parameters. The Gaussian fit nicely describes the data of the Gaussian source with a λ parameter, i. e. the height of the fitted Gaussian, of one. Deviations between the fit and the correlation function of the Lorentzian source are apparent. The fit can not describe the shape of the correlation function; importantly for this study, the λ parameter is lowered to about 0.6. In the case of the admixture of a Lorentzian component to the Gaussian source, the Gaussian fit describes the data; however the height of the Gaussian fit is reduced to $\lambda \approx 0.9$.

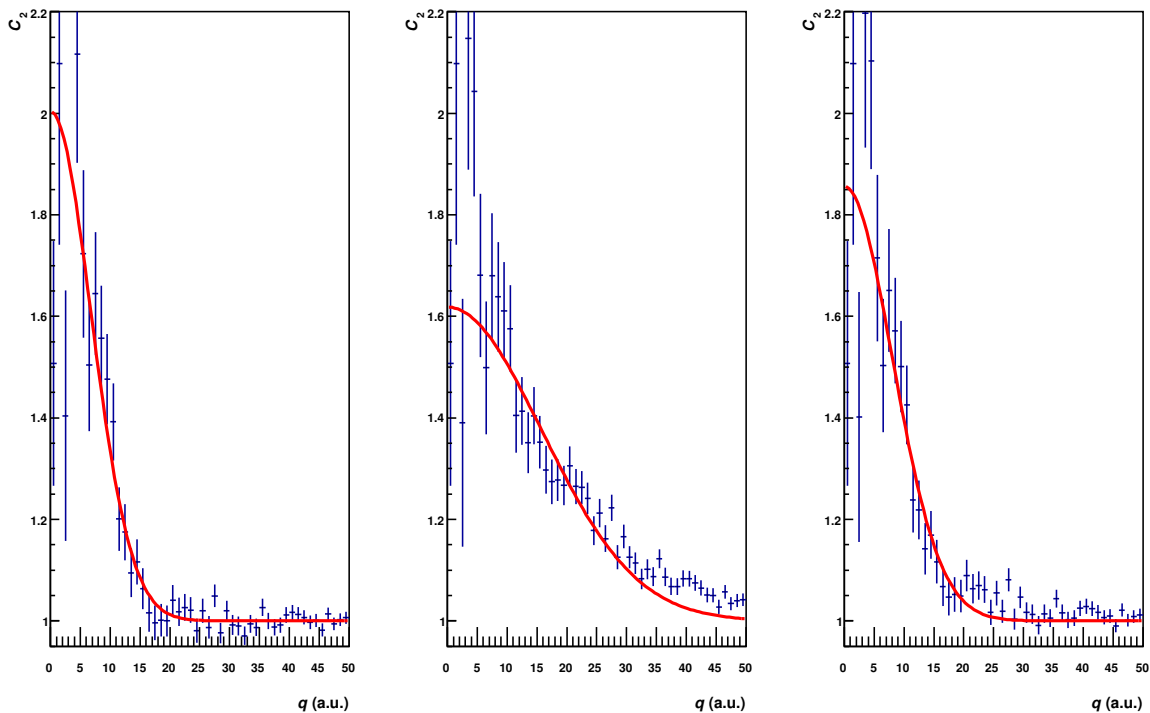


Figure 6.15: Correlation function according to a Fourier transformation of a source with the profile of a Gaussian (left), a Lorentzian (center), and a mix of the two (right) sampled with finite statistics mimicking the q^2 phase-space dependence of pair abundances together with a Gaussian fit.

A realistic model which incorporates the effect of resonances is Therminator [301]. It inherited from SHARE [351] its database of more than 300 particles and their decay tables. Therminator events are generated by performing a statistical hadronization at the freeze-out hypersurface given by a hydrodynamic calculation and tracking the subsequent evolution of the decay cascades. An analysis of these events showed [352] that the pA source (including the feed-down from strong decays) is very Gaussian compared to the pion source [287]. Furthermore

the study proved that a fit with a λ parameter of 0.95 accommodates for the effect of strongly decaying resonances in the p Λ system and recovers the size of the source.

6.9 p Λ Systematic Uncertainties

The systematic deviations of the p Λ radii with the λ parameter fixed to 0.95 are given here. For each identified source of a possible bias, the selection criteria or correction procedures were varied and new sets of corrected correlation functions were obtained. Each correlation function was fit with Eq. 6.35 propagated through the experimental momentum resolution matrix as given by Eq. 6.36. For each source of systematic uncertainty the maximal positive and negative deviation in the p Λ radius parameter R was acquired in terms ΔR (fm). The total systematic error was obtained as the quadratic sum of the single deviations.

The standard analysis uses the fraction of Λ from Σ^0 decays $f_{\Sigma^0} = N_{\Sigma^0}/(N_{\Lambda} + N_{\Sigma^0}) = 0.268$ from Therminator [301]. In order to assess the uncertainty on this ratio, the values of the study by Andronic *et al.* [307] and Becattini *et al.* [302] were used as well. The model by Andronic *et al.* uses a standard value for the temperature $T = 156$ MeV, which yields the fraction $f_{\Sigma^0} = 0.293$. Also incorporated was here a temperature change of $\Delta T = \pm 4$ MeV. For both temperatures, the model gives $f_{\Sigma^0} = 0.286$. The study by Becattini *et al.* [302] not only gives particle ratios at the chemical freeze-out, but also uses a hadronic cascade [353] to obtain the particle ratios at the hadronization stage. The value is $f_{\Sigma^0} = 0.275$ for both the chemical freeze-out and the value at hadronization. Note that all model variations departed from the standard value for $f_{\Sigma^0} = 0.268$ only to higher values with the maximum deviation observed for the standard temperature of the model by Andronic *et al.* of $f_{\Sigma^0} = 0.293$. The impact on the extracted p Λ radii was evaluated by redoing the purity correction procedure of Eq. 6.25 and obtaining the p Λ radius from the alternate corrected correlation function. The change in radii can be seen in Table 6.2. The largest deviation seen was -0.08 fm at low m_T in the 0–10% most central collisions, where also the radius itself is the largest; the relative systematic uncertainty here arising from the contribution of the electromagnetic decay is $\approx 1\%$.

The contribution from weak decays is only 10% in the Λ sample. Varying the yield of all multi-strange particles simultaneously by $\pm 5\%$ changes the Λ feed-down fraction by only around $\pm 0.5\%$. Looking at the numbers given in Table 6.3, it becomes clear that the systematic errors are highly correlated across m_T and centrality.

The parametrization of the pair momentum resolution matrix was changed by ± 0.2 MeV/ c in both width and offset, only one parameter was changed at the same time. With each matrix a new fit was performed. See Tab. 6.4 for the quantitative effects on the radii.

Andronic, $f_{\Sigma^0} = 0.293$				Andronic ± 4 MeV, $f_{\Sigma^0} = 0.286$			
m_T (GeV/ c^2)	0–10%	10–30%	30–50%	m_T (GeV/ c^2)	0–10%	10–30%	30–50%
1.0–1.4	-0.08			1.0–1.4	-0.06		
1.4–1.6	-0.06	-0.06		1.4–1.6	-0.04	-0.04	
1.6–1.9	-0.07		-0.05	1.6–1.9	-0.05		-0.03
1.9 \leq	-0.07	-0.05		1.9 \leq	-0.04	-0.04	

Becattini std. & new tech., $f_{\Sigma^0} = 0.275$			
m_T	0–10%	10–30%	30–50%
1.0–1.4	-0.02		
1.4–1.6	-0.02	-0.01	
1.6–1.9	-0.02		-0.01
1.9 \leq	-0.02	-0.01	

Table 6.2: Systematic errors from EM decays quantified as ΔR (fm).

multi-strange -5%				multi-strange +5%			
m_T (GeV/ c^2)	0–10%	10–30%	30–50%	m_T (GeV/ c^2)	0–10%	10–30%	30–50%
1.0–1.4	+0.01			1.0–1.4	-0.01		
1.4–1.6	+0.01	+0.01		1.4–1.6	-0.01	-0.01	
1.6–1.9	+0.01		+0.01	1.6–1.9	-0.01		0.00
1.9 \leq	+0.01	+0.01		1.9 \leq	-0.01	-0.01	

Table 6.3: Systematic errors from weak decays as ΔR (fm).

Due to the higher number of mixed event pairs than real event pairs, the correlation function has to be normalized to unity in some region. The specific choice of the range is somewhat arbitrary, only the general guidance exists that one should not normalize too far away from the excess region at low q , but also not at too small q in order to safely exclude the excess region. The standard region is situated at $0.2 < q$ (GeV/ c) < 0.3 . For the systematic uncertainty estimation, this range was shifted by ± 0.02 GeV/ c , i. e. $\pm 10\%$. No consistent trend, i.e. larger radii for a normalization at higher q or vice versa, could be observed; the changes in radii appear to be rather random. See Table 6.5 for the systematic uncertainties from the fit range variation.

The main selection criterion for the Λ particles is the cut on the invariant mass m_{inv} . By changing the cut on m_{inv} , the whole analysis chain is tested: Different particles will contribute to, e.g. the normalization of the correlation function. Changing the cut from 4 MeV (std.)

width +0.2 MeV				width -0.2 MeV			
m_T (GeV/ c^2)	0-10%	10-30%	30-50%	m_T (GeV/ c^2)	0-10%	10-30%	30-50%
1.0-1.4	-0.01			1.0-1.4	+0.01		
1.4-1.6	0.00	0.00		1.4-1.6	+0.01	+0.01	
1.6-1.9	-0.01		0.00	1.6-1.9	0.00		+0.01
1.9 \leq	-0.01	0.00		1.9 \leq	0.00	0.00	

offset +0.2 MeV				offset -0.2 MeV			
m_T (GeV/ c^2)	0-10%	10-30%	30-50%	m_T (GeV/ c^2)	0-10%	10-30%	30-50%
1.0-1.4	-0.03			1.0-1.4	+0.04		
1.4-1.6	-0.02	-0.02		1.4-1.6	+0.03	+0.02	
1.6-1.9	-0.03		-0.01	1.6-1.9	+0.02		+0.02
1.9 \leq	-0.02	-0.02		1.9 \leq	+0.02	+0.02	

Table 6.4: Systematic errors from momentum resolution as ΔR (fm).

norm. range +0.02 GeV				norm. range -0.02 GeV			
m_T (GeV/ c^2)	0-10%	10-30%	30-50%	m_T (GeV/ c^2)	0-10%	10-30%	30-50%
1.0-1.4	-0.07			1.0-1.4	+0.02		
1.4-1.6	+0.04	+0.02		1.4-1.6	-0.04	+0.04	
1.6-1.9	0.00		-0.01	1.6-1.9	-0.05		-0.03
1.9 \leq	0.00	+0.01		1.9 \leq	+0.05	-0.01	

Table 6.5: Systematic errors from normalization as ΔR (fm).

around the Λ mass to 5 MeV around the Λ mass increases the background by +25% and thus tests the assumption of the non-correlated background. The correlation functions are corrected with the reevaluated Λ purities obtained from m_{inv} fits. The correlation functions obtained with a changed m_{inv} cut will therefore also be sensitive to a possible bias in the m_{inv} fits. The variations can be found in Table 6.6. The study on the invariant mass was done without a m_T dependence and a 1-dimensional selection on the DCA of $\text{DCA}_{xy} < 0.1$ cm.

The validity of the feed-down correction for protons was tested by tightening the 2-dimensional DCA cuts. For protons the DCA_{xy} cut was narrowed by 20% to 0.08 cm, for anti-protons the DCA_z cut was contracted by 25% to 0.15 cm. New sets of proton feed-down purities were obtained and used for the correction of the correlation functions. The change in radii can be found in Table 6.7.

$ m_{\text{inv}}(\Lambda) - m_{\text{inv}}(\text{PDG}) \leq 3 \text{ MeV}/c^2$				$ m_{\text{inv}}(\Lambda) - m_{\text{inv}}(\text{PDG}) \leq 5 \text{ MeV}/c^2$			
$m_{\text{T}} \text{ (GeV}/c^2)$	0–10%	10–30%	30–50%	$m_{\text{T}} \text{ (GeV}/c^2)$	0–10%	10–30%	30–50%
1.0–1.4				1.0–1.4			
1.4–1.6	-0.05	-0.03	-0.02	1.4–1.6	+0.02	-0.03	+0.03
1.6–1.9				1.6–1.9			
$1.9 \leq$				$1.9 \leq$			

Table 6.6: Systematic errors from m_{inv} selection.

$m_{\text{T}} \text{ (GeV}/c^2)$	tight DCA		
	0–10%	10–30%	30–50%
1.0–1.4	-0.04		
1.4–1.6	-0.10	-0.05	
1.6–1.9	+0.06		+0.10
$1.9 \leq$	-0.03	+0.04	

Table 6.7: Systematic errors from proton feed-down as ΔR (fm).

To investigate a possible residual track merging in the correlation function with the standard two-track resolution (TTR) cuts, one would want to vary the two-track cuts and study the change of radii. It was found that a correlation between $\Delta\varphi^*$ and m_{T} exists. At a given momentum difference q , a low k_{T} pair has a large opening angle $\Delta\varphi^*$ while a high k_{T} pair has a small opening angle $\Delta\varphi^*$. By changing the cut on $\Delta\varphi^*$ one thus also changes the m_{T} distributions and the $\langle m_{\text{T}} \rangle$ of the pairs. As the radius depends on m_{T} , a change in radius with a change of the $\Delta\varphi^*$ cut would be expected even with a perfect detector. Thus, a change of the $\Delta\varphi^*$ is inappropriate for a systematic study here. $\Delta\eta^*$ showed no such correlation and was varied by $\pm 10\%$ as well as $+20\%$ as can be seen in Table 6.8.

The impact of the uncertainty of the knowledge of the p Λ interaction is quantified by taking different sets of parameters. The standard analysis uses the parameters from [163]. These parameters were also chosen by E895 [339], STAR [314], HADES [340], and NA49 [294]. For the systematic variation of these interaction parameters, two important groups trying to theoretically describe the hyperon nucleon interactions were identified: The Nijmegen and the Jülich group. The Nijmegen soft core (NSC) model evolved into the extended soft core (ESC) model. There exist different sets of parameters for the ESC04 model, named ESC04a, ESC04b, ESC04c, and ESC04d [354]. There is also a further development, namely the ESC08 model. The parameters for the ESC08a" can be found in [355]. The J04 model by the Jülich group with its variation the J04c model, where some κ exchange was replaced by a contact term can

$\Delta\eta^* -10\%$				$\Delta\eta^* +10\%$			
m_T (GeV/ c^2)	0-10%	10-30%	30-50%	m_T (GeV/ c^2)	0-10%	10-30%	30-50%
1.0-1.4	-0.02			1.0-1.4	-0.02		
1.4-1.6	+0.05	+0.05		1.4-1.6	-0.03	-0.02	
1.6-1.9	+0.05		+0.01	1.6-1.9	-0.06		-0.02
1.9 \leq	+0.02	+0.01		1.9 \leq	0.00	-0.02	

$\Delta\eta^* +20\%$			
m_T (GeV/ c^2)	0-10%	10-30%	30-50%
1.0-1.4	-0.04		
1.4-1.6	-0.04	-0.03	
1.6-1.9	-0.04		-0.03
1.9 \leq	0.00	-0.04	

Table 6.8: Systematic errors from TTR treatment as ΔR (fm).

be found in [356]. There is also a recent measurement by the experimental Hires collaboration in [357]. The systematic changes in the radii are tabulated in Tab. 6.9.

The fit range was varied from the standard q (GeV/ c) < 0.20 to q (GeV/ c) $< 0.18, 0.16, 0.14,$ and 0.12 . Note that especially the q (GeV/ c) < 0.12 uses much less data. The results with the altered fit range are quantified in Table 6.10.

In order to obtain the total systematic error for each source the maximum deviation was taken, see Table 6.11. The total systematic error was evaluated as the quadratic sum of the errors for each source of Table 6.11. The total systematic error for each centrality and m_T selection is shown in Table 6.12. The systematic error is asymmetric, with a higher magnitude to the negative side. This negative error is dominated by the uncertainty of the p Λ interaction strength.

Hires				J04			
m_T (GeV/ c^2)	0–10%	10–30%	30–50%	m_T (GeV/ c^2)	0–10%	10–30%	30–50%
1.0–1.4	-0.16			1.0–1.4	-0.02		
1.4–1.6	-0.10	-0.11		1.4–1.6	+0.01	0.00	
1.6–1.9	-0.11		-0.07	1.6–1.9	+0.01		+0.02
1.9 \leq	-0.10	-0.08		1.9 \leq	0.00	-0.02	
J04c				ESC04a			
m_T (GeV/ c^2)	0–10%	10–30%	30–50%	m_T (GeV/ c^2)	0–10%	10–30%	30–50%
1.0–1.4	-0.08			1.0–1.4	-0.25		
1.4–1.6	-0.03	-0.05		1.4–1.6	-0.15	-0.17	
1.6–1.9	-0.04		-0.02	1.6–1.9	-0.16		-0.11
1.9 \leq	-0.04	-0.02		1.9 \leq	-0.14	-0.11	
ESC04b				ESC04c			
m_T (GeV/ c^2)	0–10%	10–30%	30–50%	m_T (GeV/ c^2)	0–10%	10–30%	30–50%
1.0–1.4	-0.15			1.0–1.4	-0.04		
1.4–1.6	-0.09	-0.10		1.4–1.6	-0.01	-0.02	
1.6–1.9	-0.09		-0.06	1.6–1.9	-0.01		0.00
1.9 \leq	-0.08	-0.06		1.9 \leq	-0.01	0.00	
ESC04d				ESC08a''			
m_T (GeV/ c^2)	0–10%	10–30%	30–50%	m_T (GeV/ c^2)	0–10%	10–30%	30–50%
1.0–1.4	-0.05			1.0–1.4	-0.04		
1.4–1.6	-0.02	-0.03		1.4–1.6	-0.03	-0.03	
1.6–1.9	-0.03		-0.01	1.6–1.9	-0.03		-0.02
1.9 \leq	-0.02	-0.02		1.9 \leq	-0.03	-0.02	

Table 6.9: Systematic errors from p Λ interaction parameters as ΔR (fm).

$q_{\text{inv}} < 0.18$				$q_{\text{inv}} < 0.16$			
m_{T} (GeV/ c^2)	0–10%	10–30%	30–50%	m_{T} (GeV/ c^2)	0–10%	10–30%	30–50%
1.0–1.4	+0.01	+0.01		1.0–1.4	0.00	+0.01	
1.4–1.6	0.00		0.00	1.4–1.6	-0.01		-0.01
1.6–1.9	-0.01	0.00		1.6–1.9	-0.01	0.00	
1.9 \leq	0.00			1.9 \leq	+0.01		

$q_{\text{inv}} < 0.14$				$q_{\text{inv}} < 0.12$			
m_{T} (GeV/ c^2)	0–10%	10–30%	30–50%	m_{T} (GeV/ c^2)	0–10%	10–30%	30–50%
1.0–1.4	+0.01	+0.03		1.0–1.4	-0.01	+0.02	
1.4–1.6	-0.02		+0.01	1.4–1.6	-0.05		+0.05
1.6–1.9	-0.03	-0.01		1.6–1.9	-0.06	+0.03	
1.9 \leq	0.00			1.9 \leq	0.00		

Table 6.10: Systematic errors from fit range variation as ΔR (fm).

m_T (GeV/ c^2)	0–10%	10–30%	30–50%
	EM FD Λ		
1.0–1.4	+0.00 –0.08	+0.00	
1.4–1.6	+0.00 –0.06	–0.06	
1.6–1.9	+0.00 –0.07	+0.00	+0.00 –0.05
1.9 \leq	+0.00 –0.07	–0.05	
	weak FD Λ		
1.0–1.4	+0.01 –0.01	+0.01	
1.4–1.6	+0.01 –0.01	–0.01	
1.6–1.9	+0.01 –0.01	+0.01	+0.01 –0.01
1.9 \leq	+0.01 –0.01	–0.01	
	mom. res.		
1.0–1.4	+0.04 –0.03	+0.02	
1.4–1.6	+0.03 –0.02	–0.02	
1.6–1.9	+0.02 –0.03	+0.02	+0.02 –0.01
1.9 \leq	+0.02 –0.02	–0.02	
	norm. range		
1.0–1.4	+0.02 –0.07	+0.04	
1.4–1.6	+0.04 –0.04	–0.00	
1.6–1.9	+0.00 –0.05	+0.01	+0.00 –0.03
1.9 \leq	+0.05 –0.00	–0.01	

m_T (GeV/ c^2)	0–10%	10–30%	30–50%
	m_{inv}		
1.0–1.4	+0.02 –0.05	+0.00	
1.4–1.6	+0.02 –0.05	–0.03	+0.03 –0.02
1.6–1.9	+0.02 –0.05	+0.00	
1.9 \leq	+0.02 –0.05	–0.03	
	FD proton		
1.0–1.4	+0.00 –0.04	+0.00	
1.4–1.6	+0.00 –0.10	–0.05	+0.10 –0.00
1.6–1.9	+0.06 –0.00	+0.04	
1.9 \leq	+0.00 –0.03	–0.00	
	TTR		
1.0–1.4	+0.00 –0.04	+0.05	
1.4–1.6	+0.05 –0.04	–0.03	+0.01 –0.03
1.6–1.9	+0.05 –0.06	+0.01	
1.9 \leq	+0.02 –0.00	–0.04	
	pA interaction		
1.0–1.4	+0.00 –0.25	+0.00	
1.4–1.6	+0.01 –0.15	–0.17	+0.02 –0.11
1.6–1.9	+0.01 –0.16	+0.00	
1.9 \leq	+0.00 –0.14	–0.11	
	fit range		
1.0–1.4	+0.01 –0.01	+0.03	
1.4–1.6	+0.00 –0.05	–0.00	+0.05 –0.01
1.6–1.9	+0.00 –0.06	+0.03	
1.9 \leq	+0.01 –0.00	–0.01	

Table 6.11: Maximum systematic error on R (fm) for each source of systematic error.

m_T (GeV/ c^2)	0–10%	10–30%	30–50%
	quadratic sum		
1.0–1.4	+0.05 –0.28	+0.07	
1.4–1.6	+0.07 –0.21	–0.19	+0.12 –0.13
1.6–1.9	+0.08 –0.21	+0.06	
1.9 \leq	+0.06 –0.18	–0.13	

Table 6.12: Quadratic sum of the systematic errors on R (fm).

6.10 Experimental p Λ Radii

Fig. 6.16 shows a fit of the ALICE preliminary p Λ correlation functions of Fig. 6.10 with Eq. 6.36 using a λ parameter fixed to 0.95 to take into account resonances. This leaves the radius parameter as the only quantity determined via the fit procedure. As can be seen from the figure, the fit function describes the experimental data well. The resulting radii for all centralities and m_T selections obtained within this thesis are shown in Fig. 6.17 together with preliminary results for charged pions and protons [195] and neutral kaons published in [358]. The p Λ values are also tabulated in Table 6.13. As can be seen, the m_T scaling, which is already slightly broken between pions and kaons, is clearly broken by the p Λ radii. The systematic uncertainties concerning the p Λ radii are evaluated in Section 6.9.

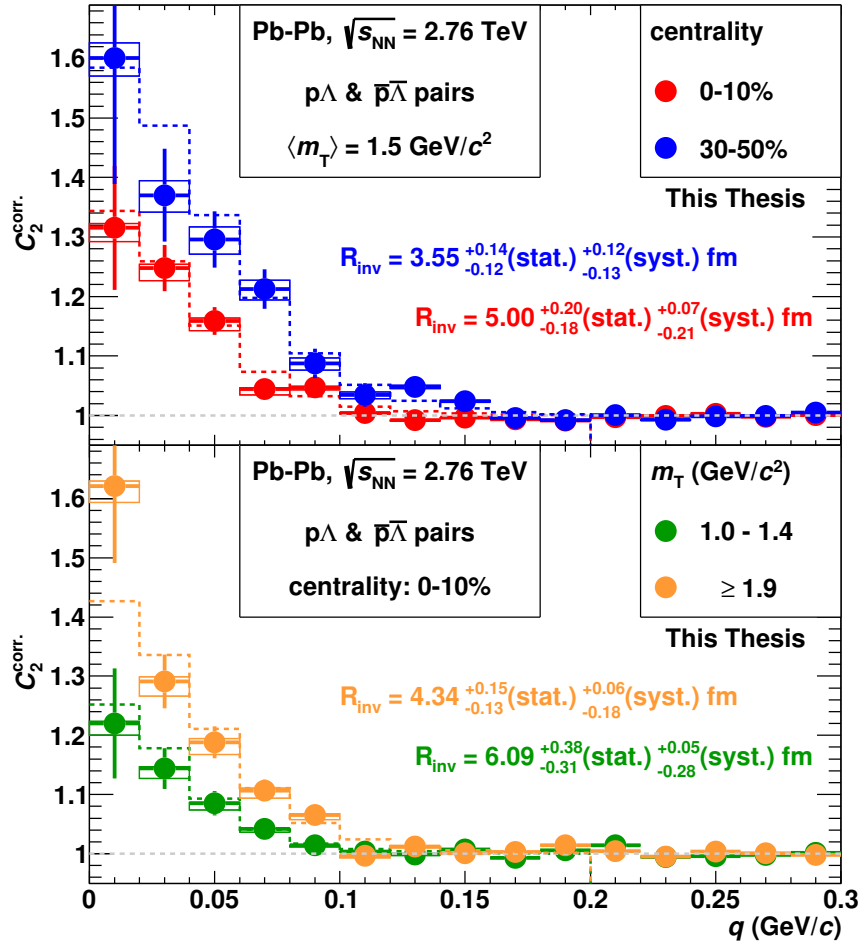


Figure 6.16: Preliminary ALICE p Λ and $\bar{p}\bar{\Lambda}$ correlation functions corrected for weak and electromagnetic decays [334] together with a fit [161, 308] with fixed $\lambda = 0.95$. Centrality dependence at the top, m_T dependence at the bottom.

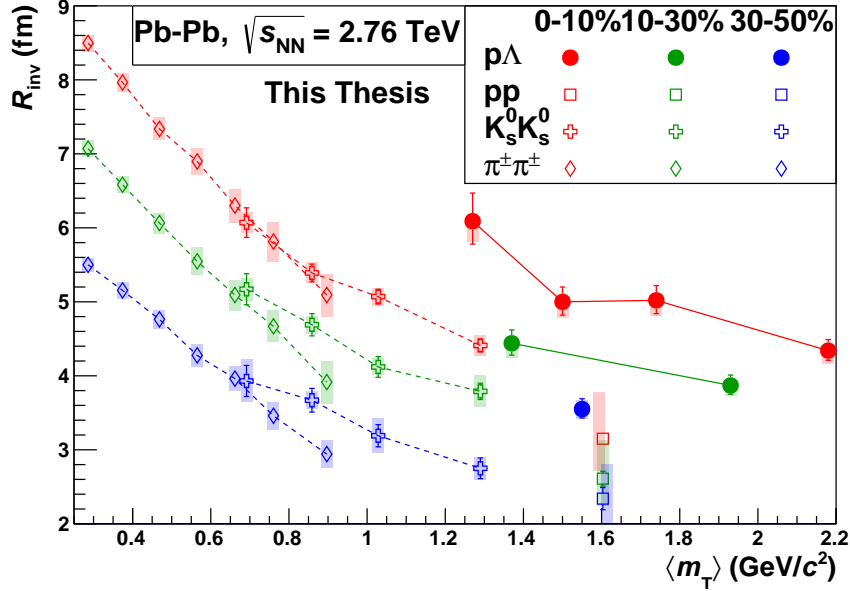


Figure 6.17: Experimentally determined p Λ radii compared to ALICE data for pions and protons [195] and neutral kaons [358]. The p Λ radii show the expected centrality and m_T dependence. The breaking of the m_T scaling, already visible from the kaon radii, is most apparent from the p Λ study.

centrality (%)	$\langle m_T \rangle$ (GeV/ c^2)	radius (fm)
0.0–10.0	1.27	$6.09^{+0.38}_{-0.31}$ (stat.) $^{+0.05}_{-0.28}$ (syst.)
0.0–10.0	1.50	$5.00^{+0.20}_{-0.18}$ (stat.) $^{+0.07}_{-0.21}$ (syst.)
0.0–10.0	1.74	$5.02^{+0.20}_{-0.18}$ (stat.) $^{+0.08}_{-0.21}$ (syst.)
0.0–10.0	2.18	$4.34^{+0.15}_{-0.13}$ (stat.) $^{+0.06}_{-0.18}$ (syst.)
10.0–30.0	1.37	$4.44^{+0.18}_{-0.16}$ (stat.) $^{+0.07}_{-0.19}$ (syst.)
10.0–30.0	1.93	$3.87^{+0.14}_{-0.12}$ (stat.) $^{+0.06}_{-0.13}$ (syst.)
30.0–50.0	1.55	$3.55^{+0.14}_{-0.12}$ (stat.) $^{+0.12}_{-0.13}$ (syst.)

Table 6.13: Centrality and m_T differential source radii from p Λ correlations with statistical and systematic uncertainties.

In a study with the HKM model [359], the observation of larger radii for kaons than for pions was linked to the large transverse flow in Pb-Pb collisions at the LHC. The HKM model predicts a scaling in k_T rather than m_T for Pb-Pb collisions at the foreseen Run 2 LHC energy of $\sqrt{s_{NN}} = 5.1$ TeV for pions and kaons above k_T 0.5 GeV/ c . The k_T scaling is supposed to be fulfilled to a lesser extent (discrepancies on the level of few percent) for $\sqrt{s_{NN}} = 2.76$ TeV [359, 360]. Fig. 6.18 shows the data of Fig. 6.17, now as a function of k_T . A better,

although not perfect, scaling behavior as a function of k_T than as a function of m_T can be observed.

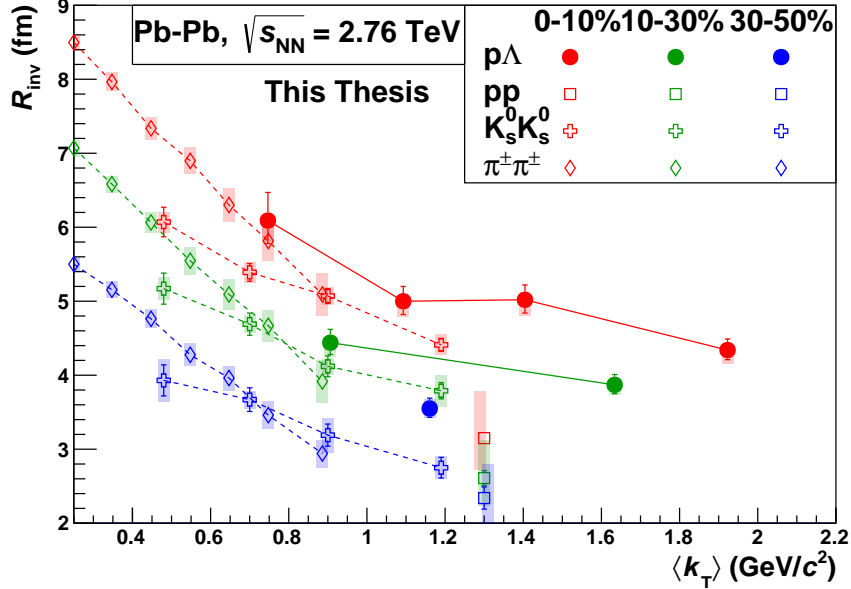


Figure 6.18: Same data as Fig. 6.17, but here as a function of k_T .

Another calculation for the source radii of identified particles at the LHC can be found in [361]. This 3+1D viscous hydrodynamical study does not incorporate a hadronic phase. With this, it aims at disentangling the possible sources of the breaking of the m_T scaling. It follows the reasoning that if m_T scaling holds in the pure hydrodynamical scenario, the origin for the breaking of the m_T scaling must lie in the hadronic phase. An approximate m_T scaling within 5% for all centralities, all m_T , and all investigated particle species, i. e. pions, kaons, and protons, was found for the three-dimensional out, side and long radii obtained in the longitudinally co-moving system. However, the scaling was found to be broken in the one-dimensional radius R_{inv} and could only be recovered by dividing R_{inv} by the empirical factor f ,

$$\begin{aligned}
 f &= \sqrt{(\sqrt{\gamma_T} + 2)/3} \\
 &= \sqrt{\left(\sqrt{\frac{m_T}{m}} + 2\right)/3},
 \end{aligned}
 \tag{6.37}$$

as visualized in Fig. 6.19. In the model, without the factor f the radii for kaons are smaller than for pions. In the observable R_{inv}/f , the faster pions are more affected by the phenomenological factor f and the m_T scaling is recovered in the model. Without the scaling factor, the experimental data in Fig. 6.17 exhibit the contrary ordering to the model of [361]. In real

data, the kaon radii are larger than the pion radii at the same m_T . Thus, the scaling factor will increase the tension between kaons and pions; the same holds true for comparing the p Λ radii to the lighter species. Fig. 6.20 shows the experimental radii with the scaling factor f applied. It is apparent that the scaling procedure worsens the agreement between the radii of the different species. In [361] it is stated that the present scenario shows the importance of the hadronic rescattering phase.

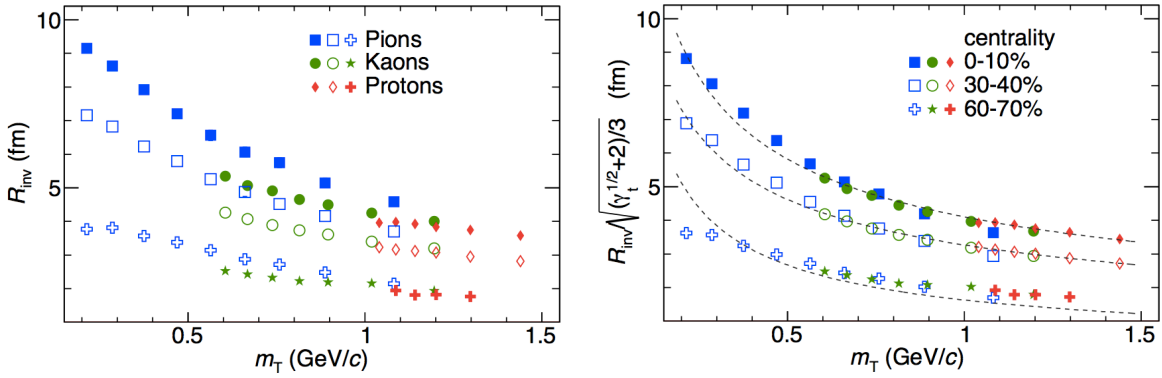


Figure 6.19: Pion, kaon, and proton radii in Pb-Pb collisions at 2.76 TeV obtained from 3+1D hydro + Therminator without a scaling factor (left) and with the scaling factor f (right). Taken from [361].

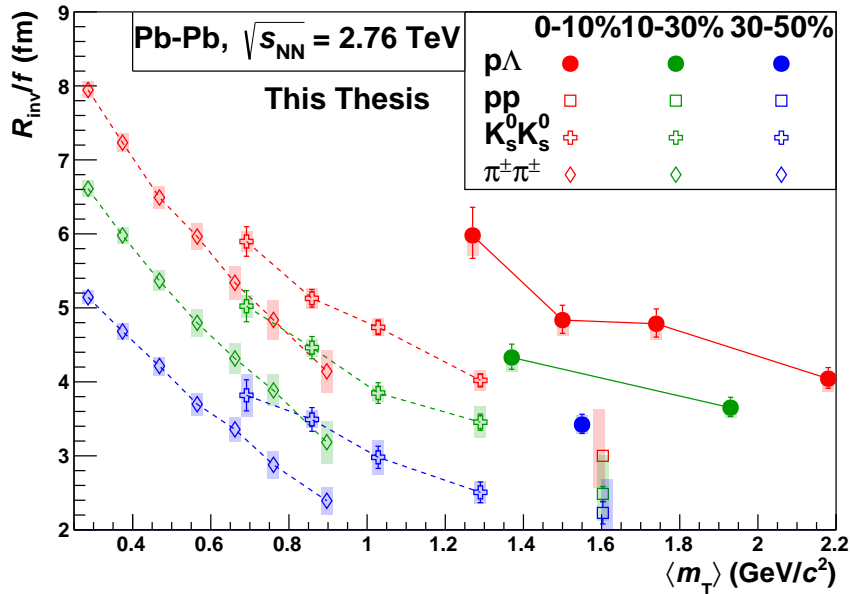


Figure 6.20: Radii of Fig. 6.17 inversely scaled with f of Eq. 6.37 following the prescription given in [361].

It should be noted that the incorporation of a hadronic phase is not the only difference between the two models [361] and [359]. Preferably, one would like to see [359] incorporating a full 3+1D viscous hydrodynamical phase and on the other hand [361] to be coupled to a hadronic afterburner to disentangle the pure effect of the hadronic phase from subtle differences in the models. It should also be kept in mind that the experimental results shown in Fig. 6.17, Fig. 6.18, and Fig. 6.20 are all only at a preliminary stage. Certainly, the situation should be re-assessed, when final, regularly published data on the m_T dependence of one-dimensional radii from correlations of $\pi\pi$, KK, and pp are available from the ALICE Collaboration.

Chapter 7

Photon-Photon Correlations

As outlined in Section 2.7, photon-photon correlations possibly allow to obtain an image of the early hot and dense phase in heavy-ion collisions; with the special potential to look past the horizon of hadronization. Here, first attempts of a measurement of photon-photon correlations with ALICE were performed. The photon-photon analysis clearly had an explorative character and did not aim yet at final results.

ALICE has the capability to reconstruct photons via conversions into e^+e^- pairs and can also directly detect photons with its electromagnetic calorimeter EMCal. The selection of photon candidates reconstructed with the conversion method is discussed in Section 7.1, the selection of photon candidates with the help of the EMCal is explored in Section 7.2, and the two-photon correlation function is studied in Section 7.3. The event selection criteria are the same as for the pA analysis with the only difference being that 0–50% most central collisions were investigated here.

The reconstructed photons consist of direct photons and photons from electromagnetic decays like $\pi^0 \rightarrow \gamma\gamma$ or $\eta \rightarrow \gamma\gamma$. The experimental pointing resolution is worse than the typical decay length of an electromagnetic decay. For the π^0 , the proper decay length $c\tau$ amounts to 25.5 nm [32]. Hence, all photons can be regarded as primary.

7.1 Photon Conversion Candidate Selection

A great convenience when analyzing photons reconstructed via the conversion method is the pre-selection of photon candidates by the photon conversion method framework discussed in Section 4.5.3. The provided candidates already show a decent momentum resolution and reasonable purity. Here, we applied further selection criteria to enhance the overall quality with focus on the specific needs for a two-particle correlation measurement.

A good momentum reconstruction is crucial for a two-particle correlation measurement as a function of the relative momentum of the pair. If the momentum vector of the photon was properly reconstructed, it should point back to the primary vertex. Technically, this was formulated as the cosine of the pointing angle $\cos(\theta)$, see Section 4.3. A requirement of $\cos(\theta) \geq 0.97$ assured a good correspondance of the true and the reconstructed momentum. Similarly, 40 reconstructed clusters in the TPC for each of the leptons certified a good quality of the daughter tracks. The rather low number of required clusters has to be seen in context of the finite length the photon might have travelled in the TPC before converting into the charged tracks. Building on the experience from $p\Lambda$ correlations, tracks with shared clusters were rejected. Decays with a large asymmetry where a daughter carries less than 6% or more than 94% of the photon momentum were refused; the asymmetry cut is, e. g., motivated in [362].

The PID capabilities of ALICE allow to identify the electrons from the bulk of produced particles. In order to obtain a rather clean sample of photon candidates and not to be biased by possible contaminations, rather strict criteria were imposed; they are summarized in Table 7.1. The clean-up of the conversion candidate sample by the PID criteria is visualized in Fig. 7.1, which shows the dE/dx of the of the positive daughter vs. the dE/dx of the negative daughter before (left) and after (right) applying the PID criteria on the analysis level. Due to their small mass, the specific energy loss of electrons is rather constant as a function of momentum in the range probed by the ALICE TPC. On the left of Fig. 7.1, we see a signal in the region A (dotted circle) consistent with e^+e^- pairs where both daughters have a dE/dx value of about 72 (a.u.). However, we also see a contamination from positive and negative particles (regions B , dashed circles) with a dE/dx of about 54 (a.u.), likely from the highly abundant pions. In Fig. 7.1 (right), we see that the contamination B is removed after applying the electron inclusion and pion rejection criteria listed in Table 7.1. Also apparent is the reduction in the region A , where the highest bin content is reduced from about 450×10^3 to about 200×10^3 . It should be noted that protons and kaons which cross the electron line also contributed in this region A before the analysis level PID cuts were applied, i. e. in the left panel of Fig. 7.1. In the right panel of Fig. 7.1 they were removed by the kaon and proton rejection criteria listed in Table 7.1. No sharp, box-like edge from applying the cuts can be seen in Fig. 7.1 (right) since the discriminating variable for the electron inclusion, TPC $N_\sigma(e)$, is not merely selecting on the measured dE/dx value but also takes into account the uncertainty σ of the dE/dx measurement, which depends on the number of measured dE/dx clusters.

selection variable	value
TPC PID signal	required
TPC $N_\sigma(e)$	≤ 4.0
TPC $N_\sigma(e), p < 0.4 \text{ GeV}/c$	≤ 3.0
TPC $N_\sigma(\pi)$	≥ 1.0
TPC $N_\sigma(K)$	≥ 1.0
TPC $N_\sigma(p)$	≥ 1.0
TOF PID signal	if present
TOF $N_\sigma(e)$	≤ 3.0

Table 7.1: PID selection criteria for the photon conversion candidate daughters applied on the analysis level.

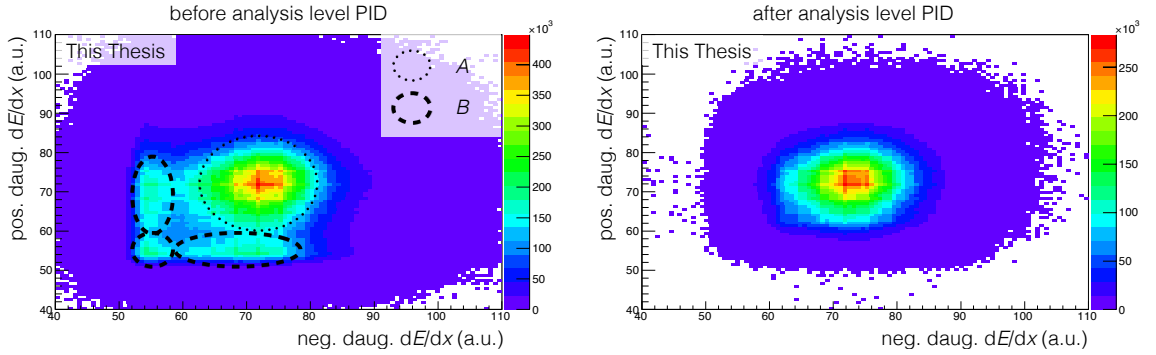


Figure 7.1: Effect of the imposed PID on the conversion candidate sample visualized as the correlation between the dE/dx of the positive photon candidate daughter vs. the one of the negative daughter before (left) and after (right) the criteria listed in Table 7.1 were applied. All momenta are shown here, the electrons are ultra-relativistic and have a constant energy loss dE/dx , independent of momentum. The electron inclusion criterion of $TPC N_\sigma(e) \leq 4.0$ does not lead to a sharp cut-off in the right panel since the N_σ variable also takes into account the precision of the dE/dx measurement for each track independently.

7.2 EMCal Photon Candidate Selection

7.2.1 Charged Particle Veto

Utilizing a Charged Particle Veto (CPV) detector located in front of an electromagnetic calorimeter has a long tradition in heavy-ion physics and was, e. g., applied by WA98 experiment at the SPS [363] and STAR [364] and particularly PHENIX at RHIC [365]. In ALICE, the so far largest CPV detector for a dedicated heavy-ion experiment was built, namely the TPC. Fig. 7.2

(left) shows for each calorimeter cluster the distance in (η, φ) to the closest charged track extrapolated from the TPC. The histogram is well described by a two-dimensional Gaussian fit, which for this particular p_T selection yields a width which is applied both in $\Delta\eta$ and $\Delta\varphi$ of $\sigma = 0.0088 \pm 1 \times 10^{-5}$. Fig. 7.2 (right) shows the distribution of the distance in η of the cluster to the nearest track as a function of p_T in the colored histogram. Apparent is a reduction in statistics for the bin $0.0 \leq p_T$ (GeV/c) < 0.5 . Primary tracks need a minimum $p_{T,\min} = 0.675$ GeV/c to not curl up before hitting the EMCal surface at a radius $R = 4.5$ m. Therefore, tracks with $p_T < 0.5$ GeV/c that reach the detector must be secondary and must stem from a decay vertex considerably far away from the primary interaction point. Also shown is the width of the aforementioned two-dimensional Gaussian as a black graph and a functional fit of the form $f(p_T) = a + b/p_T$ to the graph in the white, dashed line; the χ^2 minimization gives as parameters $a = 3.3 \times 10^{-3}$ and $b = 5.9 \times 10^{-3}$. Rejecting clusters for which the nearest charged track extrapolation falls below this simple p_T -dependent parametrization constitutes a simple and effective procedure for a charged particle veto.

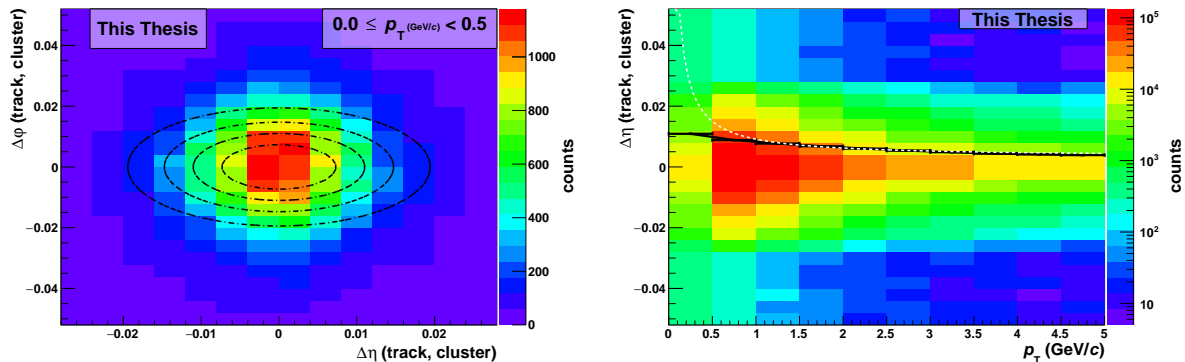


Figure 7.2: Track cluster matching in the ALICE calorimeters. Left: $(\Delta\eta, \Delta\varphi)$ of the cluster in the calorimeter to its nearest charged track extrapolation from the TPC for $0.5 \leq p_T$ (GeV/c) < 1.0 together with a two-dimensional Gaussian fit. Right: $\Delta\eta$ of the calorimeter cluster to its nearest TPC track extrapolation as a function of p_T in the colored histogram. Also shown is the width in $\Delta\eta$ of the two-dimensional Gaussian fit of the left panel as a black graph together with a functional fit to the graph with $f(p_T) = a + b/p_T$ in the white, dashed line.

7.2.2 Shower Shape Analysis

The left panel of Fig. 7.3 shows the two-dimensional, transverse and vertical, profile of an air shower of a 1 TeV gamma ray and a 1 TeV nucleon. The most prominent feature is the much narrower energy distribution in the electromagnetic shower of the hard photon. The energy loss of the photon cascade is dominated by pair creation $\gamma \rightarrow e^+e^-$ and bremsstrahlung $e \rightarrow e + \gamma$.

Both of these processes do not produce particles with a significant amount of transverse momentum. The physics processes of hadronic shower are much richer, they can however be roughly grouped into two classes. The first category consists of production of energetic secondary hadrons, which typically carry a fair fraction of the primary particles momentum. The second kind of processes are interactions with the traversed material like excitation, evaporation, spallation, et cetera, see the review article on calorimetry by C.W. Fabjan and F. Gianotti [366]. A 1 TeV proton, as it is depicted in Fig. 7.3 (left), typically stems from a galactic source [367]. The mean transverse momentum in a collision of such a 1 TeV proton with a hydrogen nucleus at rest in the atmosphere is considerably large. The center of mass energy for such a collision is $\sqrt{s} = \sqrt{2m_p^2 + 2E_p m_p} = 43.3$ GeV which corresponds to the energy range probed by the pioneering measurements at the CERN Intersecting Storage Rings (ISR). It was at the ISR where the mean transverse momentum in such hadronic collisions was quantified to be about 0.35 GeV/c [368, 369]. In contrast, the average transverse momentum in the electromagnetic pair-creation and bremsstrahlung processes is only on the order of the electron mass [370]. Thus, the transverse shower profile is a potent discriminator between electromagnetic and hadronic showers.

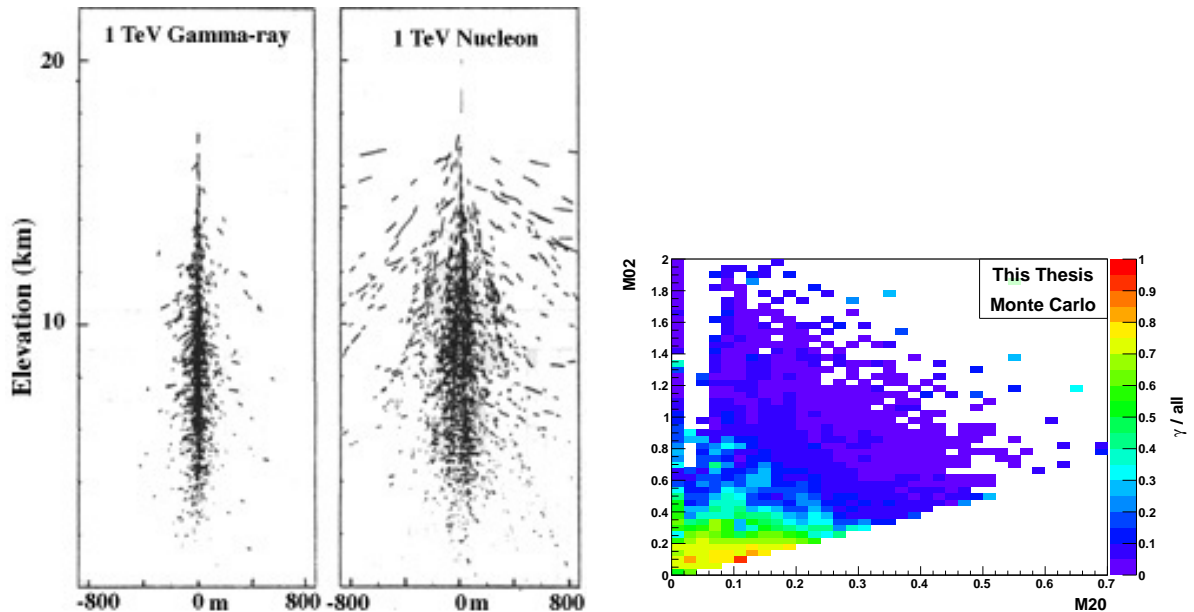


Figure 7.3: Left: Air shower for a gamma ray and a nucleon, both of 1 TeV. The energy of the gamma is dissociated in a much narrower area than for the nucleon. Taken from [371]. Right: Ratio of the number of γ over all particles as a function of the shower shape parameters $M_{0,2}$ and $M_{2,0}$, see Eq. 7.1, from a Monte-Carlo simulation including the full detector response. We see the precedence of the photons for small $M_{0,2}$.

Let us denote by $M_{0,2}$ and $M_{2,0}$ the second moments along the major and minor axis of the

shower ellipse which shall be perpendicular to the particle's propagation [372]:

$$M_{p,q} = \int_{-\infty}^{+\infty} \int_{-\infty}^{+\infty} u^p v^q f(u, v) du dv, \quad (7.1)$$

here u represents the coordinate along the minor axis, v follows the major axis, p and q take the values 0 and 2, and $f(u, v)$ is the distribution of energy within the cluster.¹ The particles from a hadronic shower are generally less abundant but more energetic and carry more transverse momentum when compared to an electromagnetic shower, as discussed before. Thus, it is expected that the second moment of the principal axis is large for a hadronic shower but small for an electromagnetic shower. This presumption is certified by the results of a Monte Carlo simulation of Pb-Pb events including the full detector response, presented in Fig. 7.3 (right). We see that the ratio of γ over all mother particles generating the shower, i. e. the purity, is augmented for small values of $M_{0,2}$. A detailed inspection reveals that the significance $\zeta = \frac{S}{\sqrt{S+B}}$ is maximized by the requirement $M_{0,2} \leq 0.44$. The typical purity of the photon candidate sample in this selected region is about 60–100%. We recognize the dependence of the photon purity in Fig. 7.3 (right) on $M_{2,0}$ and note that a more elaborate selection which includes both moments like a weighted sum or a weighted sum of squares of the two moments appears to be a more favorable selection criterion for future studies.

7.2.3 Energy Calibration of the ALICE EMCAL

Within the ALICE software, the so called EMCAL tender allows to utilize an energy response function which was determined from an electron test-beam campaign. The deviation from a simple linear correspondance between the measured Analogue to Digital Counts (ADCs) and the energy of the incident electron of the test beam is shown in full black dots in Fig. 7.4 (left); the open circles represent the deviation from a cubic parametrization. We note the depression of the full symbols below unity for energies smaller or equal 10 GeV. For the given granularity of the data, i. e. the two data points at 5 and 10 GeV, the cubic energy response function allows to correct for the energy inefficiency attributed to threshold effects and possible light-transmission losses [256].

With the cubic energy response function applied, Fig. 7.4 (right) shows the mean of Gaussian fits to the peaks in the two photon-candidate invariant mass spectrum vs. the mean cluster energy of the photon candidates in highly symmetric decays where the energy difference of the two photon candidates was less than 10% for the investigated Pb-Pb collision data sample. The full red dots signify that a π^0 peak was doubtlessly identified; the open circles give the result of the fit, however due to the particular shape of the invariant mass distributions and a bad signal to background ratio it is not given with certainty that the values represent the

¹Within ALICE, $M_{0,2}$ is also denoted with λ_0^2 and $M_{2,0}$ with λ_1^2 . A technical implementation can be found in, e. g., [274].

position of peaks from π^0 . If the test-beam response function covered all systematic effects, the mass of the π^0 should correctly show up at the value given by the particle data group of $134.98 \text{ MeV}/c^2$. Unfortunately, we see that the π^0 mass is systematically underestimated.

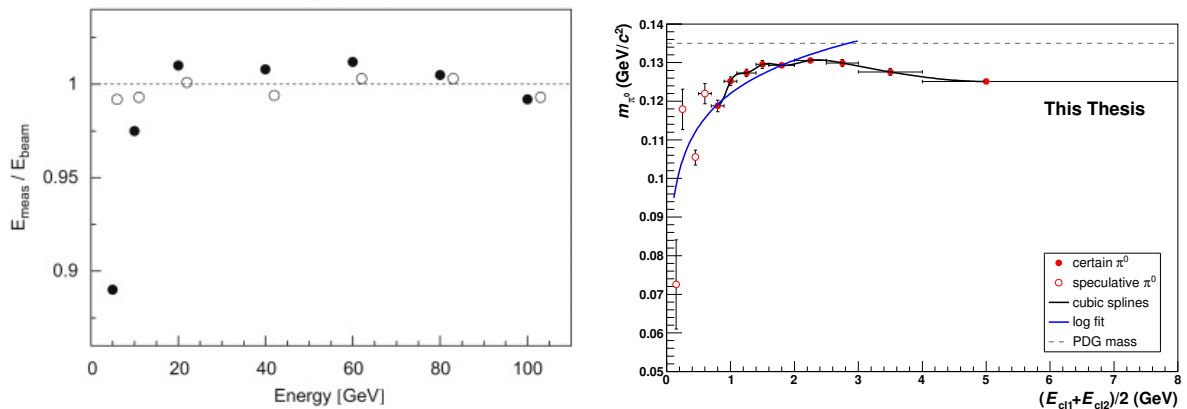


Figure 7.4: Left: Deviation from a linear correspondance between the reconstructed energy and the incident energy of the electron beam in an EMCal test-beam campaign in full black circles and deviation of the reconstructed energy from a cubic energy response function in open symbols. Taken from [256]. Right: Reconstructed mass of the neutral pion as a function of the mean cluster energy in highly symmetric decays into two photon candidates. The PDG mass of $134.98 \text{ MeV}/c^2$ is underestimated over the full dynamic range. Compare to the very similar dependence obtained in [373] for pp and p-Pb collisions.

A remedy is to apply a non-linearity correction, i. e. to simply multiply the reconstructed cluster energy by an additional correction factor. Since Fig. 7.4 (right) shows only highly symmetric decays, this correction factor is the ratio of the PDG mass over the shown reconstructed π^0 mass. In order to take into account the finite binning, the spline fit (shown in the right panel of Fig. 7.4 as a black line) is used for cluster energies from $0.8 \text{ GeV}/c^2$ and above. Below, the spline is smoothly connected to the log fit (shown as a blue line in the figure). The spline was chosen over any other function since it does not bias the correction factor to follow a particular functional shape. Additionally, the spline is easily handleable in the fitting procedure. A log-like (or similarly shaped) decrease in the π^0 mass with decreasing p_T was observed in a dedicated study of the EMCal energy response in pp and p-Pb collisions [373]. Clearly, the ad hoc energy calibration of the EMCal performed here can only be an intermediate solution and should be replaced by a centrally organized calibration of the detector.

7.3 Photon-Photon Correlation Function

The raw photon-photon correlation function was obtained in the same way as the $p\Lambda$ correlation function, see Section 6.2. With the two independent sets of photons measured in the EMCal or via the conversion method, three different combinations of photons are possible: calorimeter - calorimeter, conversion - conversion, and conversion - calorimeter.

In Fig. 7.5, the mixed event subtracted invariant mass distribution in the π^0 region as obtained with the EMCal is presented. In all p_T bins, especially above 1 GeV/ c , a π^0 peak is found. The clear signals confirm the proper selection of photons. Here, the non-linearity correction displayed in Fig. 7.4 (right) was additionally applied. We note an overshoot in the reconstructed π^0 mass, asking for a further check of the EMCal calibration procedure, specifically the non-linearity correction discussed in Section 7.2.3.

Fig. 7.6 shows the photon-photon correlation function C_2 as a function of the invariant mass² of the photon pair, where both photons were reconstructed in the EMCal. The correlation function was normalized to unity in the region $60 < m_{\text{inv}} \text{ (MeV}/c^2) < 80$ and is rather flat for $m_{\text{inv}} \gtrsim 60 \text{ MeV}/c^2$, with the exception of the high- p_T selections where the π^0 peak becomes visible also in this representation. An excess in real events is observed for $10 < m_{\text{inv}} \text{ (MeV}/c^2) < 20$ in the lowest p_T sample which shifts to $30 < m_{\text{inv}} \text{ (MeV}/c^2) < 60$ for the largest displayed p_T . The excess is followed by a strong depression down to $C_2 \approx 0$ for smaller m_{inv} . The reason for this suppression lies in the limited segmentation of the EMCal, which does not allow to obtain a signal for m_{inv} smaller than 10 to 40 MeV/ c^2 depending on the p_T of the pair.

The correlation function of two converted photons can be seen in Fig. 7.7. When comparing the width of the π^0 peak of about 3 MeV/ c^2 with the one of the EMCal of Fig. 7.5 of about 20 MeV/ c^2 , the superior momentum resolution of the photon conversion method becomes evident. In addition, pairs of photons can be reconstructed down to $m_{\text{inv}} = 0 \text{ GeV}/c^2$. This is a major advantage over, e. g., the measurement of WA98 [209]. Since no two-track separation cut was applied (we will come back to this in a moment), a residual effect from the finite two-track resolution of the charged particle detectors is present. It can be perceived most easily in the intermediate p_T range from 0.5–2.5 GeV/ c , i. e. the top center, top right, and bottom left panel of Fig. 7.7, for $0.01 \leq m_{\text{inv}} \text{ (GeV}/c^2) < 0.06$ as a depression below unity. A study [374] of the distribution of the generalized angular distance (see Section 6.3.3), reveals a typical behavior for close pairs of charged particles in the TPC, similar to what was seen for the $p\Lambda$ case. The same charge daughters of the photon pair exhibit merging for $|\Delta\eta^*| < 0.15$ and track splitting for $|\Delta\eta^*| < 0.01$. The splitting effects were observed to be mild and the merging dominant such that no strong artificial positive correlation between the photon pair would be expected due to detector effects. Rectifying the situation by requiring a minimal separation of

²Note that due to the zero mass of the photons, the invariant mass equals the invariant relative momentum.

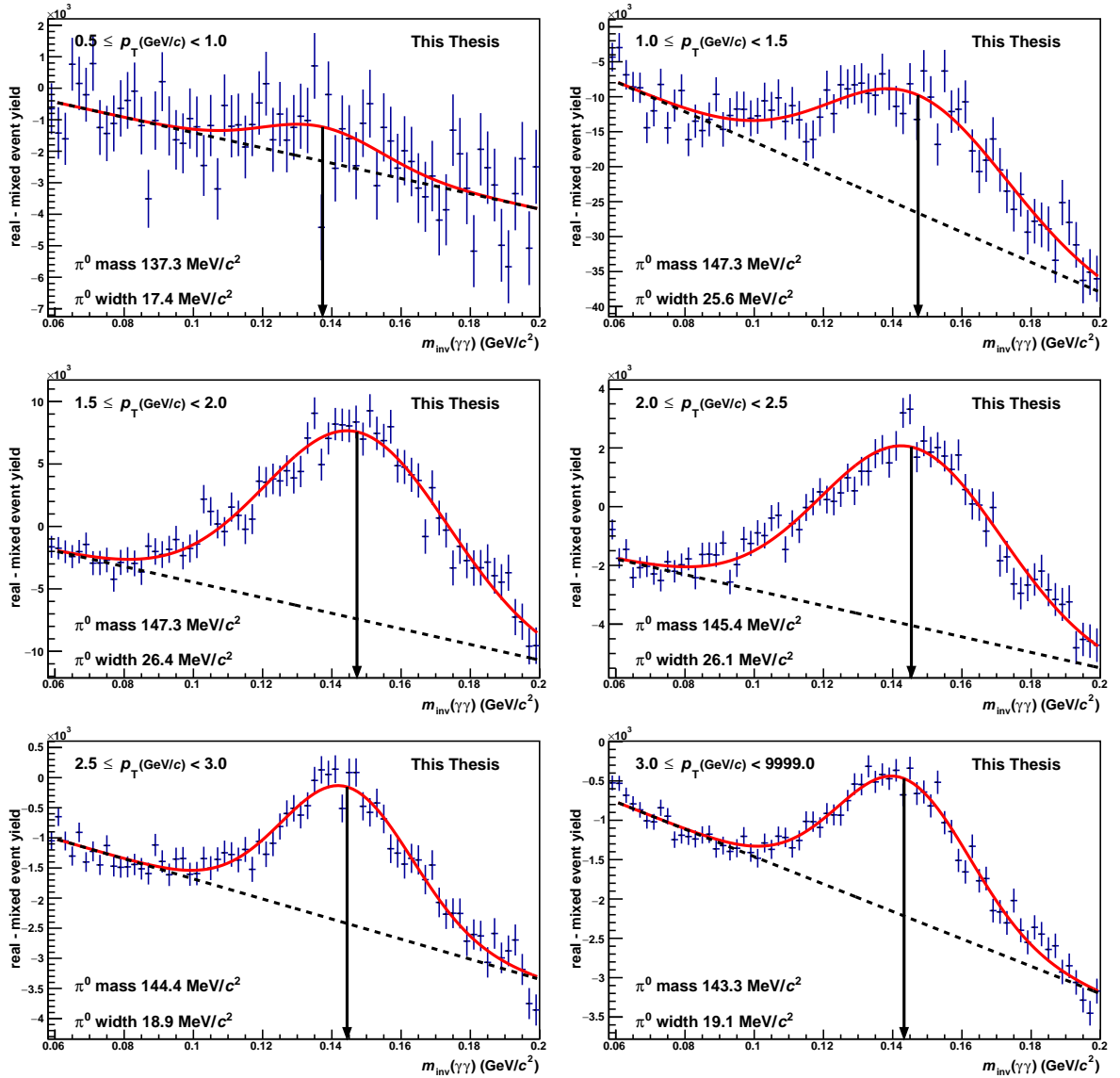


Figure 7.5: Mixed event subtracted invariant mass spectrum in the neutral pion mass region with the EMCal. A minimum cluster energy of 0.5 GeV is required. The black, vertical arrows represent the mean of the Gaussian component of the fit, i. e. the fitted mass of the peak from π^0 .

the charged daughters in the TPC seems achievable. However, the situation is complicated by the fact that four final-state, charged particles are involved. Similar as a positive correlation between the human birth rate and the stork population does not imply that babies are delivered by storks [375], the observation of a depression in the two-photon correlation function for given generalized angular distances of the positively charged lepton pair is no proof that at this distance track merging occurs; rather, it can also be that the merging occurred between the negatively charged lepton pair and the aforementioned depression is due to a correlation

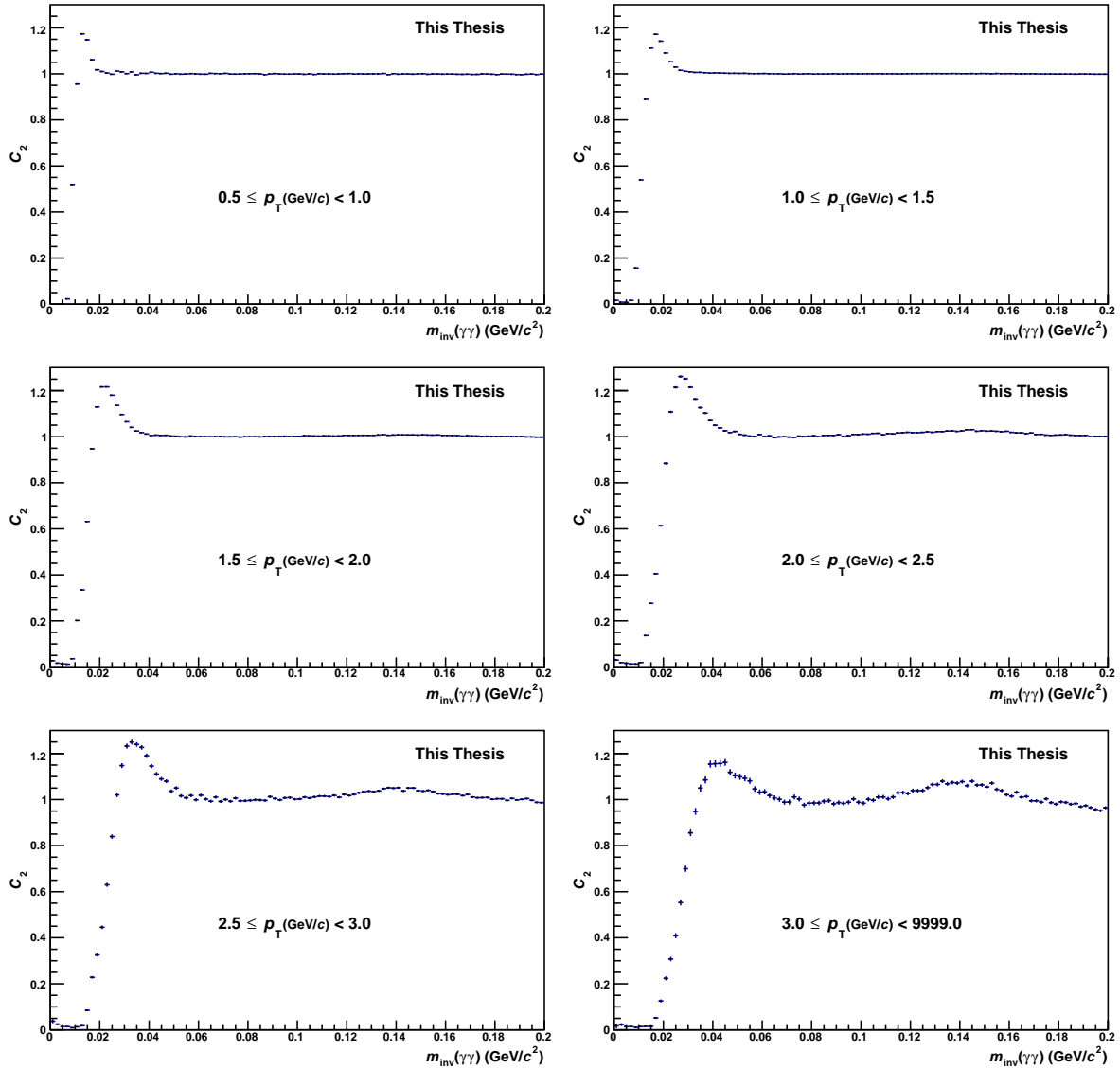


Figure 7.6: Photon-photon correlation function where both photons of the pair were reconstructed with the EMCal. Only clusters with an energy above 500 MeV were considered.

between the distances of the two lepton pairs. First attempts were made within this thesis to disentangle the correlation between the two-dimensional generalized angular distances for the two same-charge lepton pairs (totaling to a four-dimensional correlation analysis of the two-track resolution effects); however, they did not reach a conclusive stage. A comprehensive investigation, possibly including the study of requiring a smallest (radial) distance of the conversion vertices, is left for future analysis. This decision has to be seen in context with the appealing possibility to combine a conversion photon with a calorimeter photon and thus get rid of such two-track resolution effects. Here, for the combination of two conversion photons, we

quantify the excess for small relative momenta by a Gaussian and take into account the residual effect from the finite two-track resolution by adding a linear component to the parametrization. This results in the function:

$$C_2^{\text{fit}}(m_{\text{inv}}) = 1 + a + b m_{\text{inv}} + \lambda \exp\left(-\frac{m_{\text{inv}}^2}{2\sigma^2}\right), \quad (7.2)$$

where the width σ and λ resulting from the fit to the data for $m_{\text{inv}} < 60 \text{ MeV}/c^2$ are quantified in each panel of Fig. 7.7. We see that both the strength of the correlation λ and the width of the correlation σ are increasing with p_T .

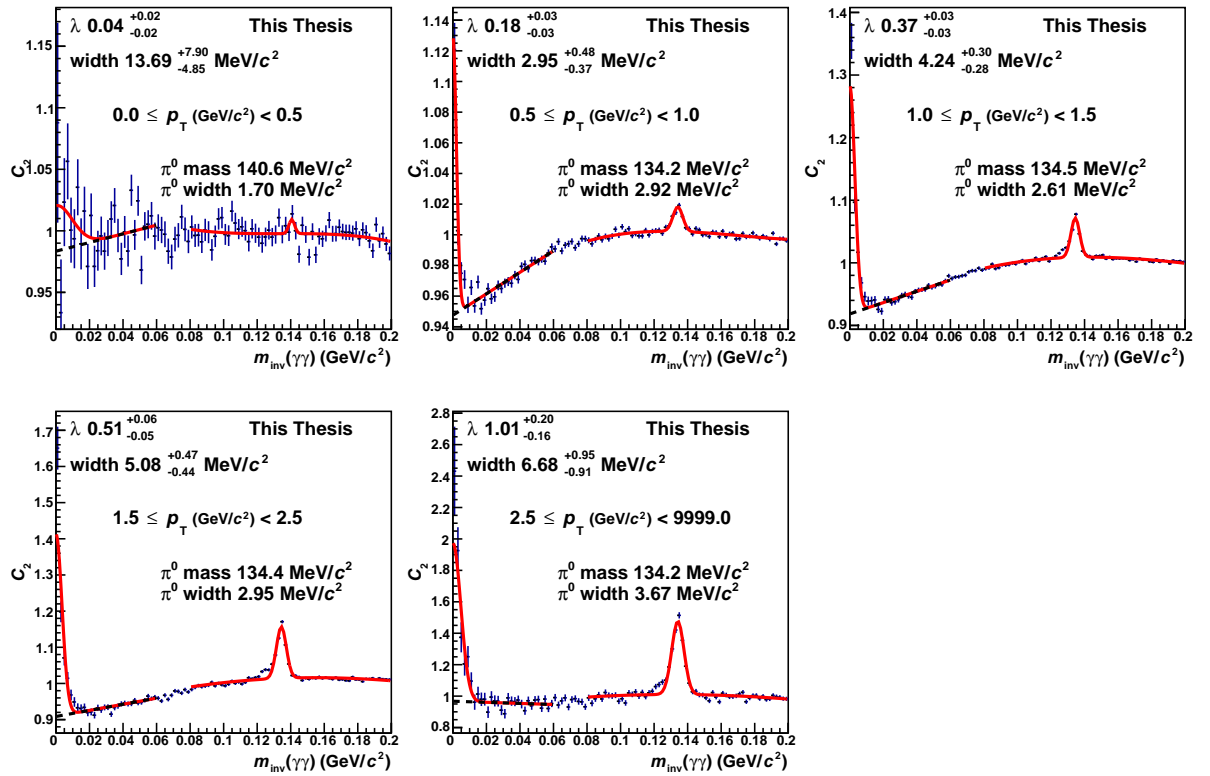


Figure 7.7: Photon-photon correlation function where both photons of the pair were reconstructed via the conversion method. No two-track cuts were applied.

The combination of a converted photon and a photon measured in the EMCAL avoids the limitation imposed by the experimental two-track resolution, as well as other experimental influences since two separate detectors are used; Fig. 7.8 shows the corresponding correlation function. Two-particle detector effects appear to be absent, as manifested in the non-appearance of the depression at small m_{inv} , which was seen for the correlation functions of two converted photons and the correlation function of two EMCAL photons. Thus, the parametrization of the excess for small m_{inv} according to Eq. 7.2 can be performed without the phenomenological

parameters a and b , i. e. by a pure Gaussian for the enhancement above unity. The correlation function again exhibits an excess for small invariant mass; the enhancement above one at zero m_{inv} is several times higher than the peak from $\pi^0 \rightarrow \gamma\gamma$ decays.

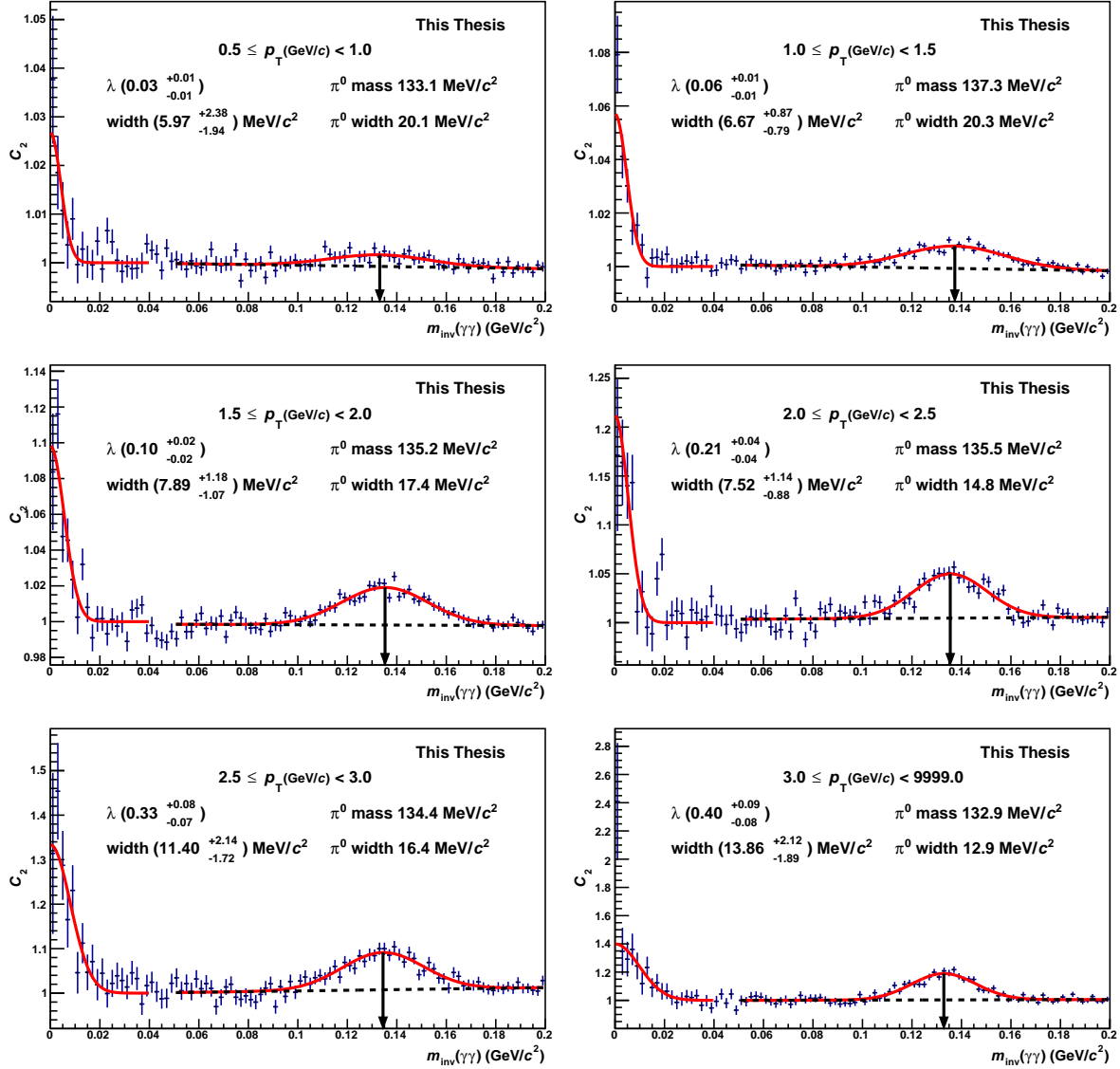


Figure 7.8: Photon-photon correlation function where one photon of the pair was reconstructed via the conversion method and the other was detected with the EMCal.

Table 7.2 quantifies the per event number of photon candidate pairs with an invariant mass smaller than $20 \text{ MeV}/c^2$ for the three different presented schemes of combining the photons reconstructed in the EMCal and via the conversion method. For $p_T < 0.5 \text{ gevc}$, a correlation function was obtained only for the combination of two conversion photon candidates. For a pair p_T between 0.5 and 2.5 GeV/c , the highest number of pairs is found for the combination

of two photon candidates from the EMCal. In this intermediate p_T range, the number of pairs from a calorimeter photon candidate and a conversion photon candidate is a factor of ten to two smaller. At higher p_T , this ordering is reversed and the combined EMCal and conversion photon method gives up to a factor of three more candidates. The number of pairs of two converted photon candidates is always about a factor of ten smaller than the number of photon candidate pairs with one candidate reconstructed in the EMCal and one via the conversion.

p_T (GeV/c)	$N(\text{calo. calo.})$	$N(\text{conv. conv.})$	$N(\text{calo. conv.})$
0.0–0.5	n/a	2.86e-03	n/a
0.5–1.0	5.21e-01	6.45e-02	2.96e-01
1.0–1.5	2.61e+00	2.85e-02	2.56e-01
1.5–2.0	3.30e-01	8.55e-03	5.04e-02
2.0–2.5	2.24e-02		1.04e-02
2.5–3.0	2.16e-03		2.34e-03
3.0–inf	2.89e-04	6.33e-04	9.46e-04

Table 7.2: Per event number of photon-candidate pairs with an invariant mass smaller than $20 \text{ MeV}/c^2$ as a function of the p_T of the pair (first column) when both photon candidates were reconstructed in the EMCal (second column), both candidates were reconstructed via their conversion (third column), and one candidate was detected in the EMCal while the other was reconstructed via its conversion (fourth column).

The preliminary data for $\gamma\gamma$ correlations at small relative momenta from STAR [376] and PHENIX [377] are shown in Fig. 7.9 in the left and right panel, respectively. The STAR Collaboration sees an excess in the correlation function for small m_{inv} . The region $m_{\text{inv}} < 0.024 \text{ GeV}/c^2$, where a strong enhancement is measured, is highlighted in pale blue. The height of the enhancement above one at zero m_{inv} is three times higher than the peak from π^0 , consistent with the findings within this thesis. A mild enhancement of the correlation function above unity can be observed in the STAR data for slightly larger m_{inv} out to $m_{\text{inv}} \approx 0.05 \text{ GeV}/c^2$. The PDG mass of the π^0 is indicated by the black vertical arrow together with an orange band of $\pm 40 \text{ MeV}/c^2$ around the PDG mass. The π^0 peak in the data reproduces the PDG mass and mostly is confined within $\pm 40 \text{ MeV}/c^2$. Each data point in the region $50 < m_{\text{inv}} (\text{MeV}/c^2) < 95$ shows a value larger than one. It is hard to judge how far exactly the π^0 peak reaches and whether an offset above unity independent from the π^0 peak is seen here. The analysis by PHENIX unfortunately does not give data points for the region $m_{\text{inv}} < 0.024 \text{ GeV}/c^2$ (highlighted in pale blue). The data for $0.025 \leq m_{\text{inv}} (\text{GeV}/c^2) < 0.05$ show a light surplus above one, qualitatively consistent with the STAR data. The π^0 peak observed by PHENIX reproduces the PDG mass (indicated by the black arrow) and is confined within $\pm 40 \text{ MeV}/c^2$ around it (orange band). Beyond $175 \text{ MeV}/c^2$ the data is consistent with unity. Also shown

is the modelled residual correlation from HBT-enhanced π^0 pairs (blue line) which reveals a slope in the correlation function; the effect is discussed in [378]. The data from the WA98 Collaboration was shown before in Fig. 2.16. Also there, an excess for small m_{inv} and the slope in the correlation, supposedly originating from π^0 pairs, was seen. It can be concluded that the data reported by all four experiments — WA98, PHENIX, STAR, and ALICE — are qualitatively consistent: an enhancement for small m_{inv} is seen and its width is on the order of 10 MeV/ c^2 . If reported, the height of correlation function at zero m_{inv} , in the absence of detector effects, is several times larger than the peak from π^0 .

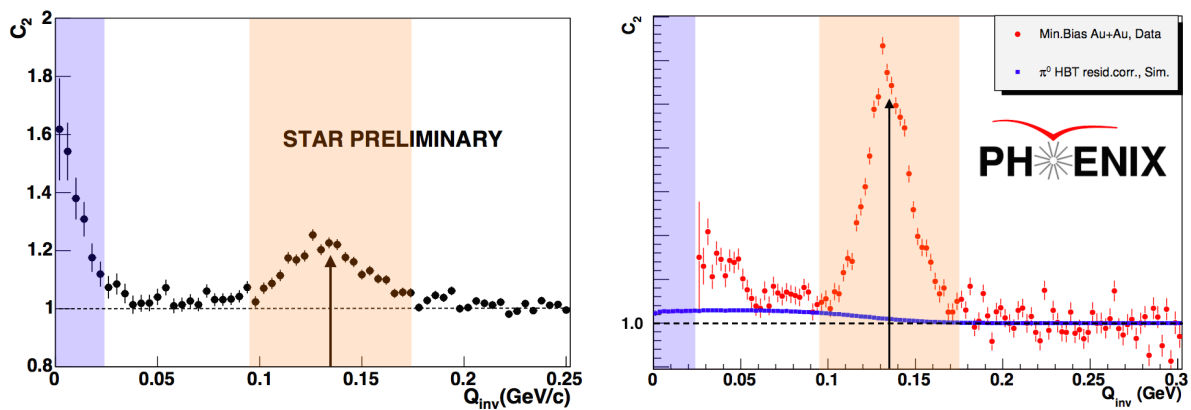


Figure 7.9: Two photon correlation as a function of invariant relative momentum as measured by STAR [376] (left) and PHENIX [377] (right). Both times, a converted photon was correlated with a photon reconstructed in a calorimeter. The blue line in the right panel quantifies the residual correlation inherited from the quantum statistical correlation of π^0 via their decay into photons.

The analysis of the ALICE data performed within this thesis substantially advances the knowledge about $\gamma\gamma$ correlations in heavy-ion collisions by presenting statistically highly significant, p_T -differential results over a p_T range of several GeV/ c . Particularly intriguing, a stark p_T dependence of the $\gamma\gamma$ correlations was found within this thesis. As visualized in Fig. 7.11, the width of the enhancement centered at zero m_{inv} (filled blue squares) doubles within the investigated p_T range and the strength of the correlation, quantified with the λ parameter, (full red circles) is found to grow by more than a factor of ten with p_T .

In order to elucidate the origin of the observed $\gamma\gamma$ correlations, the analysis of a Monte-Carlo simulation of Pb-Pb collisions with the Hijing generator [90], including a full detector response with the Geant3 code [379] reconstructed with the same algorithms as used for real data, is presented in Fig. 7.10. The different panels show the same p_T selections as the real data from Pb-Pb collisions in Fig. 7.8. The bottom right panel, which displays the highest p_T , exhibits a strong slope of the correlation function below the trivial peak from the two-body decay $\pi^0 \rightarrow \gamma\gamma$ at the π^0 mass. It follows the shape of the residual correlations from pairs of π^0 shown with

the PHENIX data (blue line in the right panel of Fig. 7.9) and is thus attributed to a remnant of an enhancement of neutral pion pairs at small relative momenta.

Monte-Carlo generators generally do not incorporate any quantum statistical correlations. Hence, the analysis of reconstructed Pb-Pb events simulated with the Hijing generator should show no excess in the correlation function at small invariant mass if the surplus in real events from Pb-Pb collisions is purely of quantum statistical origin. Fig. 7.10 reveals that this is not the case. Rather, the magnitude of both λ and the width are very similar in data and MC as visualized in Fig. 7.11.

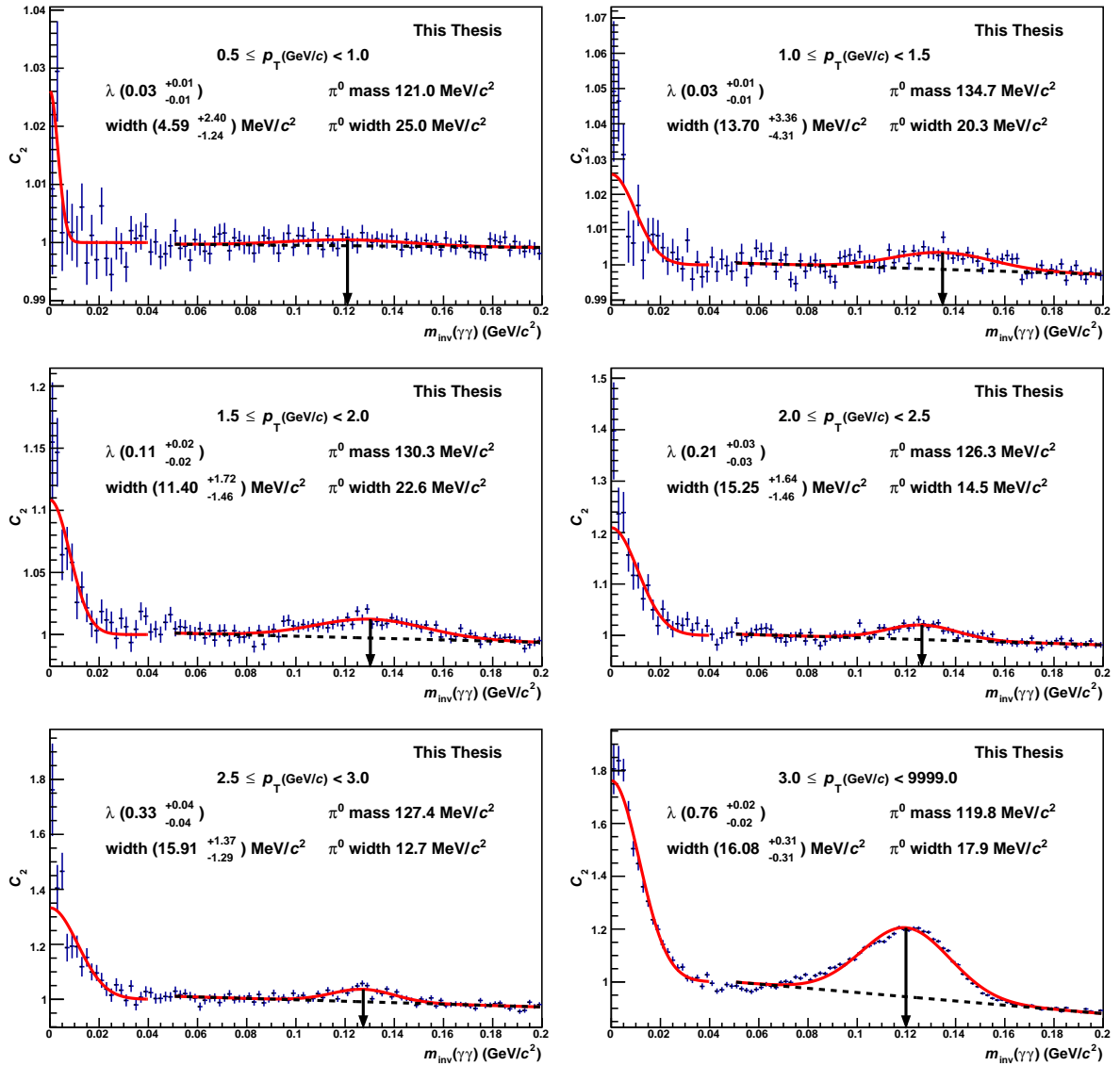


Figure 7.10: Photon-photon correlation function from a Monte Carlo simulation with the full detector response where one photon of the pair was reconstructed via the conversion method and the other was detected with the EMCal.

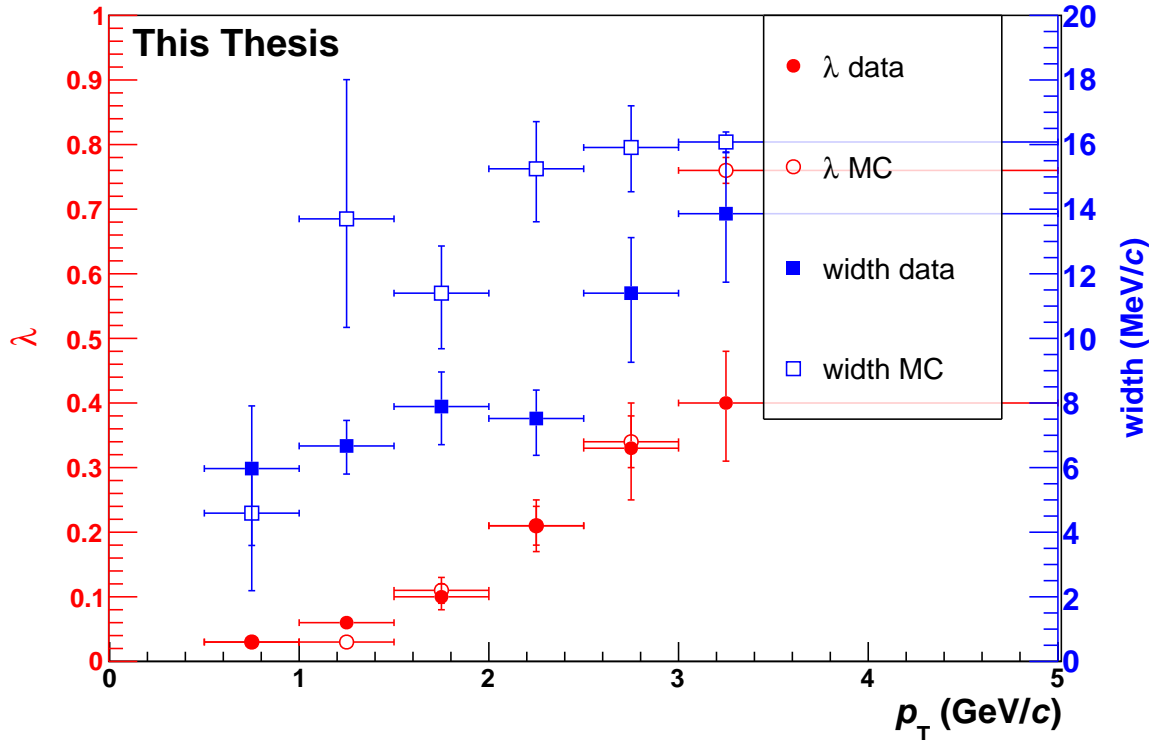


Figure 7.11: Comparison of λ (red circles) and the Gaussian width (blue squares) of the excess at small m_{inv} for data (full symbols) from Fig. 7.8 and Monte Carlo (open symbols) from Fig. 7.10. An overall fair agreement is found.

In order to further investigate the source of the striking $\gamma\gamma$ enhancement at small m_{inv} , the (Hijing+Geant) Monte-Carlo simulation was also investigated without invoking the response of the detector and the reconstruction algorithms; photons were selected using their true Monte-Carlo identity. This gives, e.g., insight into a possible auto-correlation, where one photon converts in the detector material and gets reconstructed via the conversion method, and one of the conversion leptons is also misidentified as a photon in the calorimeter. This possible source of the correlation is motivated by the findings in [380]. Fig. 7.12 evinces the presence of the signal in the simulation also at the level of true Monte-Carlo information without experimental effects. The aforementioned scenario where the daughter lepton of a converted photon is misidentified as a photon in the EMCal cannot be the (whole) origin of the correlation seen in Fig. 7.12. It is clear that the signal is no artifact of the experimental reconstruction procedure, but has its origin in a physics process.

Several production mechanisms that lead to the observed $\gamma\gamma$ correlations at zero invariant mass of the photon pair are conceivable. In [381] four photon sources are discussed: photons could originate from an initial hard scattering, the thermal QGP, from parton fragmentation

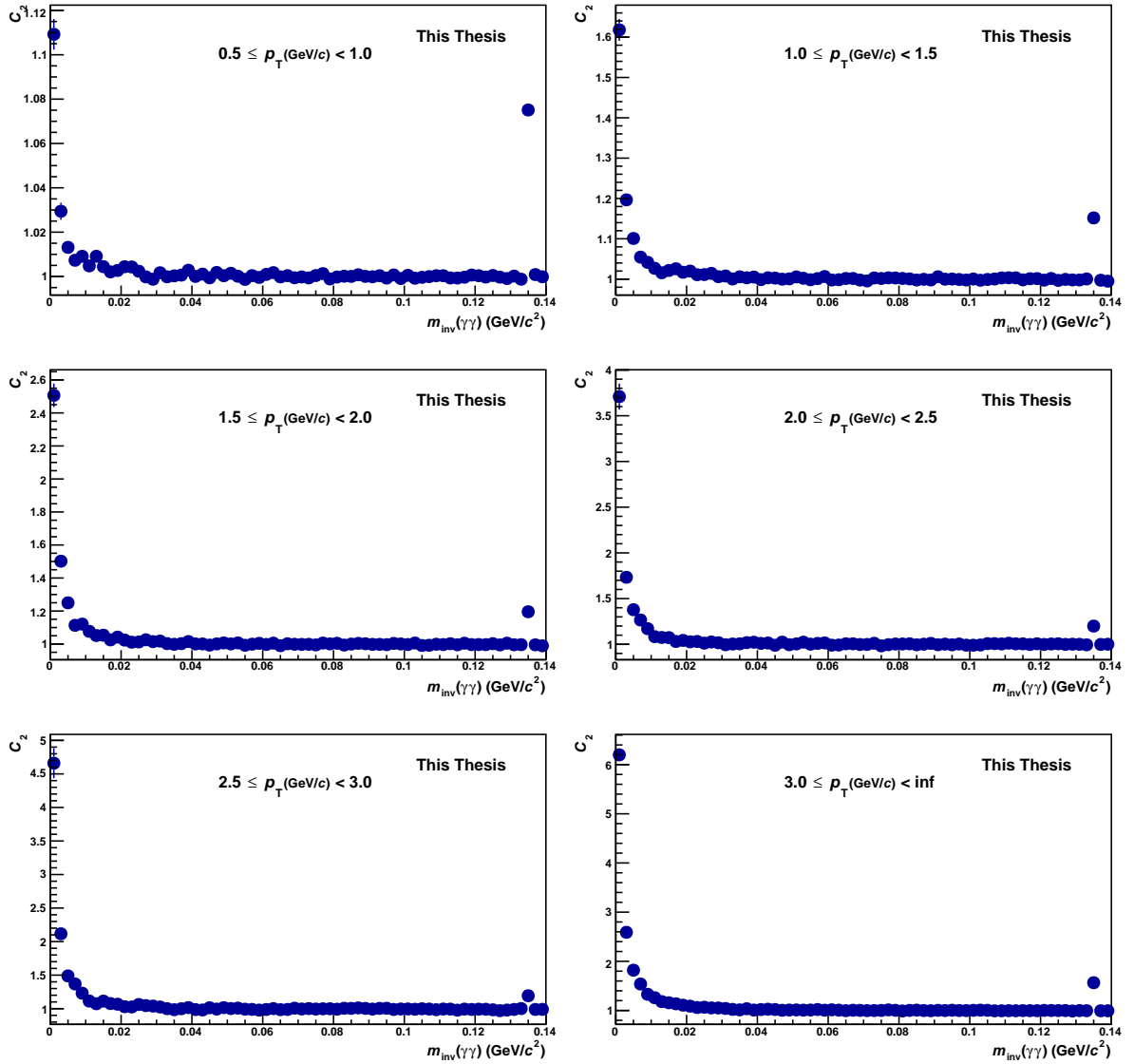


Figure 7.12: Photon-photon correlation function from a (Hijing+Geant) Monte-Carlo simulation without invoking the experimental detector response or reconstruction algorithms. Only photons identified by their true Monte-Carlo identity were selected.

or parton bremsstrahlung. The thermal photons are expected to give the quantum-statistical enhancement at zero mass of the photon pair, with the width of the correlation being inversely proportional to the size of the source. However, it may well be that the observed signal originates from the collinear emission of two photons by a high- p_T parton. This would be in line with the findings of [382], where at a transverse momentum of 2 GeV/ c more than 80% of prompt photons were identified as originating from parton fragmentation. Experimentally, one might study only photons that are emitted closely with a reconstructed jet or simply in the vicinity to a high- p_T particle, which can well serve as a proxy for the flight direction of the

parton. Such a scenario would be interesting since a direct link to the colored parton would be established. The evolution of the correlations from proton-proton to heavy-ion collisions would give direct access to the medium-induced energy-loss of the partons. Other processes are not excluded. A second-order auto-correlation effect might be that a photon converts into a lepton pair ($\gamma_1 \rightarrow e^+e^-$), one of the leptons produces another photon by bremsstrahlung in the detector material ($e^\pm \rightarrow e^\pm + \gamma_2$), and the two photons, γ_1 and γ_2 , are correlated. By energy conservation, the energy of the second photon, E_{γ_2} , must always be smaller than the energy of the first photon, E_{γ_1} . However, due to the zero mass of the photons, two collinear photons will always have an invariant mass of zero, independent of their energy difference. The energy of the two photons is experimentally accessible and as such gives an experimental handle on the suppression of such cases. In case of the correlation of two photons which were reconstructed via the conversion method, additionally the knowledge of the spatial coordinate of the conversion points and the direction of the three-momentum of the photon can be exploited. Another possible process to consider is the collinear emittance of two bremsstrahlung photons not by a parton but by a high- p_T electron. The high efficiency of the charged particle tracking in ALICE over a wide momentum range and the outstanding electron identification capabilities give confidence that also such a contamination could be subdued by rejecting photons traversing the detector close to a high- p_T electron. The Monte-Carlo sample can serve here as guidance and a litmus test. Firstly, the Monte-Carlo simulation can prove that indeed, e.g., such second-order auto-correlations factor in and it will provide a test ground for experimental means of suppressing such possible contributions. Secondly, if it can be shown that the correlations in the Monte-Carlo sample can effectively be removed and the photon-photon correlation function in the simulation is brought to unity, any signal in the photon-photon correlation function in real data will likely be stemming from the HBT correlation of thermal photons.

The wealth of possible sources for the observed $\gamma\gamma$ correlation and the manifold of further investigations lined out in the preceding paragraph obviously exceed the explorative character of the $\gamma\gamma$ analysis within this thesis. Despite that, this work extended the $\gamma\gamma$ correlation studies from the SPS [209] and RHIC [376, 377] with an unprecedented granularity of p_T -differential data of high statistical significance. Within this thesis, three qualitatively different procedures to obtain a photon-photon correlation function were successfully employed. The combination of two photons from the EMCAL gave the best overall pair statistics. The energy resolution of the EMCAL is modest as was seen from the width of the reconstructed π^0 peak of about $25 \text{ MeV}/c^2$. A major hindrance for a photon-photon study at small relative momenta is posed by the very limited spatial segmentation of the EMCAL which lead to a depression in the correlation function down to $C_2 \approx 0$ for $m_{\text{inv}} \lesssim 10 \text{ MeV}/c^2$. The combination of two calorimeter clusters is therefore considered the least suitable technique. The correlation function of two conversion photons showed the worst statistics. This downside of this method is balanced by the best resolution of the π^0 peak of circa $3 \text{ MeV}/c^2$. The correlation function was affected by two-track resolution effects to an acceptable degree, which makes the combination of two conversion photons a good

alternative procedure. The combination of a conversion photon with a photon from the EMCal showed good statistics and preserved a decent resolution of the π^0 peak of about $15 \text{ MeV}/c^2$. The major advantage is the absence of two-track resolution effects, which gave this approach preference over the other techniques. Using the combination of an EMCal and a conversion photon, first investigations on the origin of the photon-photon correlations were carried out and a clear path to uncover the puzzling emittance of photons in relativistic heavy-ion collisions was laid out. This study should be picked up and continued. So far, only the dataset of the 2011 Pb-Pb campaign was analyzed and the statistical precision does not impose a major limitation yet. The statistical significance of the observed signal might worsen when further restrictions are imposed on the data. In such a case, the combination of a converted photon with a photon reconstructed in a calorimeter can profit from the inclusion of photons from PHOS. The existing 2010 Pb-Pb dataset can further enhance the statistics for the combination of two converted photons. Overall, the potential of photon-photon correlations to advance our understanding of the evolution of heavy-ion collisions is too high to not further pursue the photon-photon correlation analysis.

Chapter 8

Summary

At the beginning of this thesis, an overview on the current status of the experimental investigation of the deconfined state of strongly interacting matter, the Quark-Gluon Plasma (QGP), was given. The potential of correlation measurements to gain knowledge about the properties of the QGP was discussed. Two-particle correlations at small relative momenta, and particularly their dependence on the pair transverse mass, were highlighted to be distinctly sensitive to the reaction dynamics of the fireball created in heavy-ion collisions. Being the heaviest system to extract a source size, proton-lambda correlations extend the studied range in pair transverse mass and are therefore well suited to study the dynamical behavior of the matter created in Pb-Pb collisions at the Large Hadron Collider. A topic of current theoretical and experimental interest, namely the possibly broken transverse mass scaling for various particle species, was pointed out to be testable by examining proton-lambda correlations. Additionally, a case was made to investigate photon-photon correlations to potentially take a picture of the fireball at early phases of the heavy-ion collision. Such an evaluation of photon-photon correlations was demonstrated to have the capability to solve the photon puzzle, i. e., the so far unexplained simultaneous observation of on the one hand a high yield and a large inverse slope parameter in the transverse momentum spectra of direct photons and on the other hand a substantial elliptic flow of direct photons.

The apparatus to perform these studies, A Large Ion Collider Experiment (ALICE), was introduced and the key particle-detection technologies, as well as the performance of the various subsystems were discussed. An automated performance monitoring framework, developed within this thesis, was presented. The reader was walked through the data reconstruction, including standardized basic analysis steps like the common preselection of photon conversion candidates. At the end of this reconstruction process stood the analysis oriented data which were the basis for the physics studies carried out within this thesis.

For the analysis of proton-lambda correlations performed here, highly significant samples

of protons and lambda particles were acquired. An outstanding feature of this analysis is the determination of, and correction for the impurities in these samples due to misidentification and weak and electromagnetic decays. Furthermore, effects arising from strong decays were taken into account. The strong disintegrations alter the particle ratios used for the correction for electromagnetic decays. Additionally, the proper lifetime of resonances (on the order of femtometer) leads to a modified source profile, which was included. The purities and contaminations were obtained directly from data where possible and calculated differential in transverse momentum, rapidity, centrality, and baryon number of the particles.

To remedy effects of the finite two-track resolution of the tracking detectors, algorithms were developed and applied that are now commonly used within the ALICE Collaboration. Conceptual and practical limitations in the standard procedure to correct for the finite momentum resolution of the detector were overcome by introducing a new approach which propagates the theoretical correlation function through an experimental response matrix. This allowed to obtain precise source radius parameters from the statistically highly significant, purity-corrected correlation functions. The centrality dependence of the extracted radii affirms the expectations of a larger source for more central collisions. Source radius parameters were attained over a span in mean pair transverse mass of more than $0.9 \text{ GeV}/c^2$. This has to be seen in context with the existing published data for pion-pion correlations in central Pb-Pb collisions by the ALICE Collaboration which extend over only less than $0.6 \text{ GeV}/c^2$. This thesis also surpassed preceding records in terms of reach in mean pair transverse mass, with a source radius extracted for a mean pair transverse mass of $2.18 \text{ GeV}/c^2$. The source size decreases with increasing transverse mass, qualitatively confirming a hydrodynamical picture even in the extreme dynamical regime probed here. The comparison of the radii extracted within this thesis with the measurements from pion-pion, kaon-kaon, and proton-proton correlations exhibits, however, a severe breaking of the elsewhere proposed scaling behavior of source radii with mean pair transverse mass for all particle species. Consistent with the findings of the three-dimensional analyses of pion-pion and kaon-kaon correlations at the Relativistic Heavy-Ion Collider, a better scaling behavior was found using the the pair transverse momentum.

ALICE allows to reconstruct photons with the ElectroMagnetic Calorimeter (EMCal) and via their conversion into an e^+e^- pair. The conversion photon candidate sample provided by the common framework used in the collaboration could further be purified by making use of the exceptional particle identification capabilities of ALICE. A good momentum resolution of the conversion candidates was asserted by additional analysis criteria. To identify photons in the EMCal, a charged particle veto and a shower shape analysis was put in place. The two independent samples of photon candidates allow for three ways of pairing. Using the EMCal only, the limited spatial segmentation of the calorimeter affected the two-photon correlation function at small relativ momenta in such a strong way that no other signal besides the depression below unity from the cluster merging could be observed. In the case of

combining two photons reconstructed via the conversion method, the correlation function was also influenced by the finite two-track resolution of the charged-particle detectors. However, the bias from the track merging proved to be only mild such that it could be accounted for by a phenomenological parametrization. For relative momenta smaller than $10 \text{ MeV}/c$, a striking excess in the correlation function was seen, with its height and width being slightly larger than the height and width of the peak from π^0 , respectively. Both, the height and width of the enhancement around zero relative momentum, were observed to monotonically grow with pair transverse momentum. For the correlation function of one calorimeter photon and one conversion photon, merging effects were proven to be absent, while a surplus in the correlation function at vanishing relative momentum comparable to the one for the two conversion case prevailed. A study of a Monte-Carlo simulation revealed that the signal at zero mass of the pair is fairly well reproduced by a (Hijing+Geant) simulation including the full detector response. Since Monte-Carlo generators typically do not incorporate quantum statistical correlations, a significant fraction of the signal likely does not stem from Hanbury Brown and Twiss correlations. In order to elucidate the origin of the observed photon correlations, the simulation was also studied without the invocation of the detector algorithms and simply taking the information on particle species and momentum from the true simulated values. Also here, a strong, positive correlation was present. One of the most intriguing explanations for such a signal may be a collinear emission of photons from a parton. However, a plentiful of other sources are conceivable too. The large number of possible origins exceeded the scope of this thesis. Further studies are needed to reveal the processes leading to the measured enhancement in the two-photon correlation function.

Appendix A

Lattice QCD: Extra Derivations

A.1 Wilson Loop

The QCD Lagrangian \mathcal{L} consists of a quarkonic and gluonic part

$$\mathcal{L}_{\text{QCD}} = \bar{\psi}_i \left(i (\gamma^\mu D_\mu)_{ij} - m \delta_{ij} \right) \psi_j - \frac{1}{4} F_{\mu\nu}^a F^{\mu\nu a}, \quad (\text{A.1})$$

$$F_{\mu\nu}^a = \delta_\mu A_\nu^a - \delta_\nu A_\mu^a + g' f^{abc} A_\mu^b A_\nu^c. \quad (\text{A.2})$$

The potentials A represent the massless gauge bosons of color charge $a, b, c = 1 \dots N^2 - 1$, with $N = 3$ for SU(3). We denote the coupling constant with g' and the structure constant by f^{abc} . The totally antisymmetric f^{abc} relates the 8 Gell-Mann matrices with their commutator $[t^a t^b] = i f^{abc} t^c$. $F_{\mu\nu}^a$ is dubbed the gluon field strength tensor. The quark field is represented by ψ , the anti-quarks correspondingly by $\bar{\psi}$. The quark mass is given by m , γ^μ embodies the Dirac matrices, D indicates the covariant derivative and δ_{ij} is the delta function.

The aforementioned (see Section 1.1) use of Euclidean space-time in the formulation of lattice QCD brings a potent connection to statistical mechanics [383]. We know that the key ingredient for a probabilistic analysis in statistical mechanics is the partition function Z . For QCD it is:

$$Z = \int \mathcal{D}A_\mu \mathcal{D}\psi \mathcal{D}\bar{\psi} e^{-S}, \quad (\text{A.3})$$

$$S = \int d^4x \left(\frac{1}{4} F_{\mu\nu}^a F^{\mu\nu a} - \bar{\psi} M \psi \right), \quad (\text{A.4})$$

with the Lagrangian appearing in the action S , where the quarkonic relation between ψ and $\bar{\psi}$, see Eq. A.1, was united in M . The anti-commuting Grassman variables ψ and $\bar{\psi}$ can be

integrated out:

$$\int d^4x \bar{\psi} M \psi = \log(\det M). \quad (\text{A.5})$$

This contains the fermionic contribution in the non-local term $\det M$. In the quenched approximation, $\det M$ is set to a constant, thus removing vacuum polarization effects from quark loops. An example where the quenched approximation is nicely explained is the calculation of the pion mass via a two-point correlation function. One simply creates a quark-antiquark pair with the quantum numbers of the pion

$$\pi^+(\vec{x}, \tau) = \bar{d}(\vec{x}, \tau) \gamma_5 u(\vec{x}, \tau) \quad (\text{A.6})$$

at time zero and looks at the evolution of the states with time, which is given by e^{-Ht} . Naturally, for large times only the low energy states will survive and the time dependence of the two-point correlation function reveals the mass quantitatively [384]. The pion correlator is illustrated in Fig. A.1 in the quenched approximation (left) and in full QCD (right). We see the additionally occurring sea-quark loops in full QCD. Quenched QCD shows confinement, asymptotic freedom and spontaneous chiral symmetry breaking and is one of the early implementations of QCD on the lattice. Its particular weakness is the missing string break-up when trying to separate two quarks — which occurs via the $q\bar{q}$ pair creation from vacuum.

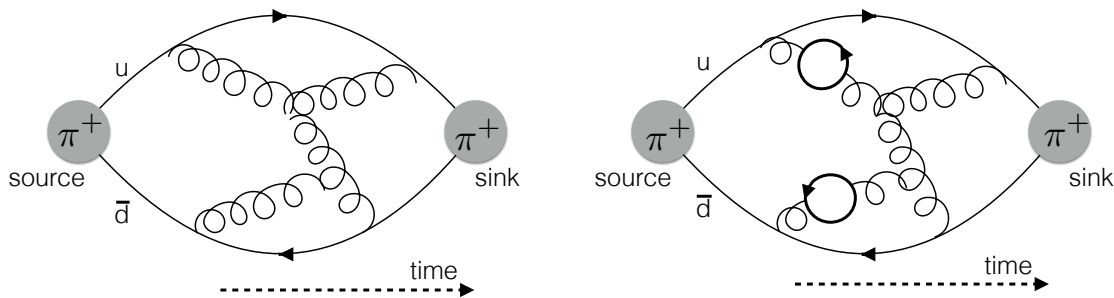


Figure A.1: Pion correlator in quenched QCD without vacuum polarizations from quark loops (left), and in full QCD with quark loops (right).

Moving beyond quenched QCD, one must first discretize the Dirac action by replacing the derivatives with the differences over one lattice spacing:

$$\bar{\psi} \not{D} \psi = \frac{1}{2a} \bar{\psi}(x) \sum_{\mu} \gamma_{\mu} \left[U_{\mu}(x) \psi(x + a\hat{\mu}) - U_{\mu}^{\dagger}(x - a\hat{\mu}) \psi(x - a\hat{\mu}) \right]. \quad (\text{A.7})$$

The meaning of this formula becomes more clear with the illustration in Fig. A.2, where it is shown that $U_{\mu}(x)$ is a gauge field link from place x to the place $x + a\hat{\mu}$. It is defined as the

integral over the gauge field A_μ

$$U_\mu(x) = \mathcal{P} \exp \left(ig \int_x^{x+a\hat{\mu}} A_\mu dx^\mu \right), \quad (\text{A.8})$$

where \mathcal{P} stands for path ordering. Adding the mass term to Eq. A.7, one ends up with the so called naive action:

$$S^N = m_q \sum_x \bar{\psi}(x)\psi(x) + \frac{1}{2a} \sum_x \bar{\psi}(x)\gamma_\mu \left[U_\mu(x)\psi(x+a\hat{\mu}) - U^\dagger(x-a\hat{\mu})\psi(x-a\hat{\mu}) \right] \quad (\text{A.9})$$

$$\equiv \sum_x \bar{\psi}(x)M_{xy}^N[U]\psi(y) \quad (\text{A.10})$$

A problem arises when looking at the free quark case $U_\mu(x) = 1$, which leads to:

$$\begin{aligned} \sum_x \bar{\psi}(x)M_{xy}^N[U]\psi(y) &= m_q \sum_x \bar{\psi}(x)\psi(x)\bar{\psi}(y)\psi(y) \\ &+ \frac{1}{2a} \sum_x \bar{\psi}(x)\gamma_\mu [\psi(x+a\hat{\mu}) - \psi(x-a\hat{\mu})] \bar{\psi}(y)\psi(y) \end{aligned} \quad (\text{A.11})$$

$$= \sum_x \bar{\psi}(x) \left(m_q \delta_{x,y} + \frac{1}{2a} \sum_\mu \gamma_\mu [\delta_{x+a\hat{\mu},y} - \delta_{x-a\hat{\mu},y}] \right) \psi(y) \quad (\text{A.12})$$

Let us Fourier transform the matrix M_{xy} :

$$\tilde{M}_{pq} = \frac{1}{|\Lambda|} \sum_{x,y \in \Lambda} e^{-ip \cdot x} M_{xy} e^{iq \cdot y} \quad (\text{A.13})$$

$$= \frac{1}{|\Lambda|} \sum_{x \in \Lambda} e^{-i(p-q) \cdot x} \left(m_q + \frac{1}{2a} \sum_\mu \gamma_\mu e^{+iq \cdot a\hat{\mu}} - e^{-iq \cdot a\hat{\mu}} \right) \quad (\text{A.14})$$

$$= \delta_{p,q} \left(m_q + \frac{i}{a} \sum_\mu \gamma_\mu \sin(p_\mu a) \right) \quad (\text{A.15})$$

$$:= \delta_{p,q} \tilde{M}_p \quad (\text{A.16})$$

\tilde{M}_p^{-1} is identified as the free field propagator which has 16 poles within $\{-\pi/2, 3\pi/2\}$ for $m_q \rightarrow 0$. The interpretation is that in addition to the physical pole at $p_\mu = (0, 0, 0, 0)$, there are 15 more unphysical poles at $p_\mu = (\pi, 0, 0, 0), (0, \pi, 0, 0), \dots$ which are called doublers [385].

There are several ways to get rid of the unphysical states. The formalism introduced by Wilson [386] adds a term to the action which gives mass to the 15 unphysical states. The disadvantage of this method is that it explicitly breaks chiral symmetry. Other used techniques are staggered fermions [387] or twisted mass [388] to just name a few.

The lattice link $U_\mu(x)$ can be thought of as a matrix having a fundamental index at x and an anti-fundamental index at $x + \hat{\mu}$. An anti-fundamental index at x is represented by $\bar{\psi}(x)$,

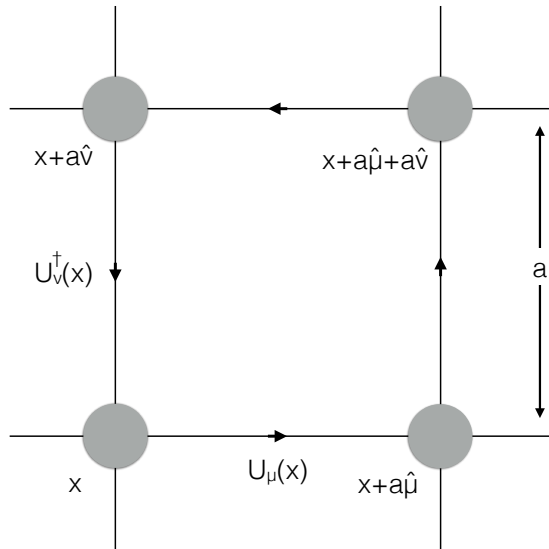


Figure A.2: Illustration for Eq. A.7: quark currents on the lattice.

and $\psi(x + \hat{\nu})$ is a fundamental index at $x + \hat{\nu}$. In order to create gauge invariant objects, each fundamental index has to be tied off against an anti-fundamental index at the same spot. Two possible gauge invariant objects are shown in Fig. A.3. The top picture in Fig. A.3 shows the $\bar{\psi}(x)$ and $\psi(x + 2\hat{\mu})$ properly connected with gauge links. The bottom shows another possibility: connecting the gauge links to them self. The trace is needed to contract the indices at an arbitrary start- and end-point against each other [389]. The bottom object is called a Wilson loop operator:

$$\mathcal{W}(c) = \text{Tr} \left(\prod_c U_\mu(x) \right), \quad (\text{A.17})$$

for a given path c . Whether or not and how $\mathcal{W}(c)$ depends on the path c will give us insight into the dynamics of QCD.

Consider a static $q\bar{q}$ pair sitting at $\vec{x}_q = \vec{0}$ and $\vec{x}_{\bar{q}} = \vec{R} = (R, 0, 0)$ as pictured on the left of Fig. A.4. Let the potential between this pair be $V(R)$; time is denoted by τ . The corresponding action $S_{q\bar{q}}$ and partition function $Z_{q\bar{q}}$ are then:

$$\begin{aligned} S_{q\bar{q}} &= \int_{\tau_a}^{\tau_b} d\tau V(R) \\ &= T V(R), \quad T = \tau_b - \tau_a, \end{aligned} \quad (\text{A.18})$$

$$Z_{q\bar{q}} = e^{-S_{q\bar{q}}} = e^{-T V(R)}. \quad (\text{A.19})$$

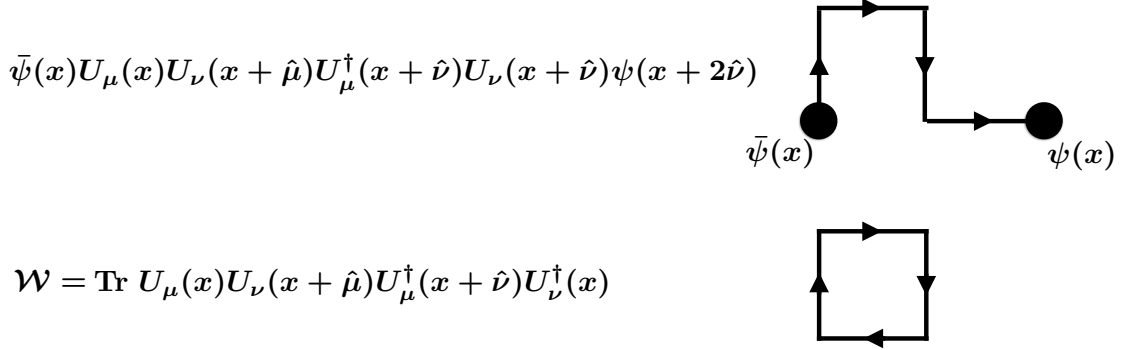


Figure A.3: Two gauge invariant lattice objects. Two fermions, one sitting at x and one at $x + 2\hat{\nu}$, with gauge links in between them (top). A loop of gauge links (bottom).

The two quarks can also be described by a quark current in time:

$$j^0(\vec{x}, \tau) = \delta^{(3)}(\vec{x}) - \delta^{(3)}(\vec{x} - \vec{R}). \quad (\text{A.20})$$

The gauge field couples to the current, giving the action:

$$S_{\text{q}\bar{\text{q}}} = -ig \int j^\mu(x) A_\mu(x) d^3\vec{x} d\tau \quad (\text{A.21})$$

$$= -ig \int_0^T A_\tau(0) d\tau + ig \int_T^0 A_\tau(R) d\tau. \quad (\text{A.22})$$

Keeping in mind that $T \gg R$, integrating over the path $c = \{(0,0) \rightarrow (T,0) \rightarrow (T,R) \rightarrow (0,R) \rightarrow (0,0)\}$ will certainly be a good approximation:

$$S_{\text{q}\bar{\text{q}}} = -ig \oint_c A_\mu(x) dx^\mu. \quad (\text{A.23})$$

The partition function from this action then is:

$$Z_{\text{q}\bar{\text{q}}} = e^{-S_{\text{q}\bar{\text{q}}}} = e^{ig \oint_c A_\mu(x) dx^\mu}. \quad (\text{A.24})$$

Reminding us of Eq. A.8, we see that this exactly corresponds to the Wilson loop operator spanning the area $T \times R$ in time \times space, which is also shown on the right of Fig. A.4. This lets us directly relate the Wilson loop operator to the $\text{q}\bar{\text{q}}$ potential $V(R)$.

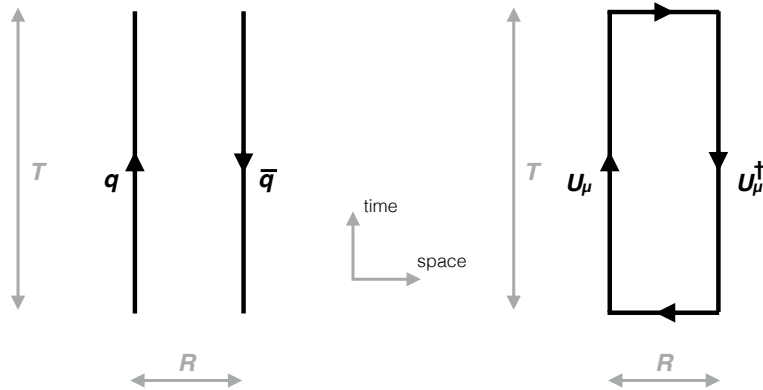


Figure A.4: Static $q\bar{q}$ pair separated by distance R (left). Wilson loop over path $c = \{(0, 0) \rightarrow (T, 0) \rightarrow (T, R) \rightarrow (0, R) \rightarrow (0, 0)\}$ (right).

A.2 Polyakov Loop

The Polyakov loop \mathcal{L} [390] is a Wilson loop spun in time:

$$\mathcal{L}(x, y, z) = \text{Tr} \left(\prod_{t=1}^{N_T} U_0(t, x, y, z) \right) \quad (\text{A.25})$$

The loop is closed because of the periodic boundary conditions on the lattice:

$$U_0(N_T + 1, x, y, z) = U_0(1, x, y, z) \quad (\text{A.26})$$

Following an analogous argumentation as done for the Wilson loop and the $q\bar{q}$ pair, the Polyakov loop gives access to the free energy of an isolated quark F_q :

$$\mathfrak{L} = e^{-F_q N_T} \quad (\text{A.27})$$

In a confined state, this free energy is infinite and thus the expectation value of the Polyakov loop is zero. However, in a state of liberated quarks and gluons, where the free energy is finite, the Polyakov loop reaches a non-zero value. This makes the Polyakov loop an order parameter for the phase transition of strongly interacting matter.

A.3 QCD Trace Anomaly

For the derivation of the trace anomaly, we follow [391]. Let us consider the simple case of a pure Yang-Mills theory in four dimensions with the Lagrangian \mathcal{L} . We can then write the

Lagrangian as

$$\mathcal{L} = -\frac{1}{4}F_{\mu\nu}^a F^{\mu\nu a}, \quad (\text{A.28})$$

$$F_{\mu\nu}^a = \delta_\mu A_\nu^a - \delta_\nu A_\mu^a + g' f^{abc} A_\mu^b A_\nu^c, \quad (\text{A.29})$$

where the notation follows the convention of Eq. A.1.

In order to specify the energy momentum tensor, we couple the theory to gravity. The action in the curved metric is then

$$S = \int d^4x \sqrt{g} \left[-\frac{1}{4}F_{\mu\nu}^a F_{\lambda\sigma}^a g^{\mu\lambda} g^{\nu\sigma} \right], \quad (\text{A.30})$$

where $g = -\det(g_{\mu\nu})$. Consider a small variation of the metric tensor

$$g^{\mu\nu}(x) \rightarrow g^{\mu\nu}(x) + \delta g^{\mu\nu}(x). \quad (\text{A.31})$$

for which the response in the action $S \rightarrow S + \delta S$ defines the energy momentum tensor

$$\delta S = \frac{1}{2} \int d^4x \sqrt{g} \Theta_{\mu\nu}(x) \delta g^{\mu\nu}(x), \quad (\text{A.32})$$

where the determinant of the metric tensor transforms as $\sqrt{g} \rightarrow \sqrt{g} (1 + \frac{1}{2}g_{\mu\nu} \delta g_{\mu\nu})$. Thus, the action changes according to

$$S \rightarrow \int d^4x \sqrt{g} \left(1 + \frac{1}{2}g_{\mu\nu} \delta g_{\mu\nu} \right) \left[-\frac{1}{4}F_{\mu\nu}^a F_{\rho\sigma}^a (g^{\mu\rho} + \delta g^{\mu\rho}) (g^{\nu\sigma} + \delta g^{\nu\sigma}) \right], \quad (\text{A.33})$$

$$\rightarrow S + \frac{1}{2} \int d^4x \sqrt{g} \left(-F_{\mu l}^a F_\nu^{la} - \frac{1}{4}g_{\mu\nu} F^{\rho\sigma a} F_{\rho\sigma}^a \right) \delta g^{\mu\nu}. \quad (\text{A.34})$$

With the definition of Eq. A.32, we identify

$$\Theta_{\mu\nu} = F_{\mu l}^a F_\nu^{la} - \frac{1}{4}g_{\mu\nu} F^{\rho\sigma a} F_{\rho\sigma}^a. \quad (\text{A.35})$$

Under a conformal transformation [392], the metric changes according to

$$g_{\mu\nu} \rightarrow \lambda^2 g_{\mu\nu}. \quad (\text{A.36})$$

The absence of any scale in our calculations implies that the action is invariant to such a transformation. From $\delta S = 0$ it follows that

$$\int d^4x \sqrt{g} \Theta_\mu^\mu(x) = 0, \quad (\text{A.37})$$

$$\Rightarrow \Theta_\mu^\mu = 0. \quad (\text{A.38})$$

The traceless energy momentum tensor is common to all conformal field theories. We have just shown that Yang-Mills theory in four dimensions is a conformal field theory. However, by introducing a scale to the interaction, the invariance will be broken.

On the side, it should be noted that the invariance of the Lagrangian under local gauge transformations makes it impossible to define a gluon propagator. Thus a gauge-fixing term is added to the Lagrangian.¹ In order to obtain physical results, which cannot depend on the choice of gauge, ghosts are added, which compensate the gauge-fixing term [393, 394].

Now, consider the cutoff of the bare interaction g_0^2 at the scale Λ , as it is realized in lattice QCD. This cutoff is gauge invariant since it is connected to the lattice spacing. The interaction now depends on the scale: $g_{0,\Lambda}^2$. The theory will be invariant under a scale transformation only, if the cutoff Λ is rescaled as well:

$$\eta^{\mu\nu} \rightarrow \lambda^2 \eta^{\mu\nu}, \quad (\text{A.39})$$

$$g_{0,\Lambda}^2 \rightarrow g_{0,\Lambda/\lambda}^2. \quad (\text{A.40})$$

The derivative with respect to the scale variation yields

$$\delta \eta^{\mu\nu} = 2 \eta^{\mu\nu} \delta \lambda, \quad (\text{A.41})$$

$$\delta \frac{1}{g_0^2} = \frac{-2}{g_0^3} (-\Lambda \delta \lambda) \frac{d}{d\Lambda} g_0. \quad (\text{A.42})$$

Consequently, the principle of stationary action gives

$$0 = \delta S = \delta \lambda \left[\int d^4x \left(\Theta_\mu^\mu \frac{1}{g_0^2} - \frac{2}{g_0^3} \left(\Lambda \frac{d}{d\Lambda} g_0 \right) \frac{1}{4} F_{\mu\nu}^a F^{\mu\nu a} \right) \right], \quad (\text{A.43})$$

$$\Theta_\mu^\mu = \frac{2}{g_0} \beta(g_0) \frac{1}{4} (F_{\mu\nu}^a F^{\mu\nu a}). \quad (\text{A.44})$$

The inclusion of fermions will lead to an additional term proportional to the quark condensate, see [395, 396].

¹In covariant gauges, the gauge-fixing term reads $\mathcal{L}_{\text{gauge-fix}} = -\frac{1}{2\omega} (\delta^\alpha A_\alpha^a)^2$, where $\omega = 0$ corresponds to the Feynman gauge.

Appendix B

Auxiliary Hydrodynamical Calculations with the MIT Bag Model

Relativistic hydrodynamics makes one strong assumption: local thermodynamic equilibrium, i. e. the mean free path in the system is small and particles do not have to be described on an individual level, but can rather be referred to as bulk matter with certain gradually varying properties. Otherwise it is a very general approach which does not need any premise for the detailed microscopical details of the interacting matter. Hydrodynamic calculations are based on the local conservation of energy and momentum and every appropriate charge like net baryon number, net strangeness or electrical charge:

$$\partial_\mu T^{\mu\nu} = 0 \quad \text{and} \quad \partial_\mu j_i^\mu = 0, \quad (\text{B.1})$$

$$\text{with} \quad T^{\mu\nu} = \int \frac{d^3\vec{p}}{(2\pi)^3 E} p^\mu p^\nu f(x, \vec{p}), \quad (\text{B.2})$$

where $T^{\mu\nu}$ is the energy-momentum tensor, j_i^μ is the current of the conserved charge i , p is the momentum and $f(x, \vec{p})$ is the probability density for the local momentum distribution¹. In the ideal fluid approximation $T^{\mu\nu}$ and j_i^μ reduce to:

$$T_{\text{id}}^{\mu\nu} = (\epsilon + \mathcal{P}_s) u^\mu u^\nu - \mathcal{P}_s g^{\mu\nu} \quad \text{and} \quad j_{i,\text{id}}^\mu = n_i u^\mu, \quad (\text{B.3})$$

where ϵ is the energy density, \mathcal{P}_s is the hydrostatic pressure, n_i is the charge density, $u = (\gamma, \gamma\vec{v})$ is the flow field, $\Delta^{\mu\nu} = g^{\mu\nu} - u^\mu u^\nu$, and $g^{\mu\nu} = \text{diag}(1, -1, -1, -1)$ is the metric tensor. More

¹A familiar example for $f(x, \vec{p})$ is the Maxwell-Boltzmann distribution for the classical, non-relativistic case.

generally the energy momentum tensor decomposes into:

$$T^{\mu\nu} = \epsilon u^\mu u^\nu - \mathcal{P} \Delta^{\mu\nu} + W^\mu u^\nu + W^\nu u^\mu + \pi^{\mu\nu}, \quad (\text{B.4})$$

$$\epsilon = u_\mu T^{\mu\nu} u_\nu, \quad (\text{B.5})$$

$$\mathcal{P} = \mathcal{P}_s + \Pi = -\frac{1}{3} \Delta_{\mu\nu} T^{\mu\nu}, \quad (\text{B.6})$$

$$W^\mu = \Delta_\alpha^\mu T^{\alpha\beta} u_\beta, \quad (\text{B.7})$$

$$\pi^{\mu\nu} = \left[\frac{1}{2} (\Delta_\alpha^\mu \Delta_\beta^\nu + \Delta_\beta^\mu \Delta_\alpha^\nu) - \frac{1}{3} \Delta^{\mu\nu} \Delta_{\alpha\beta} \right] T^{\alpha\beta}. \quad (\text{B.8})$$

The terms Π , W^μ and $\pi^{\mu\nu}$ are identified as the bulk pressure, the energy or heat flow and the shear stress tensor. Accordingly, the conserved current in the non-ideal case becomes:

$$j_i^\mu = n_i u^\mu + V_i^\mu, \quad (\text{B.9})$$

$$n_i = u_\mu j_i^\mu, \quad (\text{B.10})$$

$$V_i^\mu = \Delta_\nu^\mu j_i^\nu, \quad (\text{B.11})$$

where V_i^μ is the charge current. One recognizes the projective character of u^μ and $\Delta^{\mu\nu}$. It becomes clearer in the local rest frame (LRF), that u^μ and $\Delta^{\mu\nu}$ are projecting on the time and space component, respectively. Also, u^μ and $\Delta^{\mu\nu}$ are orthogonal to each other:

$$u^\mu = (\gamma, \gamma \vec{v}) \stackrel{\text{LRF}}{=} (1, 0, 0, 0), \quad (\text{B.12})$$

$$\Delta^{\mu\nu} = g^{\mu\nu} - u^\mu u^\nu \stackrel{\text{LRF}}{=} \text{diag}(0, -1, -1, -1), \quad (\text{B.13})$$

$$u_\mu \Delta^{\mu\nu} = u_\mu (g^{\mu\nu} - u^\mu u^\nu) = u^\nu - u_\mu u^\mu u^\nu = u^\nu - u^\nu. \quad (\text{B.14})$$

For ideal hydrodynamics it follows from Eqs. B.1 and B.3 that

$$0 = u_\nu \partial_\mu T_{\text{id}}^{\mu\nu} \quad (\text{B.15})$$

$$= \mathcal{T} \partial_\mu (s u^\mu) + \sum_i \mu_i \partial_\mu j_{i,\text{id}}^\mu. \quad (\text{B.16})$$

The full derivation can be found in [397]; the thermodynamic relation $d\epsilon = \mathcal{T} ds + \sum_i \mu_i dn_i$ was used to introduce the temperature \mathcal{T} , the entropy density s and the chemical potentials μ_i . From Eqs. B.1 and B.3 we know that $\partial_\mu j_{i,\text{id}}^\mu = 0$. Introducing the entropy current as $S^\mu = s u^\mu$, we see that the entropy is conserved in ideal hydrodynamics:

$$\partial_\mu S^\mu = 0. \quad (\text{B.17})$$

The number of unknown variables $10 + 4k$ for the symmetric 4×4 tensor $T^{\mu\nu}$ and the k conserved currents $j_i^\mu, i = 0 \dots (k-1)$ is reduced to $5 + 1k$ in the case of ideal hydrodynamics, see

Eq. B.3, where the relevant degrees of freedom are the four components of u^μ , the energy density ϵ and the k charges n_i . Still, the problem is underdetermined as there are only $4 + 1k$ equations, namely the already introduced 4 equations for the conservation of energy and momentum $\partial_\mu T^{\mu\nu} = 0$ and the k equations for the conservation of charges $\partial_\mu j_i^\mu = 0$. The missing constraint can be an equation of state which relates the pressure \mathcal{P} to the energy density ϵ and charge n :

$$\mathcal{P} = \mathcal{P}(\epsilon, n). \quad (\text{B.18})$$

With the success in determining the link between pressure and energy density in the QGP phase by numerical lattice simulations, see Fig. 1.4, state-of-the-art hydrodynamic calculations, e. g. [398–400], make use of such an equation of state [401].

Employing a simpler equation of state allows us study the impact of a phase transition on the hydrodynamic evolution. Let us start with the well known relation for the number of states in phase space

$$dj = \frac{4\pi dV}{h^3} p^2 dp, \quad (\text{B.19})$$

where d is the internal degeneracy, e. g., spin. Depending on whether they obey Bose-Einstein or Fermi-Dirac statistics, the number of particles with energy E is

$$dN_E = \frac{dj_E}{e^{\beta(E-\mu)} \pm 1}, \quad (\text{B.20})$$

where $\beta = (k_B \mathcal{T})^{-1}$. The probability distribution of the energy P_E , satisfying the normalization $\int P_E dE = 1$, for a massless particle with $E = pc$ is then given by

$$P_E dE = \frac{4\pi dV}{Nh^3} \frac{E^2}{c^3} \frac{1}{e^{\beta(E-\mu)} \pm 1} dE. \quad (\text{B.21})$$

If the particle number is not conserved, the chemical potential μ must vanish. Therefore the energy density ϵ is

$$\epsilon = \int \frac{NE}{V} P_E dE = \int \frac{4\pi dE^3}{h^3 c^3} \frac{1}{e^{\beta E} \pm 1} dE. \quad (\text{B.22})$$

Integrating, while simplifying with $\hbar = c = k_B = 1$, gives us the energy density for bosons and fermions:

$$\epsilon = \begin{cases} d_b (\pi^2/30) \mathcal{T}^4 & \text{bosons,} \\ d_f (7/8) (\pi^2/30) \mathcal{T}^4 & \text{fermions.} \end{cases} \quad (\text{B.23})$$

An ideal gas of massless pions with $d_b = 3$ is a good approximation for the hadronic phase of

relativistic heavy-ion collisions for which the pressure \mathcal{P} is easily derived:

$$\epsilon_\pi = \frac{3\pi^2}{30} \mathcal{T}^4, \quad (\text{B.24})$$

$$\mathcal{P}_\pi = \frac{1}{3} \epsilon_\pi = \frac{3\pi^2}{90} \mathcal{T}^4. \quad (\text{B.25})$$

The MIT bag model endows a finite region with a constant energy density B [402]. The effect of the energy density inside the bag is to add a term to the usual energy momentum tensor [403]:

$$T_{\text{Bag}}^{\mu\nu} = T_{\text{fields}}^{\mu\nu} + Bg^{\mu\nu}. \quad (\text{B.26})$$

The MIT bag model successfully describes a couple of features of QCD, e.g. the limiting Hagedorn temperature mentioned in the introductory chapter or the confinement of quarks and gluons inside the bag giving rise to only color-singlet hadronic solutions. The degrees of freedom within the bag model are quarks and gluons. With the help of Eq. B.23, the equation of state can be inferred from the energy density and pressure:

$$\epsilon_{\text{QGP}} = \left(d_b + \frac{7}{8} d_f \right) \frac{\pi^2}{30} T^4 + B, \quad (\text{B.27})$$

$$\mathcal{P}_{\text{QGP}} = \left(d_b + \frac{7}{8} d_f \right) \frac{\pi^2}{90} T^4 - B. \quad (\text{B.28})$$

The degeneracy factors of the QGP for various numbers of flavors can be found in Table B.1 and the resulting temperature dependence for both, the pion gas and the QGP of the pressure \mathcal{P} , and their energy densities ϵ are shown in Fig. B.1 on the left and right, respectively. All axes have been divided by the bag constant B to display the universal behavior, regardless of the value of B . It is seen that the pressure of the pion gas for temperatures lower than a critical temperature \mathcal{T}_c exceeds the pressure for the QGP equation of state, whereas for higher temperatures this condition is reversed. Considering the Gibbs criterion [404], this implies a phase transition at \mathcal{T}_c . For a given number of flavors, this critical temperature depends only on the value of the bag constant B :

$$\mathcal{T}_c^4 = \frac{90}{\pi^2} \frac{B}{d_{\text{QGP}} - d_\pi} \stackrel{N_f=2}{=} \frac{90 B}{34 \pi^2}. \quad (\text{B.29})$$

In Fig. B.1 we see the case of $N_f = 2$ in black and $N_f = 3$ in a light gray in the background. It is clear that the general behavior of the strongly interacting matter within this proposed scenario does not depend on the number of flavors. The only change in the $N_f = 3$ instance is a slight shift of the critical temperature, defined as the intersection of the lines in the pressure diagram on the left, to lower values. Also the energy density dependence on the temperature on the right manifests no qualitative alteration. While also here the slight shift of \mathcal{T}_c and a gradual modification of the slopes can be perceived, it appears that the latent heat, i.e. the

energy difference of the two phases at \mathcal{T}_c , scaled by the bag constant B stays approximately constant.

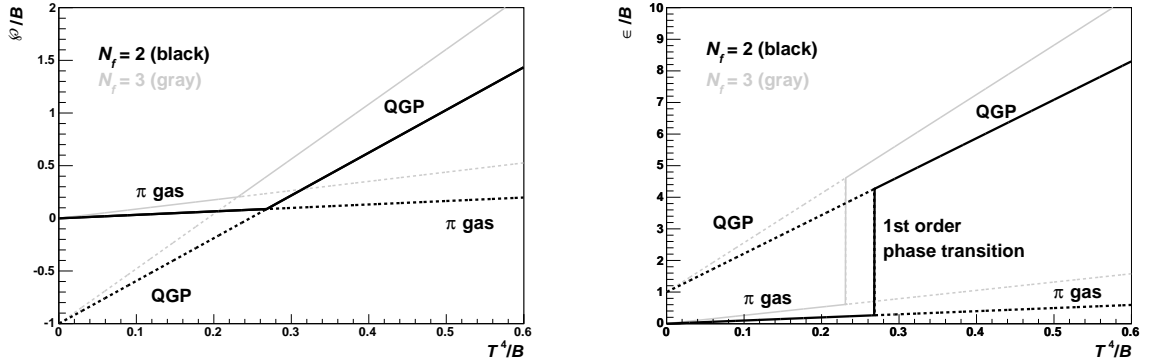


Figure B.1: Dependence of the pressure \mathcal{P} (left) and the energy density ϵ (right) on the fourth power of the temperature in a pion gas and the QGP phase following the MIT bag model. All axes have been scaled by the bag constant B to display the universal behavior which is independent of B .

N_f	0	2	3	4
$d_{q\bar{q}} = d_\pi$	0	3	8	15
d_{gluon}	16	16	16	16
d_{quark}	0	24	36	48
d_{QGP}	16	37	47.5	58

Table B.1: Degeneracy factors with $N_c = 3$ colors and N_f massless flavors of a $q\bar{q}$ pair representing pions, $d_{q\bar{q}} = d_\pi$; gluon, d_{gluon} ; quark, d_{quark} ; and the QGP, $d_{\text{QGP}} = d_{\text{gluons}} + \frac{7}{8}d_{\text{quarks}}$. Cf. [405].

In order to obtain a value for B we follow [394] and expand the β function for the running coupling of the strong interaction:

$$\beta_{\text{QCD}}(\alpha_s) = -\frac{11C_A - 2N_f}{12\pi}\alpha_s^2 + \mathcal{O}(\alpha_s^3), \quad (\text{B.30})$$

where $C_A = 3$ is the color factor for gluons. In QCD the trace anomaly of the energy momentum

tensor is intimately related to scale transformations²

$$T_\mu^\mu = \frac{\beta_{\text{QCD}}(\alpha_s)}{4\alpha_s} F_{\mu\nu}^a F_a^{\mu\nu} + \sum_f m_f \bar{q}_f q_f. \quad (\text{B.31})$$

In the bag model we can see from Eqs. B.28 and B.27 that

$$T_\mu^\mu = \epsilon - 3\mathcal{P} = 4B. \quad (\text{B.32})$$

The spectra of charmonia suggest [408] the vacuum condensate to be

$$\left\langle \frac{\alpha_s}{\pi} F_{\mu\nu}^a F_a^{\mu\nu} \right\rangle \simeq 0.012 \text{ GeV}^4 \approx (330 \text{ MeV})^4. \quad (\text{B.33})$$

Using this value³ the bag constant can be quantified. In the chiral limit of vanishing quark masses for the trace anomaly

$$B = -\frac{1}{4} \frac{\beta_{\text{QCD}}}{4\alpha_s} \langle F_{\mu\nu}^a F_a^{\mu\nu} \rangle \quad (\text{B.34})$$

$$= \frac{1}{4} \frac{33 - 2N_f}{12\pi} \alpha_s^2 \frac{1}{4\alpha_s} \langle F_{\mu\nu}^a F_a^{\mu\nu} \rangle \quad (\text{B.35})$$

$$= \frac{1}{4} \frac{33 - 2N_f}{12} \alpha_s \frac{1}{4\alpha_s} \left\langle \frac{\alpha_s}{\pi} F_{\mu\nu}^a F_a^{\mu\nu} \right\rangle \quad (\text{B.36})$$

$$\approx \frac{9}{32} (330 \text{ MeV})^4 \quad (\text{B.37})$$

$$\approx (240 \text{ MeV})^4. \quad (\text{B.38})$$

Similar derivations with almost identical values can be found in textbooks like, e. g., [405]. With this value for the bag constant B , we can now quantify the critical temperature in Eq. B.29 to $\mathcal{T}_c \approx 170 \text{ MeV}$ for $N_f = 2$ and a slightly lower value of $\mathcal{T}_c \approx 166 \text{ MeV}$ for $N_f = 3$, which is in remarkable agreement to modern lattice QCD results, e. g., presented in the introductory chapter in Fig. 1.3 (right).

As we have now all ingredients ready, we can perform a simple 1+1D boost invariant calculation of the hydrodynamic evolution of the system. It is useful to transform the coordinates to proper time τ and space-time rapidity η_s :

$$\tau = \sqrt{t^2 - z^2}, \quad (\text{B.39})$$

$$\eta_s = \frac{1}{2} \ln \frac{t+z}{t-z}. \quad (\text{B.40})$$

The inverse transformation is hereby given as $t = \tau \cosh \eta_s$ and $z = \tau \sinh \eta_s$. We ignore the

²The interested reader is referred to the detailed investigation in [406]; the simple result should rather be looked up in, e. g., Appendix A of [407]. See also the discussion in Section A.3.

³Note that the value of 0.012 GeV^4 for the vacuum gluon condensate is still used in modern lattice QCD calculations [409].

transverse expansion of the system and assume Bjorken scaling of the flow

$$v = z/t. \quad (\text{B.41})$$

This makes the flow rapidity y coincide with the space time one, and gives an easy expression for the flow field

$$y = \frac{1}{2} \ln \frac{1+v}{1-v} = \frac{1}{2} \ln \frac{1+z/t}{1-z/t} = \eta_s, \quad (\text{B.42})$$

$$u^\mu = \frac{1}{\sqrt{1-\vec{u}^2}} (1, 0, 0, z/t) = \frac{1}{\sqrt{t^2-z^2}} (t, 0, 0, z) \quad (\text{B.43})$$

$$= \frac{1}{\tau} (\tau \cosh \eta_s, 0, 0, \tau \sinh \eta_s) = (\cosh \eta_s, 0, 0, \sinh \eta_s). \quad (\text{B.44})$$

The derivatives transform like

$$\begin{pmatrix} \partial_t \\ \partial_z \end{pmatrix} = \begin{pmatrix} \frac{\partial \tau}{\partial t} & \frac{\partial \eta_s}{\partial t} \\ \frac{\partial \tau}{\partial z} & \frac{\partial \eta_s}{\partial z} \end{pmatrix} \begin{pmatrix} \partial_\tau \\ \partial_{\eta_s} \end{pmatrix} \quad (\text{B.45})$$

$$= \begin{pmatrix} \frac{t}{\sqrt{t^2-z^2}} & \frac{z}{t^2-z^2} \\ -\frac{z}{\sqrt{t^2-z^2}} & \frac{t}{t^2-z^2} \end{pmatrix} \begin{pmatrix} \partial_\tau \\ \partial_{\eta_s} \end{pmatrix} \quad (\text{B.46})$$

$$= \begin{pmatrix} \cosh \eta_s & \sinh \eta_s \\ -\sinh \eta_s & \cosh \eta_s \end{pmatrix} \begin{pmatrix} \partial_\tau \\ \frac{1}{\tau} \partial_{\eta_s} \end{pmatrix} \quad (\text{B.47})$$

One can see in Eq. B.44 that u^μ does not depend on τ , therefore only the derivative with respect to η_s is important:

$$\partial_\mu u^\mu = \begin{pmatrix} \partial_t \\ \partial_z \end{pmatrix} \begin{pmatrix} u_t & u_z \end{pmatrix} \quad (\text{B.48})$$

$$= \begin{pmatrix} \sinh \eta_s & \frac{1}{\tau} \partial_{\eta_s} \\ \cosh \eta_s & \frac{1}{\tau} \partial_{\eta_s} \end{pmatrix} \begin{pmatrix} \cosh \eta_s & \sinh \eta_s \end{pmatrix} \quad (\text{B.49})$$

$$= -\frac{1}{\tau} \sinh^2 \eta_s + \frac{1}{\tau} \cosh^2 \eta_s \quad (\text{B.50})$$

$$= \frac{1}{\tau} \quad (\text{B.51})$$

Similarly it can be shown that $u^\mu \partial_\mu = \partial_\tau$. This greatly removes complexity from the ideal hydrodynamic equations and the conservation of energy directly gives

$$\partial_\mu T_{\text{id}}^{\mu 0} = u^0 u^\mu \partial_\mu \epsilon + (\epsilon + \mathcal{P}_s) \partial_\mu u^\mu u^0 = 0 \quad (\text{B.52})$$

$$\partial_\tau \epsilon = -\frac{\epsilon + \mathcal{P}_s}{\tau} \quad (\text{B.53})$$

and the momentum conservation reduces to

$$\partial_\mu T_{\text{id}}^{\mu\alpha} = \vec{0} \quad (\text{B.54})$$

$$(\epsilon + \mathcal{P}_s) \partial_\mu u^\mu u^\alpha + u^\alpha u^\mu \partial_\mu (\epsilon + \mathcal{P}_s) - g^{\mu\alpha} \partial_\mu \mathcal{P}_s = \vec{0} \quad (\text{B.55})$$

$$(\epsilon + \mathcal{P}_s) \frac{1}{\tau} u^\alpha + u^\alpha \partial_\tau (\epsilon + \mathcal{P}_s) - g^{\mu\alpha} \partial_\mu \mathcal{P}_s = \vec{0} \quad (\text{B.56})$$

$$-u^\alpha \partial_\tau \epsilon + u^\alpha \partial_\tau (\epsilon + \mathcal{P}_s) - g^{\mu\alpha} \partial_\mu \mathcal{P}_s = \vec{0} \quad (\text{B.57})$$

$$u^\alpha \partial_\tau \mathcal{P}_s + 1 \partial_\alpha \mathcal{P}_s = \vec{0} \quad (\text{B.58})$$

$$\sinh \eta_s \partial_\tau \mathcal{P}_s + (-\sinh \eta_s \partial_\tau + \cosh \eta_s \frac{1}{\tau} \partial_{\eta_s}) \mathcal{P}_s = 0 \quad (\text{B.59})$$

$$\partial_{\eta_s} \mathcal{P}_s = 0 \quad (\text{B.60})$$

Eq. B.60 together with the laws of thermodynamics

$$0 = \left. \frac{\partial \mathcal{P}_s}{\partial \eta_s} \right|_\tau = s \left. \frac{\partial \mathcal{T}}{\partial \eta_s} \right|_\tau + n \left. \frac{\partial \mu}{\partial \eta_s} \right|_\tau \quad (\text{B.61})$$

implies that if there is no net charge n , the temperature will only depend on proper time τ , i. e., is constant on a hypersurface of constant τ .

Appendix C

Further Experimental Considerations

C.1 Medium Choice in Gaseous Detectors

The traditional TPC gas mixture P10 (Ar-CH₄ as 90%-10%) used in the TPC of STAR [410], the mix used by NA49 in the vertex TPCs (Ne-CO₂ at 91%-9%) and the main TPCs (Ar-CO₂-CH₄ at 91%-4.5%-4.5%) [411], as well as the mix used by CERES/NA45 (Ne-CO₂ at 80%-20%) [412] all consist of a large amount of noble gas and a small fraction of a polyatomic gas. (For a short review of TPCs used in heavy-ion experiments see also [413].) The reasons for this general pattern are briefly discussed in the following.

All gases have an ionizing energy E_I , i. e. the minimum energy needed to remove an electron, of 10 to 25 eV as shown in Fig. C.1. In terms of E_I , the noble gases show similar characteristics as the other gases. The reason to base the detector gas on a noble gas thus must lie deeper and can be found in the dynamics of the electron drift. Also shown in Fig. C.1 is the lowest excitation energy E_X . For the noble gases (${}^2\text{He}$, ${}^{10}\text{Ne}$, ${}^{18}\text{Ar}$, ${}^{36}\text{Kr}$, ${}^{54}\text{Xe}$, and ${}^{86}\text{Rn}$) one sees that E_X is only slightly smaller than E_I , while — with the exception of ${}^1\text{H}$ — for the other gases (${}^7\text{N}$, ${}^8\text{O}$, ${}^9\text{F}$, and ${}^{17}\text{Cl}$) E_X is much smaller than E_I . This implies that a drifting electron with an energy of a few eV will travel a noble gas without scattering inelastically with a bound electron. It is these scatterings that should be avoided to make the drifting electrons travel the gas quickly without diffusion. Additional quantum statistical effects¹ lead to a minimum of the electron cross-section at a few eV. The interactions of slow electrons in gases, especially in Argon, was experimentally first studied by C. Ramsauer [414], and J.S. Townsend and V.A. Bailey [415] in the 1920s after who the phenomenon was named Ramsauer-Townsend effect. A

¹The positively charged gas nucleus forms an electromagnetic potential well for the electron. Since the involved energy scales are small, this scattering has to be treated quantum statistically.

theoretical description of the Ramsauer-Townsend effect together with a compiled set of cross sections can be found in Chapter XVIII of [416].

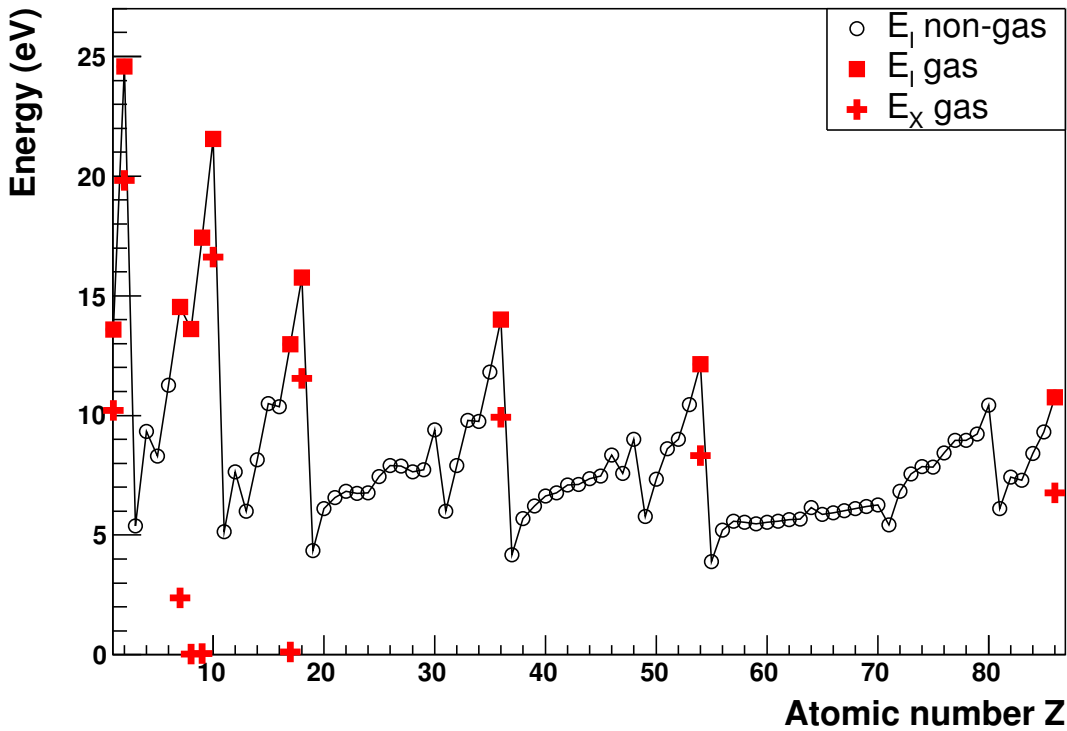


Figure C.1: Ionizing energy for non-gases in open circles and gases in red squares. Lowest excitation energy for gases in red crosses. Relative errors on ionization energies are sub per mille. Data from [417].

One also has to keep in mind the drift velocity of the ions. When the gas gets ionized, the positive ions can lead to undesired space-charge effects like a non-uniform electrical drift field. It is thus desirable that the ions quickly drift to the cathode where they neutralize. As the ratio of ion drift velocity and electrical field for a given type of ion is rather constant over a wide range of electrical drift field gradients, one usually refers to this ratio as ion mobility².

The role of the polyatomic quencher with its abundant rotational and vibrational excitation modes is to absorb the energy of drifting electrons with intermediate energies and leave electrons with small energies around the Ramsauer-Townsend minimum, where the scattering cross-section of electrons has its minimum. The quencher also absorbs the photons emitted in the de-excitation process of the noble gas, typically in the UV range³, by photodissociation. The

²Increasing the electrical field by a factor of ten, the drift velocity of Ar^+ in Ar also changes by a factor of roughly ten, but the ion mobility only changes by around ten percent [225].

³ISO 21348 *Definitions of Solar Irradiance Spectral Categories* specifies UV (Ultraviolet) as $100 \text{ nm} \leq \lambda < 400 \text{ nm}$ corresponding to $3.10 \text{ eV} < E \leq 12.40 \text{ eV}$.

photodissociation energies for, e. g., CH_4 are in the range of 4 to 10 eV [418].

C.2 Tail Cancellation and Baseline Filter

A particularity of the signal shape was found in high-multiplicity cosmic events, namely the undershoot of the signal below the baseline, see the left panel of Fig. C.2. Via studying a simulation, it was found to be caused by the slowly moving ions. Ions ending up on different parts of the detector have distinct signals, see the right panel of Fig. C.2. All ions moving towards the drift volume show the undershoot, the ions moving towards the pads show an excess. Ions that transverse towards the read-out pad can occur when an ionizing particle penetrates the MWPC and consequently produces ions between the anode wire and the pads. The secondary spikes of the signals in the figure — for ions ending on the cathode from 20 to 32 μs and for ions ending on the gating grid from 100 to 110 μs — are caused by the acceleration of the ions in the vicinity of the cathode or gating wires. The left panel of Fig. C.2 also shows a signal after processing with the ALICE TPC readout (ALTRO) chip. The undershoot of the signal was compensated by a moving average baseline correction (Baseline Correction II — BCII); additionally the positive signal tail was shortened by a tail cancellation filter (TCF) in order to reduce the cluster size in time and reduce the occupancy of the detector. Details about the ALTRO chip and its signal processing can be found in [419]. Neither the BCII nor the TCF are used so far in data taking.

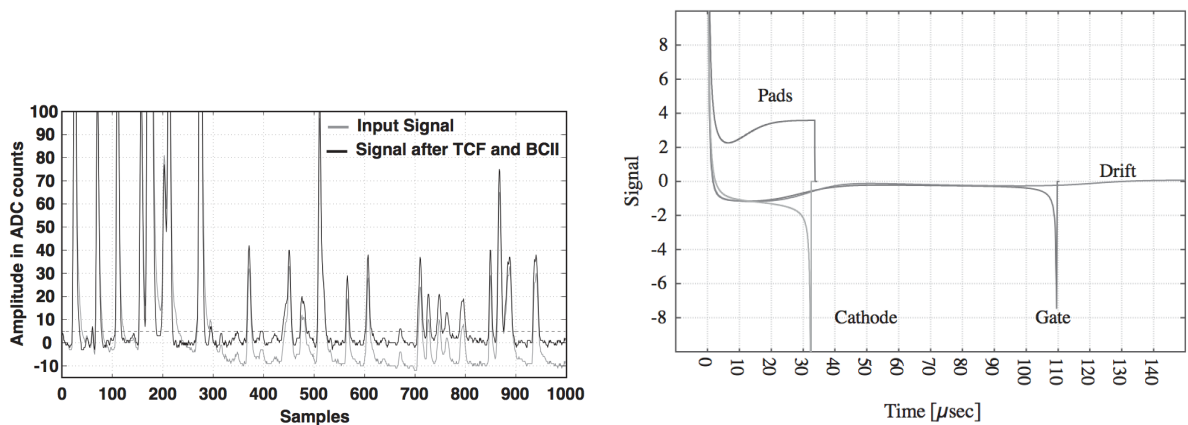


Figure C.2: Left: Signal shapes from a high-multiplicity cosmic shower before and after correction. One clearly sees the undershoot of the uncorrected signal below the baseline. Right: Simulation of signal shape from ions leaving the anode region on different paths and ending on the pads, the cathode wire, the gating grid or in the drift region. Both taken from [420].

Appendix D

Additional Reconstruction Algorithms

D.1 Seeding for the Kalman Tracker

The seeding algorithms can be grouped in two categories: I) seeds with a light primary vertex constraint and II) seeds without this constraint to allow for secondary particle finding.

The algorithm with the constraint takes each cluster on an outer pad row i and looks for a hit at pad row $j = i - 20$ in a window that projects the track within a given uncertainty to the primary vertex determined by the ITS. The allowed window for the position of the cluster j is trivial to implement in the z direction. For tracks with an infinite transverse momentum, the constraint would be straight-forward in the transverse direction as well. For track hypotheses with a finite momentum, the restriction to a minimal p_T reduces the computational effort and can assure additional efficiency in the statistically scarce high- p_T region with an acceptable impact in CPU time needed for the event reconstruction. The seeding with the vertex constraint makes use of this feature, by first seeding three times with the outer pad-row i decreasing in steps of six rows with a p_T cut-off of 200 MeV/ c . Afterwards, a finer search looks for high- p_T tracks in nine steps of two pad-rows each with a minimum p_T of 500 MeV/ c . Finally, ten extra seedings with i running in steps of ten pad-rows and a decreasing p_T limitation concludes the seeding with the primary vertex restriction.

Seeds for secondary tracks are looked for without the primary vertex constraint. Instead, a third cluster at pad-row $k = (i - j)/2$ is required, where i and j are seven rows apart and the cluster at row k has to lay in the vicinity of the straight line connecting the outer clusters i and j . An emphasis is put on the efficient reconstruction of kink daughters. The aim of the kink finding is to reconstruct the decay of the charged kaon $K^\pm \rightarrow \mu^\pm$ (anti-) ν_μ (B.R. 63%)

with a $c\tau = 3.7$ m, which is large compared to the outer radius of the ALICE TPC of 2.47 m. Accordingly, the seeding for secondary tracks is performed with each of the three outermost pad-rows for the cluster further from the center of the TPC. Supplementarily, six seedings are performed in steps of five and five more in steps of ten pad-rows.

More details about the seeding can be found in Chapter 5.1.3.2 of [271].

D.2 On-the-fly V^0 Finder

The on-the-fly finder makes use of the locality of the Kalman tracking and is run during the track reconstruction. The on-the-fly source can be found in `$ALICE_ROOT/ITS/AliITSV0Finder.cxx`. Its selection criteria are conveniently steerable from outside via an OCDB object. For 2011, it can be found on alien in `/alice/data/2011/OCDB/ITS/Calib/RecoParam/`. Several versions of these reconstruction parameters exist. The file `OCDB.root` stored together with the reconstructed data, for pass 2 of the LHC11h dataset on alien in `/alice/data/2011/LHC11h_2/$RUN/ESDs/pass2/`, contains a snapshot of the OCDB objects that were used for the reconstruction, and an identifier to link back to the employed file in the OCDB. For a set of standard parameters in the on-the-fly V^0 finding, the OCDB object `Run0_999999999_v9_s0.root` was read out. Each reconstruction parameter object can have three different subsets for cosmics, low- and high-multiplicity data taking. For Pb-Pb periods, naturally the high-multiplicity set should be used. One can easily `Dump` the `AliESDV0Params` to the shell output to study the selection criteria. The complexity of the on-the-fly finder is increased compared to its offline equivalent, it consists of roughly ten times more lines of code. Therefore only the major steps are documented here.

As in the offline version, also in the on-the-fly finder, likely primary tracks are excluded from the pairing step, which are mainly selected by an error-weighted, transverse distance to the primary vertex. Kink candidates are rejected. Non-pion tracks are exempt from the two aforementioned criteria. A ratio r_{Cls} of found clusters over findable clusters¹ for each track is formed. If this ratio r_{Cls} exceeds the limit of 0.6 in a sliding-window transverse-radius region A , the track is inhibited from forming a secondary vertex radially outwards of a radius R_{max,V^0} . For A spanning from 108–123, 100–115, 92–107, or 85–92 cm, R_{max,V^0} has the value of 140, 130, 120, or 110 cm.

In a first, rough pairing step, only simple helix parametrizations for the tracks are used to reduce the computational cost. The intersections of two helices in the (R, φ) plane are found. Two intersections of the helices will be formed if in the decay process a finite amount of momentum was released in the azimuthal direction, see Fig. D.1 for the well-known cowboy and sailor topology. The excellent spatial resolving-power of ALICE allows to neglect resolution

¹A cluster is findable if the track trajectory does not cross a dead zone like a sector boundary.

effects here. Zero momentum release in the bending orientation results in exactly one crossing, which is exploited for the photon reconstruction, see Section 4.5. For vertex candidates, the distance of closest approach of the daughter parametrizations is minimized in a parabolic iteration similar to the offline finder; the difference being that here a true distance — and not an error weighted one — is used. The candidate is rejected if the DCA exceeds a limit $\text{DCA}_{\text{max}} = \text{Min}(0.1 \text{ cm} + 0.1 \cdot R, 1 \text{ cm})$. The pointing angle θ is computed and a minimum of $\cos(\theta)$ of 0.85 is required.

All vertices surviving so far are inspected in a refined approach. The DCA is calculated again as described above. If both tracks appear to be situated closer than 3 cm in the transverse direction to the vertex,² an error parametrization based on the covariance matrix of the tracks is invoked to update the DCA with an error-weighted DCA, similar to what is done in the offline V^0 finder. In case of two helix intersections in the (R, φ) plane, the vertex with the minimal (weighted) DCA is chosen. Vertices with a (weighted) DCA of more than the aforementioned DCA_{max} are discarded. The position of the vertex is calculated as an error-weighted mean:

$$x_{V^0} = \frac{1}{2} \left((1 - w_y) \cdot x_1 + w_y \cdot x_2 + (1 - w_z) \cdot x_1 + w_z \cdot x_2 \right), \quad (\text{D.1})$$

$$y_{V^0} = (1 - w_y) \cdot y_1 + w_y \cdot y_2, \quad (\text{D.2})$$

$$z_{V^0} = (1 - w_z) \cdot z_1 + w_z \cdot z_2, \quad (\text{D.3})$$

$$w_y = \frac{\sigma_{y,1}^2}{\sigma_{y,1}^2 + \sigma_{y,2}^2}, \quad (\text{D.4})$$

$$w_z = \frac{\sigma_{z,1}^2}{\sigma_{z,1}^2 + \sigma_{z,2}^2}, \quad (\text{D.5})$$

where the single-particle positions x, y and z and their squared uncertainties are appended the subscripts ₁ and ₂ to indicate the first or second track, respectively. With the improved V^0 vertex position, the $\cos(\theta)$ selection of 0.85 is re-checked. If the radius $R_{V^0} = \sqrt{x_{V^0}^2 + y_{V^0}^2}$ exceeds the value $R_{V^0}^{\text{max}} = 220 \text{ cm}$ or falls below a value of $R_{V^0}^{\text{min}} = 0.5 \text{ cm}$, the V^0 is rejected.

The main advantage of the on-the-fly V^0 finder is that it allows to select different track hypotheses for the V^0 building. Specifically, the finder prefers tracks which have no associated ITS cluster radially inwards of the secondary vertex. Shared ITS clusters inward from the secondary vertex are punished with an additional χ^2 , as it is likely that they are erroneously associated to the track and bias the V^0 measurement in a bad way. These causality requirements improve the signal of the reconstructed V^0 . The reduced bias from wrong ITS clusters is especially beneficial for a correlation analysis involving V^0 s. The problem arising from falsely associated hits in the silicon detectors is further discussed in Chapter 5. After finding the best track prolongation in the ITS for the V^0 , a rather strict cut on the cosine of the pointing

²Take note of the Jira ticket ALIROOT-5666. Currently this criterion is that the track should be less than 3 cm further outside in the transverse direction than the vertex.

angle of 0.99 is applied (cf. $\cos(\theta) > 0.9$ in the offline finder). This is possible as the on-the-fly finder achieves a good resolution and is not aiming for reconstructing secondary V^0 s from, e. g., weakly decaying cascades. Having greatly reduced the sample of V^0 candidates, the remaining ones are flagged as reconstructed by the on-the-fly finder and attached to the ESD event.

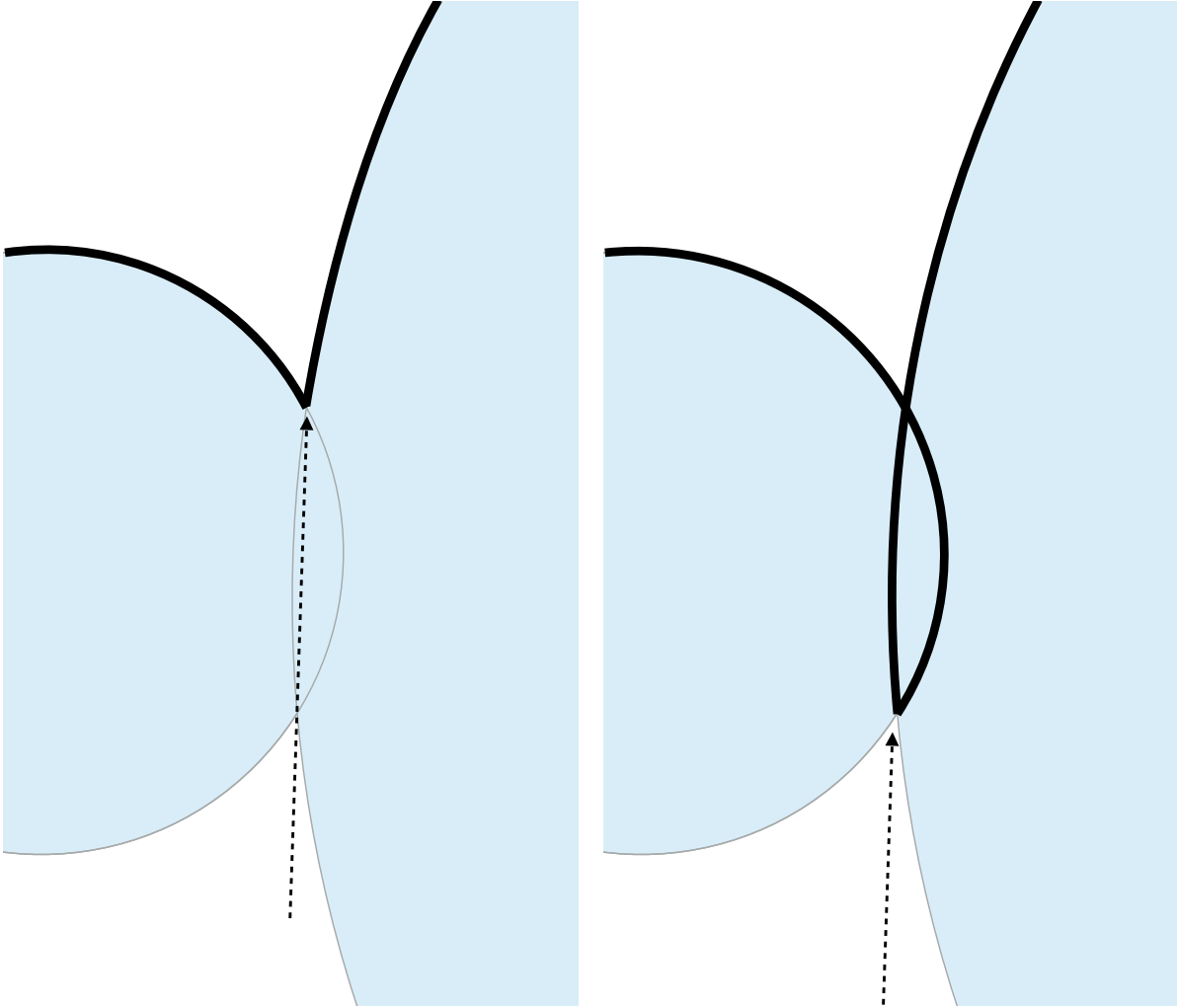


Figure D.1: Sailor (left) and cowboy (right) decay topology. The difference between the two scenarios is that in the sailor context, the azimuthal decay momentum is released in the daughters' bending direction, while in the cowboy case it is released in the opposite way.

Appendix E

Λ Selection Supplements

E.1 On-The-Fly Criteria

Selection variable	Selection value
On-the-fly status	force true
Like sign daughters	reject
Number of TPC clusters of daughters	0 or ≥ 80
DCA V^0 daughters	≤ 0.2 cm
Cosine pointing angle	≥ 0.9999
kTPCpid bit daughters	force true
$N_{\sigma}^{\text{TPC}}(\text{p})$	≤ 3.7
$N_{\sigma}^{\text{TPC}}(\pi^{-})$	≤ 3.8
$N_{\sigma}^{\text{TPC}}(\bar{\text{p}})$	≤ 3.9
$N_{\sigma}^{\text{TPC}}(\pi^{+})$	≤ 4.2
$N_{\sigma}^{\text{TOF}}(\text{p})$	if kTOFpid present: ≤ 5.0
$N_{\sigma}^{\text{TOF}}(\bar{\text{p}})$	if kTOFpid present: ≤ 5.0
DCA π^{\pm} to pri. vtx.	≥ 0.02 cm
DCA $\text{p}/\bar{\text{p}}$ to pri. vtx.	≥ 0.05 cm
$p_{\text{T}}(\Lambda)$	≥ 0.5 GeV/ c
$p_{\text{T}}(\bar{\Lambda})$	all p_{T} accepted
m_{inv} window around PDG mass	± 4 MeV/ c^2

Table E.1: Selection criteria applied on the AOD V^0 sample to obtain a highly significant Λ sample. See the discussion in Section 5.2.1 for the selection value of zero TPC clusters.

All Λ selection criteria that were additionally applied to the V^0 vertices provided by the on-the-fly finder are listed in Table E.1. As discussed in Section 5.3.1 they were chosen to maximize the significance of the Λ sample.

E.2 Motivation for Differential Purity Estimates

The necessity of a differential purity determination is best explained with a small toy model. On purpose, it is simplifying and the quantitative choices are exaggerating the effects.

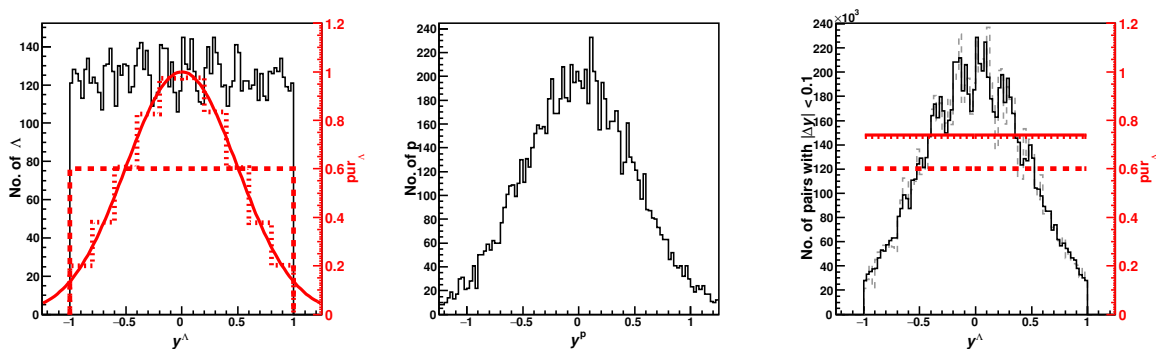


Figure E.1: Motivation for the differential determination of particle purities. Left: Number of simulated Λ vs. the rapidity of the Λ in black. Purities in red with the true Gaussian purity as a full line, the average over the full rapidity (60.2%) as the coarsely dashed line, and a binned average in the finely dashed line. Center: Number of protons versus proton rapidity. Right: Number of proton-lambda pairs with a small rapidity difference $|\Delta y| = |y^\Lambda - y^p| < 0.1$ as a function of the lambda rapidity in black. Average pair purities in red with the result from the differential (true) single-particle purity as a solid line (73.8%), the outcome from the single-particle average over the full rapidity as the coarsely dashed line (60.2%), and the calculation with the binned average as the finely dashed line (73.4%).

Let us assume some arbitrary rapidity-dependent single-particle purity. Here, we chose a Λ purity pur_Λ with a Gaussian dependency as shown with the solid red line in the left panel of Fig. E.1. Generating Λ particles flat in rapidity within ± 1 results in the distribution shown in black. The single-particle purity averaged over all lambda is 60.2%, visualized as the coarsely dashed, red histogram. Also shown is the average over finite bins with a width of 0.25 in rapidity as a finely dashed, red histogram. Naturally, the histogram with the 0.2 wide bins is a better approximation of the (true) Gaussian distribution. Protons are created according to a Gaussian centered at proton rapidity $y^p = 0$ with a width of 0.5 as displayed in the central panel.

The distribution of pairs with a small rapidity difference $|\Delta y| = |y^\Lambda - y^p| < 0.1$ is presented

in the right panel in the black, solid histogram as a function of the Λ rapidity;¹ it shows the origin in rapidity of Λ particles forming pairs. We see that the pair distribution in the right panel (which appears rather Gaussian) differs significantly from the single-particle distribution of the Λ in the left panel (which is box-shaped). Many more pairs are formed with Λ originating from the central region $|y^\Lambda| < 0.5$ than from larger rapidities $|y^\Lambda| > 0.5$. Thus, the pair-average lambda purity will be dominated by the lambda purity for central rapidities. The resulting true average pair-purity (73.8%), shown as a red, solid line in the right panel, is significantly higher than the single-particle average (60.2%), shown as a coarsely dashed line. The true average pair-purity can be recovered to a high accuracy with the binned approximation of the single-particle purity. The binned approximation yields a pair-purity of 73.4%, shown as the finely dashed line. The agreement down to 0.4% in absolute pair-purity is so good that the two lines are overlapping.

¹The pair distribution was obtained by using the single-particle information for each pair; however, it should be noted that the shape of the pair distribution for such small rapidity differences can be well approximated with a simple multiplication of the single-particle spectra. The simple multiplication — after scaling it to the number of pairs with $|\Delta y| < 0.1$ — is shown as the gray, dashed histogram in the background.

Appendix F

Adjunct Pair Observables

F.1 Raw Correlation Functions

The raw $p\Lambda$ and $\bar{p}\bar{\Lambda}$ correlation functions differential in centrality and transverse mass m_T are shown in Fig. F.1–F.4.

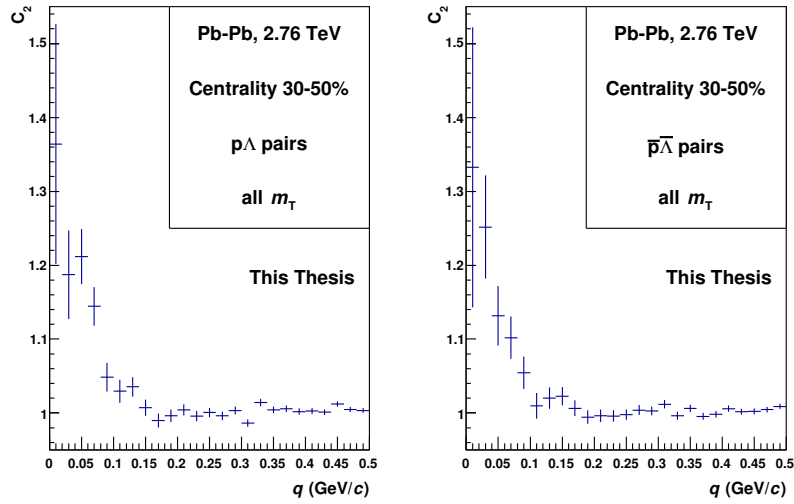


Figure F.1: Raw $p\Lambda$ correlation functions for pairs of particles and pairs of anti-particles for the 30–50% most central events in one m_T bins.

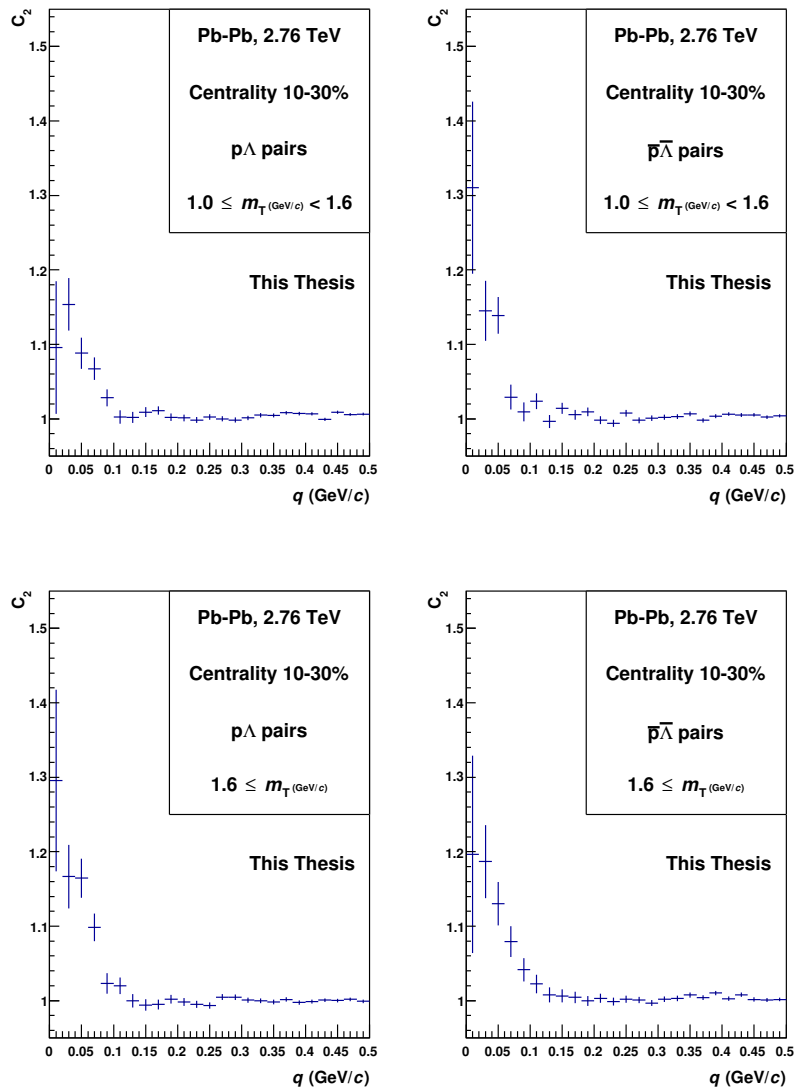


Figure F.2: Raw $p\Lambda$ correlation functions for pairs of particles and pairs of anti-particles for the 10–30% most central events in two m_T bins.

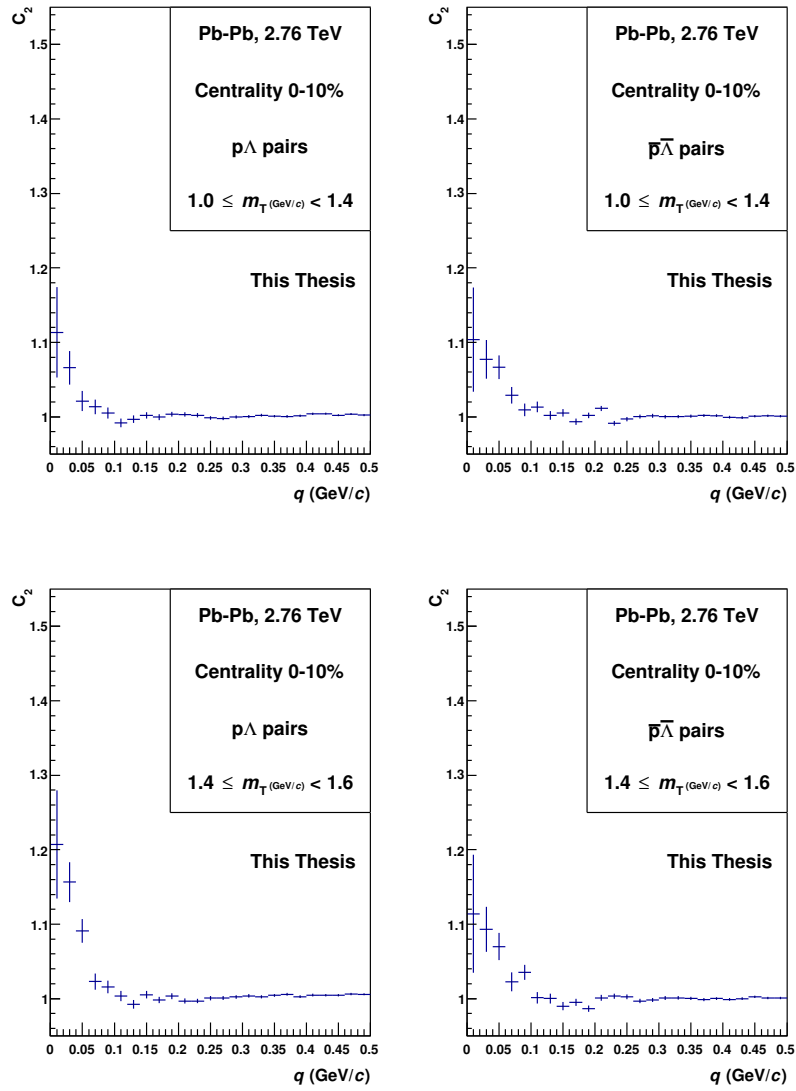


Figure F.3: Raw $p\Lambda$ correlation functions for pairs of particles and pairs of anti-particles for the 0–10% most central events in the two lower m_T bins.

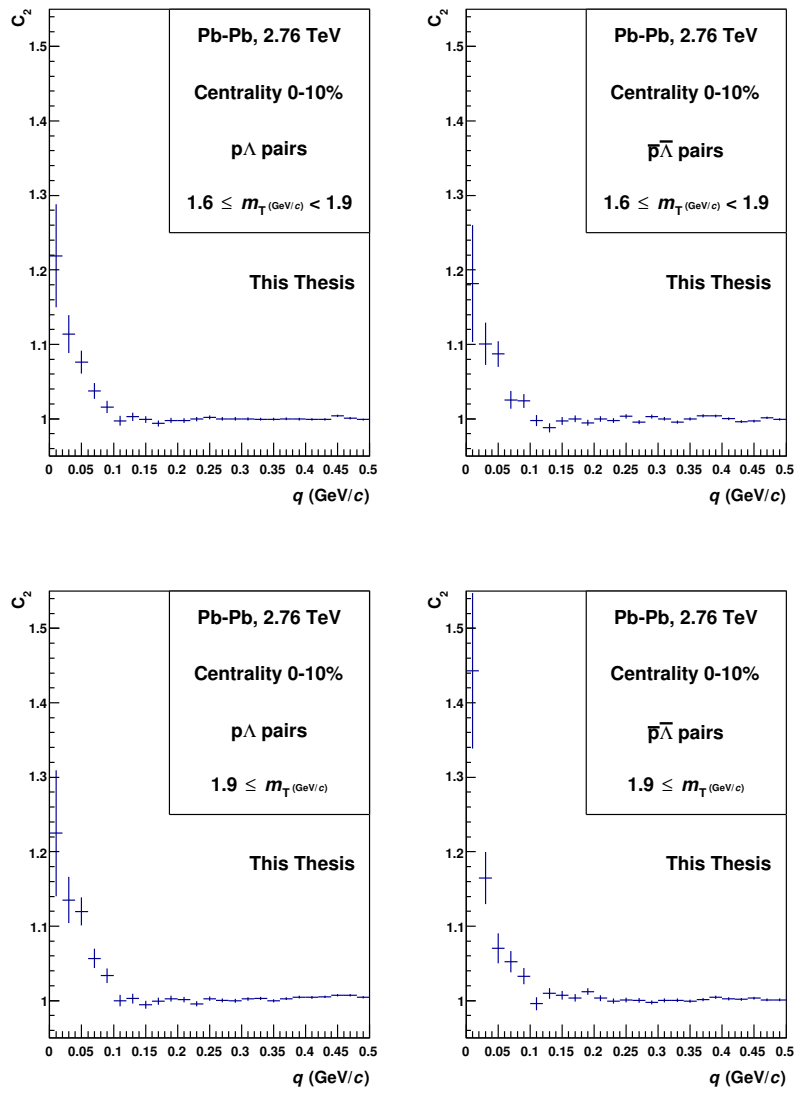


Figure F.4: Raw $p\Lambda$ correlation functions for pairs of particles and pairs of anti-particles for the 0–10% most central events in the two higher m_T bins.

F.2 Pair Statistics and Purity Fluctuations

When evaluating the pair purity, the question of the appropriate statistical uncertainty of the pair purity arises. A remedy can be found in a simple toy model with a controlled environment and known input parameters that have to be reproduced by the analysis stream. The investigated scenario is that of a single-particle purity that transforms into a pair purity.

In the experimental Pb-Pb data, the Λ purity changes with phase space, see Fig. 5.9 (right). In order to capture this variation, it was chosen here in the toy model to let the single-particle purity obey Gaussian fluctuations with a mean of 0.92 and a width of 0.015. With these values the main features of the distribution of the Λ purity in the experimental Pb-Pb data are reproduced. The purity distribution in the toy model is shown in Fig. F.5; from it, finite samples of particles are drawn. Six collections, named sample ID 0...5, with sizes ranging from $10^0 \dots 10^5$ were chosen to represent the changing number of pairs available as a function of relative pair momentum. In the simplifying spirit of toy models, each particle was assumed to only form one pair. This is a good approximation for the small relative momenta investigated in this thesis, where the number of analyzed Pb-Pb events exceeds the number of pairs at small relative momenta. The full spectrum in sampled purities for each set of finite statistics is shown in Fig. F.6.

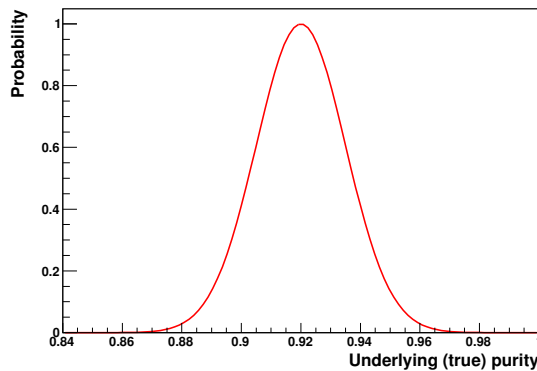


Figure F.5: True underlying purity distribution which is sampled with finite statistics in the following step.

The number of pairs is counted for each sample ID on the left side of Fig. F.7. Trivially, we find 10^0 pairs for the sample ID 0 and 10^5 for the sample ID 5. The correspondance to the raw number of pairs as a function of momentum becomes evident through the similar shapes of the distributions. (Cf. the q^2 dependence of the number of pairs in real data from phase-space.) The right side of Fig. F.7 is the distribution of the number of pairs for each sample size weighted on the pair level with the single-particle purity of Fig. F.6. With real data, the pair-purity as a function of the relative pair momentum is determined by dividing the two distributions of

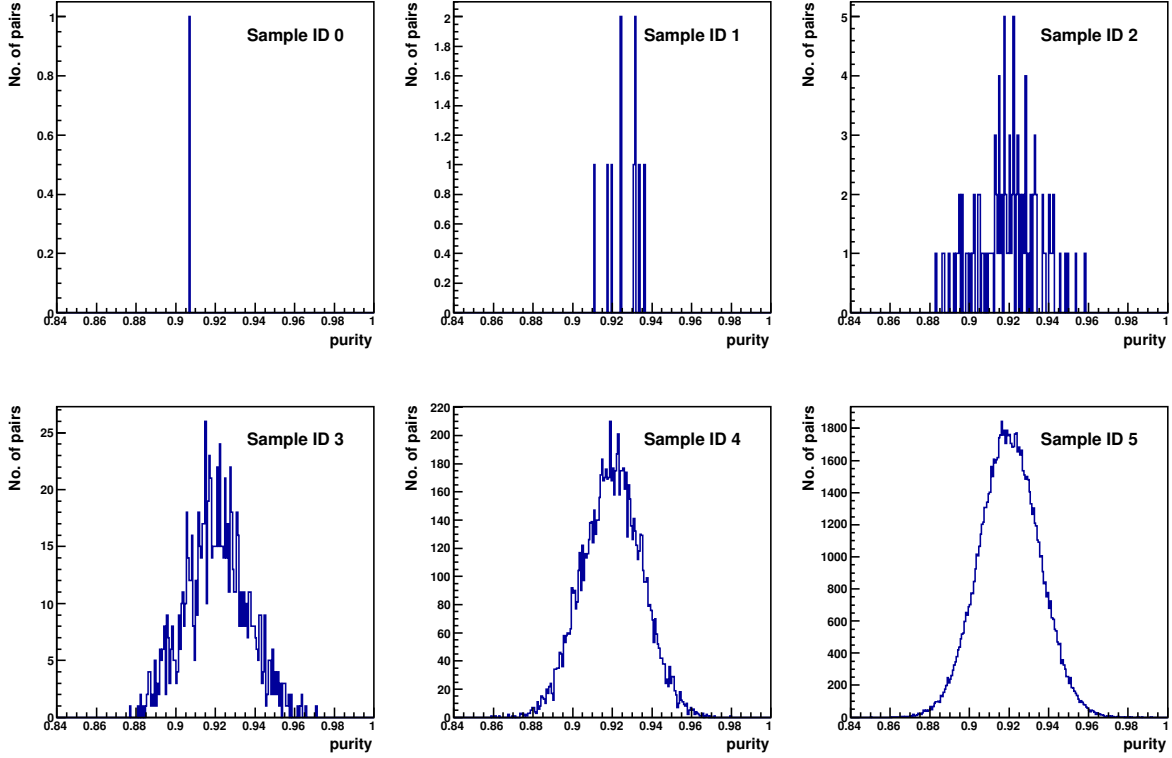


Figure F.6: Samples with the same underlying purity distribution, specifically the one of Fig. F.5, but different number of generated particles.

Fig. F.7. With the toy model, the same method is applied with various methods of calculating the statistical uncertainty. The knowledge of the true underlying distribution allows us to validate our expectations from statistical theory in a heuristic approach.

If one divides two distributions where one is a subsample of the other and a finite probability determines whether an element of the first sample also ends up in the second sample, a binomial error should describe the fluctuations of the ratio of the two distributions. In the present study of pair purities, each element, i. e. pair, of the unweighted distribution is also a member of the weighted distribution. It is therefore a natural expectation that the binomial error overestimates the fluctuation of the ratio. As can be seen on the top left plot of Fig. F.8, the binomial error calculation can not describe the fluctuation of the data points. Within the root framework, the binomial error calculation is accessible by providing “B” as an option when dividing the histograms.

The standard error calculation in a division of samples in root assumes two independent sources for the data. This standard root error is pictured in the top center plot of Fig. F.8. The assumption of uncorrelated distributions leads to the largest and most inappropriate errors of all five investigated methods. It can be concluded that doing nothing is the worst. A slightly

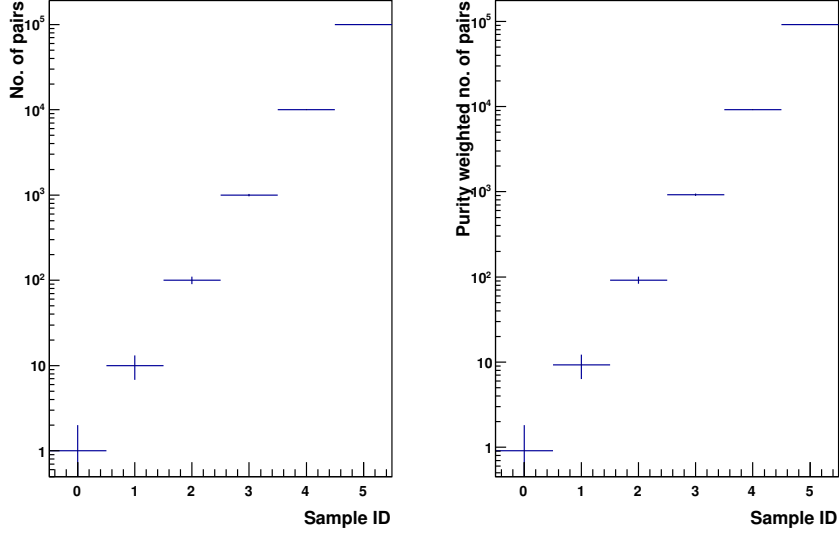


Figure F.7: Raw and purity weighed pair distribution in the toy model.

better description of the data than the standard root method is achieved when the otherwise Poissonian errors on the weighted histogram are set to zero. Still, the description of the data is worse than the binomial error.

The statistical description of the problem at hand can be found with simple considerations. We have an underlying single-particle purity distribution which fluctuates with a standard deviation of $\sigma(x)$, x represents the purity. We are interested in the mean purity for each sample ID and determine the mean with N_{Pair} probes. This situation is described by the central limit theorem, which states that the fluctuation of the experimentally determined average $\sigma(\langle x \rangle)$ decreases with the number of employed measurements N :

$$\sigma(\langle x \rangle) = \frac{\sigma(x)}{\sqrt{N}}. \quad (\text{F.1})$$

The error obtained with Eq. F.1 is shown on the bottom left of Fig. F.8. The correct representation of the statistical fluctuations for the different samples validates this approach. Scaling the binomial error with the single particle fluctuation $\sigma(x)$, i.e. 0.015 in this case, clearly underestimates the fluctuations as can be seen on the bottom center. The central limit theorem should be used for the error calculation of the purity as a function of relative momentum.

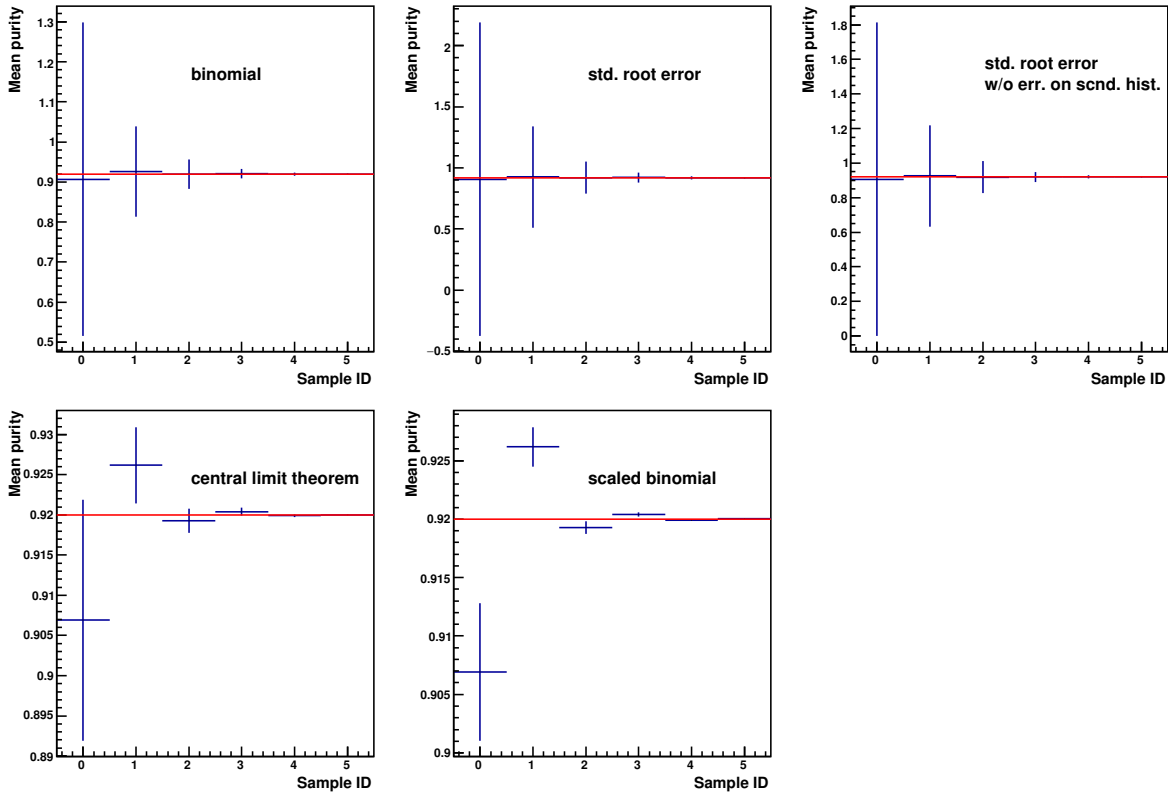


Figure F.8: Mean pair purity with different ways of calculating its uncertainty. The red line shows the expectation in the limit of infinite statistics. Only the errors derived with the central limit theorem describe the fluctuations due to the finite sampled statistics appropriately.

F.3 Possible pK_s^0 Correlation

K_s^0 can possibly be misidentified as Λ particles. Therefore, the potential exists that the $p\Lambda$ correlation function includes pairs of pK_s^0 . Within this thesis, it is assumed that such pairs would be uncorrelated. Here, we review this assumption. The pK^0 system was measured to exhibit no final-state interaction in $pp \rightarrow pK^0\Sigma^+$ events [421]. The dependence of the total cross section on the excess energy agrees with a pure phase-space effect as displayed in Fig. F.9 (left). Proton- K_s^0 correlations were also measured at the AGS by the E895 Collaboration [422]; the result is shown on the right side of Fig. F.9. No pK_s^0 correlation is visible down to lowest relative momenta. Any pK_s^0 correlation would additionally be smeared out due to the wrong mass assumption in the V^0 reconstruction. It can be concluded that the assumption of no residual correlation in the $p\Lambda$ sample from pairs of pK_s^0 indeed is justified.

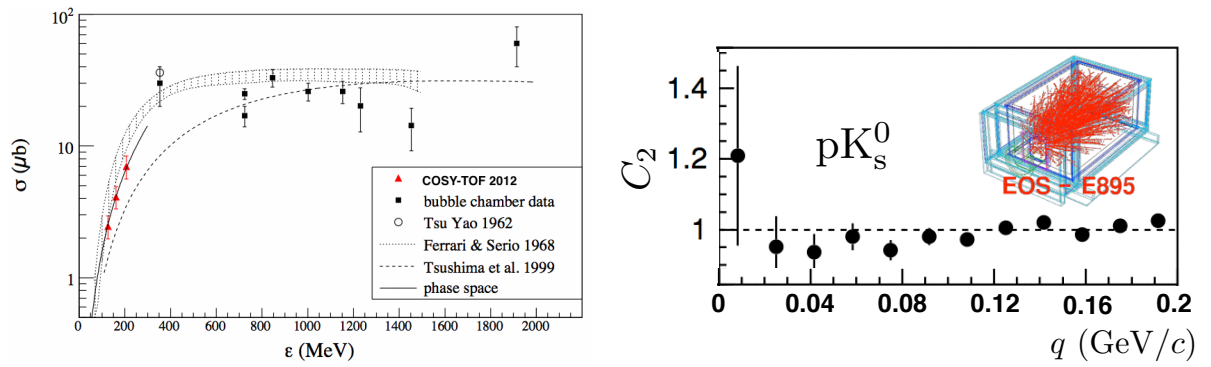


Figure F.9: Left: Cross section for $pp \rightarrow pK_s^0\Sigma^+$ as measured by the COSY-TOF Collaboration. Taken from [421]. Right: pK_s^0 correlation function as measured by the E895 experiment at the AGS. Taken from [422].

Bibliography

- [1] N. Cabibbo and G. Parisi: Exponential hadronic spectrum and quark liberation, *Phys. Lett. B* **59** (1975) 67, doi: 10.1016/0370-2693(75)90158-6.
- [2] R. Hagedorn: Statistical thermodynamics of strong interactions at high energies., *Nuovo Cimento Suppl.* **3** (1965) 147.
- [3] D.J. Gross and F. Wilczek: Ultraviolet Behavior of Non-Abelian Gauge Theories, *Phys. Rev. Lett.* **30** (1973) 1343.
- [4] H.D. Politzer: Reliable Perturbative Results for Strong Interactions?, *Phys. Rev. Lett.* **30** (1973) 1346.
- [5] O. Boyarkin: *Advanced Particle Physics: The Standard Model and Beyond*, CRC press (2011).
- [6] K.G. Wilson: Confinement of quarks, *Phys. Rev. D* **10** (1974) 2445.
- [7] A. Ukawa: Kenneth Wilson and Lattice QCD, *Journal of Statistical Physics* **0** (2015) 0, URL <http://arxiv.org/pdf/1501.04215.pdf>.
- [8] G.C. Wick: Properties of Bethe-Salpeter Wave Functions, *Phys. Rev.* **96** (1954) 1124–1134, doi: 10.1103/PhysRev.96.1124.
- [9] C.Y. Wong: *Introduction to High-Energy Heavy-Ion Collisions*, World Scientific (1994).
- [10] U. Glässner *et al.*: First evidence of N_f -dependence in the QCD interquark potential, *Phys. Lett. B* **383** (1996) 98, URL <http://arxiv.org/pdf/hep-lat/9604014.pdf>.
- [11] C.S. Fischer *et al.*: Polyakov loop potential at finite density, *Phys. Lett. B* **732** (2014) 273, URL <http://arxiv.org/pdf/1306.6022.pdf>.
- [12] S. Borsányi *et al.* (Wuppertal–Budapest Collaboration): Full results for the QCD equation of state with 2+1 flavors, *Phys. Lett. B* **730** (2014) 99, doi: 10.1016/j.physletb.2014.01.007.
- [13] A. Bazavov *et al.* (HotQCD Collaboration): Equation of state in (2 + 1)-flavor QCD, *Phys. Rev. D* **90** (2014) 094503, URL <http://arxiv.org/pdf/1407.6387v2.pdf>.

-
- [14] H. Appelshäuser *et al.* (NA49 Collaboration): Baryon Stopping and Charged Particle Distributions in Central $Pb + Pb$ Collisions at 158 GeV per Nucleon, *Phys. Rev. Lett.* **82** (1999) 2471, URL <http://arxiv.org/pdf/nucl-ex/9810014v3.pdf>.
- [15] CERN Press Release: New State of Matter created at CERN, Feb 10th 2000, URL <http://press.web.cern.ch/press-releases/2000/02/new-state-matter-created-cern>.
- [16] U. Heinz and M. Jacob: Evidence for a New State of Matter: An Assessment of the Results from the CERN Lead Beam Programme, URL <http://arxiv.org/abs/nucl-th/0002042>.
- [17] E. Laermann: Recent results from lattice QCD simulations, *Nucl. Phys. A* **610** (1996) 1c.
- [18] J.D. Bjorken: Highly relativistic nucleus-nucleus collisions: The central rapidity region, *Phys. Rev. D* **27** (1983) 141.
- [19] T. Alber *et al.* (NA49 Collaboration): Transverse Energy Production in $^{208}\text{Pb} + \text{Pb}$ Collisions at 158 GeV per Nucleon, *Phys. Rev. Lett.* **75** (1995) 3814.
- [20] I. Bearden *et al.* (NA44 Collaboration): Collective Expansion in High Energy Heavy Ion Collisions, *Phys. Rev. Lett.* **78** (1997) 2080.
- [21] H. Appelshäuser *et al.* (NA49 Collaboration): Hadronic expansion dynamics in central Pb+Pb collisions at 158 GeV per nucleon, *Eur. Phys. J. C* **2** (1998) 661.
- [22] M.M. Aggarwal *et al.* (WA98 Collaboration): Centrality dependence of neutral pion production in 158A GeV $^{208}\text{Pb} + ^{208}\text{Pb}$ collisions, *Phys. Rev. Lett.* **81** (1998) 4087.
- [23] S.K. Lee, U. Heinz, and E. Schnedermann: Search for collective transverse flow using particle transverse momentum spectra in relativistic heavy-ion collisions, *Z. Phys. C* **48** (1990) 525.
- [24] E. Schnedermann, J. Sollfrank, and U. Heinz: Thermal phenomenology of hadrons from 200A GeV S+S collisions, *Phys. Rev. C* **48** (1993) 2462.
- [25] G. Torrieri and J. Rafelski: Search for QGP and thermal freeze-out of strange hadrons, *New J. Phys.* **3** (2001) 12.
- [26] P. Braun-Munzinger, I. Heppe, and J. Stachel: Chemical equilibration in Pb+Pb collisions at the SPS, *Phys. Lett. B* **465** (1999) 15, URL <http://arxiv.org/pdf/nucl-th/9903010v2.pdf>.
- [27] F. Becattini, M. Gaździcki, and J. Sollfrank: On chemical equilibrium in nuclear collisions, *Eur. Phys. J. C* **5** (1998) 143, URL <http://arxiv.org/pdf/hep-ph/9710529v1.pdf>.
- [28] J.Y. Ollitrault: Anisotropy as a signature of transverse collective flow, *Phys. Rev. D* **46** (1992) 229, doi: 10.1103/PhysRevD.46.229.

- [29] J.Y. Ollitrault: Reconstructing azimuthal distributions in nucleus–nucleus collisions (1997), URL <http://arxiv.org/pdf/nuc1-ex/9711003v2.pdf>.
- [30] H. Appelshauser *et al.* (NA49 Collaboration): Directed and Elliptic Flow in 158 GeV/Nucleon Pb+Pb Collisions, Phys. Rev. Lett. **80** (1998) 4136, URL <http://arxiv.org/pdf/nuc1-ex/9711001v1.pdf>.
- [31] P. Kolb *et al.*: Elliptic flow at SPS and RHIC: from kinetic transport to hydrodynamics, Phys. Lett. B **500** (2001) 232, URL <http://arxiv.org/pdf/hep-ph/0012137v2.pdf>.
- [32] K.A. Olive *et al.* (Particle Data Group): 2014 Review of Particle Physics, Chin. Phys. C **38** (2014) 090001, URL <http://pdg.lbl.gov/>.
- [33] J. Rafelski and B. Müller: Strangeness Production in the Quark-Gluon Plasma, Phys. Rev. Lett. **48** (1982) 1066.
- [34] E. Andersen *et al.* (WA97 Collaboration): Strangeness enhancement at mid-rapidity in Pb–Pb collisions at 158A GeV/c, Phys. Lett. B **449** (1999) 401, doi: 10.1016/S0370-2693(99)00140-9.
- [35] B. Alessandro *et al.* (NA50 Collaboration): A new measurement of J/ψ suppression in Pb-Pb collisions at 158 GeV per nucleon, Eur. Phys. J. C **39** (2005) 335, URL <http://arxiv.org/pdf/hep-ex/0412036v1.pdf>.
- [36] T. Matsui and H. Satz: J/ψ -Suppression by Quark Gluon Plasma Formation, Phys. Lett. B **178** (1986) 416–422.
- [37] P. Debye and E. Hückel: The theory of electrolytes. I. Lowering of freezing point and related phenomena, Physikalische Zeitschrift **24** (1923) 185–206.
- [38] F. Karsch, M.T. Mehr, and H. Satz: Color screening and deconfinement for bound states of heavy quarks, Z. Phys. C **37** (1988) 617.
- [39] R. Rapp and J. Wambach: Chiral Symmetry Restoration and Dileptons in Relativistic Heavy-Ion Collisions, Advances in Nuclear Physics **25** (2002) 1, URL <http://arxiv.org/pdf/hep-ph/9909229v1.pdf>.
- [40] J. Sakurai: Theory of strong interactions, Ann. of Physics **11** (1960) 1.
- [41] C. Yang and R. Mills: Conservation of Isotopic Spin and Isotopic Gauge Invariance, Phys. Rev. **96** (1954) 191.
- [42] M. Gell-Mann and Y. Ne’Eman: The Eightfold Way, W. A. Benjamin, Inc., New York - Amsterdam (1964).
- [43] M. Gell-Mann and F. Zachariasen: Form Factors and Vector Mesons, Phys. Rev. **124** (1961) 953.

- [44] Y. Nambu: Possible Existence of a Heavy Neutral Meson, *Phys. Rev.* **106** (1957) 1366.
- [45] W. Frazer and J. Fulco: Effect of a Pion-Pion Scattering Resonance in Nucleon Structure, *Phys. Rev. Lett.* **2** (1959) 365–368.
- [46] R. Novotny for the TAPS-Collaboration: The BaF₂ Photon Spectrometer TAPS, *IEEE Trans. Nucl. Sci.* **38** (1991) 379.
- [47] T. Sjostrand: High-Energy Physics Event Generation with PYTHIA 5.7 and JETSET 7.4, *Comp. Phys. Comm.* **82** (1994) 74.
- [48] G. Alves *et al.* (E769 Collaboration): Feynman- x and Transverse Momentum Dependence of D Meson Production in 250 GeV π , K , and p Interactions with Nuclei, *Phys. Rev. Lett.* **77** (1996) 2392, URL <http://lss.fnal.gov/archive/1996/pub/Pub-96-084.pdf>.
- [49] M. Adamovich *et al.* (Beatrice Collaboration): Measurements of charmed-meson production in interactions between 350 GeV/ c π^- particles and nuclei, *Nucl. Phys. B* **495** (1997) 3, URL <http://cds.cern.ch/record/318327/files/ppe-96-180.pdf>.
- [50] G. Agakichiev *et al.* (CERES Collaboration): Low-mass $e+e^-$ pair production in 158 A GeV Pb-Au collisions at the CERN SPS, its dependence on multiplicity and transverse momentum, *Phys. Lett. B* **422** (1998) 405.
- [51] A. Drees: Low mass dilepton and photon production, *Nucl. Phys. A* **610** (1996) 536, doi: 10.1016/S0375-9474(96)00386-7.
- [52] R. Rapp and J. Wambach: Low-mass dileptons at the CERN SPS: evidence for chiral restoration?, *Eur. Phys. J. A* **6** (1999) 415.
- [53] R. Rapp and C. Gale: ρ properties in a hot meson gas, *Phys. Rev. C* **60** (1999) 024903.
- [54] R.D. Pisarski: Phenomenology of the Chiral Phase Transition, *Phys. Lett. B* **110** (1982) 115.
- [55] G.E. Brown and M. Rho: Scaling Effective Lagrangians in a Dense Medium, *Phys. Rev. Lett.* **66** (1991) 2720.
- [56] G.Q. Li, G.E. Brown, and C.M. Ko: Electromagnetic probes of dense matter in heavy-ion collisions, *Nucl. Phys. A* **630** (1998) 563.
- [57] C.M. Hung and E.V. Shuryak: Dilepton/Photon Production in Heavy Ion Collisions and the QCD Phase Transition, *Phys. Rev. C* **56** (1997) 453, URL <http://arxiv.org/abs/hep-ph/9608299>.
- [58] R. Albrecht *et al.* (WA80 Collaboration): Limits on the Production of Direct Photons in 200A GeV $^{32}\text{S}+\text{Au}$ Collisions, *Phys. Rev. Lett.* **76** (1996) 3506.
- [59] G. Agakichiev *et al.* (CERES/NA45 Collaboration): Systematic study of low-mass electron pair production in p-Be and p-Au collisions at 450 GeV/ c , *Eur. Phys. J. C* **4** (1998) 231.

- [60] U. Heinz: How to extract physics from HBT radius parameters, Nucl. Phys. A **610** (1996) 264.
- [61] H. Beker *et al.* (NA44 Collaboration): M_T -dependence of boson interferometry in heavy ion collisions at the CERN SPS, Phys. Rev. Lett. **74** (1995) 3340.
- [62] H. Appelshäuser *et al.* (NA49 Collaboration): Hadronic Expansion Dynamics in Central Pb+Pb Collisions at 158 GeV per Nucleon, Eur. Phys. J. C **2** (1998) 661, URL <http://cds.cern.ch/record/457008/>.
- [63] K.H. Ackermann *et al.* (STAR Collaboration): Elliptic flow in Au+Au collisions at $\sqrt{s_{NN}} = 130$ GeV, Phys. Rev. Lett. **86** (2001) 402, URL <http://arxiv.org/pdf/nuc1-ex/0009011v1.pdf>.
- [64] B.B. Back *et al.* (PHOBOS Collaboration): Pseudorapidity and Centrality Dependence of the Collective Flow of Charged Particles in Au+Au Collisions at $\sqrt{s_{NN}} = 130$ GeV, Phys. Rev. Lett. **89** (2002) 222301, URL <http://arxiv.org/pdf/nuc1-ex/0205021.pdf>.
- [65] K. Adcox *et al.* (PHENIX Collaboration): Flow Measurements via Two-particle Azimuthal Correlations in Au + Au Collisions at $\sqrt{s_{NN}} = 130$ GeV, Phys. Rev. Lett. **89** (2002) 212301, URL <http://arxiv.org/pdf/nuc1-ex/0204005v1.pdf>.
- [66] R.J.M. Snellings, A.M. Poskanzer, and S.A. Voloshin: Anisotropic Flow at STAR (1999), URL <http://arxiv.org/abs/nuc1-ex/9904003>.
- [67] H. Sorge: Flavor production in Pb(160A GeV) on Pb collisions: Effect of color ropes and hadronic rescattering, Phys. Rev. C **52** (1995) 3291.
- [68] M. Bleicher and H. Stöcker: Anisotropic flow in ultra-relativistic heavy ion collisions (2002), URL <http://arxiv.org/abs/hep-ph/0006147>.
- [69] P.F. Kolb, J. Sollfrank, and U. Heinz: Anisotropic transverse flow and the quark-hadron phase transition, Phys. Rev. C **62** (2000) 054909, URL <http://arxiv.org/pdf/hep-ph/0006129v2.pdf>.
- [70] D. Molnar and M. Gyulassy: Elliptic flow and freeze-out from the parton cascade MPC, Nucl. Phys. A **698** (2002) 379c, URL <http://arxiv.org/abs/nuc1-th/0104018>.
- [71] B. Back *et al.* (PHOBOS Collaboration): Charged-Particle Multiplicity near Midrapidity in Central Au+Au Collisions at $\sqrt{s_{NN}} = 56$ and 130 GeV, Phys. Rev. Lett. **85** (2000) 3100.
- [72] P. Kolb *et al.*: Elliptic Flow at SPS and RHIC: From Kinetic Transport to Hydrodynamics, Phys. Lett. B **500** (2001) 232–240, URL <http://arxiv.org/pdf/hep-ph/0012137v2.pdf>.

- [73] P.F. Kolb and U. Heinz: Hydrodynamic description of ultrarelativistic heavy-ion collisions, appeared in 'Quark Gluon Plasma 3', editors R.C. Hwa and X.-N. Wang, World Scientific, Singapore, URL <http://arxiv.org/pdf/nucl-th/0305084v2.pdf>.
- [74] P. Huovinen *et al.*: Radial and elliptic flow at RHIC: further predictions, Phys. Lett. B **503** (2001) 58, URL <http://arxiv.org/abs/hep-ph/0101136>.
- [75] The ALICE Collaboration: Long-range angular correlations of π , K and p in p-Pb collisions at $\sqrt{s_{NN}} = 5.02$ TeV, Physics Letters B **726** (2013) 164, URL <http://www.sciencedirect.com/science/article/pii/S0370269313006503>.
- [76] C. Adler *et al.* (STAR Collaboration): Identified Particle Elliptic Flow in Au+Au Collisions at $\sqrt{s_{NN}} = 130$ GeV, Phys. Rev. Lett. **87** (2001) 182301, URL <http://arxiv.org/pdf/nucl-ex/0107003.pdf>.
- [77] C. Adler *et al.* (STAR Collaboration): Azimuthal Anisotropy of K_s^0 and $\Lambda + \bar{\Lambda}$ Production at Midrapidity from Au+Au Collisions at $\sqrt{s_{NN}} = 130$ GeV, Phys. Rev. Lett. **89** (2002) 132301.
- [78] R. Snellings for the STAR and ALICE Collaborations: Anisotropic Flow from RHIC to the LHC, Eur. Phys. J. C **49** (2007) 87, URL [arXiv:nucl-ex/0610010](http://arxiv.org/abs/nucl-ex/0610010).
- [79] P. Romatschke and U. Romatschke: Viscosity Information from Relativistic Nuclear Collisions: How Perfect is the Fluid Observed at RHIC?, Phys. Rev. Lett. **99** (2007) 172301.
- [80] J.M. Maldacena: The Large N Limit of Superconformal Field Theories and Supergravity, Adv. Theor. Math. Phys. **2** (1998) 231, URL <http://arxiv.org/pdf/hep-th/9711200v3.pdf>.
- [81] P.K. Kovtun, D.T. Son, and A.O. Starinets: Viscosity in Strongly Interacting Quantum Field Theories from Black Hole Physics, Phys. Rev. Lett. **94** (2005) 111601, URL <http://arxiv.org/pdf/hep-th/0405231v2.pdf>.
- [82] J. Adams *et al.* (STAR and STAR-RICH Collaborations): Azimuthal anisotropy in Au+Au collisions at $\sqrt{s_{NN}} = 200$ GeV, Phys. Rev. C **72** (2005) 014904, URL <http://arxiv.org/pdf/nucl-ex/0409033.pdf>.
- [83] S.S. Adler *et al.* (PHENIX Collaboration): Elliptic Flow of Identified Hadrons in Au+Au Collisions at $\sqrt{s_{NN}} = 200$ GeV, Phys. Rev. Lett. **91** (2003) 182301, URL <http://arxiv.org/abs/nuclex/0305013>.
- [84] M. Luzum and P. Romatschke: Conformal Relativistic Viscous Hydrodynamics: Applications to RHIC results at $\sqrt{s_{NN}} = 200$ GeV, Phys. Rev. C **78** (2008) 034915, URL <http://arxiv.org/pdf/0804.4015.pdf>.

- [85] H. Niemi *et al.*: Influence of Shear Viscosity of Quark-Gluon Plasma on Elliptic Flow in Ultrarelativistic Heavy-Ion Collisions, *Phys. Rev. Lett.* **106** (2011) 212302.
- [86] J. Noronha-Hostler, J. Noronha, and C. Greiner: Transport Coefficients of Hadronic Matter Near T_c , *Phys. Rev. Lett.* **103** (2009) 172302.
- [87] A. Nakamura and S. Sakai: Transport coefficients of a gluon plasma, *Phys. Rev. Lett.* **94** (2005) 072305, URL <http://arxiv.org/pdf/hep-lat/0406009v1.pdf>.
- [88] J.D. Bjorken: Energy Loss of Energetic Partons in Quark-Gluon Plasma: Possible Extinction of High p_T Jets in Hadron-Hadron Collisions. (1982), FERMILAB-Pub-82/59-THY, URL <http://lss.fnal.gov/archive/1982/pub/Pub-82-059-T.pdf>.
- [89] M. Gyulassy and M. Plümer: Jet quenching in dense matter, *Phys. Lett. B* **243** (1990) 432.
- [90] X.N. Wang and M. Gyulassy: HIJING: A Monte Carlo model for multiple jet production in pp, pA, and AA collisions, *Phys. Rev. D* **44** (1991) 3501.
- [91] X.N. Wang and M. Gyulassy: Gluon Shadowing and Jet Quenching in $A + A$ Collisions at $\sqrt{s} = 200A$ GeV, *Phys. Rev. Lett.* **68** (1992) 1480.
- [92] K. Adcox *et al.* (PHENIX Collaboration): Suppression of Hadrons with Large Transverse Momentum in Central Au+Au Collisions at $\sqrt{s_{NN}} = 130$ GeV, *Phys. Rev. Lett.* **88** (2001) 022301, URL <http://arxiv.org/pdf/nuc1-ex/0109003v2.pdf>.
- [93] C. Adler *et al.* (STAR Collaboration): Centrality Dependence of High- p_T Hadron Suppression in Au+Au Collisions at $\sqrt{s_{NN}} = 130$ GeV, *Phys. Rev. Lett.* **89** (2002) 202301, URL <http://arxiv.org/abs/nuc1-ex/0206011>.
- [94] C. Adler *et al.* (STAR Collaboration): Disappearance of Back-To-Back High- p_T Hadron Correlations in Central Au+Au Collisions at $\sqrt{s_{NN}} = 200$ GeV, *Phys. Rev. Lett.* **90** (2003) 082302, URL <http://arxiv.org/pdf/nuc1-ex/0210033v1.pdf>.
- [95] J. Adams *et al.* (STAR Collaboration): Evidence from d+Au Measurements for Final-State Suppression of High- p_T Hadrons in Au+Au Collisions at RHIC, *Phys. Rev. Lett.* **91** (2003) 072304, URL <http://arxiv.org/pdf/nuc1-ex/0306024v3.pdf>.
- [96] S. Adler *et al.* (PHENIX Collaboration): Absence of Suppression in Particle Production at Large Transverse Momentum in $\sqrt{s_{NN}} = 200$ GeV d+Au Collisions, *Phys. Rev. Lett.* **91** (2003) 072303, URL <http://arxiv.org/pdf/nuc1-ex/0306021v3.pdf>.
- [97] The ALICE Collaboration: First proton-proton collisions at the LHC as observed with the ALICE detector: measurement of the charged-particle pseudorapidity density at $\sqrt{s} = 900$ GeV, *Eur. Phys. J. C* **65** (2010) 111, URL <http://arxiv.org/pdf/0911.5430v2.pdf>.

- [98] The ALICE Collaboration: Charged-particle multiplicity density at mid-rapidity in central Pb-Pb collisions at $\sqrt{s_{\text{NN}}} = 2.76$ TeV, Phys. Rev. Lett. **105** (2010) 252301, URL <http://arxiv.org/pdf/1011.3916v3.pdf>.
- [99] The ALICE Collaboration: The ALICE experiment at the CERN LHC, JINST **3** (2008) S08002, doi: 10.1088/1748-0221/3/08/S08002.
- [100] W. Busza: Trends in multiparticle production and some “predictions” for pp and PbPb collisions at LHC, J. Phys. G **35** (2008) 044040, URL <http://arxiv.org/pdf/0710.2293v1.pdf>.
- [101] W.T. Deng *et al.*: Hadron production in p+p, p+Pb, and Pb+Pb collisions with the HIJING 2.0 model at energies available at the CERN Large Hadron Collider, Phys. Rev. C **83** (2011) 014915, URL <http://arxiv.org/pdf/1008.1841v3.pdf>.
- [102] F. Bopp *et al.*: Inclusive distributions at the LHC as predicted from the DPMJET-III model with chain fusion (2007), URL <http://arxiv.org/pdf/0706.3875v1.pdf>.
- [103] M. Mitrovski *et al.*: Charged-particle (pseudo-)rapidity distributions in p + \bar{p} /p + p and Pb+Pb/Au+Au collisions from UrQMD calculations at energies available at the CERN Super Proton Synchrotron to the Large Hadron Collider, Phys. Rev. C **79** (2009) 044901, URL <http://arxiv.org/pdf/0812.2041v2.pdf>.
- [104] J.L. Albacete: CGC and initial state effects in Heavy Ion Collisions, J. Phys. Conf. Ser. **270** (2011) 012052, URL <http://arxiv.org/pdf/1010.6027v1.pdf>.
- [105] E. Levin and A.H. Rezaeian: Hadron multiplicity in pp and AA collisions at LHC from the Color Glass Condensate, Phys. Rev. D **82** (2010) 054003, URL <http://arxiv.org/pdf/1007.2430v3.pdf>.
- [106] D. Kharzeev, E. Levin, and M. Nardi: Color Glass Condensate at the LHC: hadron multiplicities in pp, pA and AA collisions, Nucl. Phys. A **747** (2005) 609, URL <http://arxiv.org/pdf/hep-ph/0408050v1.pdf>.
- [107] D. Kharzeev, E. Levin, and M. Nardi: Hadron multiplicities at the LHC (2007), URL <http://arxiv.org/pdf/0707.0811v1.pdf>.
- [108] N. Armesto, C.A. Salgado, and U.A. Wiedemann: Relating high-energy lepton-hadron, proton-nucleus and nucleus-nucleus collisions through geometric scaling, Phys. Rev. Lett. **94** (2005) 022002, URL <http://arxiv.org/pdf/hep-ph/0407018v1.pdf>.
- [109] K.J. Eskola *et al.*: Multiplicities and Transverse Energies in Central AA Collisions at RHIC and LHC from pQCD, Saturation and Hydrodynamics, Nucl. Phys. A **696** (2001) 715, URL <http://arxiv.org/pdf/hep-ph/0104010v2.pdf>.
- [110] P. Bozek *et al.*: Hydrodynamic predictions for Pb+Pb collisions at 2.76 TeV, Phys. Lett. B **694** (2010) 238, URL <http://arxiv.org/pdf/1007.2294v1.pdf>.

- [111] E.K.G. Sarkisyan and A.S. Sakharov: Relating multihadron production in hadronic and nuclear collisions, *Eur. Phys. J. C* **70** (2010) 533, URL <http://arxiv.org/pdf/1004.4390v3.pdf>.
- [112] T. Humanic: Predictions of hadronic observables in Pb+Pb collisions at $\sqrt{s_{NN}} = 2.76$ TeV from a hadronic rescattering model (2010), URL <http://arxiv.org/pdf/1011.0378v1.pdf>.
- [113] J. Stachel: First PbPb collisions at LHC at $\sqrt{s} = 2.76$ A TeV, Talk given at RETUNE2012, URL http://www.thphys.uni-heidelberg.de/~smp/RETUNE2012/talk-slides/Talk_Stachel.pdf.
- [114] The ALICE Collaboration: ALICE: Physics Performance Report, Volume I, *Journal of Physics G: Nuclear and Particle Physics* **30(11)** (2004) 1517, URL <http://stacks.iop.org/0954-3899/30/i=11/a=001>.
- [115] A. Kalweit for the ALICE Collaboration: Particle identification in the ALICE experiment, *J. Phys. G: Nucl. Part. Phys.* **38** (2011) 124073, URL <http://arxiv.org/pdf/1107.1514.pdf>.
- [116] A. Ortiz Velasquez for the ALICE Collaboration: Production of pions, kaons and protons at high p_T in $\sqrt{s_{NN}} = 2.76$ TeV Pb-Pb collisions, *Nucl. Phys. A* **904-905** (2013) 763c, URL <http://arxiv.org/pdf/1210.6995v1.pdf>.
- [117] P. Braun-Munzinger and J. Stachel: (Non)Thermal Aspects of Charmonium Production and a New Look at J/ψ Suppression, *Phys. Lett. B* **490** (2000) 196, URL <http://arxiv.org/pdf/nuc1-th/0007059v2.pdf>.
- [118] The ALICE Collaboration: J/ψ suppression at forward rapidity in Pb-Pb collisions at $\sqrt{s_{NN}} = 2.76$ TeV, *Phys. Rev. Lett.* **109** (2012) 072301, URL <http://arxiv.org/pdf/1202.1383v2.pdf>.
- [119] The ALICE Collaboration: Centrality, rapidity and transverse momentum dependence of J/ψ suppression in Pb-Pb collisions at $\sqrt{s_{NN}} = 2.76$ TeV, *Phys. Lett. B* **743** (2014) 314, URL <http://arxiv.org/pdf/1311.0214v2.pdf>.
- [120] The ATLAS Collaboration: The ATLAS Experiment at the CERN Large Hadron Collider, *JINST* **3** (2008) S08003, doi: 10.1088/1748-0221/3/08/S08003.
- [121] The CMS Collaboration: The CMS experiment at the CERN LHC, *JINST* **3** (2008) S08004, doi: 10.1088/1748-0221/3/08/S08004.
- [122] The CMS Collaboration: Observation and studies of jet quenching in PbPb collisions at $\sqrt{s_{NN}} = 2.76$ TeV, *Phys. Rev. C* **84** (2011) 024906, doi: 10.1103/PhysRevC.84.024906.
- [123] The ATLAS Collaboration: Observation of a Centrality-Dependent Dijet Asymmetry in Lead-Lead Collisions at $\sqrt{s_{NN}} = 2.76$ TeV with the ATLAS Detector at the LHC, *Phys. Rev. Lett.* **105** (2010) 252303, doi: 10.1103/PhysRevLett.105.252303.

- [124] The ALICE Collaboration: Centrality determination of Pb-Pb collisions at $\sqrt{s_{NN}} = 2.76$ TeV with ALICE, Phys. Rev. C **88** (2013) 044909, doi: 10.1103/PhysRevC.88.044909.
- [125] The ALICE Collaboration: Measurement of charged jet suppression in Pb-Pb collisions at $\sqrt{s_{NN}} = 2.76$ TeV, Journal of High Energy Physics **2014** (2014) 13, doi: 10.1007/JHEP03(2014)013.
- [126] The ATLAS Collaboration: Measurement of the jet radius and transverse momentumdependence of inclusive jet suppression in lead-lead collisions at $\sqrt{s_{NN}} = 2.76$ TeV with the ATLAS detector, Phys. Lett. B **719** (2013) 220, doi: 10.1016/j.physletb.2013.01.024.
- [127] C.A. Salgado and U.A. Wiedemann: Calculating quenching weights, Phys. Rev. D **68** (2003) 014008, URL <http://arxiv.org/abs/hep-ph/0302184>.
- [128] T. Schuster and A. László for the NA49 Collaboration: High p_T spectra of identified particles produced in Pb+Pb collisions at 158-A-GeV beam energy, J. Phys. G **32** (2006) S479, URL <http://arxiv.org/pdf/nuc1-ex/0606005.pdf>.
- [129] S.S. Adler *et al.* (PHENIX Collaboration): Scaling Properties of Proton and Antiproton Production in $\sqrt{s_{NN}} = 200$ GeV Au+Au Collisions, Phys. Rev. Lett. **91** (2003) 172301, URL <http://arxiv.org/pdf/nuc1-ex/0305036.pdf>.
- [130] J. Adams *et al.* (STAR Collaboration): Measurements of identified particles at intermediate transverse momentum in the STAR experiment from Au+Au collisions at $\sqrt{s_{NN}} = 200$ GeV, submitted to PRC, URL <http://arxiv.org/pdf/nuc1-ex/0601042v1.pdf>.
- [131] The ALICE Collaboration: K_S^0 and Λ Production in Pb-Pb Collisions at $\sqrt{s_{NN}}=2.76$ TeV, Phys. Rev. Lett. **111** (2013) 222301, doi: 10.1103/PhysRevLett.111.222301.
- [132] H. Song and U. Heinz: Suppression of elliptic flow in a minimally viscous quark-gluon plasma, Phys. Lett. B **658** (2008) 279, URL <http://arxiv.org/pdf/0709.0742v2.pdf>.
- [133] H. Song and U. Heinz: Causal viscous hydrodynamics in 2 + 1 dimensions for relativistic heavy-ion collisions, Phys. Rev. C **77** (2008) 064901, URL <http://arxiv.org/pdf/0712.3715v2.pdf>.
- [134] K. Werner: Lambda-to-Kaon Ratio Enhancement in Heavy Ion Collisions at Several TeV, Phys. Rev. Lett. **109** (2012) 102301, URL <http://arxiv.org/pdf/1204.1394v1.pdf>.
- [135] M. Veldhoen for the ALICE Collaboration: Proton to Pion Ratio in Di-Hadron Correlations, Nucl. Phys. A **910** (2013) 306, doi: 10.1016/j.nuclphysa.2012.12.103.
- [136] The ALICE Collaboration: Elliptic flow of identified hadrons in Pb-Pb collisions at $\sqrt{s_{NN}} = 2.76$ TeV, URL <http://arxiv.org/pdf/1405.4632v1.pdf>.
- [137] H. Song *et al.*: 200 AGeV Au+Au collisions serve a nearly perfect quark-gluon liquid, Phys. Rev. Lett. **106** (2011) 192301, URL <http://arxiv.org/pdf/1011.2783v2.pdf>.

- [138] H. Song *et al.*: Hadron spectra and elliptic flow for 200 A GeV Au+Au collisions from viscous hydrodynamics coupled to a Boltzmann cascade, Phys. Rev. C **83** (2011) 054910, URL <http://arxiv.org/pdf/1101.4638v2.pdf>.
- [139] H. Song, S. Bass, and U. Heinz: Spectra and elliptic flow for identified hadrons in 2.76 A TeV Pb+Pb collisions, Phys. Rev. C **89** (2014) 034919, URL <http://arxiv.org/pdf/1311.0157v2.pdf>.
- [140] The CMS Collaboration: Observation of long-range, near-side angular correlations in pPb collisions at the LHC, Phys. Lett. B **718(3)** (2013) 795, doi: 10.1016/j.physletb.2012.11.025.
- [141] The ALICE Collaboration: Long-range angular correlations on the near and away side in p–Pb collisions at $\sqrt{s_{NN}} = 5.02$ TeV, Phys. Lett. B **719** (2013) 29–41, doi: 10.1016/j.physletb.2013.01.012.
- [142] P. Bożek and W. Broniowski: Correlations from hydrodynamic flow in pPb collisions, Phys. Lett. B **718** (2013) 1557, URL <http://arxiv.org/pdf/1211.0845.pdf>.
- [143] K. Dusling and R. Venugopalan: Azimuthal collimation of long range rapidity correlations by strong color fields in high multiplicity hadron-hadron collisions, Phys. Rev. Lett. **108** (2012) 262001, URL <http://arxiv.org/pdf/1201.2658v2.pdf>.
- [144] The ALICE Collaboration: Long-range angular correlations of π , K and p in p–Pb collisions at $\sqrt{s_{NN}} = 5.02$ TeV, Phys. Lett. B **726** (2013) 164, doi: 10.1016/j.physletb.2013.08.024.
- [145] Q. Wang for the CMS Collaboration: Azimuthal anisotropy of charged particles from multiparticle correlations in pPb and PbPb collisions with CMS, Nucl. Phys. A **931** (2014) 997, doi: 10.1016/j.nuclphysa.2014.10.005.
- [146] The ALICE Collaboration: Freeze-out radii extracted from three-pion cumulants in pp, p-Pb and Pb-Pb collisions at the LHC, Phys. Lett. B **739** (2014) 139, doi: 10.1016/j.physletb.2014.10.034.
- [147] S. Adler *et al.* (PHENIX Collaboration): Systematic Studies of the Centrality and $\sqrt{s_{NN}}$ Dependence of the $dE_T/d\eta$ and $dN_{ch}/d\eta$ in Heavy Ion Collisions at Mid-rapidity, Phys. Rev. C **71** (2005) 034908, URL <http://arxiv.org/pdf/nucl-ex/0409015.pdf>.
- [148] F.R. Brown *et al.*: On the existence of a phase transition for QCD with three light quarks, Phys. Rev. Lett. **65** (1990) 2491, doi: 10.1103/PhysRevLett.65.2491.
- [149] Y. Aoki *et al.*: The order of the quantum chromodynamics transition predicted by the standard model of particle physics, Nature **443** (2006) 675, doi: 10.1038/nature05120.
- [150] R.H. Brown and R. Twiss: A Test of a NEW Type of Stellar Interferometer on Sirius, Nature **178** (1956) 1046.

- [151] G. Goldhaber *et al.*: Influence of Bose-Einstein Statistics on the Antiproton-Proton Annihilation Process, *Phys. Rev.* **120** (1960) 300.
- [152] M. Lisa *et al.*: Femtoscopy in Relativistic Heavy Ion Collisions: Two Decades of Progress, *Ann. Rev. Nucl. Part. Sci.* **55** (2005) 357, URL <http://arxiv.org/pdf/nucl-ex/0505014.pdf>.
- [153] R. Lednický: Proceedings CORINNE 90, Nantes, France (1990), World Scientific, Ed. D. Ardouin, p. 42.
- [154] R. Lednicky: Progress in correlation femtoscopy, URL <http://arxiv.org/pdf/nucl-th/0212089v1.pdf>.
- [155] G.I. Kopylov and M.I. Podgoretskij: Correlations of Identical Particles Emitted by Highly Excited Nuclei, *Sov. J. Nucl. Phys.* **15** (1972) 219.
- [156] G.I. Kopylov and M.I. Podgoretskij: Multiple production and interference of particles emitted by moving sources, *Sov. J. Nucl. Phys.* **18** (1973) 336.
- [157] G.I. Kopylov, V.L. Lyuboshits, and M.I. Podgoretskij: Particle Correlations with small relative momentum, JINR-P2-8096, Communications of the Joint Institute of Nuclear Research, Dubna (1974).
- [158] V.L. Lyuboshits and M.I. Podgoretskij: Interference correlations in detection of pairs of neutral K mesons, *Sov. J. Nucl. Phys.* **30** (1979) 407.
- [159] M.D. Steinpreis for the ALICE Collaboration: Neutral kaon femtoscopic correlations in Pb-Pb collisions with ALICE at the LHC, talk given at WPCF 2014, URL <https://indico.cern.ch/event/300974/session/10/contribution/74/material/slides/0.pdf>.
- [160] S.E. Koonin: Proton Pictures of High-Energy Nuclear Collisions, *Phys. Lett. B* **70** (1977) 43.
- [161] R. Lednicky and V.L. Lyuboshits: Effect of the final-state interaction on pairing correlations of particles with small relative momenta, *Sov. J. Nucl. Phys.* **35** (1982) 770.
- [162] M. Gyulassy, S.K. Kauffmann, and L.W. Wilson: Pion interferometry of nuclear collisions. I. Theory, *Phys. Rev. C* **20** (1979) 2267.
- [163] F. Wang and S. Pratt: Lambda-Proton Correlations in Relativistic Heavy Ion Collisions, *Phys. Rev. Lett.* **83** (1999) 3138, URL <http://arxiv.org/pdf/nucl-th/9907019v2.pdf>.
- [164] R. Lednický *et al.*: How to measure which sort of particles was emitted earlier and which later, *Phys. Lett. B* **373** (1996) 30.
- [165] S. Voloshin *et al.*: Relative space-time asymmetries in pion and nucleon production in non-central nucleus-nucleus collisions at high energies, *Phys. Rev. Lett.* **79** (1997) 4766, URL <http://arxiv.org/pdf/nucl-th/9708044v1.pdf>.

- [166] R. Bellwied: Hadron formation in the deconfined matter at RHIC and LHC, PoS **BORMIO2012** (2012) 045, URL http://pos.sissa.it/archive/conferences/160/045/Bormio2012_045.pdf.
- [167] R. Stock: Relativistic nucleus–nucleus collisions: from the BEVALAC to RHIC (2004), URL <http://arxiv.org/abs/nucl-ex/0405007>.
- [168] J. Goldhaber: Bevalac Had 40-Year Record of Historic Discoveries, Berkely Lab Science Articles Archive, URL <http://www2.lbl.gov/Science-Articles/Archive/Bevalac-nine-lives.html>.
- [169] S. Fung *et al.*: Observation of Pion Interferometry in Relativistic Nuclear Collisions, *Phys. Rev. Lett.* **41** (1978) 1592.
- [170] W.A. Zajc *et al.*: Two-pion correlations in heavy ion collisions, *Phys. Rev. C* **29** (1984) 2173.
- [171] D. Beavis *et al.*: Pion source parameters in Ar on KCl collisions, *Phys. Rev. C* **27** (1983) 910.
- [172] S. Pratt: Pion Interferometry for Exploding Sources, *Phys. Rev. Lett.* **53** (1984) 1219.
- [173] D. Teaney, J. Lauret, and E. Shuryak: Flow at the SPS and RHIC as a Quark-Gluon Plasma Signature, *Phys. Rev. Lett.* **86** (2001) 4783.
- [174] S. Akkelin and Y. Sinyukov: The HBT-interferometry of expanding sources, *Phys. Lett. B* **356** (1995) 525.
- [175] T. Csörgő and B. Lorstad: Bose-Einstein Correlations for Three-Dimensionally Expanding, Cylindrically Symmetric, Finite Systems, *Phys. Rev. C* **54** (1996) 1390, Lund Preprint LUNFD6 (NFPL-7082) (1994), URL <http://arxiv.org/pdf/hep-ph/9509213v3.pdf>.
- [176] S. Chapman, P. Scotto, and U. Heinz: Model Independent Features of the Two-Particle Correlation Function, *Heavy Ion Phys.* **1** (1995) 1, Regensburg University Preprint TPR-94-29 (1994), URL <http://arxiv.org/pdf/hep-ph/9409349v2.pdf>.
- [177] S. Pratt: Pion interferometry of quark-gluon plasma, *Phys. Rev. D* **33** (1986) 1314, doi: 10.1103/PhysRevD.33.1314.
- [178] G.F. Bertsch: Pion Interferometry As A Probe Of The Plasma, *Nucl. Phys. A* **498** (1989) 173C, doi: 10.1016/0375-9474(89)90597-6.
- [179] S. Chapman, P. Scotto, and U. Heinz: A new cross term in the two-particle Hanbury-Brown-Twiss correlation function, *Phys. Rev. Lett.* **74** (1995) 4400, URL <http://arxiv.org/pdf/hep-ph/9408207v4.pdf>.
- [180] S. Pratt: The Long Slow Death of the HBT Puzzle, *Nucl. Phys. A* **830** (2009) 51c, URL <http://arxiv.org/pdf/0907.1094v3.pdf>.

- [181] C. Adler *et al.* (STAR Collaboration): Pion Interferometry of $\sqrt{s_{\text{NN}}} = 130$ GeV Au+Au Collisions at RHIC, Phys. Rev. Lett. **87** (2001) 082301, URL <http://arxiv.org/pdf/nucl-ex/0107008v1.pdf>.
- [182] K. Adcox *et al.* (PHENIX Collaboration): Transverse-Mass Dependence of Two-Pion Correlations in Au+Au Collisions at $\sqrt{s_{\text{NN}}} = 130$ GeV, Phys. Rev. Lett. **88** (2002) 192302, URL <http://arxiv.org/pdf/nucl-ex/0201008v3.pdf>.
- [183] D. Teaney: Effect of shear viscosity on spectra, elliptic flow, and Hanbury Brown–Twiss radii, Phys. Rev. C **68** (2003) 034913, URL <http://arxiv.org/pdf/nucl-th/0301099.pdf>.
- [184] P. Božek: Flow and HBT radii from ideal and viscous hydro, talk given at the workshop on Flow and dissipation in ultrarelativistic Heavy Ion Collisions, Trento 2009, URL http://th.physik.uni-frankfurt.de/~huovinen/ect/Thursday/Bozek_Trento.pdf.
- [185] P. Božek: Flow and interferometry in (3+1)-dimensional viscous hydrodynamics, Phys. Rev. C **85** (2012) 034901, URL <http://arxiv.org/pdf/1110.6742v2.pdf>.
- [186] I.A. Karpenko and Y.M. Sinyukov: Kaon and pion femtoscopy at the highest energies available at the BNL Relativistic Heavy Ion Collider (RHIC) in a hydrokinetic model, Phys. Rev. C **81** (2010) 054903.
- [187] M. Csanád, T. Csörgő, and B. Lörstad: Buda–Lund hydro model for ellipsoidally symmetric fireballs and the elliptic flow at RHIC, Nucl. Phys. A **742** (2004) 80, URL <http://arxiv.org/pdf/nucl-th/0310040v2.pdf>.
- [188] T. Humanic: Femtoscopic signatures of collective behavior as a probe of the thermal nature of relativistic heavy ion collisions, talk given at WPCF 2009, URL <http://indico.cern.ch/event/54173/session/8/contribution/14/material/slides/1.pdf>.
- [189] L. Adamczyk *et al.* (STAR Collaboration): Freeze-out Dynamics via Charged Kaon Femtoscopy in $\sqrt{s_{\text{NN}}}=200$ GeV Central Au+Au Collisions, Phys. Rev. C **88** (2013) 034906, URL <http://arxiv.org/pdf/1302.3168v2.pdf>.
- [190] S. Afanasiev *et al.* (PHENIX Collaboration): Charged Kaon Interferometric Probes of Space-Time Evolution in Au + Au Collisions at $\sqrt{s_{\text{NN}}} = 200$ GeV, Phys. Rev. Lett. **103** (2009) 142301, URL <http://arxiv.org/pdf/0903.4863.pdf>.
- [191] M. Csanád and T. Csörgő: Kaon HBT radii from perfect fluid dynamics using the Buda-Lund model, Acta Phys. Polon. Supp. **1** (2008) 521, URL <http://arxiv.org/pdf/0801.0800.pdf>.
- [192] F. Siklér for the CMS Collaboration: Femtoscopy with identified hadrons in pp, pPb, and peripheral PbPb collisions in CMS, URL <http://arxiv.org/pdf/1411.6609v1.pdf>.

- [193] The ALICE Collaboration: Two-pion Bose–Einstein correlations in central Pb–Pb collisions at $\sqrt{s_{\text{NN}}} = 2.76$ TeV, *Phys. Lett. B* **696** (2011) 328–337, doi: 10.1016/j.physletb.2010.12.053.
- [194] L.K. Graczykowski for the ALICE Collaboration: Pion femtoscopy measurements in ALICE at the LHC, *EPJ Web of Conferences* **71** (2014) 00051, doi: 10.1051/epj-conf/20147100051.
- [195] M.P. Szymański for the ALICE Collaboration: Meson and baryon femtoscopy in heavy-ion collisions at ALICE, *Nucl. Phys. A* **904–905** (2013) 447c, doi: 10.1016/j.nuclphysa.2013.02.045.
- [196] H. Beck for the ALICE Collaboration: Femtoscopy at High m_{T} in Heavy-Ion Collisions with ALICE, *J. Phys.: Conf. Ser.* **446** (2013) 012013, doi: 10.1088/1742-6596/446/1/012013.
- [197] V. Loggins for the ALICE Collaboration: Azimuthally differential pion femtoscopy in Pb–Pb collisions at 2.76 TeV with ALICE at the LHC, *Nucl. Phys. A* **931** (2014) 1088–1092, doi: 10.1016/j.nuclphysa.2014.08.061.
- [198] S. Turbide, R. Rapp, and C. Gale: Hadronic production of thermal photons, *Phys. Rev. C* **69** (2004) 014903.
- [199] A. Adare *et al.* (PHENIX Collaboration): Enhanced Production of Direct Photons in Au+Au Collisions at $\sqrt{s_{\text{NN}}} = 200$ GeV and Implications for the Initial Temperature, *Phys. Rev. Lett.* **104** (2010) 132301, URL <http://arxiv.org/pdf/0804.4168.pdf>.
- [200] A. Adare *et al.* (PHENIX Collaboration): Observation of Direct-Photon Collective Flow in Au+Au Collisions at $\sqrt{s_{\text{NN}}} = 200$ GeV, *Phys. Rev. Lett.* **109** (2012) 122302.
- [201] F. Bock for the ALICE Collaboration: Direct-photon spectra and flow in Pb-Pb collisions at the LHC measured with the ALICE experiment, talk given at Quark Matter 2014, URL <https://indico.cern.ch/event/219436/session/16/contribution/152/material/slides/0.pdf>.
- [202] M. Wilde for the ALICE Collaboration: Measurement of Direct Photons in pp and Pb–Pb Collisions with ALICE, *Nucl. Phys. A* **904–905** (2013) 573c, doi: 10.1016/j.nuclphysa.2013.02.079.
- [203] D. Lohner for the ALICE Collaboration: Measurement of Direct-Photon Elliptic Flow in Pb-Pb Collisions at $\sqrt{s_{\text{NN}}} = 2.76$ TeV, *J. Phys.: Conf. Ser.* **446** (2013) 012028, doi: 10.1088/1742-6596/446/1/012028.
- [204] C. Shen *et al.*: Thermal photons as a quark-gluon plasma thermometer reexamined, *Phys. Rev. C* **89** (2014) 044910, URL <http://arxiv.org/pdf/1308.2440v4.pdf>.

- [205] R. Chatterjee *et al.*: Elliptic flow of thermal photons from an event-by-event hydrodynamic model, Phys. Rev. C **88** (2013) 034901, URL <http://arxiv.org/pdf/1305.6443v1.pdf>.
- [206] H. van Hees, C. Gale, and R. Rapp: Thermal photons and collective flow at energies available at the BNL Relativistic Heavy-Ion Collider, Phys. Rev. C **84** (2011) 054906, URL <http://arxiv.org/pdf/1108.2131v1.pdf>.
- [207] M. Dion *et al.*: Viscous photons in relativistic heavy ion collisions, Phys. Rev. C **84** (2011) 064901, URL <http://arxiv.org/pdf/1109.4405v3.pdf>.
- [208] O. Linnyk *et al.*: Photon elliptic flow in relativistic heavy-ion collisions: Hadronic versus partonic sources, Phys. Rev. C **88** (2013) 034904, URL <http://arxiv.org/pdf/1304.7030v2.pdf>.
- [209] M.M. Aggarwal *et al.* (WA98 Collaboration): Interferometry of Direct Photons in Central $^{208}\text{Pb}+^{208}\text{Pb}$ Collisions at 158 AGeV, Phys. Rev. Lett. **93** (2004) 022301, URL <http://arxiv.org/pdf/nuc1-ex/0310022.pdf>.
- [210] CERN: A magnet worthy of ALICE, CERN Bulletin **BUL-NA-2002-143(46/2002)** (2002) 1, cover article, URL <https://cds.cern.ch/record/46083>.
- [211] The ALICE Collaboration: Technical Design Report of the Dimuon Forward Spectrometer, CERN, Geneva (1999), URL <https://edms.cern.ch/document/470838/1>.
- [212] The ALICE Collaboration: Addendum to the Technical Design Report of the Dimuon Forward Spectrometer, CERN, Geneva (2000), URL http://aliceinfo.cern.ch/secure/system/files/documents/technical_coordination/tdr2-main.pdf.
- [213] L. Betev and P. Chochula: Definition of the ALICE Coordinate System and Basic Rules for Sub-detector Components Numbering, ALICE Internal note: ALICE-INT-2003-038, URL <http://edms.cern.ch/document/406391>.
- [214] The ALICE Collaboration: ALICE Inner Tracking System (ITS): Technical Design Report, CERN, Geneva (1999), CERN/LHCC/1999-12.
- [215] E. Bruna *et al.*: Vertex reconstruction for proton-proton collisions in ALICE (2009), URL <http://cds.cern.ch/record/1225497>.
- [216] The ALICE Collaboration: Performance of the ALICE Experiment at the CERN LHC, International Journal of Modern Physics A **29** (2014) 1430044, doi: 10.1142/S0217751X14300440.
- [217] J. Adams *et al.* (STAR Collaboration): Open Charm Yields in d+A Collisions at $\sqrt{s_{\text{NN}}} = 200$ GeV, Phys. Rev. Lett. **94** (2005) 062301, URL <http://link.aps.org/doi/10.1103/PhysRevLett.94.062301>.

- [218] L. Adamczyk *et al.* (STAR Collaboration): Measurements of D^0 and D^* production in p+p collisions at $\sqrt{s} = 200$ GeV, Phys. Rev. D **86** (2012) 072013, URL <http://link.aps.org/doi/10.1103/PhysRevD.86.072013>.
- [219] B.I. Abelev *et al.* (STAR Collaboration): Charmed hadron production at low transverse momentum in Au+Au collisions at RHIC, submitted to PRL, URL <http://inspirehep.net/record/784947/>.
- [220] Y.V. Fisyak *et al.*: Overview of the inner silicon detector alignment procedure and techniques in the RHIC/STAR experiment, Journal of Physics: Conference Series **119(3)** (2008) 032017, URL <http://stacks.iop.org/1742-6596/119/i=3/a=032017>.
- [221] S. LaPointe: D meson reconstruction at STAR using the silicon vertex tracker (svt), Dissertation, Wayne State University (2010), URL http://digitalcommons.wayne.edu/oa_dissertations/247.
- [222] C. Grupen and I. Buvat: Handbook of Particle Detection and Imaging, Springer (2012).
- [223] The ALICE Collaboration: ALICE Technical Design Report of the Time Projection Chamber, CERN, Geneva (2000), URL <http://cds.cern.ch/record/451098>.
- [224] J. Alme *et al.*: The ALICE TPC, a large 3-dimensional tracking device with fast readout for ultra-high multiplicity events, Nucl. Inst. Meth. A **622** (2010) 316, URL <http://arxiv.org/pdf/1001.1950v1.pdf>.
- [225] H.W. Ellis *et al.*: Transport Properties of Gaseous Ions Over a Wide Energy Range, Atomic data and nuclear data tables **17** (1976) 177.
- [226] The ALICE Collaboration: Upgrade of the ALICE Time Projection Chamber, CERN, Geneva (2013), URL <https://cds.cern.ch/record/1622286/files/ALICE-TDR-016.pdf>.
- [227] A. Kühmichel: New developments in high precision, high particle density tracking with time projection chambers, Nucl. Inst. Meth. A **360** (1995) 52, proceedings of the Sixth Pisa Meeting on Advanced Detectors, doi: 10.1016/0168-9002(94)01221-0.
- [228] A. Sharma: Properties of some gas mixtures used in tracking detectors, ICFA Instrumentation Bulletin **16** (1998) 3, URL <http://www.slac.stanford.edu/pubs/icfa/summer98/paper3/paper3.pdf>.
- [229] W. Leo: Techniques for Nuclear and Particle Physics Experiments: A How-to Approach, Springer (2012).
- [230] J. Baechler for the ALICE Collaboration: The ALICE TPC, proceedings of the 9th Conference on Astroparticle, Particle and Space Physics, Detectors and Medical Physics Applications, Villa Olmo, Como, Italy, 17 – 21 October 2005, URL <http://www.phys.uni-heidelberg.de/~dwiedner/DetektorenBeschleunigerWS1112/ALICETPC.pdf>.

- [231] L.D. Landau: On the energy loss of fast particles by ionization, J. Exp. Phys. (USSR) **8** (1944) 201.
- [232] J. Moyal: XXX. Theory of Ionization Fluctuations, Phil. Mag. **46** (1955) 263, doi: 10.1080/14786440308521076.
- [233] V.L. Ginzburg and I.M. Frank: Radiation of a uniformly moving electron due to its transition from one medium into another, J. Phys. USSR **9** (1945) 353.
- [234] J.D. Jackson: Classical Electrodynamics, John Wiley and Sons, Inc., third edition (1999).
- [235] F. de Abajo: Optical excitations in electron microscopy, Rev. Mod. Phys. **82** (2010) 209, URL <http://arxiv.org/pdf/0903.1669.pdf>.
- [236] The ALICE Collaboration: ALICE Technical Design Report of the Transition Radiation Detector, CERN, Geneva (2001).
- [237] X. Lu: Exploring the performance limits of the ALICE Time Projection Chamber and Transition Radiation Detector for measuring identified hadron production at the LHC, Ph.D. thesis, University of Heidelberg (2013).
- [238] M. Fasel: Single-electron analysis and open charm cross section in proton-proton collisions at $\sqrt{s} = 7$ TeV, Ph.D. thesis, Technical University of Darmstadt (2012).
- [239] D. Lohner: Anisotropic flow of direct photons in Pb-Pb collisions at $\sqrt{s_{NN}} = 2.76$ TeV, Ph.D. thesis, University of Heidelberg (2013), URL <http://archiv.ub.uni-heidelberg.de/volltextserver/15650/1/phdthesis.pdf>.
- [240] A. Wilk: Particle Identification Using Artificial Neural Networks with the ALICE Transition Radiation Detector, Ph.D. thesis, University of Münster (2010).
- [241] J. Klein for the ALICE Collaboration: Triggering with the ALICE TRD, Nucl. Inst. Meth. A **706** (2013) 23, TRDs for the Third Millennium; Proceedings of the 4th Workshop on Advanced Transition Radiation Detectors for Accelerators and Space Applications; Bari, Italy September 14-16, 2011, URL <http://www.sciencedirect.com/science/article/pii/S0168900212004986>.
- [242] J. Stiller for the ALICE Collaboration: Gain calibration of the ALICE TRD using the decay of ^{83m}Kr by internal conversion, Nucl. Inst. Meth. A **706** (2013) 20, TRDs for the Third Millennium; Proceedings of the 4th Workshop on Advanced Transition Radiation Detectors for Accelerators and Space Applications; Bari, Italy September 14-16, 2011, URL <http://www.sciencedirect.com/science/article/pii/S0168900212005062>.
- [243] C. Adler *et al.* (ALICE TRD Collaboration): Position reconstruction in drift chambers operated with Xe, CO₂ (15%), Nucl. Inst. Meth. A **540** (2005) 140, URL <http://arxiv.org/pdf/physics/0511233.pdf>.

- [244] E. Mathieson: Cathode charge distributions in multiwire chambers: 4. Empirical formula for small anode-cathode separation, Nucl. Inst. Meth. A **270** (1988) 602.
- [245] E. Sicking: Alignment of ALICE TRD Modules Using Cosmic Ray Data, Diploma thesis, University of Münster (2009).
- [246] J. Book: J/psi Production in Pb-Pb collisions with ALICE at the LHC, Ph.D. thesis, University of Frankfurt (2014), URL https://www.uni-frankfurt.de/54952831/PHD_THESIS_JULIAN_BOOK.pdf.
- [247] E. Bravin *et al.*: First results of the LHC collision rate monitors, in M. Marx *et al.*, editors, Proceedings of DIPAC2011, Hamburg, Germany (2011), p. 497, URL <http://adweb.desy.de/mpy/DIPAC2011/papers/tupd82.pdf>.
- [248] O.S. Brüning *et al.*: LHC Design Report, CERN, Geneva (2004).
- [249] E. Zeballos *et al.*: The Multigap Resistive Plate Chamber, SLAC-JOURNAL-ICFA **12** (1996) 2.
- [250] The ALICE Collaboration: Forward Detectors: FMD, T0, V0 Technical Design Report, CERN, Geneva (2004), CERN-LHCC-2004-025.
- [251] A. Alici for the ALICE Collaboration: Particle identification with the ALICE Time-Of-Flight detector at the LHC, Nucl. Inst. Meth. A **0** (2014) 0, in press, URL <http://www.sciencedirect.com/science/article/pii/S0168900214005993>.
- [252] R. Bellwied for the ALICE EMCAL Collaboration: ALICE EMCAL Physics Performance Report, URL <http://arxiv.org/abs/1008.0413>.
- [253] S.W. Moser *et al.*: Principles and Practice of Plastic Scintillator Design, Radiat. Phys. Chem. **41** (1993) 31.
- [254] E. Segré: Nuclei and Particles, Benjamin, New York (1964), URL <http://archive.org/details/ost-physics-segre-nucleiparticles>.
- [255] The ALICE Collaboration: ALICE - The Electromagnetic Calorimeter, Addendum to the Technical Proposal, CERN, Geneva (2006), CERN-LHCC-2006-014.
- [256] J. Allen *et al.*: Performance of prototypes for the ALICE electromagnetic calorimeter, Nucl. Inst. Meth. A **615** (2010) 6, URL <http://arxiv.org/pdf/0912.2005v1.pdf>.
- [257] The ALICE Collaboration: The ALICE Offline Bible, URL <http://aliceinfo.cern.ch/Offline/AlRoot/Manual.html>.
- [258] F. Antinori: Naming scheme for ALICE trigger classes, URL <http://aliweb.cern.ch/secure/Offline/sites/aliceinfo.cern.ch/secure/Offline/files/uploads/trigger/class-naming-01.pdf>.

- [259] The ALICE Collaboration: Performance of the ALICE VZERO system, *JINST* **8** (2013) P10016, doi: 10.1088/1748-0221/8/10/P10016.
- [260] T. Karavicheva for the ALICE Collaboration: ALICE Fast Interaction Trigger detector for the future, talk given at the XXX-th International Workshop on High Energy Physics, Protvino, June 23rd 2014, URL <https://indico.cern.ch/event/269671/session/1/contribution/15/material/slides/1.pdf>.
- [261] A. Maevskaya for the ALICE Collaboration: Start and Trigger Detector T0 of the ALICE Experiment, talk given at the XXI International Baldin Seminar on High Energy Physics Problems, Dubna, September 12th 2012, URL http://relnp.jinr.ru/ishepp_/presentations/Maevskaya.pdf.
- [262] The ALICE Collaboration: Kalman Filtering Application for Track Recognition and Reconstruction in ALICE Tracking System, URL <http://inspirehep.net/record/928426/files/INT-1997-24.pdf>.
- [263] B.D.O. Anderson and J.B. Moore: Optimal Filtering, Prentice-Hall, Inc., New Jersey (1979).
- [264] National Academy of Engineering: Charles Stark Draper Prize for Engineering, URL <https://www.nae.edu/Projects/Awards/DraperPrize.aspx>.
- [265] The Nobel Foundation: The Sveriges Riksbank Prize in Economic Sciences in Memory of Alfred Nobel 2011, URL http://www.nobelprize.org/nobel_prizes/economic-sciences/laureates/2011/.
- [266] The Nobel Foundation: Announcement of the 2011 Prize in Economic Sciences, URL <http://www.nobelprize.org/mediaplayer/index.php?id=1630>.
- [267] T. Sargent and J. Stachurski: Quantitative Economics, URL http://quant-econ.net/_static/pdfs/quant-econ.pdf.
- [268] L. Ljungqvist and T.J. Sargent: Recursive Macroeconomic Theory, MIT press (2012).
- [269] E. Crescio *et al.*: Performance of the ITS stand-alone tracker in pp collisions, ALICE Internal Note ALICE-INT 2009-046, URL <https://edms.cern.ch/file/1055075/1/ALICE-INT-2009-046.pdf>.
- [270] S. Bufalino for the ALICE Collaboration: Performance of ALICE Silicon Tracking Detectors, PoS **Vertex 2012** (2012) 048, URL http://pos.sissa.it/archive/conferences/167/048/Vertex%202012_048.pdf.
- [271] The ALICE Collaboration: ALICE: Physics Performance Report, Volume II, *J. Phys. G: Nucl. Part. Phys.* **32** (2006) 1295, doi: 10.1088/0954-3899/32/10/001.

- [272] A. Maire: Production des baryons multi-étranges au LHC dans les collisions proton-proton avec l'expérience ALICE, Ph.D. thesis, Université de Strasbourg (2011), URL <https://tel.archives-ouvertes.fr/tel-00746248v2/document>.
- [273] The ALICE Collaboration: ALICE Electromagnetic Calorimeter Technical Design Report, CERN, Geneva (2008), URL https://aliceinfo.cern.ch/static/Documents/EMCAL/TDR/All/alice_emcal.pdf.
- [274] X. Zhu: Neutral pion-hadron correlations in pp and Pb-Pb collisions at $\sqrt{s_{NN}} = 2.76$ TeV with ALICE, poster presented at Quark Matter 2012, URL <https://indico.cern.ch/event/181055/session/37/contribution/451/material/slides/0.pdf>.
- [275] A. Gheata: ALICE experience with ROOT I/O, talk given at the ROOT I/O Workshop and Future Plans, URL <http://indico.cern.ch/event/311573/contribution/4/material/slides/0.pptx>.
- [276] D. Vranic: ALICE TPC, talk given at the 2006 LHC days in Split, URL <http://indico.cern.ch/event/6428/contribution/28/material/slides/1.pdf>.
- [277] K. Koch: Measurement of π^0 and η mesons with photon conversions in ALICE in proton-proton collisions at $\sqrt{s} = 0.9, 2.76, 7$ TeV, Ph.D. thesis, University of Heidelberg (2012), URL <http://www.ub.uni-heidelberg.de/archiv/13113>.
- [278] S. Gorbunov and I. Kisel: Reconstruction of decayed particles based on the Kalman filter, CBM-SOFT-note-2007-003, URL <http://www.alt.gsi.de/documents/DOC-2007-May-14-1.pdf>.
- [279] F. Bock: ALICE Capabilities for Studying Photon Physics with the Conversion Method at LHC Energies, Bachelor's thesis, University of Heidelberg (2010), URL <http://www.physi.uni-heidelberg.de//Publications/Bock-Bachelorthesis.pdf>.
- [280] K. Koch for the ALICE Collaboration: π^0 and η measurement with photon conversions in ALICE in proton-proton collisions at $\sqrt{s} = 7$ TeV, Nucl. Phys. A **855** (2011) 281, URL <http://arxiv.org/pdf/1103.2217v1.pdf>.
- [281] J. Podolanski and R. Armenteros: III. Analysis of V-events, The London, Edinburgh, and Dublin Philosophical Magazine and Journal of Science: Series 7 **45** (1954) 13, doi: 10.1080/14786440108520416.
- [282] F. Bock: Neutral Pion and Eta Meson Production in pp and Pb-Pb Collisions at the LHC with the ALICE Detector, Master's thesis, University of Heidelberg (2012), URL <http://www.physi.uni-heidelberg.de//Publications/Bock-Masterthesis.pdf>.
- [283] R. Engel, J. Ranft, and S. Roesler: Hard diffraction in hadron-hadron interactions and in photoproduction, Phys. Rev. D **52** (1995) 1459, URL <http://arxiv.org/pdf/hep-ph/9502319v1.pdf>.

- [284] R. Engel and J. Ranft: Hadronic photon-photon interactions at high energies, Phys. Rev. D **54** (1996) 4244, URL <http://arxiv.org/pdf/hep-ph/9509373v1.pdf>.
- [285] T. Dahms: Measurement of photons via conversion pairs with the PHENIX experiment at RHIC, Master's thesis, Stony Brook University (2005), URL http://www.phenix.bnl.gov/phenix/WWW/publish/tdahms/master-thesis/tdahms_thesis.pdf.
- [286] A. Kisiel: Global tracking forces some pairs of tracks to have almost the same momentum, ALICE internal, URL <https://alice.its.cern.ch/jira/browse/ALIR00T-2493>.
- [287] The ALICE Collaboration: Freeze-out radii extracted from three-pion cumulants in pp, p-Pb and Pb-Pb collisions at the LHC, Phys. Lett. B **739** (2014) 139, doi: 10.1016/j.physletb.2014.10.034.
- [288] The ALICE Collaboration: Definitions of TPC related track properties, available in AliRoot under TPC/doc/Definitions/Definitions.pdf.
- [289] W. Blum, W. Riegler, and L. Rolandi: Particle Detection with Drift Chambers, Springer (2008).
- [290] The ALICE Collaboration: Midrapidity Antiproton-to-Proton Ratio in *pp* Collisions at $\sqrt{s} = 0.9$ and 7 TeV Measured by the ALICE Experiment, Phys. Rev. Lett. **105** (2010) 072002, doi: 10.1103/PhysRevLett.105.072002.
- [291] N.G.G. Ortiz: Heavy Flavour Electron Elliptic Flow, Master's thesis, University of Amsterdam (2011), URL <http://dare.uva.nl/cgi/arno/show.cgi?fid=222994>.
- [292] The ALICE Collaboration: ALICE Time-Of Flight system (TOF): addendum to the Technical Design Report, CERN, Geneva (2002).
- [293] M. Floris for the ALICE Collaboration: Identified particles in pp and Pb-Pb collisions at LHC energies with the ALICE detector, J. Phys. G **38** (2011) 124025, URL <http://arxiv.org/pdf/1108.3257v1.pdf>.
- [294] T. Anticic *et al.* (NA49 Collaboration): Proton- Λ correlations in central Pb+Pb collisions at $\sqrt{s_{NN}} = 17.3$ GeV, Phys. Rev. C **83** (2011) 054906, URL <http://arxiv.org/pdf/1103.3395v1.pdf>.
- [295] H. Beck: Proton-Lambda Korrelationen in zentralen Pb+Pb Kollisionen bei 158A GeV, Diploma thesis, University of Frankfurt (2009), URL https://edms.cern.ch/file/1110981/1/Hans_Beck.pdf.
- [296] A. Kalweit: Production of light flavor hadrons and anti-nuclei at the LHC, Ph.D. thesis, TU Darmstadt (2012), URL <http://tuprints.ulb.tu-darmstadt.de/3063/>.
- [297] T. Anticic *et al.* (NA49 Collaboration): System-size dependence of Lambda and Xi production in nucleus-nucleus collisions at 40A and 158A GeV measured at the CERN

- Super Proton Synchrotron, Phys. Rev. C **80** (2009) 034906, URL <http://arxiv.org/pdf/0906.0469v2.pdf>.
- [298] The ALICE Collaboration: Multi-strange baryon production at mid-rapidity in Pb-Pb collisions at $\sqrt{s_{NN}} = 2.76$ TeV, Phys. Lett. B **734** (2014) 409, doi: 10.1016/j.physletb.2013.11.048.
- [299] E. Schnedermann, J. Sollfrank, and U. Heinz: Thermal phenomenology of hadrons from 200A GeV S+S collisions, Phys. Rev. C **48** (1993) 2462, URL <http://arxiv.org/pdf/nucl-th/9307020v1.pdf>.
- [300] A. Andronic *et al.*: The statistical model in Pb-Pb collisions at the LHC, Nucl. Phys. A **904–905** (2013) 535c, URL <http://arxiv.org/pdf/1210.7724v1.pdf>.
- [301] A. Kisiel *et al.*: THERMINATOR: THERMal heavy-IoNgenerATOR, Comput. Phys. Commun. **174** (2006) 669, URL <http://arxiv.org/pdf/nucl-th/0504047v2.pdf>.
- [302] F. Becattini *et al.*: Hadronization, Chemical Equilibrium and Chemical Freeze-Out, PoS (CPOD 2013) (2013) 010, URL http://pos.sissa.it/archive/conferences/185/010/CPOD%202013_010.pdf.
- [303] A. Andronic, P. Braun-Munzinger, and J. Stachel: Hadron production in central nucleus-nucleus collisions at chemical freeze-out, Nucl. Phys. A **772** (2006) 167, URL <http://arxiv.org/pdf/nucl-th/0511071v3.pdf>.
- [304] The ALICE Collaboration: Centrality dependence of π , K, and p production in Pb-Pb collisions at $\sqrt{s_{NN}} = 2.76$ TeV, Phys. Rev. C **88** (2013) 044910, doi: 10.1103/PhysRevC.88.044910.
- [305] The ALICE Collaboration: $K^*(892)^0$ and $\phi(1020)$ production in Pb-Pb collisions at $\sqrt{s_{NN}} = 2.76$ TeV, submitted to Phys. Rev. C, URL <http://arxiv.org/pdf/1404.0495v2.pdf>.
- [306] M. Floris: Hadron yields and the phase diagram of strongly interacting matter, Nucl. Phys. A **931** (2014) 103, URL <http://arxiv.org/pdf/1408.6403v3.pdf>.
- [307] A. Andronic, P. Braun-Munzinger, and J. Stachel: Thermal hadron production in relativistic nuclear collisions: the hadron mass spectrum, the horn, and the QCD phase transition, Phys. Lett. B **673** (2009) 142, URL <http://arxiv.org/pdf/0812.1186v3.pdf>.
- [308] R. Lednicky: Femtoscopy with unlike particles, URL <http://arxiv.org/pdf/nucl-th/0112011v1.pdf>.
- [309] The CMS Collaboration: Femtoscopy with identified charged hadrons in pp, pPb, and peripheral PbPb collisions at LHC energies, CMS Physics Analysis Summary CMS-PAS-HIN-14-013, URL <http://cds.cern.ch/record/1703272/files/HIN-14-013-pas.pdf>.

- [310] J.L. Gramling: Azimuthally Sensitive Hanbury Brown–Twiss Interferometry measured with the ALICE Experiment, Diploma thesis, University of Heidelberg (2011), CERN-THESIS-2012-088, URL <http://cds.cern.ch/record/1463351/files/CERN-THESIS-2012-088.pdf>.
- [311] D. Antonczyk: Detailed Analysis of Two Particle Correlations in Central Pb-Au Collisions at 158 GeV per Nucleon, Ph.D. thesis, TU Darmstadt (2007), URL <http://tuprints.ulb.tu-darmstadt.de/epda/000915/>.
- [312] H. Beck: Two-track resolution study update, talk given in the ALICE femtoscopy group, Feb. 27th 2013, ALICE internal, URL <https://indico.cern.ch/event/237410/contribution/2/material/slides/0.pdf>.
- [313] H. Beck: Two-track resolution update, talk given in the ALICE femtoscopy group, Mar. 27th 2013, ALICE internal, URL <https://indico.cern.ch/event/243799/contribution/2/material/slides/0.pdf>.
- [314] J. Adams *et al.*: Proton- Λ correlations in central Au+Au collisions at $\sqrt{s_{NN}} = 200$ GeV, Phys. Rev. C **74** (2006) 064906, URL <http://arxiv.org/pdf/nuc1-ex/0511003v2.pdf>.
- [315] H. Appelshäuser: Zeiteilchenkorrelation in zentralen Blei-Blei-Reaktionen bei 158 GeV pro Nukleon, Ph.D. thesis, University of Frankfurt (1997), URL <http://cds.cern.ch/record/465800/files/sis-2000-259.pdf>.
- [316] S. Afanasiev *et al.*: The NA49 large acceptance hadron detector, Nucl. Inst. Meth. A **430** (1999) 210, URL <http://cds.cern.ch/record/377079/files/cer-000302576.pdf>.
- [317] J. Salzwedel for the ALICE Collaboration: Λ baryon femtoscopy in Pb-Pb collisions at ALICE, talk given at WPCF, URL <https://indico.cern.ch/event/300974/session/10/contribution/73/material/slides/0.pdf>.
- [318] L. Graczykowski for the ALICE Collaboration: Baryon femtoscopy in $\sqrt{s_{NN}} = 2.76$ TeV Pb-Pb collisions at ALICE, Talk given at WPCF 2012, URL <http://fias.uni-frankfurt.de/fileadmin/fias/wpcf/talks/monday/Graczykowski.pdf>.
- [319] D. Miskowicz: Two track resolution of the E877 forward spectrometer, April 3 1997, URL <http://web-docs.gsi.de/~misko/mye877/2track-resol.ps.gz>.
- [320] H. Yukawa: On the Interaction of Elementary Particles. I., Proc. Phys. Math. Soc. Japan **17** (1935) 48, URL <http://ptps.oxfordjournals.org/content/1/1.1.full.pdf>.
- [321] A. Kisiel, H.P. Zbroszczyk, and M. Szymański: Extracting baryon-antibaryon strong interaction potentials from $p\bar{\Lambda}$ femtoscopic correlation functions, Phys. Rev. C **89** (2014) 054916, URL <http://arxiv.org/abs/1403.0433>.
- [322] V. Shapoval *et al.*: Extracting $p\Lambda$ scattering lengths from heavy ion collisions, URL <http://arxiv.org/pdf/1405.3594v1.pdf>.

- [323] H.P. Zbroszczyk for the STAR Collaboration: Proton - proton, anti-proton - anti-proton, proton - anti-proton correlations in Au+Au collisions measured by STAR at RHIC, Eur. Phys. J. C **49** (2007) 75, URL <http://hal.in2p3.fr/in2p3-00131699/document>.
- [324] H.P. Zbroszczyk: Studies of Baryon-Baryon Correlations in Relativistic Nuclear Collisions Registered at the STAR Experiment, Ph.D. thesis, Warsaw University of Technology (2008), URL https://drupal.star.bnl.gov/STAR/files/Zbroszczyk_Hanna.pdf.
- [325] H.P. Zbroszczyk for the STAR Collaboration: Two-proton femtoscopy at STAR, PoS **WPCF2011** (2011) 006, URL http://pos.sissa.it/archive/conferences/154/006/WPCF2011_006.pdf.
- [326] H.P. Zbroszczyk for the STAR Collaboration: Proton femtoscopy in STAR, EPJ Web of Conferences **71** (2014) 00144, doi: 10.1051/epjconf/20147100144.
- [327] F. Wang: Residual correlation in two proton interferometry from Lambda proton strong interactions, Phys. Rev. C **60** (1999) 067901, URL <http://arxiv.org/pdf/nuc1-th/9907032v2.pdf>.
- [328] N. Shah for the STAR Collaboration: Femtoscopy of identified particles at STAR, Nucl. Phys. A (2013) 443cURL <http://arxiv.org/pdf/1210.5436v2.pdf>.
- [329] L. Adamczyk *et al.* (STAR Collaboration): The $\Lambda\Lambda$ Correlation Function in Au+Au collisions at $\sqrt{s_{NN}} = 200$ GeV, accepted in Phys. Rev. Lett., URL <http://arxiv.org/pdf/1408.4360v2.pdf>.
- [330] S. Sewerin *et al.* (COSY-11 Collaboration): Comparison of Λ and Σ^0 Production near Threshold in Proton-Proton Collisions, Phys. Rev. Lett. **83** (1999) 682, doi: 10.1103/PhysRevLett.83.682.
- [331] P. Kotwina *et al.* (COSY-11 Collaboration): Energy dependence of the Λ/Σ^0 production cross section ratio, EPJ A **22** (2004) 293, URL <http://arxiv.org/pdf/nuc1-ex/0402008.pdf>.
- [332] M. Abdel-Bary *et al.* (COSY-TOF Collaboration): Production of Λ and Σ^0 hyperons in proton-proton collisions, EPJ A **46** (2010) 27, doi: 10.1140/epja/i2010-11023-0.
- [333] H. Beck: Statistics and Pair Purity, talk given in the ALICE femtoscopy group, Oct. 31st 2012, ALICE internal, URL <https://indico.cern.ch/event/213396/contribution/2/material/slides/0.pdf>.
- [334] H. Beck for the ALICE Collaboration: Femtosopic $p\Lambda$ Correlations in Pb-Pb Collisions at $\sqrt{s_{NN}} = 2.76$ TeV, XXIV Quark Matter, Darmstadt, May 19th–24th 2014, URL <https://indico.cern.ch/event/219436/session/2/contribution/237/material/poster/0.pdf>.

- [335] R. Lednický and V.L. Lyuboshitz: The influence of final state interaction on two-particle correlations in multiple production of particles and resonances, *Heavy Ion Physics* **3** (1996) 93, doi: 10.1007/BF03053635.
- [336] H. Bethe and E. Salpeter: A Relativistic Equation for Bound-State Problems, *Phys. Rev.* **84** (1951) 1232, doi: 10.1103/PhysRev.84.1232.
- [337] L.D. Landau and E.M. Lifshitz: *Quantum Mechanics, Non-relativistic Theory*, Pergamon Press, 2nd edition (1965), URL https://archive.org/details/QuantumMechanics_104.
- [338] R.G. Newton: *Scattering Theory of Waves and Particles*, Dover, New York, 2nd edition (2002).
- [339] P. Chung *et al.* (E895 Collaboration): Comparison of Source Images for protons, π 's and Λ 's in 6 AGeV Au+Au collisions, *Phys. Rev. Lett.* **91** (2003) 162301, URL <http://arxiv.org/pdf/nuc1-ex/0212028.pdf>.
- [340] G. Agakishiev *et al.* (HADES Collaboration): Λ -p femtoscopy in collisions of Ar+KCl at 1.76A GeV, *Phys. Rev. C* **82** (2010) 021901, URL <http://arxiv.org/pdf/1004.2328v1.pdf>.
- [341] S. Pratt: CRAB - CoRrelations After Burner, URL <http://www.pa.msu.edu/~pratts/freecodes/crab/home.html>.
- [342] S. Pratt *et al.*: Testing Transport Theories with Correlation Measurements, *Nucl. Phys. A* **566** (1994) 103c, doi: 10.1016/0375-9474(94)90614-9.
- [343] The ALICE Collaboration: Two-pion Bose-Einstein correlations in central Pb-Pb collisions at $\sqrt{s_{NN}} = 2.76$ TeV, *Phys. Lett. B* **696** (2011) 328, doi: 10.1016/j.physletb.2010.12.053.
- [344] The ALICE Collaboration: Femtoscopy of pp collisions at $\sqrt{s} = 0.9$ and 7 TeV at the LHC with two-pion Bose-Einstein correlations, *Phys. Rev. D* **84** (2011) 112004, doi: 10.1103/PhysRevD.84.112004.
- [345] The ALICE Collaboration: K0s-K0s correlations in pp collisions at $\sqrt{s} = 7$ TeV from the LHC ALICE experiment, *Phys. Lett. B* **717** (2012) 151, doi: 10.1016/j.physletb.2012.09.013.
- [346] The ALICE Collaboration: Charged kaon femtoscopic correlations in pp collisions at $\sqrt{s} = 7$ TeV, *Phys. Rev. D* **87** (2013) 052016, doi: 10.1103/PhysRevD.87.052016.
- [347] A. Kisiel *et al.*: Femtoscopy in hydro-inspired models with resonances, *Phys. Rev. C* **73** (2006) 064902, URL <http://arxiv.org/pdf/nuc1-th/0602039v2.pdf>.

- [348] E. Frodermann, U. Heinz, and M.A. Lisa: Fitted HBT radii versus space-time variances in flow-dominated models, *Phys. Rev. C* **73** (2006) 044908, URL <http://arxiv.org/pdf/nucl-th/0602023v2.pdf>.
- [349] I.A. Karpenko and Y.M. Sinyukov: Energy dependence of pion interferometry scales in ultra-relativistic heavy ion collisions, *Phys. Lett. B* **688** (2010) 50, URL <http://arxiv.org/pdf/0912.3457v3>.
- [350] The ALICE Collaboration: Two- and three-pion quantum statistics correlations in Pb-Pb collisions at $\sqrt{s_{NN}} = 2.76$ TeV at the CERN Large Hadron Collider, *Phys. Rev. C* **89** (2014) 024911, doi: 10.1103/PhysRevC.89.024911.
- [351] G. Torrieri *et al.*: SHARE: Statistical Hadronization with Resonances, *Comput. Phys. Commun.* **167** (2005) 229, URL <http://www.physics.arizona.edu/~gtshare/SHARE/>.
- [352] A. Kisiel: Private communication.
- [353] H. Petersen *et al.*: Fully integrated transport approach to heavy ion reactions with an intermediate hydrodynamic stage, *Phys. Rev. C* **78** (2008) 044901, URL <http://arxiv.org/abs/0806.1695>.
- [354] T.A. Rijken and Y. Yamamoto: Extended-soft-core baryon-baryon model. II. Hyperon-nucleon interaction, *Phys. Rev. C* **73** (2006) 044008, URL <http://arxiv.org/pdf/nucl-th/0603042.pdf>.
- [355] T.A. Rijken, M.M. Nagels, and Y. Yamamoto: Baryon-baryon interactions: Nijmegen extended-soft-core models, *Prog. Theor. Phys. Suppl.* **185** (2010) 14, doi: 10.1143/PTPS.185.14.
- [356] J. Haidenbauer and U.G. Meißner: Jülich hyperon-nucleon model revisited, *Phys. Rev. C* **72** (2005) 044005, URL <http://arxiv.org/abs/nucl-th/0506019>.
- [357] A. Budzanowski *et al.* (Hires Collaboration): High resolution study of the Λp final state interaction in the reaction $p+p \rightarrow K^+ + (\Lambda p)$, *Phys. Lett. B* **687** (2010) 31, URL <http://arxiv.org/abs/arXiv:1003.0290>.
- [358] M. Steinpreis: Neutral Kaon Femtoscopy in Pb-Pb Collisions at $\sqrt{s_{NN}} = 2.76$ TeV at the LHC with ALICE, Ph.D. thesis, Ohio State University (2014), URL http://rave.ohiolink.edu/etdc/view?acc_num=osu1417696971.
- [359] V.M. Shapoval *et al.*: Femtoscopy correlations of kaons in Pb+Pb collisions at LHC within hydrokinetic model, *Nucl. Phys. A* **929** (2014) 1, URL <http://arxiv.org/abs/1404.4501>.
- [360] Y. Sinyukov *et al.*: Talk given at WPCF2014, URL <https://indico.cern.ch/event/300974/session/0/contribution/28/material/slides/0.pdf>.

- [361] A. Kisiel, M. Gałażyn, and P. Bożek: Pion, kaon, and proton femtoscopy in Pb–Pb collisions at $\sqrt{s_{NN}} = 2.76$ TeV modeled in 3+1D hydrodynamics., Phys. Rev. C **90** (2014) 064914, URL <http://arxiv.org/pdf/1409.4571v1.pdf>.
- [362] PHENIX Collaboration: High- p_T π^0 production with respect to the reaction plane in Au+Au collisions at $\sqrt{s_{NN}} = 200$ GeV, Phys. Rev. C **80** (2009) 054907, doi: 10.1103/PhysRevC.80.054907.
- [363] K. Reygers: Aufbau eines Streamer-Tube Detektors mit Pad-Auslese durch einen integrierten Schaltkreis, Diploma thesis, University of Münster (1995), URL <http://qgp.uni-muenster.de/thesisdb/dipl-reyg.ps.zip>.
- [364] A.M. Hamed for the STAR Collaboration: High- p_T direct photon azimuthal correlation measurements, Nucl. Phys. A **931** (2014) 706, doi: 10.1016/j.nuclphysa.2014.08.091.
- [365] PHENIX Collaboration: Direct photon production in d+Au collisions at $\sqrt{s_{NN}} = 200$ GeV, Phys. Rev. C **87** (2013) 054907, doi: 10.1103/PhysRevC.87.054907.
- [366] C.W. Fabjan and F. Gianotti: Calorimetry for Particle Physics, Rev. Mod. Phys. **75** (2003) 1243, URL <https://cds.cern.ch/record/692252/files/RevModPhys.75.1243.pdf>.
- [367] E. Waxman: Viewpoint: The Beginning of Extra-Galactic Neutrino Astronomy, Physics **7** (2014) 88, doi: 10.1103/Physics.7.88.
- [368] P.K.F. Grieder: Extensive Air Showers: High Energy Phenomena and Astrophysical Aspects - A Tutorial, Reference Manual and Data Book, Springer (2010).
- [369] A.M. Rossi *et al.*: Experimental study of the energy dependence in proton-proton inclusive reactions, Nucl. Phys. B **84** (1975) 269, doi: 10.1016/0550-3213(75)90307-7.
- [370] T. Stanev: High Energy Cosmic Rays, Springer (2010).
- [371] E. de Oña Wilhelmi: Separación Gamma/Hadrón con el telescopio MAGIC, Diploma thesis, Universidad Complutense de Madrid (2001), URL <http://www.gae.ucm.es/tesis/tesina-eow.ps.gz>.
- [372] R.N. Bracewell: The Fourier Transform and its Applications, McGraw-Hill (2000).
- [373] J. Kamin for the ALICE Collaboration: Neutral Pions Measured in the ALICE Electromagnetic Calorimeter in pp $\sqrt{s} = 2.76$ TeV and p-Pb $\sqrt{s_{NN}} = 5.02$ TeV, poster presented at Quark Matter 2014, URL <https://aliceinfo.cern.ch/node/24810>.
- [374] H. Beck: $\gamma\gamma$ (HBT-)Correlations - Status, presentation given in the photon conversions PAG (ALICE internal), March 2015, URL <https://indico.cern.ch/event/382445/contribution/3/material/slides/0.pdf>.
- [375] R. Matthews: Storks Deliver Babies ($p=0.008$), Teaching Statistics **22** (2000) 36, doi: 10.1111/1467-9639.00013.

- [376] D. Das *et al.* for the STAR Collaboration: Preliminary Results on Direct Photon-Photon HBT Measurements in $\sqrt{s_{NN}} = 62.4$ GeV and 200 GeV Au+Au Collisions at RHIC, NUKLEONIKA **51** (2006) S55, URL <http://arxiv.org/pdf/nucl-ex/0511055v1.pdf>.
- [377] D. Peressounko for the PHENIX Collaboration: Bose Einstein Correlations of Direct Photons in Au+Au Collisions at $\sqrt{s_{NN}} = 200$ GeV, Int. J. Mod. Phys. E **16** (2007) 2235, URL <http://arxiv.org/pdf/0704.0852v1.pdf>.
- [378] D. Peressounko: Hanbury Brown–Twiss interferometry of direct photons in heavy ion collisions, Phys. Rev. C **67** (2003) 014905, doi: 10.1103/PhysRevC.67.014905.
- [379] R. Brun *et al.*: GEANT Detector Description and Simulation Tool, CERN Program Library Long Writeup W5013.
- [380] G.C. Balbastre: Identification of particles and hard processes with the spectrometer PHOS of the ALICE experiment, Ph.D. thesis, University of Valencia and University of Nantes (2005), URL <https://tel.archives-ouvertes.fr/tel-00084765>.
- [381] S.S. Adler *et al.* (PHENIX Collaboration): Measurement of Identified π^0 and Inclusive Photon Second-Harmonic Parameter v_2 and Implications for Direct Photon Production in $\sqrt{s_{NN}} = 200$ GeV Au+Au, Phys. Rev. Lett. **96** (2006) 032302, doi: 10.1103/PhysRevLett.96.032302.
- [382] M. Klasen *et al.*: How robust is a thermal photon interpretation of the ALICE low- p_T data?, Journal of High Energy Physics **2013** (2013) 119, URL <http://arxiv.org/pdf/1307.7034v1.pdf>.
- [383] K. Symanzik: Euclidean quantum field theory, in Local quantum field theory, p. 152, edited by R. Jost (New York: Academic Press 1969).
- [384] A. Walker-Loud: Topics in Effective Field Theory for Lattice QCD, Ph.D. thesis, University of Washington (2006), URL <http://arxiv.org/pdf/hep-lat/0608010.pdf>.
- [385] R. Gupta: Introduction to Lattice QCD, Elsevier, New York (2008), URL <http://arxiv.org/pdf/hep-lat/9807028v1.pdf>.
- [386] K.G. Wilson (editor A. Zichichi): New Phenomena in Subnuclear Physics, Plenum Press (1977).
- [387] A.S. Kronfeld: Lattice gauge theory with staggered fermions: how, where, and why (not), Proceedings of Science **LAT2007** (2007) 016, URL <http://arxiv.org/pdf/0711.0699v2.pdf>.
- [388] A. Shindler: Twisted mass lattice QCD, Phys. Rept. **461** (2008) 37.
- [389] G.D. Moore: Informal Lectures on Lattice Gauge Theory, Mc Gill University (2003), URL http://www.physics.mcgill.ca/~guymoore/latt_lectures.pdf.

- [390] A. Polyakov: Thermal properties of gauge fields and quark liberation, *Phys. Lett. B* **72** (1978) 477, URL <http://www.sciencedirect.com/science/article/pii/0370269378907372>.
- [391] J. Preskill: Field Theory Lecture Notes: Quantum Chromodynamics, Caltech, URL <http://www.theory.caltech.edu/~preskill/notes.html#qcd>.
- [392] D. Tong: Lectures on String Theory, University of Cambridge, URL <http://arxiv.org/pdf/0908.0333v3.pdf>.
- [393] R.K. Ellis: Quantum Chromodynamics (2005), lectures given at Fermilab, URL <http://theory.fnal.gov/people/ellis/Talks/>.
- [394] R.K. Ellis, W.J. Stirling, and B.R. Webber: *QCD and Collider Physics*, Cambridge University Press (1996).
- [395] S.L. Adler, J.C. Collins, and A. Duncan: Energy-momentum-tensor trace anomaly in spin-1/2 quantum electrodynamics, *Phys. Rev. D* **15** (1977) 1712, doi: 10.1103/PhysRevD.15.1712.
- [396] R.A. Soltz *et al.*: Lattice QCD Thermodynamics with Physical Quark Masses, URL <http://arxiv.org/pdf/1502.02296.pdf>.
- [397] A. Bilandzic: Anisotropic Flow Measurements in ALICE at the Large Hadron Collider, Ph.D. thesis, Universiteit Utrecht (2012), URL <http://cds.cern.ch/record/1432210/files/CERN-THESIS-2012-018.pdf>.
- [398] B. Schenke, S. Jeon, and C. Gale: (3+1)D hydrodynamic simulation of relativistic heavy-ion collisions, *Phys. Rev. C* **82** (2010) 014903, URL <http://arxiv.org/pdf/1004.1408v2.pdf>.
- [399] B. Schenke, S. Jeon, and C. Gale: Elliptic and Triangular Flow in Event-by-Event $D = 3 + 1$ Viscous Hydrodynamics, *Phys. Rev. Lett.* **106** (2011) 042301, URL <http://arxiv.org/pdf/1009.3244v2.pdf>.
- [400] B. Schenke, S. Jeon, and C. Gale: Higher flow harmonics from (3 + 1)D event-by-event viscous hydrodynamics, *Phys. Rev. C* **85** (2012) 024901, URL <http://arxiv.org/pdf/1109.6289v2.pdf>.
- [401] C. Gale, S. Jeon, and B. Schenke: Hydrodynamic Modeling of Heavy-Ion Collisions, *Int. J. of Mod. Phys. A* **28** (2013) 1340011, URL <http://arxiv.org/pdf/1301.5893v1.pdf>.
- [402] A. Chodos *et al.*: New extended model of hadrons, *Phys. Rev. D* **9** (1974) 3471.
- [403] A. Chodos *et al.*: Baryon structure in the bag theory, *Phys. Rev. D* **10** (1974) 2599.
- [404] J. Gibbs: A Method of Geometrical Representation of the Thermodynamic Properties of Substances by Means of Surfaces, *Transactions of the Connecticut Academy* **2** (1873) 382.

- [405] K. Yagi, T. Hatsuda, and Y. Miake: Quark-Gluon Plasma: From Big Bang to Little Bang, Cambridge University Press (2006).
- [406] J. Collins, A. Duncan, and S. Joglekar: Trace and dilatation anomalies in gauge theories, Phys. Rev. D **16** (1977) 438.
- [407] V. Gogokhia: Energy From The Nonperturbative QCD Vacuum, URL <http://arxiv.org/pdf/hep-ph/0508224v2.pdf>.
- [408] M. Shifman, A. Vainshtein, and V. Zakharov: QCD and Resonance Physics. Applications, Nucl. Phys. B **147** (1979) 448.
- [409] D.E. Miller: Lattice QCD calculations for the physical equation of state, Physics Reports **443** (2007) 55.
- [410] H. Wieman *et al.*: STAR TPC at RHIC, IEEE Transactions on Nuclear Science **44(3)**.
- [411] S. Afanasiev *et al.* (NA49 Collaboration): The NA49 Large Acceptance Hadron Detector, Nucl. Instrum. Meth. A **430** (1999) 210, URL <https://edms.cern.ch/document/815848/1>.
- [412] A. Marin for the CERES Collaboration: First results from the CERES radial TPC, Nucl. Phys. A **661** (1999) 673c, Quark Matter 99, Proc. Int. Conf. on Ultra-Relativistic Nucleus-Nucleus Collisions, Torino, 1999.
- [413] J. Lien *et al.*: Time projection chambers (TPC) in heavy ion experiments, Eur. Phys. J. C **33** (2004) s1017, doi: 0.1140/epjd/s2004-03-1799-6.
- [414] C. Ramsauer: Über den Wirkungsquerschnitt der Gasmoleküle gegenüber langsamen Elektronen, Annalen der Physik **369** (1921) 513–540, URL <http://gallica.bnf.fr/ark:/12148/bpt6k153664/f515.image.langFR>.
- [415] J. Townsend and V. Bailey: The motion of electrons in argon, Philosophical Magazine Series 6 **43** (1922) 593, URL <http://www.tandfonline.com/doi/pdf/10.1080/14786442208633916>.
- [416] N.F. Mott and H.S.W. Massey: The theory of atomic collisions, Oxford: Clarendon Press, third edition (1965).
- [417] A. Kramida *et al.*: Atomic Spectra Database, National Institute of Standards and Technology, <http://physics.nist.gov/asd> (2013).
- [418] R. van Harrevelt: Photodissociation of methane: Exploring potential energy surfaces, The Journal of Chemical Physics **125** (2006) 124302.
- [419] R. Bramm: Characterisation of the ALICE TPC READOUT CHIP, Ph.D. thesis, University of Frankfurt (2005), URL <http://publikationen.ub.uni-frankfurt.de/files/3103/Doktorarbeit.pdf>.

-
- [420] B. Mota *et al.*: Performance of the ALTRO chip on data acquired on an ALICE TPC prototype, Nucl. Inst. Meth. A **535** (2004) 500, proceedings of the 10th International Vienna Conference on Instrumentation, doi: 10.1016/j.nima.2004.07.179.
- [421] M. Abdel-Bary *et al.* (COSY-TOF Collaboration): The $pK^0\Sigma^+$ final state in proton-proton collisions, Eur. Phys. J. A **48** (2012) 23, doi: 10.1140/epja/i2012-12023-8.
- [422] P. Chung for the E895 Collaboration: Neutral strange particle dynamics in Au+Au collisions at AGS energies, J. Phys. G: Nucl. Part. Phys. **28** (2002) 1567.

Curriculum Vitae

Hans Beck

Born May 31st 1984 in Friedberg (Hessen), Germany

Education

- 2010–2015 **Doctoral student** at the Goethe University Frankfurt,
Thesis “Femtoscopic $p\Lambda$ and $\gamma\gamma$ Correlations in Pb-Pb collisions at $\sqrt{s_{\text{NN}}} = 2.76$ TeV with ALICE”, advisor Prof. Dr. C. Blume, member of the Helmholtz Research School for Quark Matter Studies, member of the Helmholtz Graduate School for Heavy Ion Research, member of the Frankfurt Institute for Advanced Studies
- 2010 **Diploma** in physics **with distinction**,
mark “very good” (**best achievable mark**)
Thesis “Proton-Lambda Korrelationen in zentralen Pb+Pb-Kollisionen bei 158A GeV”, advisor Prof. Dr. C. Blume
- 2007–2015 Member of the high-energy nuclear physics group at the
Institut für Kernphysik at the Goethe University Frankfurt
- 2006 Pre diploma, mark “very good” (**best achievable mark**)
- 2004–2010 Physics course at the Goethe University Frankfurt
- 2003 Abitur at the Main-Taunus-Schule in Hofheim, Germany